

IMS'2001, IEEE MTT-S Int. Microwave Symp. Digest, 2001, Vol. 3, pp. 1441–1444.

41. M. Houdart, Coplanar lines: application to broadband microwave integrated circuits, *Proc. EuMC'76, 6th European Microwave Conf.*, 1976, pp. 49–53.
42. L. Nenert, A. Cenac, L. Billonnet, B. Jarry, P. Guillon, C. Quendo, E. Rius, and G. Tanne, Use of coplanar technology advantages for tunable active planar looped filter structures optimised in noise, *Proc. EuMC'2000, 30th European Microwave Conf.*, 2000.
43. E. Rius, T. Le Gouguec, K. Hettak, J. Ph. Coupez, and S. Toutain, Broadband high directivity 3 dB coupler using coplanar waveguide technology, *IMS'95, IEEE MTT-S Int. Microwave Symp. Digest*, 1995, pp. 671–674.
44. M. Delmond, L. Billonnet, B. Jarry, and P. Guillon, High-order monolithic active recursive filter based upon multicellular approach, *IMS'96, IEEE MTT-S Int. Microwave Symp. Digest*, 1996, Vol. 2, pp. 623–626.

ACTIVE FILTERS: TOOLS AND TECHNIQUES FOR ACTIVE-FILTER DESIGN

LAURENT BILLONNET
BERNARD JARRY
BRUNO BARELAUD
University of Limoges
Limoges Cedex, France

1. INTRODUCTION

Whatever the application is, all communications systems—whether cellular, PCS, cable or satellite—require, in increasing quantity, a range of microwave filters with near-ideal characteristics to maximize communication capacity and signal processing efficiency and thus lower system costs. To satisfy these demands, engineers try to come up with design innovations and improved manufacturing processes of new filtering devices to reduce the cost of high-frequency communications. Since the early 1990s, engineers have also been increasingly interested in using active techniques for their compatibility with planar integrated monolithic technologies. Since the first microwave circuit was designed using a GaAs-based process, more and more attempts have been done nowadays to switch to silicon-based processes because of the resulting compact size and low-cost aspects.

We follow and gradually illustrate this tendency in this article. We first discuss the use of CAD tools for microwave and RF filter design, focusing particularly on optimization tools. We emphasize that, without any strong microwave design background and experience, this kind of tool unavoidably leads to nonreproducible and nonsystematic solutions. We then show the necessary implementation of analytical procedures to set and verify some essential characteristics of low-noise active devices, with examples of electrical stability criteria and noise performance calculation, prediction, and optimization. These two

examples are illustrated through many integrated filter designs and measurements.

Section 3 deals with the description of tools and techniques for filter improvements. We first begin with an extended consideration of compensation techniques based not only on loss compensation but also on response selectivity and circuit dimensions. The technique is illustrated with the design of a one-pole interdigital filter and a two-pole coplanar filter in which response and size have been improved using this approach. We then generalize this principle to the “active-impedance profile” (AIP) technique and present an example application to multistandard and pseudomultipole filters.

In Section 4, novel approaches and new technologies for new microwave and RF communications needs are detailed. We first discuss the new application constraints driven by new communication standards. We then discuss GaAs processes to silicon-based technologies, emphasizing the differences between the two technologies in terms of processes themselves, and in terms of CAD tools, component implementation, compactness, relative size, and cost with two basic circuit examples. Migration to silicon-based processes also involves novel implementation approaches among which differential circuits. This last approach is illustrated with experimental results.

2. ANALYTICAL TOOLS AND PROCEDURES FOR ACTIVE FILTER DESIGN

2.1. Numerical CAD Optimization Tools

Since 1980, scientific production on microwave filters has grown extensively. This extension finds its sources from a technical perspective in:

- A permanent growth in device complexity
- A constant objective of reduction in size and weight
- The use of new materials and new technologies (superconductor materials, MEMs, planar monolithic technologies, etc.)

However, any experimented engineer knows that this growth of production is fueled mostly by novel modern computing systems and by the extraordinarily growing computation capabilities.

Without this computation power, many application would still be only perspectives:

- The development of precise electromagnetic simulation methods for planar (2D or 2.5D) or volumic (3D) circuits, such as the finite-element method, method of lines, or modal analysis
- The development of numerical synthesis methods taking into account a larger number of parameters such as losses or process limitations
- Global analysis methods simultaneously coupling in a single step various sorts of analysis that are sometimes very different

From the beginning of their careers today's engineers can use numbers of synthesis, analysis, and statistical tools, and more importantly of optimization tools that can strongly help the design. For the beginner, the danger is in believing that this complete set of tools can lead, with security, to synthesis and analysis of any microwave function without either a strong knowledge or preliminary analytical studies. In particular, the riskiest tool is, without any doubt, the optimizer, which is still for some designer a "miracle" (or panacea) tool that always leads to the "best" solution.

In fact, any optimiser must be used with great care and attention:

- In practice, it should be used only at the last step of a design, after the synthesis procedure, to fine-tune the different parameters of the problem. If not, it does not mean any reproducibility in the approach and is based only on a hazardous random starting point. It does not enable any understanding or feedback of the results obtained.
- It never leads in a systematic way to "the" best solution, but usually only to a mathematically local set of parameters.
- Depending on the number of optimization constraints and the nature of each separate constraint (response level, noise, compression point, etc.), the major difficulty is the weight of the different constraints from one to the other. The optimizer then does not permit one to systematically analyze the influence of a given parameter (geometric or electrical) on the whole set of circuit characteristics.

Using such tools without any theoretical background, without experience, or without any preliminary analytical study, even simplified, does not reveal an efficient, fast, and operational investigator. The primary objective must be the implementation of rigorous analytical procedures to investigate any problem that can be encountered at each design step of an active device.

2.2. Examples of Analytical Tools and Procedures at Microwaves

We describe here two examples of analytical procedures that can facilitate understanding of the influence of a parameter on a given filter characteristic. These two examples focus on low-noise circuits in the linear regime.

2.2.1. Analysis and Optimization of Noise Performance. For any applications using circuits with active elements, the problem of noise performance is a critical point that must be studied. In this subsection, the purpose is not to describe well-known methods or formalisms classically applied at the component level (e.g., how to determine the optimal loads of a transistor to be at the minimum noise power); rather this discussion is dedicated to determining

- The contribution of an active function in terms of system components, to the noise of a more complex structure (e.g., an amplifier within a recursive filter, or a negative resistance within a resonator-based filter)
- The optimal location of an active function within a global structure [1]
- An analytical optimization method of the noise characteristics of a global structure in which is integrated an active function, while maintaining given filtering characteristics

The discussion here is intended to help the designer better predict the influence of active parts or components by analytical means.

Several methodologies have been studied to evaluate or model noise performances, depending on the type of electrical parameters that are considered. Here, we choose to use a noise-wave formalism described by Wedge and Rutledge [2]. This formalism takes advantage of the S -parameter description. However, other formalisms using currents or voltages instead of power waves also exist, based on the same principles.

Analytical derivation of noise performance using the noise-wave formalism is done by gradually reconnecting parts of a global device for which S parameters and the noise matrix are known. An interesting way to illustrate the approach is to evaluate the noise factor of microwave active recursive filters. Other structures are studied in Ref. 3. As shown in Fig. 1, the noise-wave formalism consists in modeling the noise of a two-port device with internal noise-wave generators c_1 and c_2 .

Their contribution to the output scattering waves b_1 and b_2 can be expressed in the following manner, where S is the scattering matrix of the two-port Q :

$$\begin{pmatrix} b_1 \\ b_2 \end{pmatrix} = \begin{pmatrix} S_{11} & S_{12} \\ S_{21} & S_{22} \end{pmatrix}_Q \begin{pmatrix} a_1 \\ a_2 \end{pmatrix} + \begin{pmatrix} c_1 \\ c_2 \end{pmatrix} \quad (1)$$

Regarding the first-order recursive topology of the article ACTIVE FILTERS: OVERVIEW OF ACTIVE-FILTER STRUCTURES, Section 4.2, the circuit consists in two power dividers/combiners, one delay element, and one amplifier. Depending on where the amplifier is placed within the structure (in the feedback or in the direct branch), two topologies can be derived (Fig. 2). In the passband case, the problem is then to find, for each topology, the gain value G , noise factor value F_A , and the two coupling values

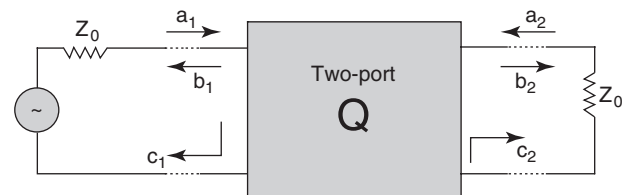


Figure 1. Two-port circuit described by noise waves and scattering parameters.

- A systematic approach for the analytical derivation of noise performances

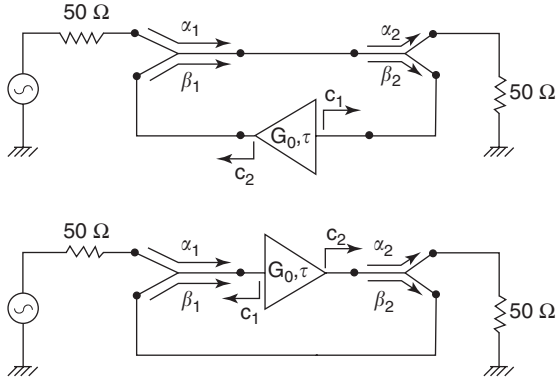


Figure 2. First-order recursive filter topologies: amplifier placed (a) in the feedback branch and (b) in the direct branch.

at the input and output of the filter, to obtain a given response shape with a minimum noise factor at center frequency. To calculate the minimum noise factors of the two topologies, we first consider the R and V selectivity parameters that set the filtering performances. These parameters must not be modified during the improvement process of the noise factor and set the frequency shape of the response. f_0 is the center frequency.

$$R = \frac{|S_{21}|_{\max}}{|S_{21}|_{\min}} = \frac{|S_{21}(f_0)|}{|S_{21}(f_0/2)|}, \quad V = \frac{R-1}{R+1} \quad (2)$$

The two corresponding filters are considered as equivalent when they are characterized by the same V parameter even if they do not achieve the same gain at the center frequency f_0 . The transfer functions of the two topologies can then be expressed as follows with the selectivity parameter $V = \beta_1\beta_2G_0$, $G = G_0 e^{-2j\pi f\tau}$, where G_0 is a positive real gain and the delay time τ is introduced:

$$H_i(f) = \frac{K_i}{1 - V e^{-2j\pi f\tau}} \quad (3)$$

For topology 1 (Fig. 2a), the transfer function and the noise factor at f_0 , the center frequency, are analytically derived through the reconnecting method, as functions of β_1 , G_0 , and F_A (the noise factor of the amplifier that can also be derived from the same noise-wave formalism):

$$H_1(f) = \frac{\alpha_1\alpha_2}{1 - G\beta_1\beta_2}; \quad F_1 = 1 + \left(\frac{\beta_1}{\alpha_1}\right)^2 (F_A - 1)G_0^2 + \left(\frac{\beta_2 - \beta_1G_0}{\alpha_1\alpha_2}\right)^2 \quad (4)$$

F_1 can also be expressed as a function of β_1 , G_0 , F_A and more importantly of V to maintain the filter response shape. For a given amplifier, β_1 appears as a degree of freedom that can be used to optimize the noise factor. It can even be shown that for the optimal value of $\beta_1 = \beta_{1\text{opt}}$, $F_1 < F_A$ when $G_0 \rightarrow \infty$.

Using the same methodology for topology 2, the transfer function $H_2(f)$ and the corresponding noise factor F_2

are given by:

$$H_2(f) = \frac{G\alpha_1\alpha_2}{1 - G\beta_1\beta_2}; \quad F_2 = 1 + \frac{(F_A - 1)}{\alpha_1^2} + \left(\frac{\beta_2 - \beta_1G_0}{\alpha_1\alpha_2G_0}\right)^2 \quad (5)$$

The expression of $\beta_{1\text{opt}}$ is the same as for topology 1 but leads to $F_2 > F_A$ at f_0 . The analytical procedure enables us to find that topology 1 is better than topology 2 in terms of the noise factor, which could not have been derived by using a classical CAD optimizer. Simulations show on one hand the noise factors increase when the selectivity increases, and on the other hand when the gain is increased (for the same F_A of the amplifier), the noise factor of the filter decreases as expected.

To experimentally validate our approach, we have designed a first-order recursive filter from topology 1 in MMIC technology. This filter, the layout of which is given in Fig. 3, has the same filtering performance as that described in Section 4.2 (Fig. 20) of the article overviews active-filter structures [cited above, immediately following Eq. (1)]. Couplings (through the use of Lange couplers [4,5]) and gain values are chosen to obtain the lowest noise factor according to the analysis presented. Measured noise figure is equal to 2.1 dB, in contrast to the initial 11.7 dB.

2.2.2. Analytical Tools for Electrical Stability Analysis and Optimization. Several stability criteria are used at microwaves to evaluate the electrical stability of a circuit. Most techniques used are based on the Rollett factor K [6,7] defined through two-port S parameters. However, these factors are not quantitative, and additional parameters must be calculated to get more information. Plots of μ factor [8] or stability circles can then be calculated to give the reader an idea of the stability margin and the location, respectively, of the load impedances that can lead to instability.

In terms of design, these criteria present many disadvantages:

- In most cases, filters are designed to be terminated (directly or in cascade with other modules) with 50 Ω impedances. In case of conditional stability, the

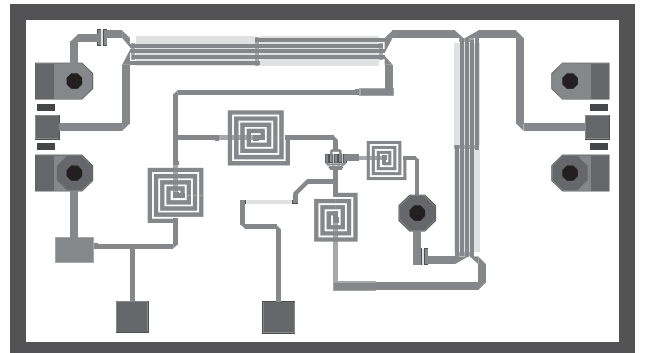


Figure 3. Layout of the low-noise first-order active recursive filter.

Rollett factor does not predict the impedances for which the instability is observed. It is then necessary to plot the stability circles, thus clearly complicating the engineer's work.

- Another important point directly concerns the validity of classical parameters. Indeed, interpretation of classical parameters (including stability circles) leads to a valid evaluation of stability only when the circuit is intrinsically stable, independently of the terminations. The designer must then, in a first step, be sure of the intrinsic stability of the device.
- Finally, for more complex circuits, classical stability parameters cannot analytically predict the influence of a component or a circuit characteristic, and therefore lead to efficient modification of the adequate parameter in case of instability.

Many researchers have attempted to solve the problem with methods derived from Bode's theory [9] among which Ohtomo [10] and Platzker [11]. We describe this last approach here. The normalized determinant function (NDF) approach is an extension of Bode's theory for circuits with more than two ports and multiple feedbacks. Without discussing the details, analysis of a mathematical complex function leads to a plot in an image complex plane. The function considered here is defined as the ratio of the determinant of the nodal description matrix of the circuit when all the sources are in ON state, to the determinant of the same matrix when all the sources are in OFF state. Interpretation of the resulting plot in the image plane results from Cauchy's theorem. If the plot encircles the origin of the image plane in the clockwise direction, then the circuit is unstable. There are as many instabilities as encirclements. Frequencies of instabilities can be extracted by searching the roots of the NDF.

The originality of the method resides in the return ratio (RR) principle [12], which allows analysis with a classical CAD package. With this method, each transistor is modeled as a voltage-controlled current source. All these sources, one by one, are driven by an external voltage instead of their initial internal voltage. The corresponding

RR is then defined as the ratio of the initial internal voltage to the external one. At each step of the calculation, all sources for which the RR has been calculated are turned off. Finally, expression of the NDF is derived from the n RRs (for a n -source or a n -transistor circuit).

Note that this approach, when numerically used through a CAD package, does not allow any interpretation of any parameter on the circuit stability. However, in this case, classical optimization is still possible.

With a strict calculation approach, analytical expression of the NDF can be obtained, thus allowing the evaluation of each parameter influence not only on the stability itself but also on the frequency where instabilities occur. To illustrate this point, we consider the first-order filter discussed in Section 4.2 (Fig. 19) of the article cited above [following Eq. (1)], where Lange couplers are used for division/summation of the signals within the structure [13]. We first model the ideal amplifier of the structure with an equivalent voltage-controlled current source terminated with two $50\ \Omega$ impedances. In Fig. 4, the ideal amplifier has been replaced by its equivalent dependent source. Because of the unilaterality property of this source, we now obtain a new open-loop two-port device loaded by a generator of internal impedance $50\ \Omega$ at the input, and with a $50\ \Omega$ impedance at the output. Initial input and output ports are also assumed to be terminated with a $50\ \Omega$ impedance. The current source is controlled by an external voltage V_{ext} .

The NDF is then derived through the RR calculation. It shows that the zeros location in the complex plane for $\text{NDF}(f)$ (i.e., the location of instabilities) is equivalent to the zeros location of the denominator of the transfer function of the filter $H(f)$. In other words, zeros of the NDF are equivalent to the poles of the response.

Using the same principles, we now consider a second-order recursive filter, for which the two amplifiers G_1 and G_2 are substituted with dependent current sources. Calculation of the NDF is obtained in two steps corresponding to the calculation of the two RRs:

$$\text{NDF}(f) = (1 + \text{RR}_1(f)) \cdot (1 + \text{RR}_2(f))$$

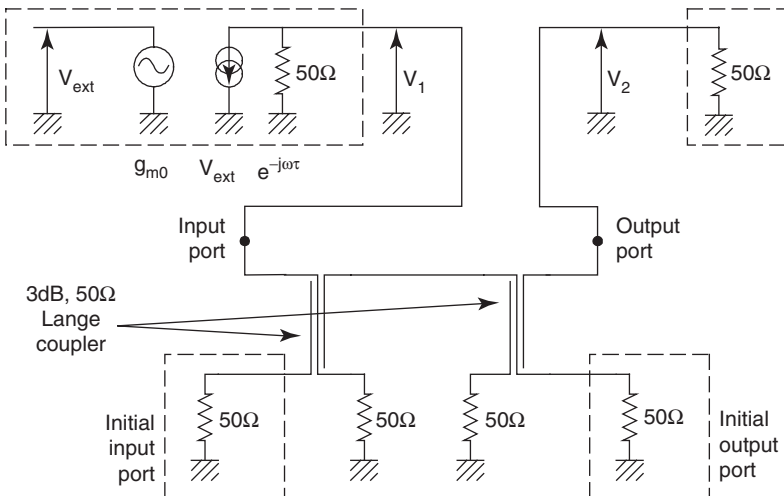


Figure 4. New “open loop” equivalent circuit of a first-order recursive filter.

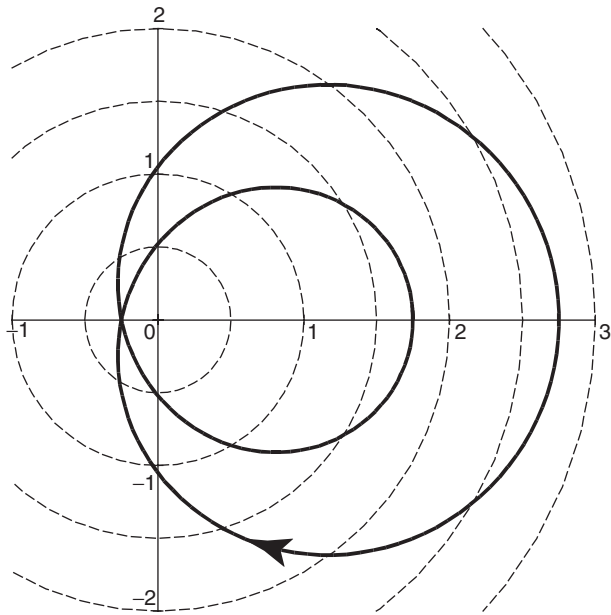


Figure 5. Unstable case of a second-order recursive filter: NDF plot for $G_1 = -5$ and $G_2 = -2$.

Here again, the NDF is the same as the denominator of the transfer function of the filter, thus validating the NDF calculation process. Figure 5 shows how instability can be predicted when the NDF encircles the origin for $G_1 = -5$ and $G_2 = -2$. In the same manner, Fig. 6 illustrates the stable state of the circuit, when the NDF does not encircle the origin for $G_1 = -4$ and $G_2 = -2$.

3. EXAMPLES OF PERFORMANCE IMPROVEMENT

For most engineers and researchers, the use of active components or functions is limited to loss compensation of passive structures. Nevertheless, active parts can play various roles in a global system. By identifying two main filter families in the active-filter structure overview article cited above, we have underlined a filter category for which active functions play an essential role. Gain, unilaterality or phase shift are directly implicated in the response and do not operate only for a simple loss compensation.

In fact, it is reasonable to imagine that active modules associated to passive filters could enable

- A significant reduction in size of the circuits
- An improvement of the response selectivity, even the control or the reconfigurability of the working band (passband or stopband)
- An automatic control process of frequency and level of the response elicited by external parasitics (e.g., temperature drift)
- Novel topologies for original filter structures
- Improved variable components [14]

In this section, we illustrate the possible improvements of filter responses and size due to such techniques for the

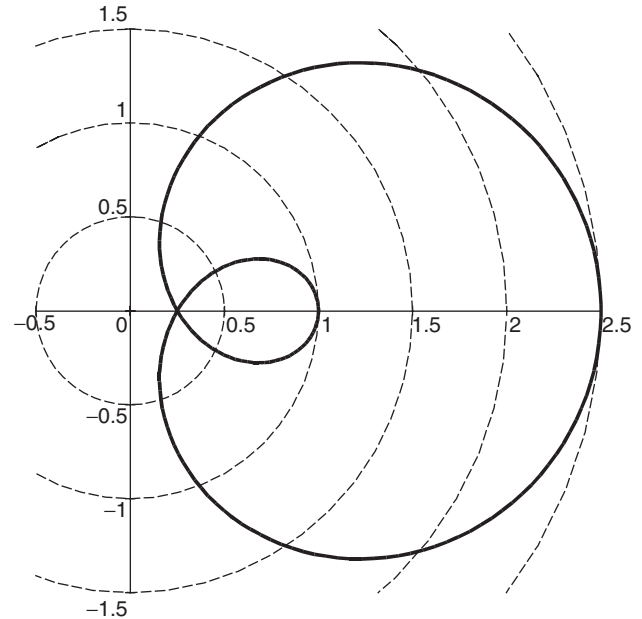


Figure 6. Stable case of a second-order recursive filter: NDF plot for $G_1 = -3$ and $G_2 = -3$.

two filter categories identified in the active-filter structure overview article cited above. We also describe automatic frequency control techniques and show an experimental validation.

3.1. Loss Compensation and Size Reduction

Miniaturized high-selectivity microwave bandpass filters are highly desirable for the next generation of satellite and mobile communications systems. Traditional interdigital and combline filters [15] based on TEM mode coupling are well suited for the design of narrowband passive filters. Unfortunately, the design of such filters with classical technologies (e.g., microstrip technology) leads to very high insertion losses in the operating band, especially when high selectivity is required. Indeed, due to low unloaded Q factors, it is not possible to obtain narrowband bandpass filters achieving 0 dB insertion losses with only passive elements, except with superconducting techniques.

An original technique is presented here, using classical passive interdigital filters in association with a MMIC active component circuit. Two filters, one of the first order and one of the second order, are discussed in reference to microstrip and coplanar technologies, respectively [16].

3.1.1. First-Order Microstrip Filter. A very classical first-order filter is studied using a standard design procedure [16]. The initial passive structure is designed to fit the following characteristics: 3.46 GHz for the center frequency and 91 MHz for the 3 dB bandwidth (2.63%). Measured insertion losses of the passive filter are about 7 dB at the center frequency. In a second step, the passive filter is geometrically modified in order to insert the MMIC circuit, while keeping the same center frequency. By taking into account the value of the imaginary part of the active

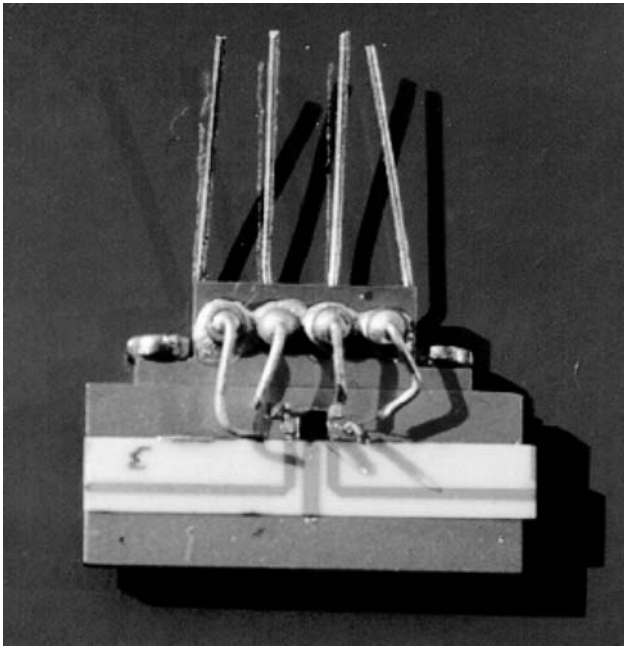


Figure 7. Photograph of the active one-pole microstrip filter.

component, the length of the resonator can be approximately divided by 2. A photograph of the active microstrip filter is shown in Fig. 7. Comparison of passive parts of the two versions are compared in Fig. 8. Measurements in Fig. 9 show a 3.27 GHz central frequency at a 85 MHz 3 dB bandwidth (2.6%). The insertion losses have been compensated at 0 dB.

3.1.2. Second-Order Coplanar Bandpass Filter. Many studies have shown that coplanar wave-guides can be considered as a good alternative to microstrip lines for many applications [17]. It is well known that low-level coupling coefficients are needed when designing narrowband bandpass filters. In the case of interdigital filters, a separating ground plane can be placed between the two coupled strips in order to obtain low-level couplings. With this approach, it is possible to efficiently control low coupling coefficients by adjusting the dimension of this ground plane. This method allows one to design compact low-coupled sections [18]. Another advantage of the coplanar technology is the flexibility in the design of the passive circuits. Indeed, a large number of geometric parameters can be chosen to design any transmission line with a given impedance. Electrical characteristics can then be improved by properly defining the ratio of the strip length to the slot length.

By taking into account all these advantages, a second-order filter is designed in coplanar technology. In this case, two MMIC components are placed at the open end of each resonator. A layout and a photograph of the coplanar active filter are respectively shown in Figs. 10 and 11. Measurements have been made over a wide frequency range in order to verify the bandstop responses (Fig. 12). No spurious resonances appear up to 9.5 GHz. Measurements also show a 1.98 GHz center frequency and a 75 MHz 3 dB

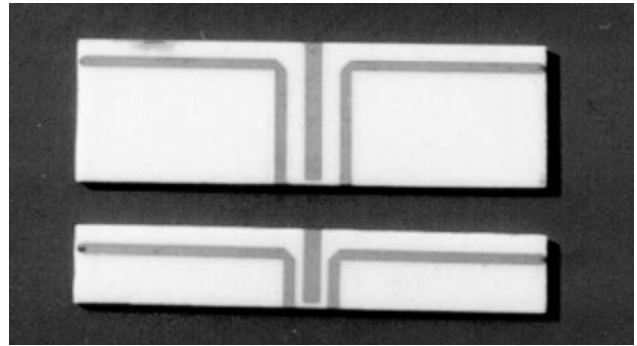


Figure 8. Comparison of the initial and optimized passive parts of the one-pole filter.

bandwidth (3.8%). In comparison to the purely passive case, the imaginary part of the MMIC chip has increased the response selectivity; 0 dB insertion losses have also been measured. In order to compare the reduction in size provided by the imaginary part of the active component, the same filter without the active components has been simulated. The center frequency of the filter is shifted to 2.6 GHz, resulting in a size reduction of about 0.8. Insertion losses are -7 dB in this case.

3.2. Active-Impedance Profile

In the previous subsection, interdigital structures were presented and improved in microstrip and coplanar technologies. However, these structures are not adequate when frequency switching or tuning is needed. Generally, the response of a passive filter is optimal at a given frequency. Tunability of the center frequency then implies a variation of one of the filter component parameters (such as electrical lengths) that can damage one or more electrical characteristics of the filters (matching, losses, bandwidth, etc.). In particular, for all planar filters using a varactor-based tuning or a switching process, any decrease of the center frequency is associated with a proportional reduction in bandwidth [19,20].

Nevertheless, beyond loss compensation and circuit size reduction, results presented above indicate a significant

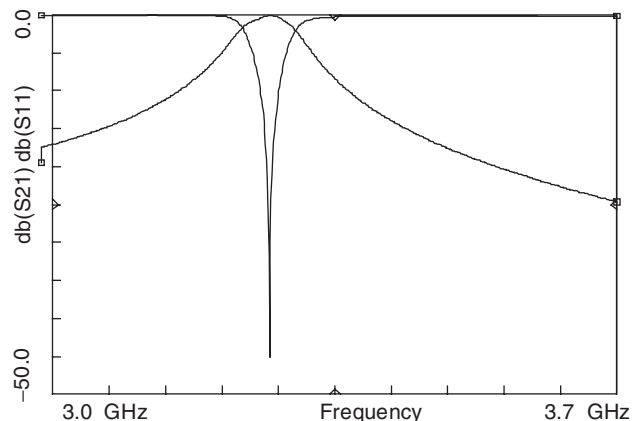


Figure 9. Experimental results of the active one-pole microstrip filter.

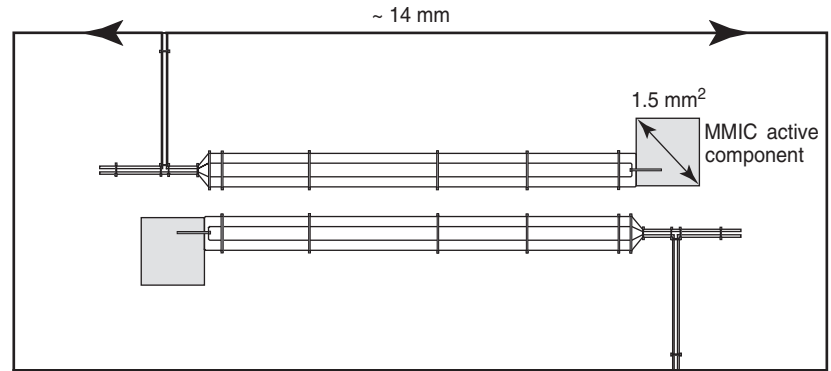


Figure 10. Layout of the compensated coplanar two-pole filter.

increase of the response selectivity in comparison to the corresponding passive filters. It should then be possible, using the same approach, to control simultaneously the bandwidth and the center frequency owing to the imaginary parts presented by compensation circuits.

In particular, it can easily be verified by simulations that these imaginary parts contribute to the improvement of the response in two ways:

- The value of the imaginary part at the input of the compensation circuit sets or corrects the center frequency of the filter. At a given frequency, this value is equivalent to a resonator length added to or withdrawn from a passive resonator.
- For this filter topology, the slope of the imaginary part around the chosen center frequency directly commands the response selectivity.

We now show two examples to illustrate how these simple impedance considerations, called active-impedance-profile (AIP), can be interpreted and applied for the design of multistandard and pseudomultipole filters.

3.2.1. Application of AIP to Multistandard Filters for Mobile Communications. The objective here is to build electrically tunable filters for multistandard mobile communication applications. To do this, frequency tuning must be achieved while maintaining a correct and constant level within the passband. Losses due to the passive

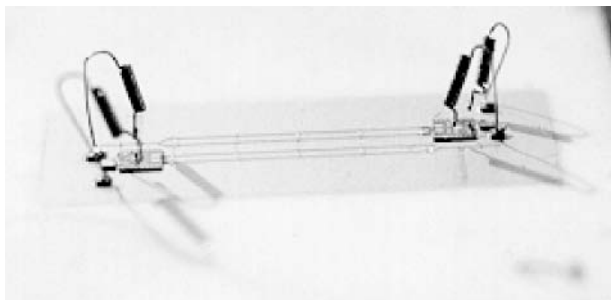


Figure 11. Photograph of the compensated coplanar two-pole filter.

parts of the circuit, but also those introduced by the tuning elements, must be compensated and controlled.

Generally, the response of a passive filter is optimal at a given frequency. To control the effects of one of the tuning parameters on filter performance, the filter structure has to be selected in reference to the target application. In our case, several tests on various elementary resonator-based structures have shown that interdigital filter structures exhibit an acceptable tolerance concerning the center frequency variation [21]. For example, a 10% increase of the resonator electrical length (by means of an additional capacitor at the end of the resonator or by the physical modification of the resonator length) achieves a 10% decrease of f_0 with a limited effect (less than 3%) on the bandwidth.

We apply our technique to the design of a second-order interdigital bandpass filter in coplanar technology. The filter topology is the same as in Fig. 10. The center frequency is electronically tuned in relation to the biasing voltages supplied to the varactor diodes located on the resonators. Each NIC-based AIP circuit is placed onto the ground plane (near the open end of each resonator) and is connected in series (using a bounding wire) with a varactor diode at the open end of the resonator. The filter is intended here to cover three telecommunications standards at

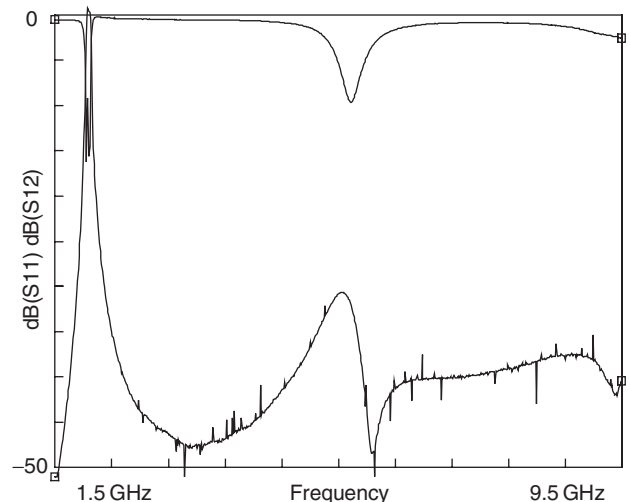


Figure 12. Experimental results of the compensated coplanar two-pole filter over a wide frequency range.

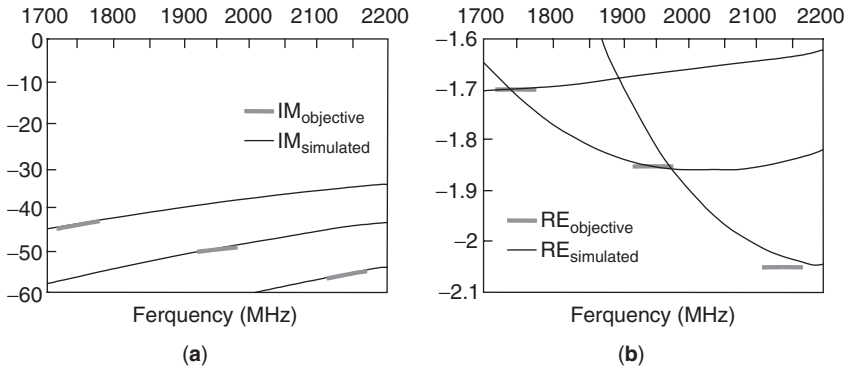


Figure 13. Objective and simulated AIP+diode impedance: (a) imaginary part; (b) real part.

- 1748 MHz (DCS1800 transmission band)
- 1950 MHz (UMTS transmission band)
- 2140 MHz (UMTS reception band)

For all standards, the objective bandwidth is set to 60 MHz relative to the UMTS standard. The design process is then done in four steps:

1. The designer sets the circuit dimensions referring to the desired center frequencies for the different communication standards and to the desired circuit size reduction.
2. This step focuses on the search, for each standard (three in this example), of the impedance characteristics in terms of real and imaginary parts to produce through the AIP associated with the varactor diode.
3. Considering that the switching between the standards is made through the varactor diode, one varactor bias voltage must be chosen in a third step for each standard. These choices can be set by the designer, but in a more general approach, an optimization process can help in finding the most adequate biasing points.
4. This last step consists in finding the real and imaginary part profiles over a frequency band covering all the standards. This impedance profile is obtained by deembedding the varactor diode impedance from the one obtained in step 3 around each standard center frequency.

Figure 13 shows the imaginary and real parts of the set AIP/varactor diode obtained at step 3 with classical packaged abrupt junction varactor diodes and for the three chosen bias voltages. A good agreement is obtained for each bias point between the objective correction impedance around each standard center frequency and the impedance performed.

Figure 14 shows the excellent results obtained for the global filter. A constant bandwidth of 60 MHz is obtained for each standard with a perfect loss compensation within the passbands.

3.2.2. Application of AIP to Pseudomultipole Filter. We now present the design of a pseudomultipole filter, based

on a one-pole passive filter topology. We apply the AIP technique to enlarge the bandwidth of the response. We start from the passive one-pole topology of Fig. 15. Transmission response initially presents a poor selectivity and a nonnegligible loss level at the center frequency (about 5 dB).

The idea is now to use the impedance profile principle to enlarge the response bandwidth. The objective is to search for the imaginary part to add to the passive filter, by means of the AIP, to reproduce the one-pole resonance not only at the initial central frequency but also at different frequency points in the objective passband. Figure 16 presents the imaginary parts of the AIP respectively necessary for a simple loss compensation (no effect of the imaginary part) and for a pseudomultipole effect. With this imaginary part profile, the resonance condition is reproduced for each frequency of the objective bandwidth. The result is a pseudomultipole filter based on a one-pole topology. The real part of the AIP allows for loss compensation, while the corresponding imaginary part increases the bandwidth with a flat gain, and with good rejection levels. The bandwidth of the filter is then 240 MHz for the same center frequency. Filter response is presented in Fig. 17 and validates the approach.

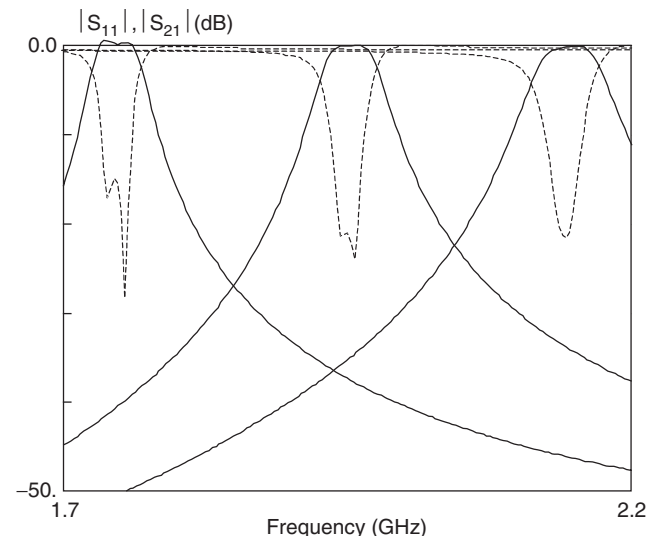


Figure 14. Simulated results of the 3-standard active filter.

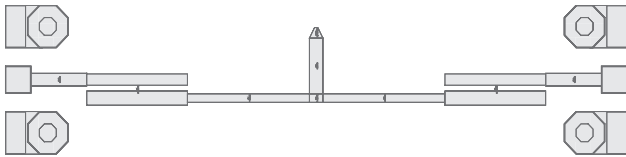


Figure 15. Distributed one-pole filter topology.

3.3. Automatic Frequency Control Techniques

This section deals with the application of phase-locked and magnitude-locked loops to achieve the automatic frequency control of microwave active filters. Indeed, analog filters are characteristically vulnerable to fabrication tolerances and temperature drifts and must be stabilized and controlled. Automatic frequency control (AFC) using the popular master–slave approach is the most feasible solution to control these characteristics [22]. This problem has been solved for a microwave filter [23–25] by using a typical phase-locked loop (PLL) based on a voltage-controlled oscillator (VCO) matched to the slave filter.

In contrast to the VCO-PLL, we propose here automatic frequency control based on the use of a voltage-controlled filter (VCF) PLL. We also propose an AFC based on the use of a VCF-based magnitude locked loop (MLL). These two techniques are attractive because they simplify the frequency control circuitry. They are applied to control the center frequency of a microwave bandpass VCF, implemented in planar hybrid technology on a duroid substrate and tunable over the 3.8–4.9 GHz range.

We first present a theoretical analysis establishing the control technique principles using a VCF and a MLL or a PLL. A transient-time analysis validates these results at low frequencies. We present measured results for a microwave tunable bandpass filter.

3.3.1. Theoretical Analysis. Figures 18 and 19 present an automatic tuning schemes using VCFs based on a MLL

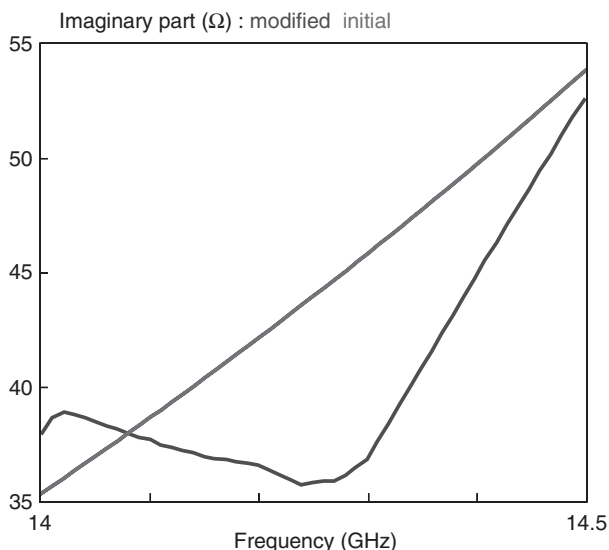


Figure 16. Loss compensation and pseudomultipole (AIP) profile imaginary parts for the distributed one-pole filter.

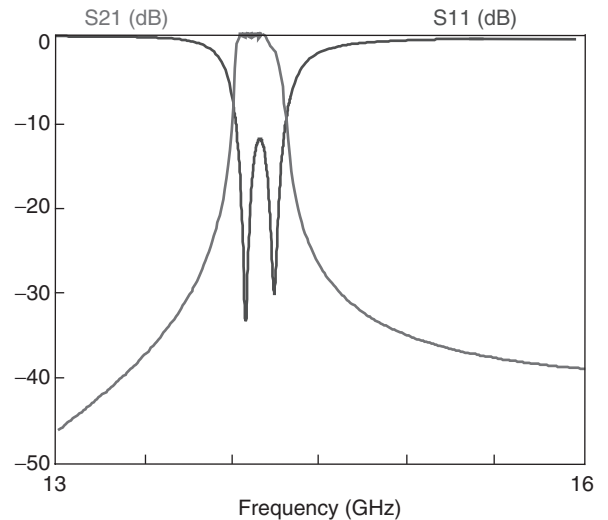


Figure 17. Global pseudomultipole AIP-based filter response.

and a PLL, respectively. Theoretical principles of the two techniques are pointed out by considering the particular case of an ideal second-order biquadratic band-pass VCF.

The voltage-controlled center frequency expression is given by $\omega_0(t) = \omega_0(t=0) + KV_c(t)$, where K is the VCF conversion factor (in radians per second per volt) and V_c the control voltage (volts). In the MLL-based AFC circuit scheme of Fig. 18, the amplitude of the reference signal is compared to VCF signal. The magnitude error is amplified and returned to control the filter center frequency ω_0 . The loop is magnitude-locked when the term $\Delta\omega = \omega_r - \omega_0$ is minimized ($\Delta\omega \rightarrow 0$) with ω_r , the reference signal frequency.

In the PLL-based AFC circuit of Fig. 19, the master filter is phase-locked to the reference signal. The phase of the reference signal is compared to the phase of the signal after the biquad filter by a phase comparator. The phase error is filtered out by the lowpass filter, then amplified and fed back to adjust the center frequency ω_0 of the filter. The loop is locked when the difference between the phase of the bandpass filter output signal and the phase of the reference signal is minimized, resulting in $\omega_0 \approx \omega_r$.

The differential equations that govern the control system based on a MLL or a PLL are given by Quintanel et al. [26]. The control response can be characterized for different tracking signal shapes by numerically solving the equations. Results given in Figs. 20 and 21 are obtained by considering $f_r(t)$ as frequency steps. Others results show that the system based on a MLL or a PLL is able to accurately track different time-variable reference frequencies, like ramps or steps. It is also shown that for the same parameter values, the PLL method is more accurate than the MLL technique. In Figs. 20 and 21, the control system based on a MLL is not able to track the reference signal for negative variations. The control system locks on a nonvalid solution. A method to solve this problem consists in taking a smaller $f_0(t=0)$ value to be sure to start with a positive variation and avoid a negative one.

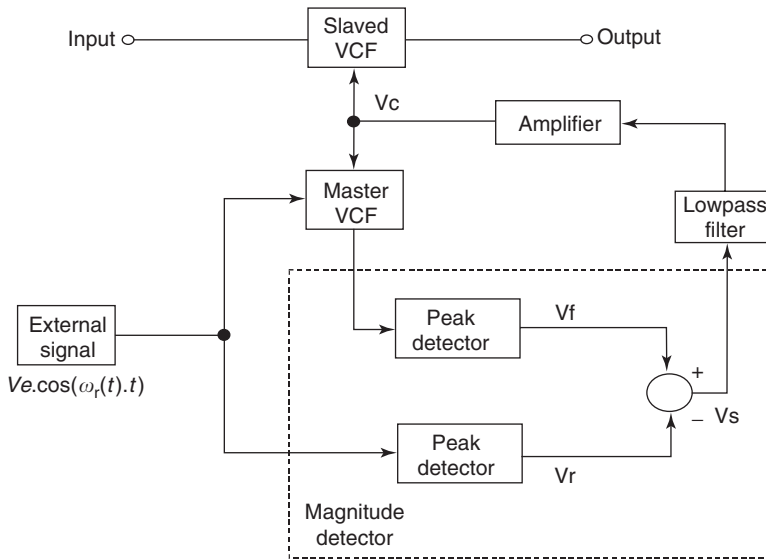


Figure 18. Automatic tuning scheme using a VCF based on a MLL.

3.3.2. AFC Systems Applied at Microwave Frequencies. In this section, we present an application of the AFC methods discussed above to a tunable microwave filter. Figure 22 presents the final functional scheme using the MLL or the PLL techniques. The VCF is a microwave bandpass planar filter based on a distributed half-wave hybrid resonant structure. The tunable element is a varactor diode used as a voltage-controlled capacitor (VCC). It is placed at the middle of the resonator to electronically tune the filter center frequency. The filter is implemented on a duroid substrate with a thickness of 0.5 mm and a dielectric constant of 2.43. It is tunable over the 3.8–4.9 GHz range. The VCC is a MACOM beam-lead constant-gamma GaAs varactor (MA46580).

To split the power reference signal between the reference and the filtered channels, we use a two-way Wilkinson power divider. The Wilkinson divider is fabricated on a duroid substrate and matched to $50\ \Omega$ at all ports. It exhibits a good isolation between output ports over the

3–5 GHz range. Phase detection is realized by using a microwave double-balanced mixer. Magnitude detection is achieved with zero-bias Schottky diodes. All RF elements are implemented on a duroid substrate. A DC amplifier is used to amplify the error signal of the loop.

Measurements are performed for different external reference frequencies and for each control technique. Table 1 summarizes the tracking performances of the two control techniques. The results demonstrate that the AFC based on a PLL or a MLL is possible and feasible in the microwave frequency domain. The PLL method offers a precision error varying from 0% to 0.19% over the 4.0–4.6 GHz range. Finally, the MLL method has a precision of 0.5–3.6% over the same frequency range. The control technique based on a PLL offers a better precision than does the MLL method because the losses of the microwave filter at the center frequency are not constant over the tuning frequency range. Nevertheless, the MLL technique is attractive for microwave applications

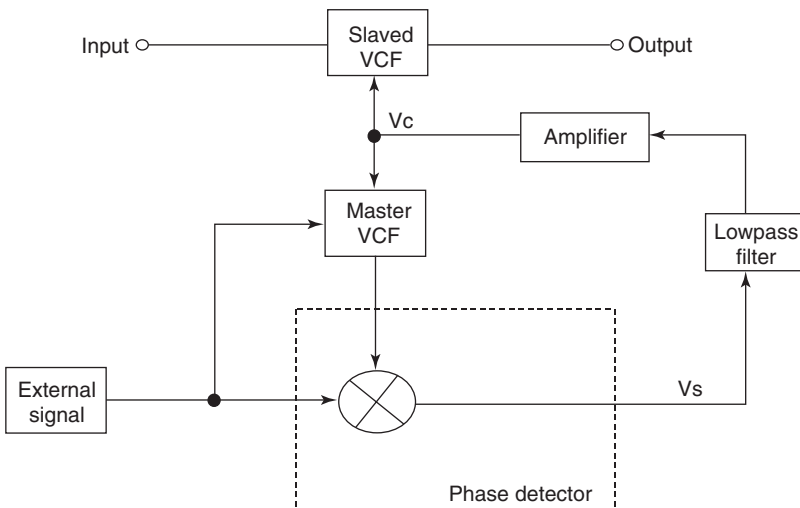


Figure 19. Automatic tuning scheme using a VCF based on a PLL.

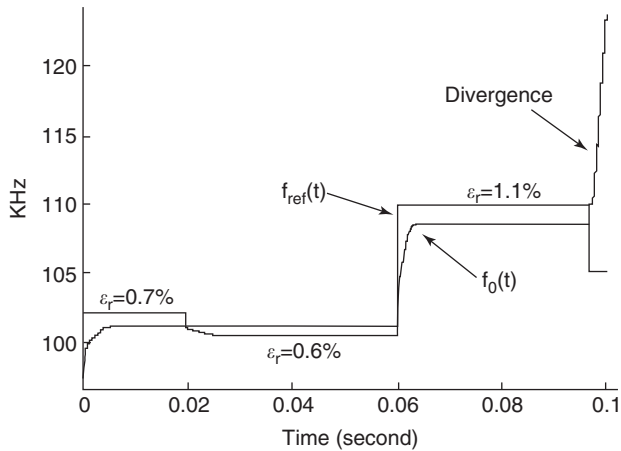


Figure 20. System response to frequency steps with a MLL control system.

because it avoids the critical phase sensitivity of the PLL method.

4. NEW APPROACHES AND NEW TECHNOLOGIES

The preceding paragraphs have shown that microwave and RF filter design is a complex art because it involves a nonnegligible number of steps, each step needing a wide spectrum of competences. In addition to a strong theoretical background, this diversity supposes the definition of a rigorous and efficient work methodology. However, even when all these tools are well known and effectively used, designers must keep in mind that, around all these skills and competences, new technologies and new needs that can modify their own approaches arise daily.

In this section, we give a brief review of new needs and new technologies in which planar active filters can be involved.

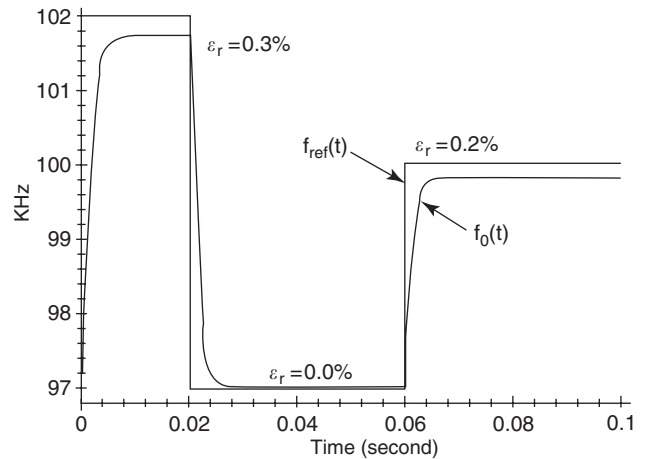


Figure 21. System response to frequency steps with a PLL control system.

4.1. New needs and constraints

Migration of microwave systems for public market applications, in particular for mobile communications, has led to new unavoidable constraints:

- For mass production, cost considerations are essential. In practice, it is necessary to minimize the design time, and to make the design processes more reliable. Inherently, this is based on reliable low-cost integrated technologies.
- From the communication standards point of view, frequency bands allocated to different services are increasingly narrow, while the demand is always increasing. So the objective is to use at best these frequency bands in order, on one hand, to avoid interferences between services, and on the other hand, to augment the systems capabilities.

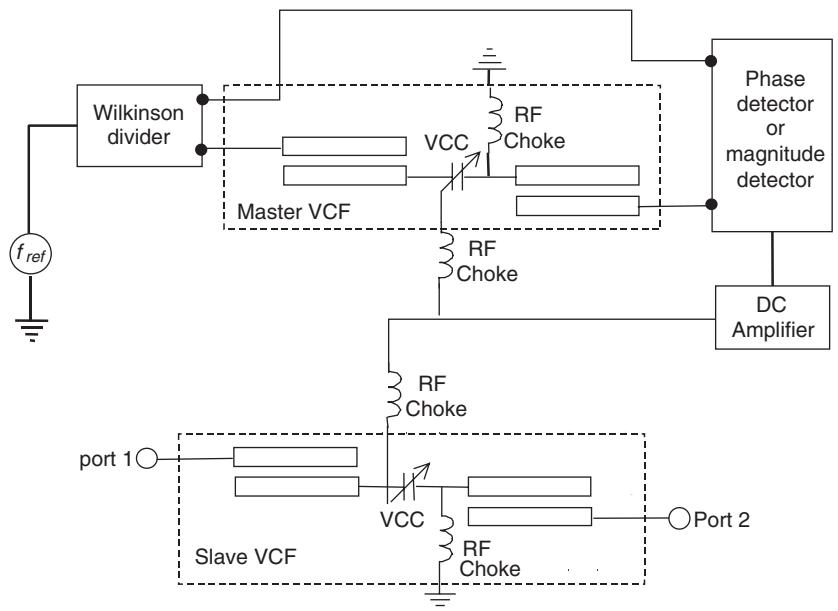


Figure 22. Microwave filter slaved to control system based on a PLL or a MLL.

Table 1. Tracking Performance of the Control Systems

F_{ref} (GHz)	4	4.1	4.2	4.3	4.4	4.5	4.6
f_0 (GHz) PLL method	4.005	4.092	4.197	4.302	4.398	4.503	4.600
f_0 (GHz) MLL method	4.005	4.092	4.171	4.250	4.363	4.495	4.635
ε_r % PLL method	0.12	0.19	0.007	0.004	0.004	0.006	0
ε_r % MLL method	0.12	0.19	0.6	1.1	0.8	0.1	0.7

- Device miniaturization is an essential constraint, synonymous with commercial success, especially for mobile handsets. From a technical perspective, this miniaturization involves a capability of integrating pre- or postprocessing digital circuits with analog microwave functions. At this step, mixed analog–digital technologies and methods are required.
- Finally, in terms of daily use, acceptable power autonomy of mobile handsets involves the use of low-current and low-consumption processes and circuits.

In any recent telecommunication system, filters take in a large number an important place in front-end transmitters/receivers; For example

- A duplexer located after an antenna is classically composed of two filters separating the transmission/reception frequency bands.
- In the reception channel, a filter can be found before the input low-noise amplifier (LNA) to improve its high-level signal performances, and simultaneously eliminate parasitic frequencies coming at the input of the front-end receiver.
- In the same channel, two other filters can be found, one after the LNA before the first downconversion mixer, and another one at intermediate frequency before the baseband downconversion.
- In the transmission channel, a filter can be found after each element of the chain, to eliminate or reduce noise and other possible distortions, linear or nonlinear.

With these considerations, and with the wide diversity of mobile telecommunication standards, it has rapidly become necessary to design multimode/multistandard portable terminals that could allow users to roam on a global scale. For this reason, frequency-tunable active filters have found an increasing interest. Indeed, tunable filter capabilities obviously lead to

- Elimination of redundant functions such as standard switches or analog/digital converters (ADCs)
- Considerable reduction in size of the global system
- Lower system complexity, and associated constraints

Because of their interesting gain capability, tunable active filters can replace very advantageously the LNAs and their associated filters. This approach can then permit (1) Elimination of one or more amplifiers in the transmission/reception chain and (2) Distribution of different constraints of noise, power-handling behavior, and response performance imposed on the other functions, thus relaxing

these specific constraints and providing more ease in the design of each functional block.

In this way, the use of tunable active filters is very attractive. However, to apply this principle with success, it is necessary to adapt the design tools, even to create new ones, but more importantly to adapt the original design method to new technologies.

4.2. New Integrated Technologies for Microwave Design: Silicon versus Gallium Arsenide

Even though some technologies have existed basically unchanged for decades, they can be seen in a totally novel aspect when used at frequencies for which they were not originally implemented. In this way, silicon-based technologies (Si and SiGe technologies) can be considered as novel for microwave active-filter applications.

Silicon-based technologies have been widely used at low frequencies for both digital and analog applications [27]. Because of the great advances of silicon and silicon–germanium technologies since the mid-1990s, silicon-based ICs have found an increasing importance for RF and microwave applications. Since 1998 only, some articles on the international scientific production have reported some interesting elements concerning the transposition of circuits classically implemented on GaAs to silicon-based processes [28,29]. Table 2 presents some general comparison elements between GaAs and SiGe capabilities.

The term *SiGe BiCMOS HBT* refers to heterojunction bipolar transistor, for which the base is doped with germanium. With this technology, chips work much faster while ensuring the reliability and the stability of such a process. These chips can be designed for wireless applications, increasing the performance of these products while decreasing their size and power consumption. Besides, the BiCMOS HBT SiGe technology takes advantage of the integration capability of CMOS process, which leads to greater compactness.

There are two different ideas on the issue of using SiGe technology. On one hand, Si and SiGe technologies are found to be very advantageous, because of their capability to achieve more compact and cost-effective circuits. On the other hand, the degree of maturity of Si/SiGe technologies is still not comparable to that of GaAs technologies. According to some designers, Si technology does not enable

Table 2. Comparison Elements of GaAs versus SiGe

Substrate type	Transistors	f_t (GHz)	F_{min} (dB)	Cost (\$/mm ²)
GaAs	PHEMT	>70	0.9 at 12 GHz	1000
SiGe	HBT-CMOS	>40	0.7 at 2 GHz	700
	BiCMOS	>50		

integration of a complete microwave system. It may then be necessary to use mixed technologies, which tends to be more expensive than a complete development on GaAs.

Moreover, in spite of obvious advantages of cost-effectiveness and compactness, SiGe technology involves some nonnegligible constraints, one of the most important of which is still the lack of a proper library model in conventional microwave and high-frequency circuit simulators. To become more familiar with Si and SiGe technologies, and before confronting the realization of circuits, designers will often have to test several processes through their design kits to have in mind the problems that have to be faced:

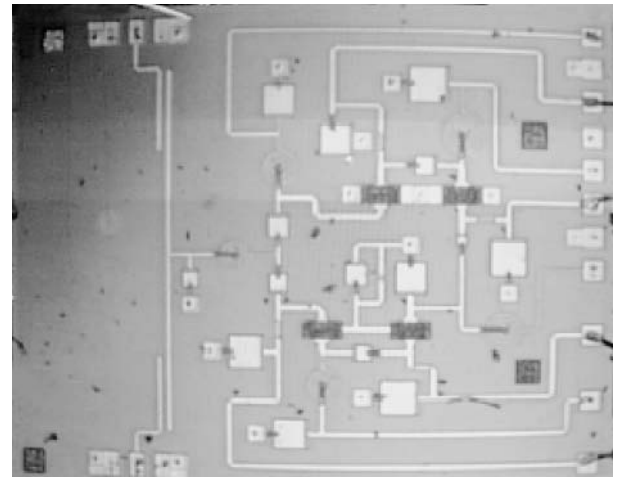
1. The first major problem is encountered at the level of the CAD tools. Because of the classical use of silicon technology for digital and analog applications at low frequencies, most component libraries were developed primarily for CAD software using the same approach. Of course, the design philosophy of these circuits is very far from that used for microwave analog circuits.
2. The second problem arises from the fact that some component models are sometimes not available in simulator libraries or not parameterized, thus making any optimization a difficult task. As a result, some components such as inductors are not available because they are not classically used at low frequencies. They have to be designed using specific tools. In some processes, this is also the case for varactor diodes.
3. From the design perspective, this third problem arises from the specific conductivity of the doped silicon (SiGe) substrate and its poor isolation (some tenths of an $\Omega \cdot \text{cm}$ compared to $10^5 \Omega \cdot \text{cm}$ for pure silicon). This leads to considerable increase in the number of parasitic capacitors in a circuit. For example, in the case of the MOSFET, it is necessary to take into account not only the parasitic capacitors C_{gs} and C_{gd} but also capacitors C_{db} , C_{bs} , and C_{gb} (parasitic capacitors between the substrate and respectively the drain, the source, and the gate). These capacitances are nonnegligible regarding the other capacitances of the circuits.

Note that these problems are now partially solved; some SiGe foundries now supply models for classical CAD packages, with microwave design facilities such as constant gain, stability, and noise circles.

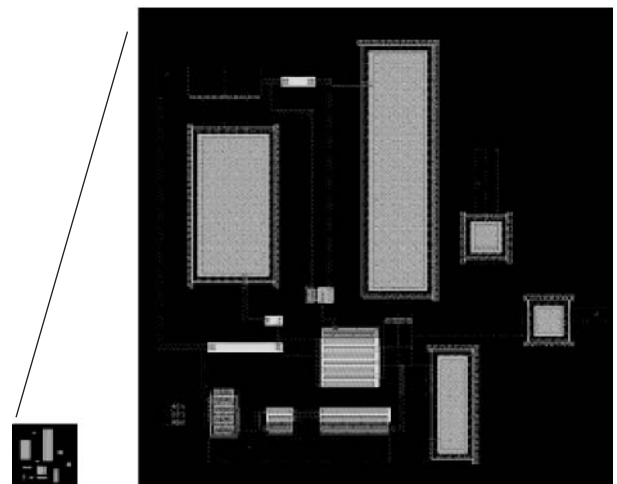
Design rules of Si-based technology are also very different from those used with GaAs processes, even for the design of simple circuits. For technological reasons, the ground plane of a circuit on silicon is located on the top of the substrate. It is then not possible to strictly consider microstrip lines. However, some reports have shown the feasibility of transmission lines in polymers, such as benzocyclobutene (BCB), allowing performances close to those obtained with GaAs [28]. Particular attention should be also paid to the leakage currents due to the specific conductivity of the substrate. To solve this problem, many manufacturers use guard rings. These guard rings are buried layers, surrounding partially or totally the component to be protected by acting as a p-n junction biased in inverse. All these protection processes clearly allow a more

compact implementation in comparison to GaAs, leading to very different design rules and component placement than those applied for conventional microwave GaAs technology. This mainly explains the differences in size that can be observed for the same function from one technology to the other. To illustrate these differences in terms of component implementation, size, consumption, and cost, we now give two comparative design examples and the corresponding layouts.

Example 1. In a first-order filter based on a parallel LC resonator, ports are decoupled by low-value capacitances. [The GaAs version is discussed in Section 3.4.3 (see also Fig. 12) of the active-filter structure overview article cited above; see also Ref. 30 of this present article.] In the same way, a SiGe version has been realized [30] using the BYR process from AMS [31]. This filter is designed to work in the UMTS reception band (2110–2170 MHz). Transistors are BiCMOS HBTs and PMOS. Losses are perfectly compensated within the passband. Figures 23a and 23b



(a)



(b)

Figure 23. Layouts of the active LC filter in (a) GaAs and (b) SiGe (+ zoom) technologies.

compare the two circuit layouts. The high-compactness of the SiGe version can be easily noted. The reduction in surface is done with a ratio of 150 corresponding to a reduction of cost of 170. With other circuits found in the literature, the mean reduction ratio in surface and in cost can be estimated respectively at 50 and 55. With the technologies used, the power consumption ratio is ~ 21 (48 mW for SiGe version against 1040 mW for the GaAs version).

Example 2. In this example, two different NIC topologies have voluntarily been chosen to try to emphasize one or the other technology. The GaAs version uses the ED02Ah process from OMMIC [32] with HEMT transistors. The circuit works in the 1.9–2.3 GHz range and belongs to the infinite transconductance NIC category (see active-filter structure overview article cited above). The SiGe version has been realized with the AT46000 from ATMEL [33]. It is based on a classical differential topology using BiCMOS transistors. This circuit works in the 0.1–3 GHz range. Figures 24a and 24b compare the two circuit layouts. The reduction in size here is ~ 55 , corresponding to a cost ratio

of 65. Power consumption is divided by 4 (18 mW for the SiGe version vs. 73 mW for the GaAs version). Simulation results of these two NICs inserted within a filter give a clear advantage to the SiGe version.

4.3. Realisation Examples

Example 1 focuses on a topology proposed in Refs. 34 and 35. It consists of a grounded active inductor using a low-cost 0.8- μm BiCMOS HBT technology [30]. This inductor topology is based on the use of two HBTs in a feedback configuration. Note that in this case there is no need for an integrated inductor (Fig. 25).

The quality factor Q_1 is biased by a voltage-controlled current source built with bipolar transistors. V_{tune} allows tuning of the associated real part while maintaining the inductance value. Using this approach, a quality factor of some thousands can be performed for an inductance value of 9.20 nH.

By associating a capacitor in parallel with the active inductance, a bandpass response can also be obtained. The active LC resonator is decoupled by two small value capacitors. Figures 26 and 27 respectively present the layout of

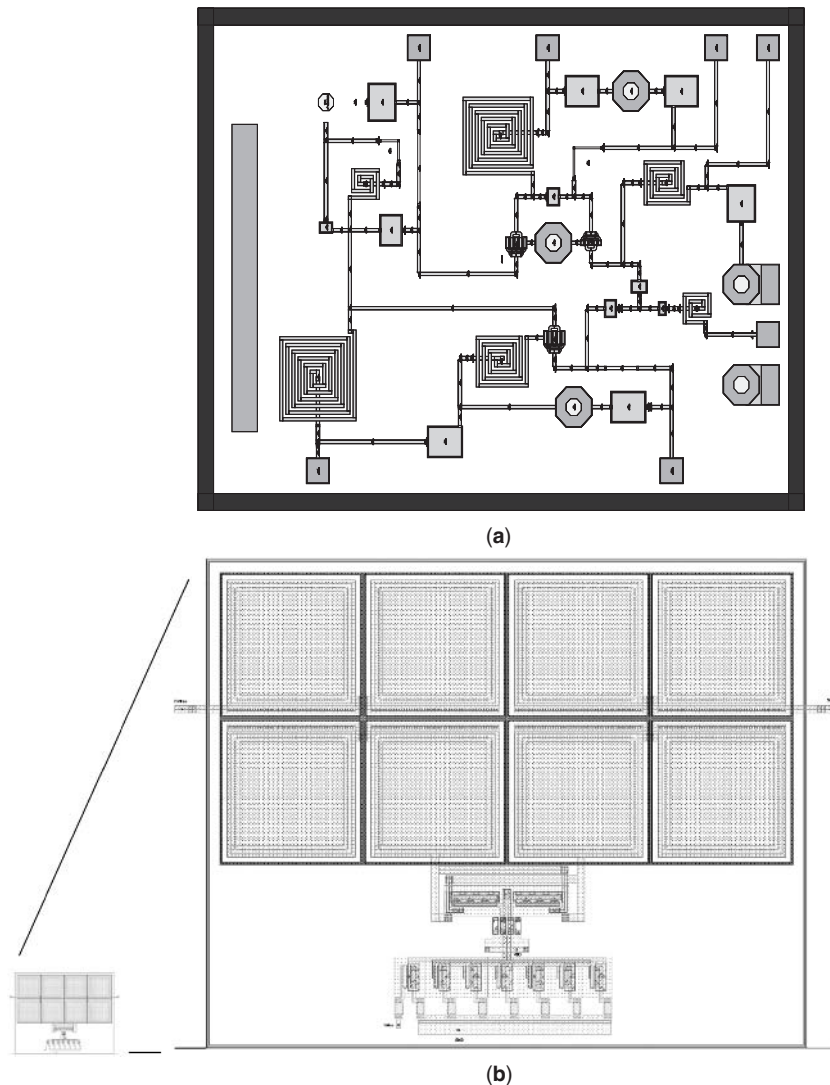


Figure 24. Layouts of the two negative-resistance chips in (a) GaAs and (b) SiGe (+ zoom) technologies.

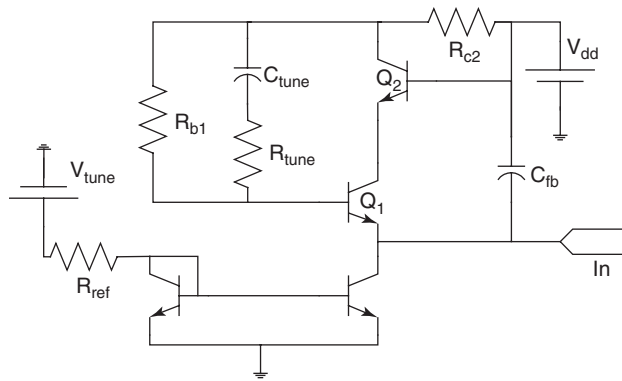


Figure 25. Schematic of the active inductor.

the filter and the simulated response. Dimensions of this circuit are $150 \times 170 \mu\text{m}$. Total consumption is about 15 mW. Losses are totally compensated at 1.86 GHz, with a quality factor of ~ 150 .

4.4. Differential Circuits

For many years, differential structures have been limited to low-frequency applications. Differential structures have the following advantages compared to single-ended topologies:

- They are insensitive to noise and interference coupled through supply lines and substrate.

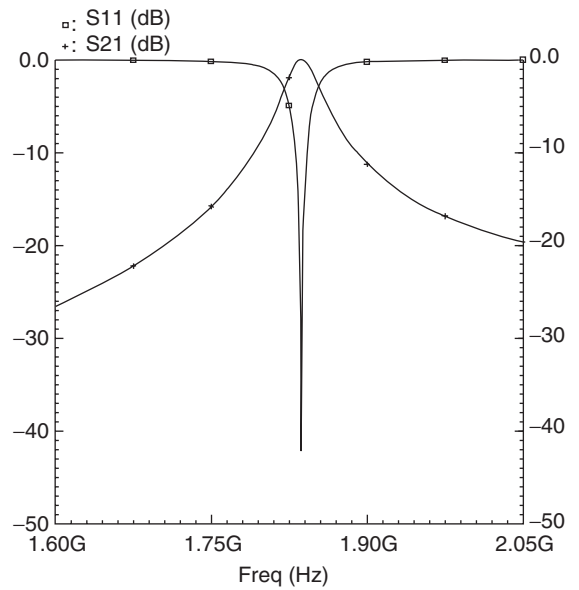


Figure 27. Layout-based simulated results of the integrated active LC filter.

- Many linearization methods used for transconductance stages can also be used for low-noise amplifiers and filters using this approach.
- They have smaller even-order distortion.

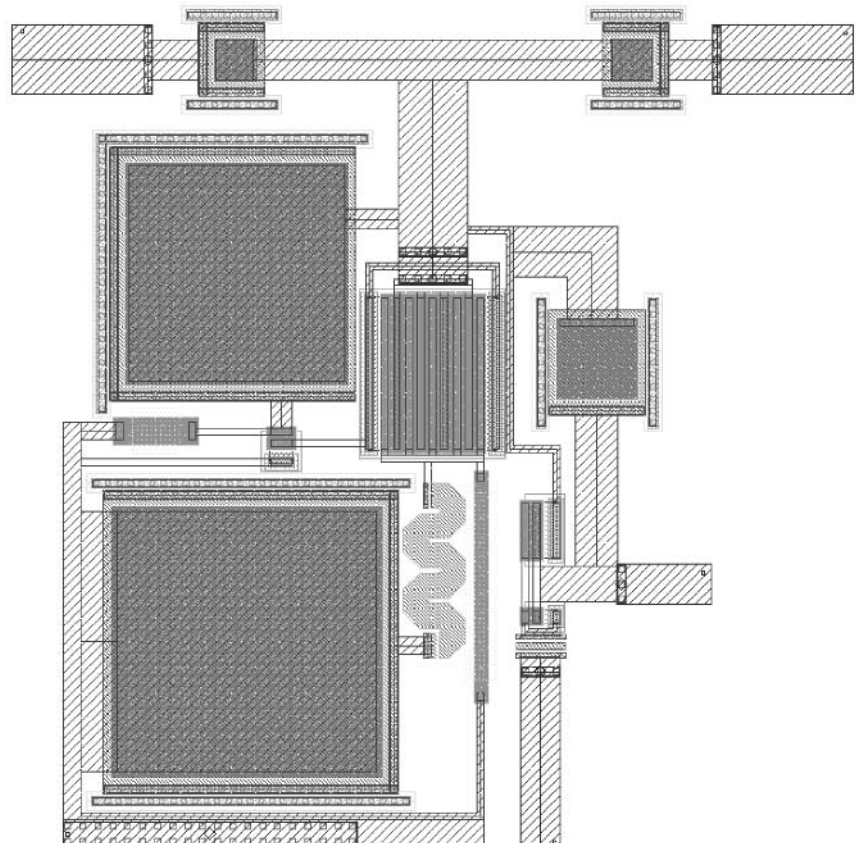


Figure 26. Layout of the integrated active LC filter in BiCMOS HBT technology.

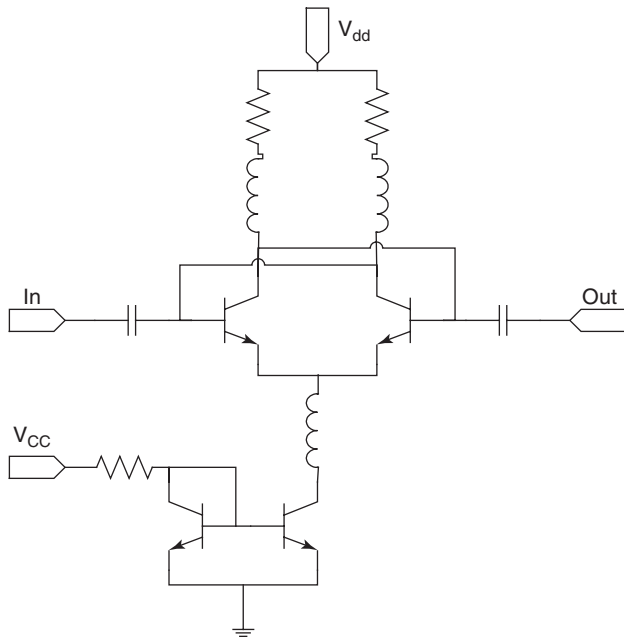


Figure 28. Schematic of the differential negative resistance.

Example 1 (above) focuses on a differential LC active filter in which losses are compensated with a differential negative resistance [36]. We begin with a brief description of the negative-resistance topology. The circuit uses a BiCMOS SiGe HBT technology. Such topologies generally present a real part of the impedance not strongly frequency-dependent and are recommended for wideband applications. A schematic and the layout of the circuit are presented in Figs. 28 and 29, respectively. Three integrated inductors are used to bias and stabilize HBTs. A current source sets the emitter current. Symmetric performances are obtained between the two ports. The imaginary part can be considered as a negative capacitance. Circuit dimensions are $690 \times 800 \mu\text{m}$. The negative resistance performed is about -10Ω at 1.8 GHz. The imaginary part is equivalent to a -2.4 pF negative capacitance. Power consumption is about 46 mW.

A differential LC filter circuit is now presented. The previous differential negative resistance is used to compensate for insertion losses introduced by the inductors of the resonator. Two transconductances are also used to tune the center frequency and the gain of the filter. A schematic of this circuit is presented in Fig. 30. A band-pass response is obtained with a quality factor of ~ 125 at 2 GHz. The S parameters are presented in Fig. 31. The noise figure is $\sim 4.5 \text{ dB}$ at 2 GHz.

Finally, we show a 2-GHz single-ended first-order recursive filter integrated using the QuBIC4 silicon MMIC

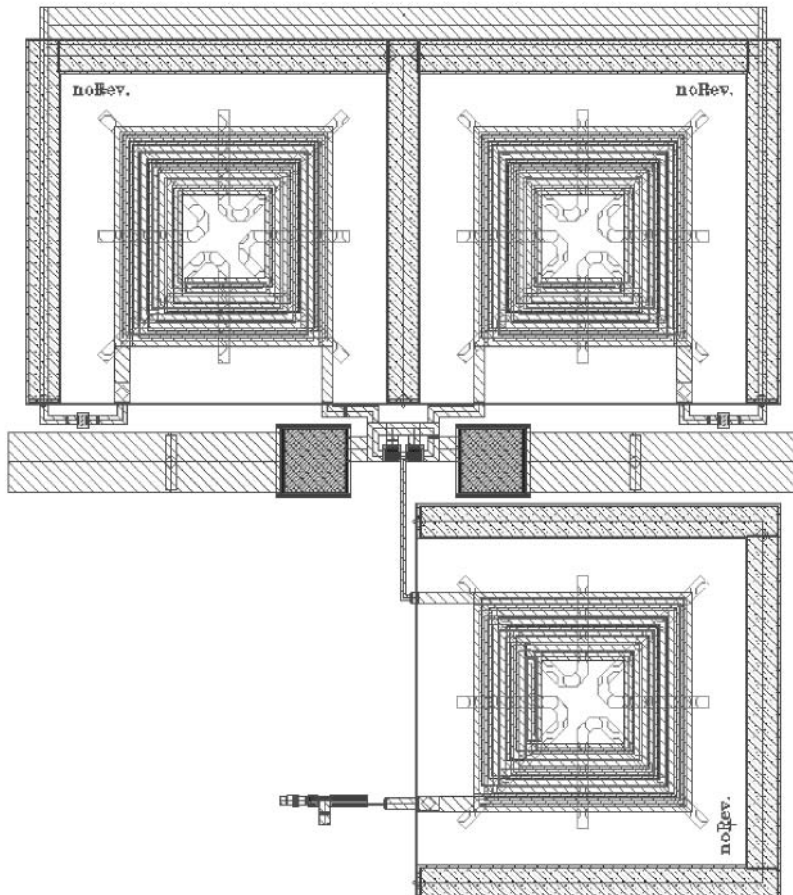


Figure 29. Layout of the differential negative resistance.

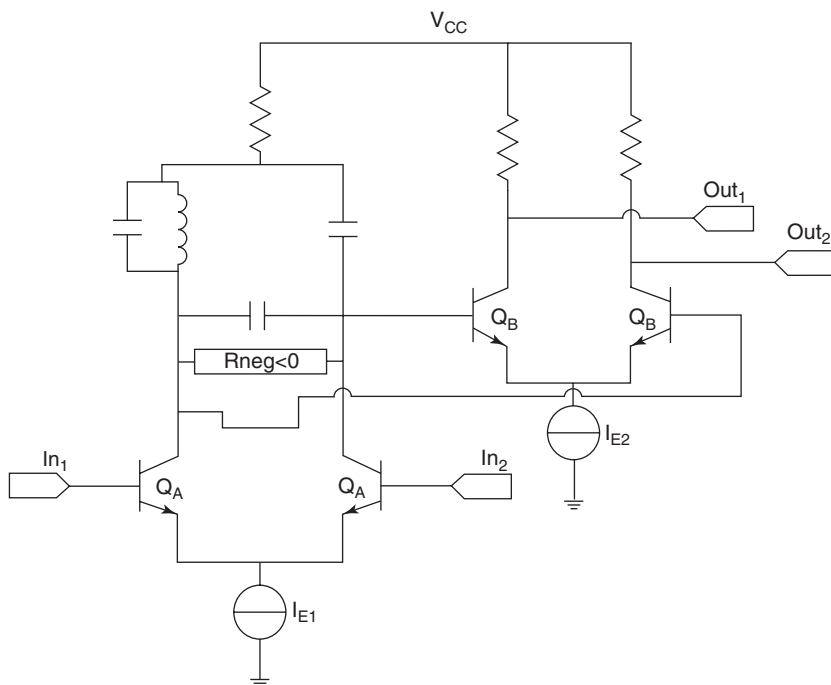


Figure 30. Schematic of the differential filter.

process from Philips [37]. The differential property is used here for an original recombination of input and delayed feedback signals within a first-order recursive structure. Figure 32 presents the basic principle of the circuit. With A_d , the differential-mode voltage gain of the amplifier structure, the voltage gain of the filter can be expressed as a first-order recursive filter response:

$$G_v(f) = \frac{V_{out}(f)}{V_{in}(f)} = \frac{-\frac{A_d}{2}}{1 + \frac{A_d}{2} e^{-j2\pi f\tau}}$$

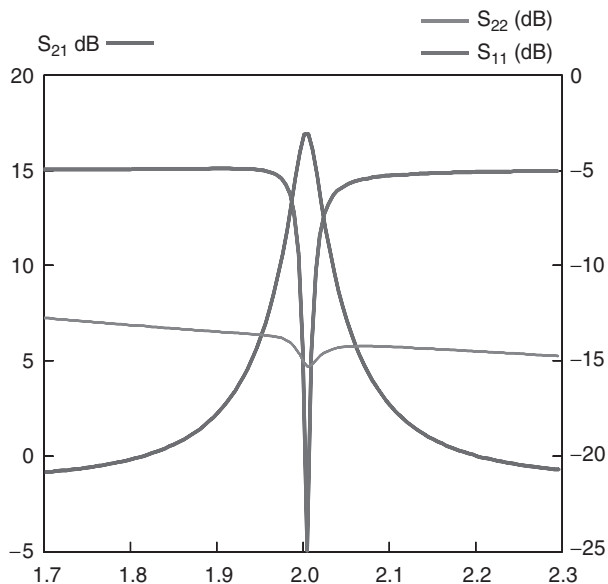


Figure 31. S parameters of the differential filter.

The circuit layout is shown in Fig. 33. Dimensions of the chip are 1.12×1 mm. Measurements presented in Fig. 34 are in good agreement with simulations. Input/output matching is less than -12 dB within the passband. The filter exhibits a 260 MHz 3 dB bandwidth at 1.94 GHz, with a gain close to 10 dB for a power consumption of 32 mW. Input/output matchings are lower than -12 dB for 1 GHz around the center frequency. Isolation, which is not

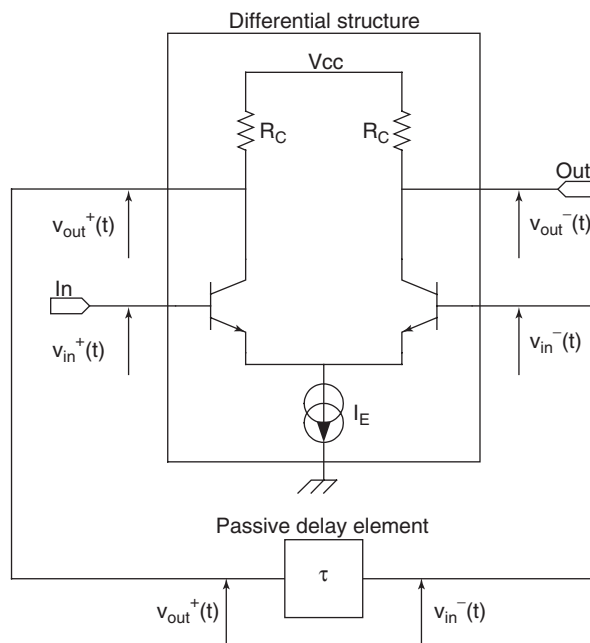


Figure 32. Schematic of a differential-based recursive filter.

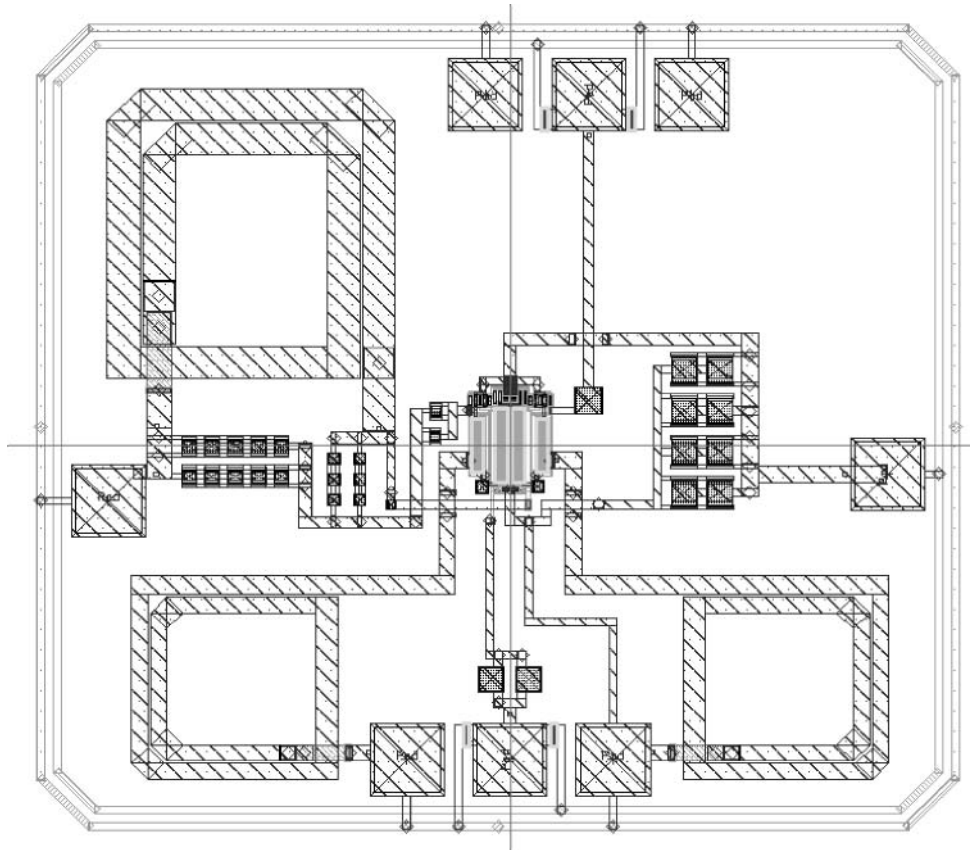


Figure 33. Differential-based recursive filter layout.

presented here, is greater than 30 dB in the 0.5–3.5 GHz range. The noise figure is equal to 4.6 dB at the center frequency. The –1 dB compression point is obtained for an output power of –11.7 dBm.

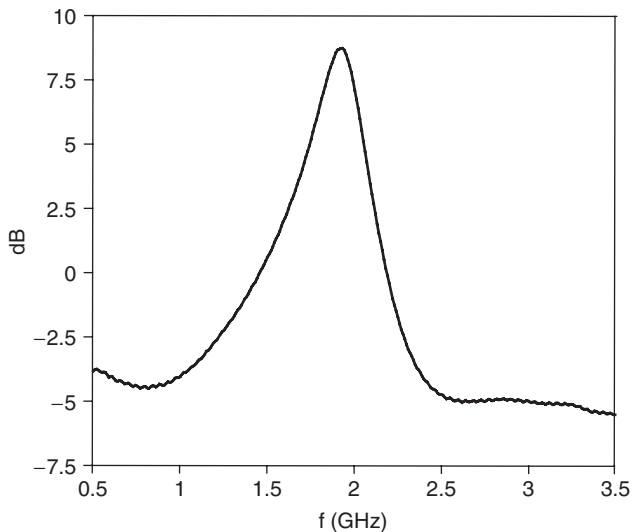


Figure 34. Measured gain of the differential-based recursive filter.

BIBLIOGRAPHY

1. P. Gardner and D. K. Paul, Optimum noise measure configurations for transistor negative resistance amplifiers, *IEEE Trans. Microwave Theory Tech.* **MTT-45**(5):580–586 (1997).
2. S. Wedge and D. Rutledge, Wave techniques for noise modeling and measurement, *IEEE Trans. Microwave Theory Tech.* **MTT-40**:2004–2012 (1992).
3. H. Ezzedine, L. Billonnet, B. Jarry, and P. Guillon, Optimization of noise performance for various topologies of planar microwave active filters using noise wave techniques, *IEEE Trans. Microwave Theory Tech.* **MTT-46**(12):2484–2492 (1998).
4. J. Lange, Interdigitated stripline quadrature hybrid, *IEEE Trans. Microwave Theory Tech.* **MTT-17**:1150–1151 (1969).
5. R. M. Osmani, Synthesis of Lange couplers, *IEEE Trans. Microwave Theory Tech.* **MTT-29**(2):168–170 (1981).
6. J. Rollett, Stability and power-gain invariants of linear two-ports, *IRE Trans. Circ. Theory* **9**(1):29–32 (1962).
7. R. P. Meys, Review and discussion of stability criteria for linear 2-ports, *IEEE Trans. Circ. Syst.* **37**(11):1450–1452 (1990).
8. M. L. Edwards, A new criterion for linear 2-port stability using a single geometrically derived parameter, *IEEE Trans. Microwave Theory Tech.* **MTT-40**(12):2303–2311 (1992).
9. H. W. Bode, *Network Analysis and Feedback Amplifier Design*, Van Nostrand, New York, 1945.
10. M. Ohtomo, Stability analysis and numerical simulations of multidevice amplifiers, *IEEE Trans. Microwave Theory Tech.* **MTT-41**(6/7):983–990 (1993).

11. A. Platzker, W. Struble, and K. T. Kketzler, Instabilities diagnosis and the role of K in microwave circuits, *IMS'93, IEEE MTT-S Int. Microwave Symp. Digest*, 1993, pp. 1185–1187.
12. A. Platzker and W. Struble, A rigorous yet simple method for determining stability of linear N-port networks, *Proc. GaAs IC Symp.* 1993, pp. 251–254.
13. M. Delmond, L. Billonnet, B. Jarry, and P. Guillon, Microwave tunable active filter design in MMIC technology using recursive concepts, *IMS'95, IEEE MMWMC-S Microwave and Millimeter-Wave Monolithic Circuits Symp. Digest*, 1995, pp. 105–108.
14. S. Kolev, B. Delacressonnière, and J.-L. Gautier, Using a negative capacitance to increase the tuning range of a varactor diode in MMIC technology, *IEEE Trans. Microwave Theory Tech.* **MTT-49**(12):2425–2430 (2001).
15. G. Matthaei, L. Young, and E. M. T. Jones, *Microwave Filters, Impedance-Matching Networks, and Coupling Structures*, Artech House, 1964.
16. F. Biron, L. Billonnet, B. Jarry, P. Guillon, G. Tanné, E. Rius, F. Mahé, and S. Toutain, Microstrip and coplanar bandpass filters using MMIC negative resistance circuits for insertion losses compensation and size reduction, *Proc. EuMC'99, 29th European Microwave Conf.* 1999, Vol. 1, pp. 72–75.
17. M. Houdart, Coplanar lines: Application to broadband microwave integrated, *Proc. EuMC'76, 6th European Microwave Conf.* 1976, pp. 49–53.
18. E. Rius, T. Le Gougec, K. Hettak, J. Ph. Coupeuz, and S. Toutain, Broadband high directivity 3dB coupler using coplanar waveguide technology, *IMS'95, IEEE MTT-S Int. Microwave Symp. Digest*, 1995, pp. 671–674.
19. Y. H. Shu, J. A. Navarro, and K. Chang, Electronically switchable and tunable coplanar waveguide-slotline band-pass filters, *IEEE Trans. Microwave Theory Tech.* **MTT-39**(3): 548–554 (1991).
20. J. A. Navarro, and K. Chang, Varactor-tunable uniplanar ring resonators, *IEEE Trans. Microwave Theory Tech.* **MTT-41**(5):760–766 (1993).
21. G. Tanné, E. Rius, F. Mahé, S. Toutain, F. Biron, L. Billonnet, B. Jarry, and P. Guillon, Improvements in losses and size of frequency tunable coplanar filter structures using MMIC negative resistance chips for multistandard mobile communication systems, *IMS'2000, IEEE MTT-S Int. Microwave Symp. Digest*, 2000, Vol. 2, pp. 1165–1168.
22. Y. P. Tsvividis and J. O. Voorman, *Integrated Continuous-Time Filters*, IEEE Press, New York, 1993.
23. P. Katzin, B. Bedart, and Y. Ayasli, Narrow-band MMIC filter with automatic tuning and Q-factor control, *IEEE MTT-S Int. Microwave Symp. Digest*, 1993, pp. 403–406.
24. V. Aparin and P. Katzin, Active GaAsMMIC bandpass filters with automatic frequency tuning and insertion loss control, *IEEE J. Solid-State Circ.* **30**(10):1068–1073 (1995).
25. H. Serhan, B. Jarry, and P. Guillon, Automatic frequency control techniques for microwave active filters, *IMS'97, IEEE MTT-S Int. Microwave Symp. Digest*, 1997.
26. S. Quintanel, H. Serhan, B. Jarry, L. Billonnet, and P. Guillon, Theoretical and experimental analysis of automatic frequency control techniques for microwave active filters, *Microwave Opt. Technol. Lett.* **27**(1):23–27 (2000).
27. P. R. Gray and R. G. Meyer, *Analysis and Design of Analog Integrated Circuits*, Wiley, 1977.
28. J. D. Cressler, A new contender for Si-based RF and microwave circuit applications (invited paper), *IEEE Trans. Microwave Theory Tech.* **MTT-46**(5):572–589 (1998).
29. D. Li and Y. Tsvividis, Active LC filters on silicon, *IEEE Proc. Circ. Devices Syst.* **147**(1) (2000).
30. H. Bazzi, F. Biron, S. Bosse, L. Delage, B. Barelaud, L. Billonnet, and B. Jarry, Microwave planar active filters in GaAs and SiGe technologies, *IMS'2002, IEEE MTT-S Int. Microwave Symp. Digest*, 2002.
31. BYR monolithic process, AMS, www.advanced-monolithic.com/index.html.
32. ED02Ah monolithic process, OMMIC, *ED02Ah Design Manual*, GaAs Foundry and ASIC Design Center, <http://www.ommic.fr> (2000).
33. AT46000 monolithic process, ATMEL, www.eu.atmel.com.
34. K. W. Kobayashi and A. K. Oki, A novel heterojunction bipolar transistor VCO using an active tunable inductance, *IEEE Microwave Guided Wave Lett.* **4**(7):235–237 (1994).
35. J. Caldinhas Vaz, L. Delage, and J. Costa Freire, GHz SiBiCMOS active inductors, *ConfTele 2001*, Figueira da Foz, Portugal, 2001.
36. H. Bazzi, S. Bosse, L. Delage, B. Barelaud, L. Billonnet, and B. Jarry, Using HBT BiCMOS differential structures at microwaves in SiGe technologies, *Proc. GAAS'2002, 10th European Gallium Arsenide and Related III-V Compounds Applications Symp.*, 2002.
37. QuBIC4 monolithic process, PHILIPS, www-eu3.semiconductors.philips.com/index.html.

ADAPTIVE ARRAY ANTENNAS

CHEN SUN

Nanyang Technological
University
Singapore

NEMAI C. KARMAKAR
Monash University
Victoria, Australia

1. INTRODUCTION

Demands for better-quality and new value-added services of existing wireless communication infrastructures have risen beyond all expectations. It is estimated that half a billion handsets will be put into the context of the third-generation system (UMTS, IMT 2000), which will provide an up to 2 MB (megabytes of) bandwidth for each user [1]. The challenging demand is to increase the spectrum efficiency and the system capacity of the current wireless networks. These demands have brought technological challenges to service providers. Because of the ability of suppressing interference and combating against fading and providing new services, adaptive array antennas or “smart” antennas have become one of the key technologies to realize third-generation (3G) and even fourth-generation (4G) wireless communications. We start with an overview of the evolution of wireless communication systems, calling for new technologies to support its new applications and improved qualities. Adaptive array antennas or smart antennas turn out to be solutions in the process of the evolution. We will present various applications of smart antenna technologies in wireless communications.

After that, different architectures of adaptive array antennas are presented with illustrations followed by descriptions of some algorithms. Finally, we compare the adaptive array antennas architectures and their suitability to different applications.

2. DEMANDS FOR ADAPTIVE ARRAY ANTENNAS

In 1899, Guglielmo Marconi transmitted signals across the English Channel, between Wimereux and Dover. In 1901, the first transatlantic wireless transmission was demonstrated [2]. Intrigued by that, scientists and engineers had been investigating new wireless communications methods and services. The era of wireless communications had just begun.

The wireless communication industry has experienced phenomenal technological advancement manifested in various application scenarios, including wireless remote control, codeless telephony, paging, wireless networks, terrestrial cellular telephone systems, and satellite communications [3]. Among them, the cellular telephone systems have been developing from the first-generation systems that were deployed firstly by Nippon Telephone and Telegraph (NTT). Through the 2G systems [i.e., Global System for Mobile Communications (GSM) and Digital Cellular System 1800 (DCS 1800) in Europe, Personal Communication System 1900 (PCS 1900), interim standard 95 (IS-95) and IS-136 in North America and Personal Digital Cellular (PDC) in Japan], the wireless system is evolving to the 3G system [i.e., wideband code-division multiple access (WCDMA) and CDMA 2000], and will approach the 4G system in the near future [3–5].

The 3G system is a universal, multifunctional, globally compatible digital mobile radio system. It allows users to communicate anyone, anywhere, at anytime. The system integrates paging, cordless, cellular, wireless network, and satellite communication systems into a single mobile terminal. The user can use the 3G terminal for conventional voice phonecall, broadband access to the Internet, high-speed package data services, and position tracking [3–12].

The main features of 3G and beyond communications systems are

- *High-Data-Rate Communications.* The minimum requirements of the user data rates in different environments are 144 kbps (kilobits per second) for vehicular applications, 384 kbps for pedestrian, 2 Mbps for indoor office, and 9.6 kbps for satellite communications. These goals require a significantly increased frequency efficiency that is measured by the bps/Hz.
- *New Services.* New services include intelligent transportation, position location (PL) services, and ad hoc networks. These location-aware services require new techniques to provide position information.
- *More Subscribers.* The wireless communications will be so ubiquitous that more subscribers or users are accommodated. This feature demands a dramatic increase in the mobile radio system capacity measured by the number of users within a given frequency spectrum.

During the migration from the 2G system to the 3G system, great efforts have been directed toward the development of the modulation, coding, and protocols on the 2G systems, such as code-division multiple access (CDMA) with IS-95, time-division multiple access (TDMA) with IS-136, and GSM. These techniques have been exhausted to the limit because of the large number of subscribers within the limited channel capacity. Antennas have gained much interest among researchers. The smart antenna system, in the form of adaptive arrays, can mitigate three major impairments caused by wireless channels: *fading*, *delay spread*, and *cochannel interference*. It can also bring many benefits to the existing wireless communication system, such as the enhancement of coverage for portable mobile applications, improved signal-to-interference ratio (SIR) and an increased channel capacity [13,14], lower transmitted power, and higher transmission data rate. Employing adaptive array antennas into current wireless communication infrastructures also brings value-added services, such as general packet radio service (GPRS), users' PL, and the intelligent transportation system [13,15].

3. CURRENT APPLICATIONS OF ADAPTIVE ARRAY ANTENNAS

Along with the evolving development of smart antenna technologies, the applications of adaptive array antennas have extended from the early forms such as diversity and sectoring to the recent employment such as space-division multiple access (SDMA) and multiple-input multiple-output (MIMO) communications. In this section, we give a brief introduction on some applications of adaptive array antennas in the wireless communications.

3.1. Diversity Scheme

The earliest application of adaptive array antennas is diversity. The scheme has found many applications over the years. It has been in wide use in a variety of present-day microwave systems [16–20]. The aims of this scheme are to extract information from several independent signal paths, to combine the multiple signals, and to reduce the effect of excessively high signal fade [21]. Because the probability of two independent signals having a deep fade at the same time is rare, combining them reduces the effect of the fades.

There are many mechanisms to provide diversity. They are space diversity (with spaced array elements), frequency diversity [multicarrier CDMA, orthogonal frequency division multiplexing (OFDM)], angle of arrival (AOA) or angular diversity (impinging waves with different directions), polarization diversity (transmitting signals with different polarized waves), time diversity (signal repetition), and multipath diversity (rake receiver technique) [16]. Among them, space diversity is the easiest one to implement. However, space diversity needs an array antenna with sufficient interelement spacing. Therefore, considering space limitation in a mobile phone, the polarization diversity provides a compact installation [22–26].

Geographically there are two kinds of diversity schemes: the macroscopic diversity scheme and the microscopic

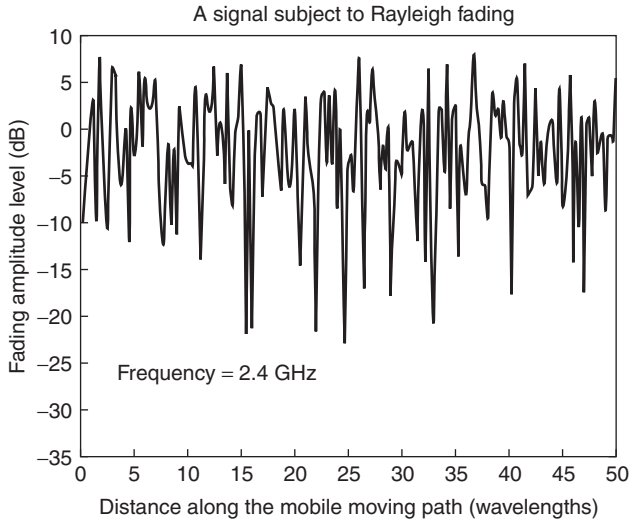


Figure 1. Rayleigh fading envelope.

diversity scheme. A *macroscopic diversity scheme* is used to combat against random shadowing effects where the signal power may drop to a point lower than the value predicted by a long-distance path loss model. The undulation of terrain contours determines the duration of the envelope variations during a long-term fading. The diversity scheme is employed by selecting signals from two separated base stations. On the other hand, in the *microscope cells*, clusters surround mobile users. Time dispersion caused by multipath propagation delays and the random frequency modulation due to varying Doppler shifts on different multiple signals result in fluctuations of the signal power at both base stations (BSs) and mobile terminals. This is commonly known as *Rayleigh fading* (see Fig. 1) [21]. Figure 2 shows the envelope correlation of two signal samples at distance/spacing ζ , where λ is wavelength of the carrier signal. The model assumes that the direction of arrivals (DoAs) of multipath signals are

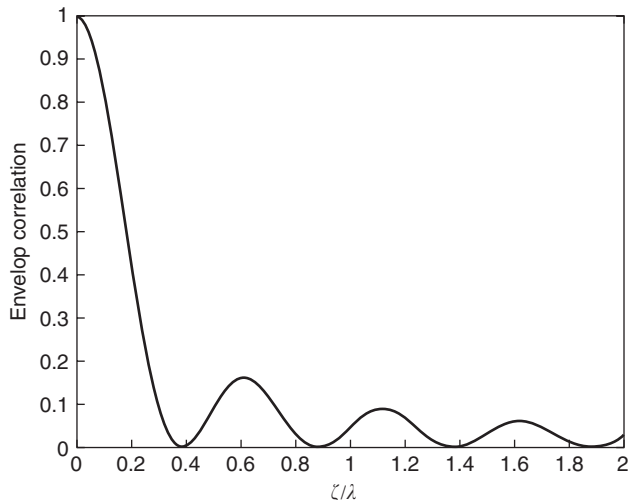


Figure 2. Envelope correlation spacing in a two-dimensional (2D) Clarke scenario.

uniformly distributed over 360° . Spacing of 0.13λ achieves a correlation lower than 0.7. For practical implementations of a microscopic diversity scheme, array antennas with interelement spacing of 0.38λ for a mobile station (MS) or tens of wavelength for a BS can provide independent signals at separate elements [17]. Ericsson has proved the improvement of the uplink performance employing both space and polarization diversities [27,28]. The international team of Ericsson has built a testbed to study the performance of the smart antenna receiver for digital advanced mobile phone service (AMPS). The uplink receiver uses space and polarization diversities. The interelement spacing is 15λ . The system provides a 3.5 dB gain in signal-to-noise ratio (SNR).

3.2. Sectoring

The ultimate goal of implementing a wireless cellular system is to achieve high capacity while satisfying quality-of-service (QoS) expectations. Cell splitting is a simple way to reduce cochannel interference (CCI). Currently most existing cellular and personal communication service (PCS) systems [3] make use of the sectoring technique in addition to the spatial diversity scheme. Each cell is divided into radial sectors with widebeam directional antennas installed at the BS [3,4,18,29]. Typically, those cells are divided into three sectors, which are 120° wide or six sectors that are 60° wide. Let us consider a cellular system with the cluster size of 7. The 120° cell sectoring reduces the number of the first-tier CCIs from 6 to 2 and brings a 6.8 dB SIR gain [1]. In addition to CCI suppression, another attractive benefit of sectoring is that frequency resources can be reused more frequently; thereby each cell can accommodate a larger traffic density without adding extra base stations.

Higher-order sectorization can be employed via beamforming or employing directional panel antennas to increase the frequency reuse and thus further improve the system capacity [29]. Sectoring via adaptive beamforming even allows more flexible allocation of transmit power at the BS [29]. However, handover will be initiated more frequently. Therefore, the system complexity is also increased.

3.3. Interference Suppression with Adaptive Beamforming

Adaptive antennas date back to 1959. The original work was attributed to L. C. Van Atta's work, *Electromagnetic Reflection* [U.S. Patent 29,080,002 (1959)]. Since then, adaptive beamforming techniques have been employed to remove unwanted noise and jamming from the output, mainly in military applications [4]. With the thriving commercial wireless communication industry and the advancing microprocessor technologies, the adaptive beamforming techniques have found their applications in commercial wireless communications. With powerful DSP hardware at the baseband, algorithms could control antenna beam patterns adaptively to the real signal environment, forming beams toward the desired signals while forming nulls to cochannel interferers. Thus, the system performance is optimized in terms of link quality and system capacity.

Field trials of both multibeam antennas and adaptive arrays have demonstrated performance improvements. Promising results substantiate the potential benefits of the adaptive beamforming technologies [30–37]. Meta-wave has extensively studied the range increase of multibeam antennas. Employing a 24-beam 15° beamwidth system, switching combining from two strongest directional beams achieves a 5 dB gain in a typical cellular environment [30]. An increased interference tolerance of 9 dB in the IS-136 system with a four-element adaptive antenna is demonstrated by Ericsson [31–33,37]. Lucent/AT&T has demonstrated the operation with an equal-power interferer next to the desired mobile terminal several miles from the base station in an IS-136 system with a four-element adaptive antenna [33]. Field trials have also been done for Digital European Cordless Telecommunications (DECT) system under the European TSUNAMI project [34]. Commercial products include a four-beam smart antenna incorporated into a GSM base station product by Nortel, and adaptive array processing using two base-station antennas incorporated into an IS-136 base station product by Ericsson [33–36].

However, the extensive implementation of adaptive antennas has been a problem. Because of system complexity, the fabrication cost, and the operational expenditure, adaptive antennas are limited to base stations or military applications. Researchers are endeavoring to make low-profile and low-power-consumption antennas for mobile terminals. Parasitic array antennas have become an active research topic. The antennas normally has one active element connected to the radiofrequency (RF) port, and beam pattern adaptation is achieved by switching among parasitic elements or by adjusting the loaded reactance at the passive elements. Being a less complicated structure, it offers an economical way to design low power consumption adaptive array antennas.

3.4. Space-Division Multiple Access

Filtering in the space domain separates spectrally and temporally overlapping signals from multiple MSs. Thus, the spatial dimension can be exploited as a hybrid multiple-access technique complementing existing multiple access schemes such as frequency-division multiple access (FDMA), TDMA, and CDMA. This approach is usually referred to as *space-division multiple access* (SDMA). The realization of this filtering technique is accomplished by using a smart antenna, which is capable of modifying its time, frequency, and spatial response by means of the amplitude and phase weighting and the internal feedback control (see Fig. 3). The SDMA scheme enables multiple users within the same radio cell to be accommodated on the same frequency or timeslot. Thus, it will increase the system capacity significantly [13,38–43]. The concept of the SDMA scheme is demonstrated by the TSUNAMI project. A uniform linear array consists of eight elements with a beamforming card developed by ERA Technology [44] used at the BS. The multiple signal classification (MUSIC) algorithm is used to find the direction of the MS. The Kalman filter is used to track the MS [34].

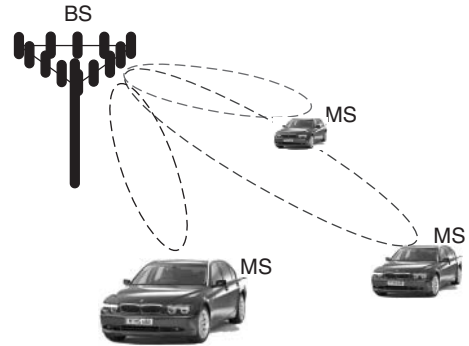


Figure 3. Space-division multiplexing (SDM) using spot beams at BS.

In addition to applications at terrestrial cellular systems, the SDMA scheme has been employed in satellite communications where each spot beam services a geographic area [39]. For an L-band mobile satellite communication system, to increase the frequency reuse in the spatial domain, multiple-beam satellite antennas are used for coverage of Canada and the United States. In comparison with a single-beam antenna, frequency reuse is increased by a factor of 4/3 using a four-beam antenna and 12/3 using a 12-beam antenna [39]. In Japan, a six-beam satellite antenna is used for 22-GHz band satellite broadcasting [45].

4. INCOMING APPLICATIONS OF ADAPTIVE ARRAY ANTENNAS

In addition to the aforementioned applications, new applications will be incorporated into future wireless communications standards of the 3G and 4G systems. Extensive investigations have been carried out to bring these new applications into reality.

4.1. Ad Hoc Networks

An ad hoc network is a dynamic wireless network established by peer-to-peer communications among mobile nodes (e.g., laptops, PDAs) without the help of any infrastructure such as a wire/wireless backbone [9,46–50]. The concept is shown in Fig. 4, in which each mobile terminal directs its beam toward the neighboring node to form a mesh where each node is a potential router. Changing together a sequence of neighboring nodes dynamically changes the routing of an information packet from an information source to a destination. Researchers are investigating media access control (MAC) protocols of ad hoc networks. Adaptive array antennas are a critical part, as many MAC protocol designs include the antenna beam pattern control [47,48]. With a properly oriented beam (toward the desired node), each node can resolve signals from neighboring nodes. The idea is the same as for an SDMA system. The DoA information from the antenna is used in routing selection. Another important issue of the ad hoc network is power consumption. Because mobile terminals for an ad hoc network have a limited battery life (around 3–4 h for a laptop), adaptive array

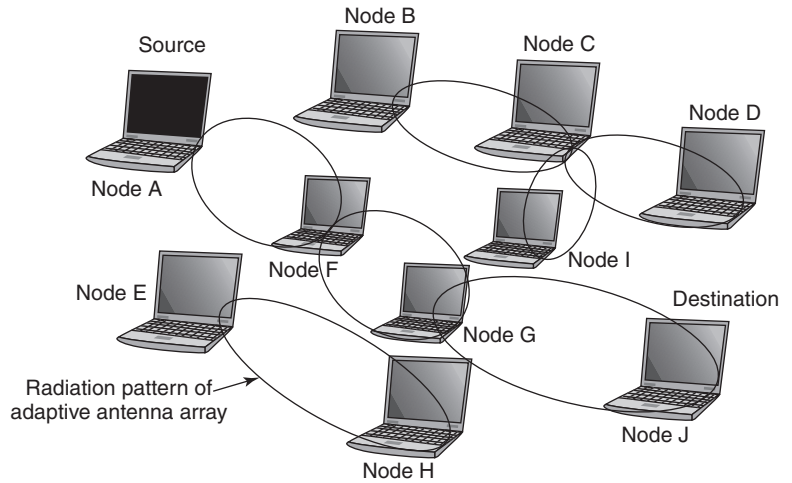


Figure 4. Ad hoc network with directional antenna at each mobile terminal.

antennas for this application are also required to have easy beam pattern control and consume as little power as possible.

4.2. Position-Location-Based Services

Safety is the primary motivation for PL services. In the United States, the Federal Communications Commission has mandated PL services within 125m accuracy on wireless emergency calls [13,18,51]. Using adaptive antennas, direction finding systems provide a mobile user’s position information. This location information aids emergency rescue, law enforcement, and other emergency calls. With the position location information, other promising applications such as accident reporting, navigational services, automated billing, fraud detection, roadside assistance, and cargo tracking are also becoming reality [15].

Currently, there are many existing PL systems, including the Global Positioning System (GPS), Global Navigation Satellite System (GLONASS), signpost navigation, and cellular geolocation [13]. Among them, cellular geolocation is the most attractive. It only needs to implement the smart antenna system, which has DoA estimation ability, into the existing wireless communication systems. The realization is based mainly on three mechanisms [51]: beacon location methods, DoA estimation techniques, and time-difference-of-arrival (TDoA) techniques. The concept of geolocation technique is shown in Fig. 5. The BSs located near the MSs estimate the DoA of the impinging wave from the terminal. From the DoA estimate, a line of bearing (LoB) from the base station to the mobile transmitter can be drawn. Multiple LoBs, drawn from different BS locations, intersect at the estimated location of the mobile terminal.

4.3. High-Data-Rate Transmission over MIMO Systems

The goal of the 3G communications systems is to provide high-data-rate transmission [5–8,11,52]. The goal urges a significant increase of channel capacity or, say, spectrum efficiency. MIMO systems have shed light in the tunnel to higher-data-rate transmissions. In commercial and

economical aspects the MIMO system is the most promising candidate as it offers such a significant capacity upgrade that high-data-rate transmission can be achieved [52–59].

Multipath fading has long been viewed as impairment to the wireless communications link. Techniques such as diversity combining, equalization, and adaptive beamforming have been investigated to reduce the fading. A different view is that exploiting multipath fading realizes higher-data-rate transmission. In a multipath-rich environment, antenna arrays that provide uncorrelated signal outputs are installed at both transmitters and receivers to build MIMO wireless communication channels [60–65]. The multipath phenomenon achieves an information-theoretic channel capacity that increases with the number of array antenna elements. In Fig. 6, Tx and Rx are the numbers of transmit antennas and receive antennas. We observe that the capacity grows significantly when Tx and Rx increase.

Transmission STC through MIMO systems takes advantage of spatial and temporal diversities to increase the data rate over fading channels [53]. Field tests and experimental results substantiate the capacity gain achieved by MIMO systems [66,67]. Lucent Technologies has achieved

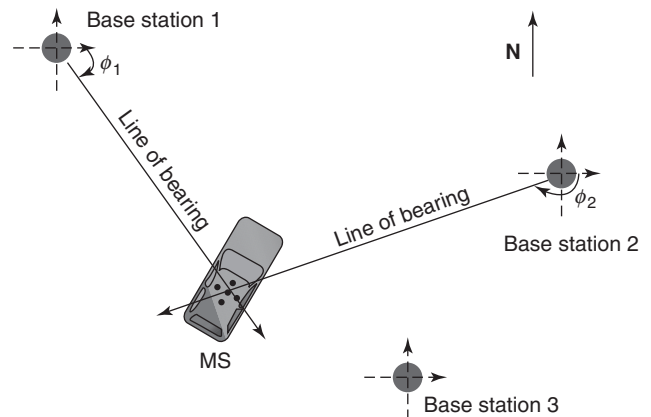


Figure 5. Concept of cellular geolocation.

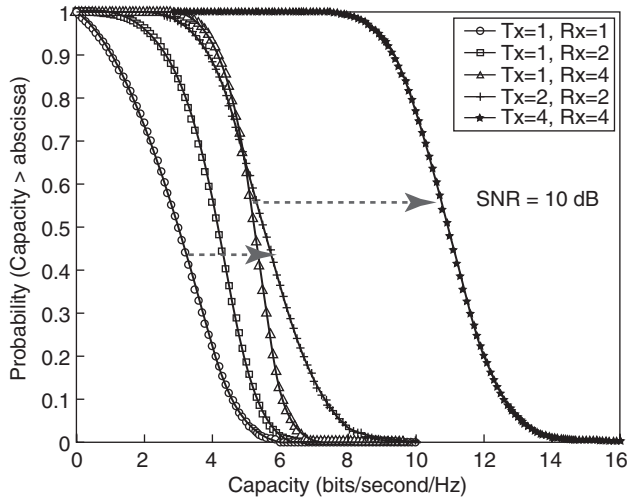


Figure 6. MIMO information-theoretic channel capacities with different numbers of transmit antenna and receive antennas.

a transmission data rate of 40 bps/Hz at a 30 dB SNR indoor flat fading environment using 8 transmit and 12 receive antennas vertical Bell Labs layered spacetime (V-BLAST) architecture [68,69].

5. ARCHITECTURES AND IMPLEMENTATIONS OF ADAPTIVE ARRAY ANTENNAS

In the previous section, we presented the applications of smart antenna technologies. Various applications require different functions from adaptive array antennas. For example, SDMA requires fine beamforming ability. PL services demand for DoA estimation, and MIMO systems require decorrelation among signal samples. In this section, we examine various realizations and implementation issues of adaptive array antennas. Figure 7 shows the tree structure of various smart antenna implementation architectures.

5.1. Switched-Beam Antennas

A switched-beam antenna system consists of several highly directive, fixed, predefined beams [13,14,18,63,70–72]. In practice, multiple beams can be formed by a beamforming

network, which consists of an involved feeding system and multiple input ports. The feeding network that provides adequate excitation to the array elements can steer the beam pattern to the desired direction. It can be implemented at either RF stage or intermediate-frequency (IF) stage. The functional block diagram of a switched-beam antenna is shown in Fig. 8. An example of the beam-forming network is the Butler matrix [14,18,71,73], which consists of power splitters and phase shifters. It has been used extensively over the years in radar, electronic warfare (electronic support measures), and satellite systems. Figure 9 depicts a 4 × 4 Butler matrix. Figure 10 illustrates the produced beam patterns with the 4 × 4 Butler matrix.

The receiver chooses from the one of the several beams to give the best performance. The decision making stage can be implemented at the IF stage, based on the criterion of the maximum received power using a received signal strength indicator (RSSI) or at the baseband digital stage by examining the lowest signal bit error rate (BER). In Ref. 74, an 8 × 8 Butler matrix is used to generate eight Woodward Lawson beams. Microstrip patch antennas are chosen as the array elements. Mutual coupling between elements is reduced to a level of less than -15 dB by using H-shaped slot feeding technique. Measurement results show that 13 dBi directivity gain is achieved for the eight beams covering a 114° angular range. A beam selector chooses either one of the eight fixed beams or two neighboring beams by examining the output signal BER.

In a sense, a switched beam is an extension of the conventional sector beam antenna in that it divides a sector into several microsectors [63]. Therefore, the switched-beam antenna system is the easiest solution to upgrade the existing system, which employs 120° sector antennas and dual diversity per sector. However, switched-beam antennas also have drawbacks. They do not exploit multipath. In addition, the signal power from the mobile terminal drops greatly when the mobile terminal moves into the margin of a beam or the area between two beams. Furthermore, owing to the inability to distinguish a desired user from interferers, switched-beam antennas are not effective in combating against CCI. If a strong interfering signal is at the center of a selected beam and the desired user is away from the center of that beam, the interfering signal can be enhanced far more than the desired signal. One solution of the aforementioned problems has

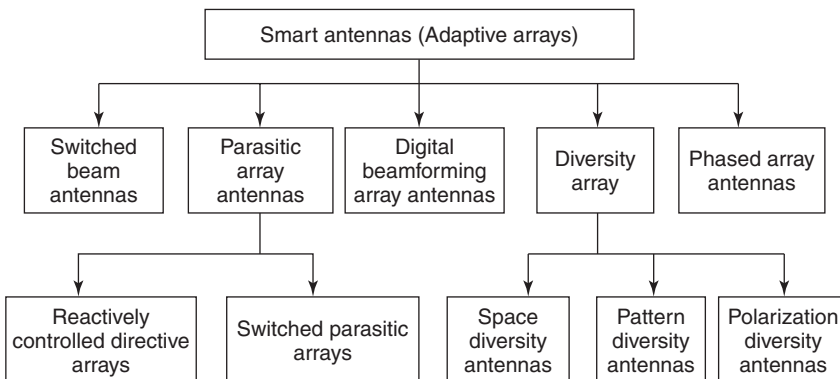


Figure 7. Various architectures of adaptive array antennas.

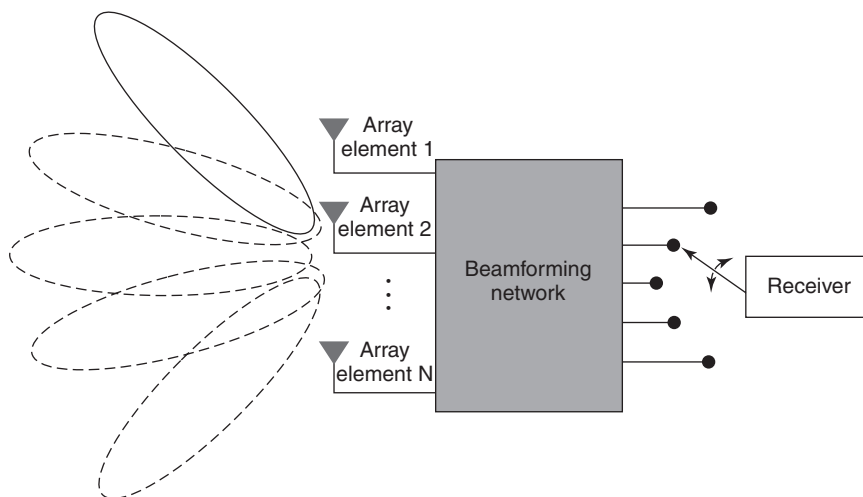


Figure 8. Functional block diagram of switched-beam antennas.

been presented in Refs. 75–77, where phase shifters are added to the switching system. The structure achieves a smoother transition from one beam to another.

5.2. Phased-Array Antennas

Research and development (R&D) of phased-array antennas for radar systems has been ongoing in the United States since 1950s [78]. Since then, phased-array antennas have been extensively utilized in radar, military scenarios, and satellite communications. Now the antennas are used more for space-based communications applications because of their advantages in scanning, reconfigurability, weight, and power. In satellite communications, adaptive array antennas function as input–output ports of the link at both satellite and ground segments. In Japan, phased-array antennas were first applied when Japanese Defense developed a passive array antenna consisting of element antennas equipped with phase shifters and power divider/combiners in the 1960s [78]. The Communication Research laboratory (CRL) and National Space Development Agency of Japan (NASDA) developed an onboard Ka-band (20/30-GHz) scanning spot beam active phased array

antenna for the experimental high data rate (gigabit) communication satellite [79]. Both the transmit and receive antennas use a meanderline polarizer and 64 pyramidal horn element antennas, and realize circularly polarized scanning spot beams. Each antenna is connected with four independent 4-bit digital phase shifters to achieve four independent beams, respectively. In Australia a 12-element land mobile terminal phased-array antenna is designed for continuous tracking of the Mobilesat satellite while the terminal is moving [80]. The role of a phased-array antenna for mobile terminal in satellite communication scenario is to enable transmission and reception of microwave signals and to track the satellite while the vehicle is moving. As shown in Fig. 11, the terminal is equipped with phased-array antenna as the mobile antenna, an antenna electronic unit (AEU), a transceiving unit, and a satellite tracking unit. The functional block diagram of the mobile antenna is depicted in Fig. 12. The beamforming network consists of power dividers, couplers, switches, phase shifters, biasing networks, and

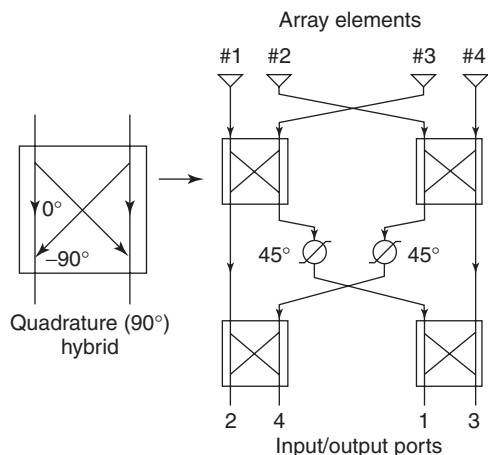


Figure 9. A four-port Butler matrix for fixed beamforming [71].

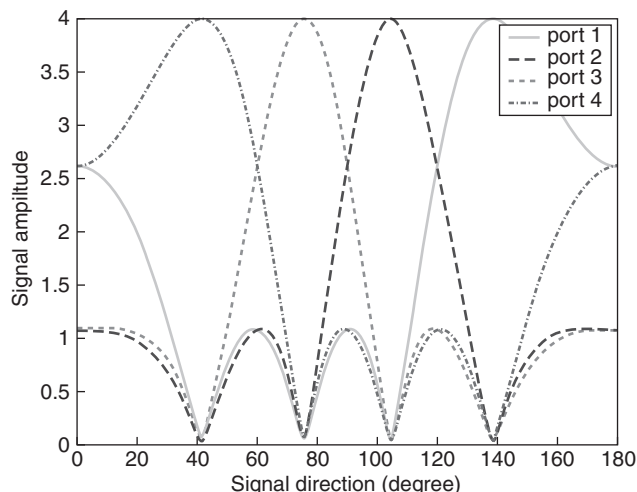


Figure 10. A set of four beams produced using a 4 × 4 Butler matrix. (This figure is available in full color at <http://www.mrw.interscience.wiley.com/erfme>.)

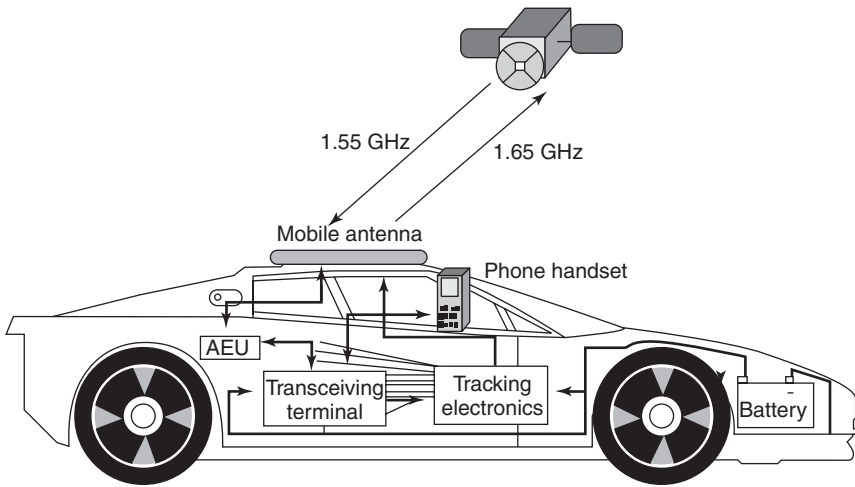


Figure 11. Functional block diagram of a mobile satellite communication terminal and a phased-array antenna mounted on a car.

circularly polarized (CP) patch antennas as array elements. The system conforms with the Australian mobile satellite specifications:

- *Polarization.* right-hand circular
- *Frequency.* 1646.5–1660.5 MHz for transmission; 1545.0–1559.0 MHz for reception
- *Coverage.* full 360° in azimuth and 28–66° in elevation
- *Gain.* 10–12 dBi desirable with a minimum of 7 dBi

In the design presented in Ref. 80, single-feed stacked patch elements presented in Ref. 75 (see Fig. 13) are selected as the best candidates for constructing the planar phased array. The detailed view of the developed multilayer phased-array antenna is shown in Fig. 14. The multilayer design includes stacked CP patch antenna arrays and two foam layers to achieve an increased antenna beamwidth, a slotted ground layer for coupling, and an antenna beamforming network layer as shown in Fig. 15. The beamforming network layer consists of a 12-way feed power division/combination network as required for 12 patch antenna elements arranged in two rings of 8 and 4 elements. Twelve 3-bit digital phase shifters (including a 180° switched-line phase shifter and 45° and 90° loaded line phase shifters), located at the outputs of the 12-way divider, are coupled to individual antenna elements via aperture coupling.

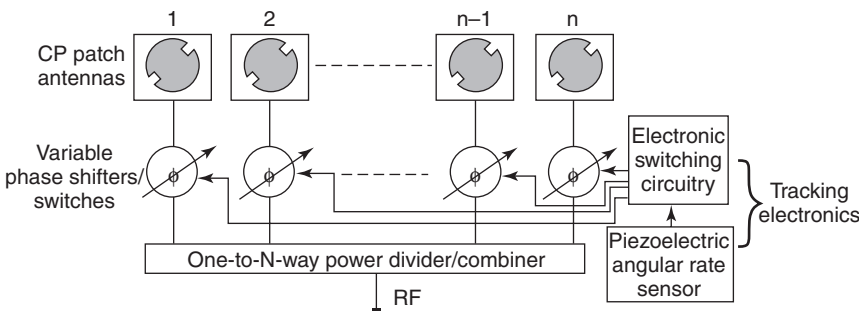


Figure 12. Functional block diagram of a phased-array antenna at land mobiles for satellite communications.

Phased-array antennas contain a multitude of radiating elements, typically arranged in a rectangular or triangular tessellation. Beam pattern steering of phased-array antennas is achieved by implementing phase shift of signals from array elements [18,63,70,75,80–82]. Dynamic phased arrays make use of the DoA information from a desired user and steer a beam maximum toward that user, thus improving the capabilities of a switched-beam antenna [63]. Tracking is needed to continuously steer the beam toward the desired user. However, the disadvantage of the phased-array antenna is the relatively high cost as expensive PIN diodes are used in phase shifters required by beamforming networks [75].

5.3. Digital Beamforming Array Antennas

The technological progress of DSP has introduced the concept of beamforming in the digital stage [14,18,37,39,63,70,82–84]. In comparison with switched-beam antennas and phased-array antennas, smoother pattern direction tuning and higher-resolution direction finding can be achieved with high-speed DSP and high-resolution ADC. The functional block diagram of a DBF array antenna is shown in Fig. 16. Each downconversion channel has a low-noise amplifier, a frequency converter, and an ADC. Signals received by individual antenna elements are downconverted to the baseband, digitized, and then fed into a DSP chip where algorithms are carried out. A fine steering is achievable by employing high-resolution sampling and

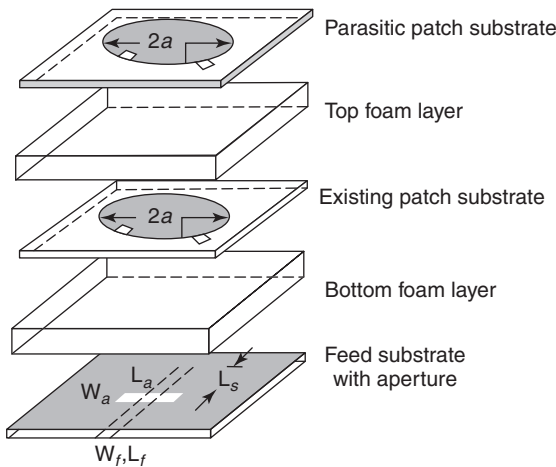


Figure 13. Stacked patch with perturbation segments [75].

quantization in an A/D conversion process. Many beamforming and DoA estimation algorithms have been studied [3,4,8,37,39,63,85–89]. Simulations and tests show that they are fruitful in improving the system capacity and enhancing system performance [37,39,87].

However, high-resolution A/D conversion dissipates a substantial amount of DC power. Furthermore, since a DBF antenna needs the same number of A/D converters as does the number of antenna elements, the fabrication cost increases with the number of antenna elements. In addition, because A/D conversion cannot be carried out directly in the RF stage, same amount of power are also consumed at the frequency converters [14,82,90]. For these reasons, the use of DBF antennas has been restricted to military applications, satellite communications, or at the base station for terrestrial wireless communications.

5.4. Parasitic Array Antennas

To circumvent the disadvantages of the aforementioned systems, adaptive beamforming based on parasitic antennas has been explored [82,90–107]. In a parasitic array antenna, the active element, which is excited by the transmitted or

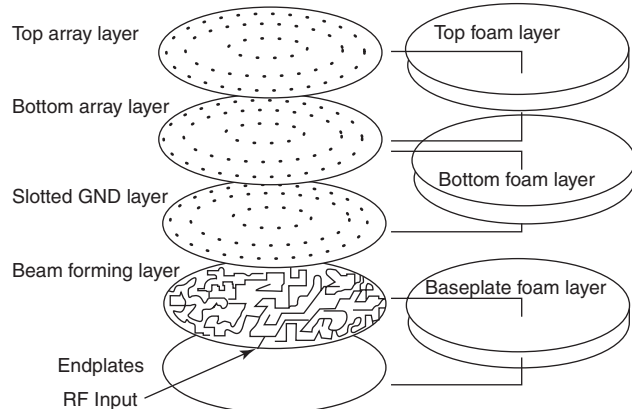


Figure 14. Detailed view of the developed multilayer phased-array antenna.

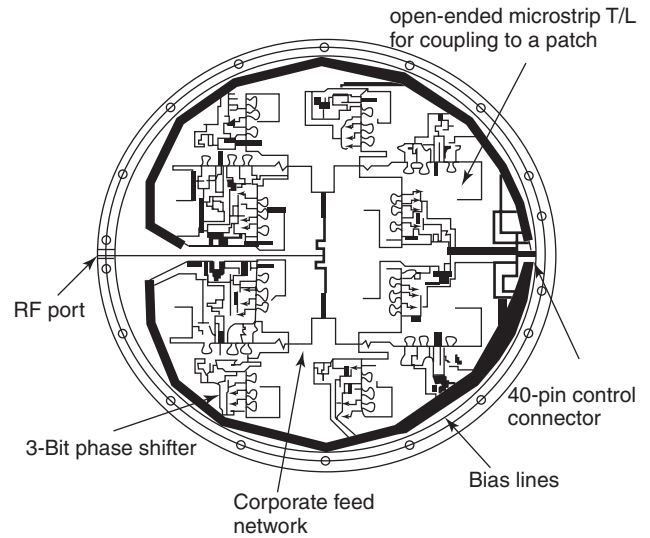


Figure 15. Detailed view of the beamforming layer.

the received signal sources, is surrounded by a number of parasitic elements, which are not connected to the signal source. In the presence of neighboring elements, the performance of each element depends not only on that element's current but also the currents of neighboring elements. For resonant elements with no current excitation of their own, a substantial current could be induced by radiation from another source [108]. The far-field radiation pattern is formed by superposition of the radiation of all antenna array elements [109]. Thus, by changing the radiation of each element, it is possible to direct the antenna beam toward desired directions.

The use of parasitic elements for controlling antenna beam patterns goes back to the work of Yagi and Uda during the 1930s [108]. This antenna array has been patented in various forms for numerous applications. Various electronically steered Yagi–Uda arrays have been designed. A reflector formed by short-circuited elements is arranged behind the active element. Figure 17 illustrates the formation of Yagi-Uda array with the switched parasitic elements. By controlling the states (ON or OFF) of the PIN diode switches of the parasitic elements, different sets of short-circuited monopoles function as directors and reflectors around the active central monopole. Therefore, directive beams are steered toward the desired directions [91–93,96,97,100,102,103]. Instead of using one active element at a fixed position, multiple active elements give more choices of producing multiple beams [97,98,101,107]. Similar to those wire antenna elements switched by diodes, it is also possible to use switches to control the radiation pattern of parasitic patch elements and thereby change the beam direction of a parasitic patch array antenna [99]. The aforementioned antennas are categorized as “switched parasitic antennas” [105]. Using switched parasitic antennas, beam directions can be selected only among predefined directions. Analogous to switched-beam antennas, this limits performance.

Another category of parasitic array antennas is the “reactively controlled directive array antenna,” which

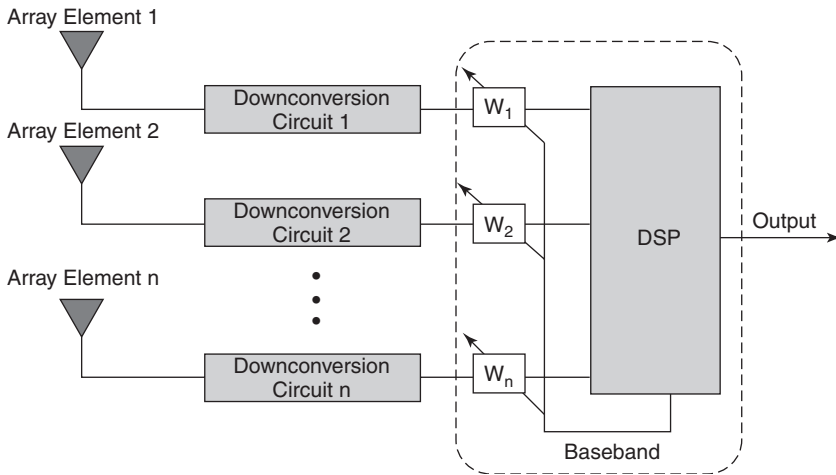


Figure 16. Functional block diagram of DBF array antennas.

dates back to Harrington’s work in 1978 [94]. The parasitic array is formed with one active and several surrounding monopoles on the ground plane. The functional block diagram is shown in Fig. 18. Changing the reactance of the parasitic elements alters the radiation of each element. Therefore, by adjusting the reactance loaded on the parasitic elements, directive beam patterns can be formed. With this configuration, it is possible to achieve a smoother beam pattern tuning. In Ref. 95, the array elements are realized microstrip patches. The loads on the parasitic elements are carried out by terminating a transmission line by a variable-reflection phase shifter. Adaptive beamforming is realized by the steepest-gradient optimization method. More recently, extensive investigations on adaptive beamforming and DoA estimation using this type of structure are carried out. A seven-element antenna called the *electronically steerable parasitic array radiator* (ESPAR) [90,104,110–112] has been developed.

Figure 19 shows the configuration of a seven-element ESPAR antenna. One active central element (monopole) is surrounded by six parasitic elements uniformly placed on a circular grid of radius R on a circular grounded baseplate. The length of each monopole L and the radius R of the circular grid are one-quarter wavelength ($\lambda/4$) of the transmitting RF signal at 2.484 GHz. According to Harrington [94], wide spacing among elements (e.g., $\lambda/2$) leads to reduced gain and significant backlobes. Moreover, further reduction of interelement spacing to $\lambda/8$ leads to a

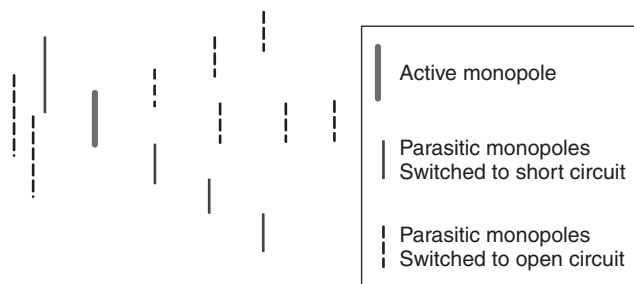


Figure 17. Structure of a switched parasitic array antenna.

supergain array. Therefore, a realistic design for spacing $= \lambda/4$ is chosen. The baseplate transforms monopoles with their images to dipoles with a length of $2L$. The central monopole is connected to a RF receiver, and each parasitic monopole is loaded with a tunable varactor that is realized with a reversely biased diode.

The working principle of ESPAR antennas is different from that for DBF array antennas. The antenna generates a directional beam based on tuning load reactances (x_1, x_2, \dots, x_6) on the parasitic monopoles. Signals received or transmitted from the central RF port excite the parasitic monopoles with substantial induced mutual currents on them. Let us first assume that the antenna is working in transmitting mode, where vectors \mathbf{i} and \mathbf{v} represent the currents and the voltages on the monopoles, respectively:

$$\mathbf{i} = [i_0 \ i_1 \ i_2 \ i_3 \ i_4 \ i_5 \ i_6]^T \quad (1)$$

$$\mathbf{v} = [v_0 \ v_1 \ v_2 \ v_3 \ v_4 \ v_5 \ v_6]^T \quad (2)$$

The superscript “T” represents the transpose; i_0 and v_0 represent the current and the voltage on the active central

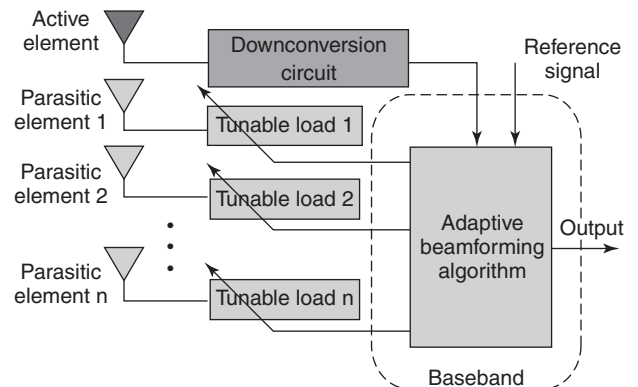


Figure 18. Functional block diagram of reactively controlled directive array antennas.

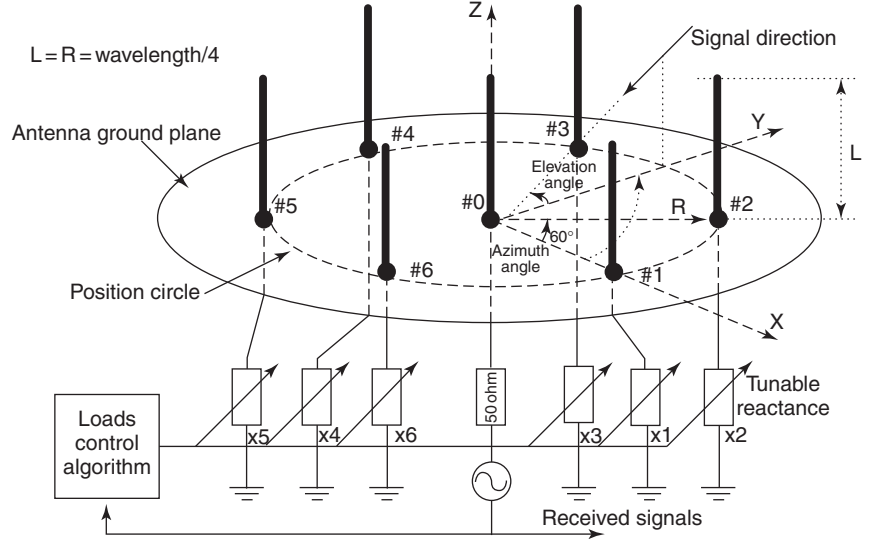


Figure 19. Configuration of a seven-element ESPAR antenna. The length of each monopole L and the radius R of the circular grid are one-quarter wavelength $\lambda/4$ of the transmitting RF signal at 2.484 GHz.

element (0), respectively. Mutual admittances are represented by the matrix \mathbf{Y}_C with each entity y_{ij} denoting the mutual admittance between the i th element and the j th element. The induced currents are represented with mutual admittances:

$$\mathbf{i} = \mathbf{Y}_C \mathbf{v} = \begin{bmatrix} y_{00} & y_{01} & y_{02} & y_{03} & y_{04} & y_{05} & y_{06} \\ y_{10} & y_{11} & y_{12} & y_{13} & y_{14} & y_{15} & y_{16} \\ y_{20} & y_{21} & y_{22} & y_{23} & y_{24} & y_{25} & y_{26} \\ y_{30} & y_{31} & y_{32} & y_{33} & y_{34} & y_{35} & y_{36} \\ y_{40} & y_{41} & y_{42} & y_{43} & y_{44} & y_{45} & y_{46} \\ y_{50} & y_{51} & y_{52} & y_{53} & y_{54} & y_{55} & y_{56} \\ y_{60} & y_{61} & y_{62} & y_{63} & y_{64} & y_{65} & y_{66} \end{bmatrix} \begin{bmatrix} v_0 \\ v_1 \\ v_2 \\ v_3 \\ v_4 \\ v_5 \\ v_6 \end{bmatrix}. \quad (3)$$

These values can be obtained using a numerical electromagnetic code (NEC) simulator [113]. The voltages on the active central monopole and the m th parasitic monopole are represented by v_0 and v_m , respectively. Let z_0 be the characteristic impedance at the RF port and v_s represent the transmitted voltage signal source with the amplitude and the phase from the driving RF port at the central element. Following the analysis in [90], we obtain

$$\mathbf{i} = v_s (\mathbf{Y}_C^{-1} + \mathbf{X}_L)^{-1} \mathbf{u}_1 \quad (4)$$

where $\mathbf{X}_L = \text{diag}[z_0, jx_1, \dots, jx_6]$ and $\mathbf{u}_1 = [1 \ 0 \ 0 \ 0 \ 0 \ 0 \ 0]^T$. The far-field radiation pattern is the superposition of all monopoles' radiation patterns [108]. Therefore, the far-field current signal in the azimuthal direction ϕ with its amplitude and the phase is represented as

$$y_{\text{far}}(\phi) = \mathbf{i}^T \mathbf{p} \mathbf{h} \alpha(\phi) = [(\mathbf{Y}_C^{-1} + \mathbf{X}_L)^{-1} \mathbf{u}_1]^T \mathbf{p} \mathbf{h} \alpha(\phi) v_s \quad (5)$$

where $\alpha(\phi)$ is the 7×1 dimensional steering vector corresponding to azimuth angle ϕ . It is expressed as

follows:

$$\alpha(\phi) = \begin{bmatrix} 1 & e^{j(\pi/2) \cos(\phi)} & e^{j(\pi/2) \cos(\phi - (\pi/3))} & e^{j(\pi/2) \cos(\phi - (2\pi/3))} \\ e^{j(\pi/2) \cos(\phi - \pi)} & e^{j(\pi/2) \cos(\phi - (4\pi/3))} & e^{j(\pi/2) \cos(\phi - (5\pi/3))} \end{bmatrix}^T \quad (6)$$

In (5), we denote $(\mathbf{Y}_C^{-1} + \mathbf{X}_L)^{-1} \mathbf{u}_1$ as \mathbf{w}_E and term it the “equivalent-weight vector” because of its resemblance to a (7×1) -dimensional beamforming weight vector in the array processing literature [90]. According to the reciprocity theory for radiation patterns [108], if the antenna is working in the receiving mode, the voltage signal, say, $y(t)$ at the RF port is expressed as

$$y(t) = \mathbf{w}_E^T \alpha(\phi) s(t) \quad (7)$$

where $s(t)$ represents the far-field impinging current waves with the amplitude and the phase in the azimuthal direction ϕ . It is clear that \mathbf{w}_E is dependent on the reactance values of the reactances at those parasitic elements; therefore a beamsteering pattern is achieved by properly adjusting reactance values. For the designed ESPAR antenna, the adjustable load reactances at the parasitic elements are realized with reversely biased diodes as shown in Fig. 20. The implementation achieves a frequency-dependent reactance value ranging from $-45.8j\Omega$ to $-3.6j\Omega$.

Since the load reactances and switches are realized by the diodes, there is only a small leakage current. Therefore, the power consumption of the parasitic array antennas is very small. Furthermore, the system normally has only one RF port and one subsequent downconversion circuit. In terms of power consumption and fabrication cost, it is obvious that parasitic array antennas are suitable for mass implementations of adaptive array antennas, especially for battery-powered portable mobile terminals.

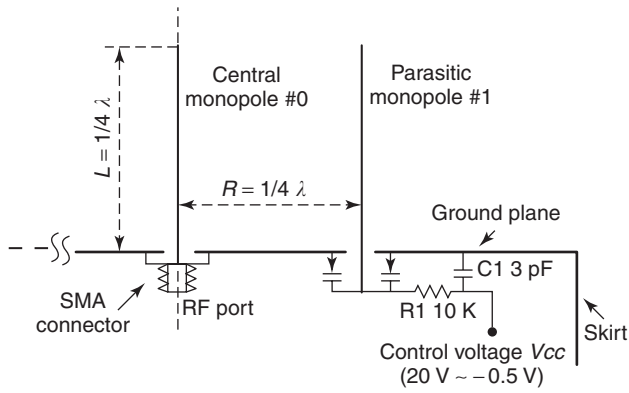


Figure 20. Vertical cross-sectional view of ESPAR antenna and a reactance circuit of one of the six parasitic elements. The length of each monopole is one-quarter wavelength ($\lambda/4$) of the transmitting RF signal at the frequency of 2.484 GHz [90].

5.5. Diversity Antennas

Diversity antennas combat against multipath fading and improve channel quality for a given radio spectrum in comparison with that from a single-port antenna [13,20,35,105,114]. Because the correlation among signals from the multiple ports of array antennas undermines diversity combining performance [16,20], the challenge of diversity antenna design is how to achieve signal decorrelation. This is particularly difficult in handphones where antenna elements are mounted within small spacing, for a given incident wave distribution scenario.

Colburn et al. [115] have presented three candidate dual-diversity antenna configurations: two side-mounted

planar-inverted F antennas (PIFAs), a back-mounted PIFA with a top-mounted helix, and a top-mounted PIFA with a flip monopole. Experimental results show sufficient signal decorrelation of these configurations. The diversity gain obtained with polarization diversity has been demonstrated with dual-polarized diversity obtained by an aperture-coupled patch antenna or by two slanted dipoles over an infinite ground plane [24]. Vaughan [102] presented diversity antennas using various parasitic array antenna structures. In one of the designs, three directional patterns are formed with three subsets of a parasitic array as shown in Fig. 17. By selecting one of the patterns pointing in different directions, angular diversity advantage is achieved. In another design, 16 parasitic monopoles are placed uniformly in the circle of radius 0.25 wavelength, and an active monopole is located at the center of the circle. The directional beam pattern with 90° half-power beamwidth (HPBW) is rotated, 360/16° each step, by shifting switch setting of parasitic elements. For adjacent beam patterns with 22.5° angular spacing, the envelope correlation of complex beam patterns is 0.91. For patterns with larger angular separation, say, 45°, the envelope correlation of 0.7 is achieved. The Virginia Tech Antenna Group has evaluated the envelope correlation, power imbalance, and diversity gain with space diversity, polarization diversity, and pattern diversity at handheld terminals [116]. The spatial diversity is achieved with two parallel half-wavelength dipoles with inter-element spacing variable from 0.1 to 0.5 wavelength. The dual-polarization diversity antenna is constructed with a dipole and a printed wheel antenna separated vertically by 0.3 wavelength. As for the pattern diversity, it is achieved with two dipoles, with 0.25 wavelength interelement

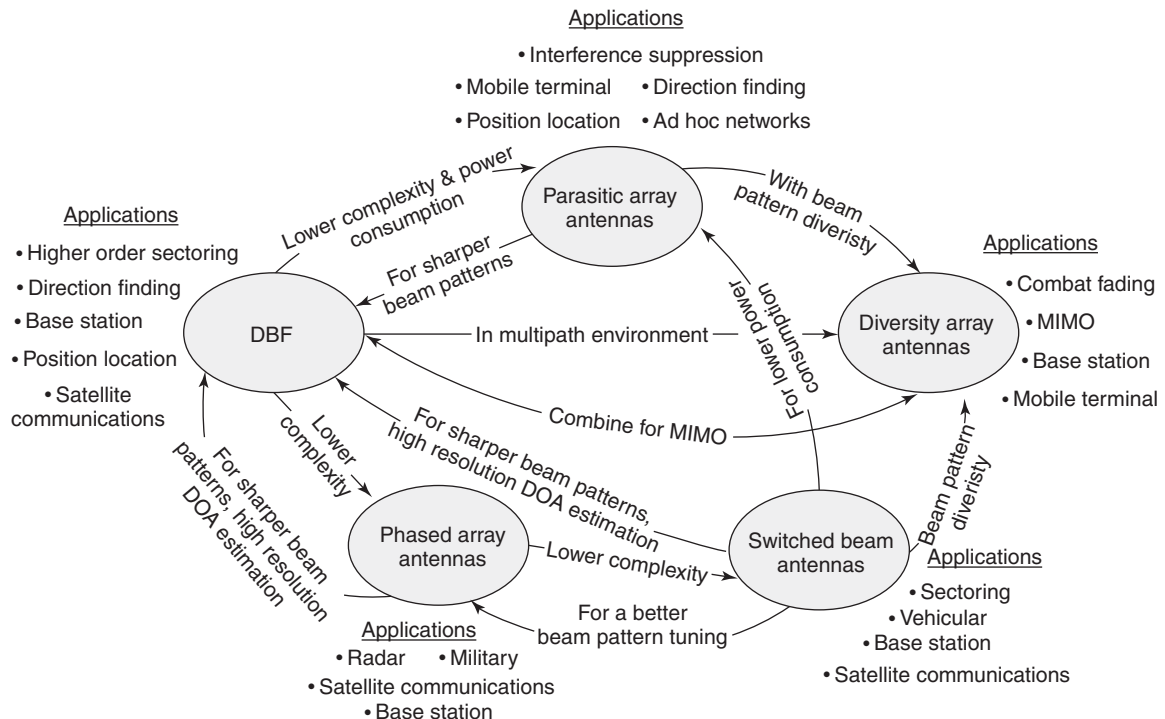


Figure 21. Relation of various adaptive array antenna structures and their applications.

Table 1. Comparison of Various Adaptive Array Antennas and Related References

Adaptive Array Architecture	Implementation stage	Decision–Control Stage	Applications	Refs.
Switched-beam antenna	RF/IF	Baseband/IF	Cellular base station, satellite communications	13, 14, 18, 63, 70–77
Phased-array antenna	RF	Baseband	Military, radar, satellite communications	18, 63, 70, 78–82
Digital beamforming (DBF)	Baseband DSP	Baseband	Cellular base station, satellite communications, radar, high-resolution direction finding	3, 4, 8, 14, 18, 37, 39, 63, 70, 82–89
Parasitic array	RF	Baseband	Power consumption limited mobile terminal, direction finding	82, 90–108, 110–112
Diversity array	Providing uncorrelated signals at RF stage	Baseband/IF	Mobile terminals, combating multipath fading, MIMO communications	20, 24, 105, 115, 116

spacing, connected to a quadrature (90°) hybrid (see Fig. 9). The structure provides two orthogonal beams at the two ports. Measured results in various multipath environments have clearly justified the feasibility of diversity at handheld terminals.

6. CONCLUSIONS

The wireless communications system is evolving with a fast pace. Better-quality wireless communications, new services and applications will become available with the technological advances. With different structures, adaptive array antennas play important roles in the evolution of wireless communications systems. Figure 21 and Table 1 generalize the tradeoff between the performance and complexities of various forms of adaptive array antennas, implementation stages and some of their applications. For applications where cost and power consumption are the main limiting factors, parasitic array antennas and switched-beam antennas are suitable. DBF array antennas and phased-array antennas dominate in the applications such as satellite communications and BS applications, where high performance is desired. In addition to combating fading, diversity antennas can also be employed to realize high-speed MIMO wireless transmissions.

BIBLIOGRAPHY

- G. L. Stuber, *Principle of Mobile Communication*, 2nd ed., Kluwer Academic Publishers, 2001.
- A. Paulraj, R. Nabar, and D. Gore, *Introduction to Space-Time Wireless Communications*, Cambridge Univ. Press, 2003.
- T. S. Rappaport, *Wireless Communications: Principles and Practice*, 2nd ed., Prentice-Hall PTR, Upper Saddle River, NJ, 2002.
- J. S. Bloch and L. Hanzo, *Third-Generation Systems and Intelligent Wireless Networking: Smart Antennas and Adaptive Modulation*, IEEE Press, 2002.
- S. Y. Hui and K. H. Yeung, Challenges in the migration to 4G mobile systems, *IEEE Commun. Mag.* **41**(12):54–59 (Dec. 2003).
- L. M. Correia and R. Prasad, An overview of wireless broadband communications, *IEEE Commun. Mag.* **35**(1):28–33 (Jan. 1997).
- P. Chaudhury, W. Mohr, and S. Onoe, The 3GPP proposal for IMT-2000, *IEEE Commun. Mag.* **37**(12):72–81 (Dec. 1999).
- P. H. Lehne and M. Pettersen, An overview of smart antenna technology for mobile communications systems, *IEEE Commun. Surve.* **2**(4):2–13 (fourth quarter, 1999).
- M. Frodigh, S. Parkvall, C. Roobol, P. Johansson, and P. Larsson, Future-generation wireless networks, *IEEE Pers. Commun. Mag.* **8**(5):10–17 (Oct. 2001).
- J. H. Park, Wireless internet access for mobile subscribers based on the GPRS/UMTS network, *IEEE Commun. Mag.* **40**(4):38–49 (April 2002).
- T. S. Rappaport, A. Annamalai, R. M. Buehrer, and W. H. Tranter, Wireless communications: Past event and a future perspective, *IEEE Commun. Mag.* **40**(5):148–161 (May 2002).
- J. D. Vriendt, P. Lainé, C. Lerouge, and X. F. Xu, Mobile network evolution: A revolution on the move, *IEEE Commun. Mag.* **40**(4):104–111 (April 2002).
- G. V. Tsoulos, Smart antennas for mobile communication systems: benefits and challenges, *Electron. Commun. Eng. J.* **11**(2):84–94 (April 1999).
- A. U. Bhohe and P. L. Perini, An overview of smart antenna technology for wireless communication, *Proc. IEEE Aerospace Conf.* March 2001, Vol. 2, pp. 875–883.
- T. S. Rappaport, J. H. Reed, and B. D. Woerner, Position location using wireless communications on highways of the future, *IEEE Commun. Mag.* **34**(10):33–41 (Oct. 1996).
- M. Schwartz, W. R. Bennett, and S. Stein, *Communication Systems and Techniques*, McGraw-Hill, 1966.
- W. C. Jakes, *Microwave Mobile Communications*, Wiley, 1974.
- J. C. Liberti and T. S. Rappaport, *Smart Antennas for Wireless Communications: IS-95 and Third Generation CDMA Applications*, Prentice-Hall PTR, Upper Saddle River, NJ, 1999.
- D. G. Brennan, Linear diversity combining techniques, *IEEE Proc.* **91**(2):331–356 (Feb. 2003).
- R. Vaughan and J. B. Andersen, *Channels, Propagation and Antennas for Mobile Communications*, IEEE UK, 2003.
- W. C. Y. Lee, *Mobile Communications Engineering, Theory and Applications*, 2nd ed., McGraw-Hill, New York, 1997.

22. M. R. Andrew, P. P. Mitra, and R. de Carvalho, Tripling the capacity of wireless communications using electromagnetic polarization, *Nature* **409**:316–318 (Jan. 2001).
23. T. Svantesson, A physical MIMO radio channel model for multi-element multi-polarized antenna systems, *Proc. IEEE 54th Vehicular Technology Conf.*, Oct. 2001, pp. 1083–1087.
24. B. Lindmark and M. Nilsson, On the available diversity gain from different dual-polarized antennas, *IEEE J. Select. Areas Commun.* **19**(2):1193–1204 (Feb. 2001).
25. R. U. Nabar, H. Bolcskei, V. Erceg, D. Gesbert, and A. J. Paulraj, Performance of multiantenna signaling techniques in the presence of polarization diversity, *IEEE Trans. Signal Process.* **50**(10):2553–2562 (Oct. 2002).
26. C. Sun and N. C. Karmakar, Environment-oriented beamforming for space-time block coded multiuser MIMO communications, *Proc. IEEE Antennas and Propagation Society Int. Symp.*, June 2004, Vol. 2, pp. 1744–1747.
27. B. Hagerman, T. Ostman, K. J. Molnar, and G. E. Bottomley, Field test performance results for D-AMPS in PCS bands with array processing, *Proc. IEEE 47th Vehicular Technology Conf.*, Kyoto, Japan, May 1997, Vol. 3, pp. 1582–1586.
28. K. Molnar, Space-time processing in an evolution of IS-136 system, *Proc. 5th Stanford Smart Antennas Mobile Wireless Communications Workshop*, 1998.
29. K. I. Pedersen, P. E. Mogensen, and J. Ramiro-Moreno, Application and performance of downlink beamforming technique in UMTS, *IEEE Commun. Mag.* **41**(10):134–143 (Oct. 2003).
30. Y. Li, M. Feuerstein, P. Perini, and D. Reudink, Gain improvement of a cellular base station multibeam antenna, *Proc. IEEE 46th Vehicular Technology Conf.*, May 1996, Vol. 3, pp. 1680–1684.
31. S. Anderson, U. Forssen, J. Karlsson, T. Witzschel, P. Fischer, and A. Krug, Ericsson/Mannesmann GSM field-trials with adaptive antennas, *Proc. IEEE 47th Vehicular Technology Conf.*, May 1997, Vol. 3, pp. 1587–1591.
32. S. Anderson, U. Forssen, J. Karlsson, T. Witzschel, P. Fischer, and A. Krug, Ericsson/Mannesmann GSM field-trials with adaptive antennas, *Proc. IEEE Colloquium on Advanced TMP Techniques and Applications*, Oct. 1996, Vol. 1996/234, pp. 6/1–6/6.
33. J. H. Winters and G. D. Golden, Adaptive antenna applique field test, *Proc. 4th Workshop on Smart Antennas in Wireless Mobile Communications*, 1997.
34. G. V. Tsoulos, M. Beach, and J. McGeehan, Wireless personal communications for the 21st century: European technological advances in adaptive antennas, *IEEE Commun. Mag.* **35**(9):102–109 (1997).
35. J. H. Winters, Smart antennas for wireless systems, *IEEE Personal Commun. Mag.* **5**(1):23–27 (Feb. 1998).
36. Ericsson Press Releases, Ericsson and Mannesman rollout the world's first GSM adaptive antenna base stations, (online), <http://www.ericsson.com/press/archive/2000Q2/20000417-0026.html>.
37. A. O. Boukalov and S. G. Häggman, System aspects of smart-antenna technology in cellular wireless communications—an overview, *IEEE Trans. Microwave Theory Tech.* **48**(6):919–929 (June 2000).
38. M. Marcus and S. Das, The potential use of adaptive antennas to increase land mobile frequency reuse, *Proc. IEEE Int. Conf. Radio Spectrum Conversation Techniques*, Birmingham, UK, Sept. 1983, pp. 113–117.
39. J. Litva, *Digital Beamforming in Wireless Communications*, Artech House, Norwood, MA, 1996.
40. T. Ohgane, Y. Ogawa, and K. Itoh, A study on a channel allocation scheme with an adaptive array in SDMA, *Proc. IEEE 47th Vehicular Technology Conf.*, May 1997, Vol. 2, pp. 725–729.
41. G. V. Tsoulos, J. McGeehan, and M. Beach, Space division multiple access (SDMA) field trials. Part 1: Tracking and BER performance, *IEEE Proc. Radar Sonar Nav.* **145**(1):73–78 (Feb. 1998).
42. C. Sun and N. C. Karmakar, Null-forming SDMA scheme based on channel responses correlation coefficient, *Proc. IEEE Antennas and Propagation Society Int. Symp.*, June 2003, Vol. 1, pp. 85–88.
43. C. Sun and N. C. Karmakar, Duplicate channel allocation of null-forming based SDMA in the presence of antenna array mutual coupling, *Proc. IEEE 4th Int. Conf. Information, Communication and Signal Processing*, Singapore, Dec. 2003, Vol. 2, pp. 1096–1100.
44. DBF1108 Digital Beamforming Device 0361.82.01.92, ERA Technology Ltd., Leatherhead, Surrey, UK.
45. S. Makino and N. Miyahara, Satellite onboard reflector antennas, *IEICE Trans. Commun.* **E86-B**(3):944–953 (March 2003).
46. C. K. Toh, *Wireless ATM and Ad-Hoc Networks*, Kluwer Academic Publishers, 1997.
47. A. Nasipuri, S. Ye, J. You, and R. E. Hiromoto, A MAC protocol for mobile ad hoc networks using directional antennas, *Proc. IEEE Wireless Communications and Networking Conf.*, Sept. 2000, Vol. 3, pp. 1214–1219.
48. Y. Ko, V. Shankarkumar, and N. H. Vaidya, Medium access control protocols using directional antennas in ad hoc networks, *Proc. 19th Annual Joint Conf. IEEE Computer and Communications Societies*, March 2000, Vol. 1, pp. 13–21.
49. C. K. Toh, *Ad Hoc Mobile Wireless Networks: Protocols and Systems*, Prentice-Hall, Upper Saddle River, NJ, 2001.
50. R. Ramanathan and J. Redi, A brief overview of ad hoc networks: Challenges and directions, *IEEE Commun. Mag.* **40**(5):20–22 (May 2002).
51. K. J. Krizman, T. E. Biedka, and T. S. Rappaport, Wireless position location: fundamentals, implementation strategies, and sources of error, *Proc. IEEE 47th Vehicular Technology Conf.*, May 1997, Vol. 2, pp. 919–923.
52. A. J. Paulraj, D. A. Gore, R. U. Nabar, and H. Bolcskei, An overview of MIMO communications—a key to gigabit wireless, *Proc. IEEE* **92**(2):198–218 (Feb. 2004).
53. A. F. Naguib, N. Seshadri, and A. R. Calderbank, Increasing data rate over wireless channels, *IEEE Signal Process. Mag.* **17**(3):76–92 (May 2000).
54. R. T. Derryberry, S. D. Gray, D. M. Ionescu, G. Mandyam, and B. Raghothaman, Transmit diversity in 3G CDMA systems, *IEEE Commun. Mag.* **40**(4):68–75 (April 2002).
55. R. D. Murch and K. B. Letaief, Antenna systems for broadband wireless access, *IEEE Trans. Inform. Theory* **40**(4):76–83 (April 2002).
56. D. Gesbert, L. Haumont, H. Bolcskei, R. Krishnamoorthy, and A. J. Paulraj, Technologies and performance for non-line-of-sight broadband wireless access networks, *IEEE Commun. Mag.* **40**(4):86–95 (April 2002).
57. D. Avidor, D. Furman, J. Ling, and C. Papadias, On the financial impact of capacity-enhancing technologies to wireless operators, *IEEE Wireless Commun. Mag.* **10**(4):62–65 (Aug. 2003).
58. S. D. Blostein and H. Leib, Multiple antenna systems: Their role and impact in future wireless access, *IEEE Commun. Mag.* **41**(7):94–101 (2003).

59. S. N. Diggavi, N. Al-Dhahir, A. Stamoulis, and A. R. Calderbank, Great expectations: The value of spatial diversity in wireless networks, *IEEE Proc.* **92**(2):219–270 (Feb. 2004).
60. J. Salz, Digital transmission over cross-coupled linear channels, *AT&T Tech. J.* **64**(6):1147–1159 (1985).
61. G. J. Foschini and M. J. Gans, On limits of wireless communications in fading environment when using multiple antennas, *Wireless Pers. Commun.* **6**(3):311–335 (March 1998).
62. E. Telatar, Capacity of multi-antenna Gaussian channels, *Eur. Trans. Telecommun.* **10**(6):589–595 (Nov. 1999).
63. R. Janaswamy, *Radiowave Propagation and Smart Antennas for Wireless Communications*, Kluwer, Amsterdam, 2001.
64. M. A. Khalighi, K. Raof, and G. Jourdain, Capacity of wireless communication systems employing antenna arrays, a tutorial study, *Wireless Pers. Commun.* **23**(3):321–352 (Dec. 2002).
65. D. Gesbert, M. Shafi, D. Shiu, P. J. Smith, and A. Naguib, From theory to practice: An overview of MIMO space-time coded wireless systems, *IEEE J. Select. Areas Commun.* **21**(3):281–302 (April 2003).
66. G. J. Foschini, Layered space-time architecture for wireless communication in a fading environment when using multi-element antennas, *Bell Labs Tech. J.* **2**(1):41–59 (1996).
67. G. J. Foschini, G. D. Golden, R. A. Valenzuela, and P. W. Wolniansky, Simplified processing for high spectral efficiency wireless communication employing multi-element arrays, *IEEE J. Select. Areas Commun.* **17**(11):1841–1852 (Nov. 1999).
68. P. W. Wolniansky, G. J. Foschini, G. D. Golden, and R. A. Valenzuela, V-BLAST: An architecture for realizing very high data rates over the rich-scattering wireless channel, *Proc. URSI Int. Symp. Signals, Systems, and Electronics*, 1998, pp. 295–300.
69. G. D. Golden, C. J. Foschini, R. A. Valenzuela, and P. W. Wolniansky, Detection algorithm and initial laboratory results using V-BLAST space-time communication architecture, *Electron. Lett.* **35**(1):14–16 (Jan. 1999).
70. L. C. Godara, Applications of antenna arrays to mobile communications, part I: Performance improvement, feasibility, and system considerations, *IEEE Proc.* **85**(7):1029–1030 (1997).
71. B. Pattan, *Robust Modulation Methods & Smart Antennas in Wireless Communications*, Prentice-Hall PTR, Upper Saddle River, NJ, 2000.
72. S. Bello Fiore, C. A. Balanis, J. Foutz, and A. S. Spanias, Smart-antenna systems for mobile communication networks. Part 1. Overview and antenna design, *IEEE Anten. Propag. Mag.* **44**(3):145–154 (2002).
73. J. P. Shelton and K. S. Kelleher, Multiple beams from linear arrays, *IEEE Trans. Anten. Propag.* **9**(2):154–161 (March 1961).
74. H. Novak, *Switched Beam Adaptive Antenna System*, Ph.D. dissertation, Technische Univ. Wien, Vienna, Austria, Nov. 1999.
75. N. C. Karmakar, *Antennas for Mobile Satellite Communications*, Ph.D. dissertation, Univ. Queensland, Australia, Aug. 1998.
76. N. C. Karmakar and M. E. Bialkowaski, A compact switched-beam array antenna for mobile satellite communications, *Microwave Optical Technol. Lett.* **21**(3):186–191 (May 1999).
77. N. C. Karmakar and M. E. Bialkowaski, A beam-forming network for a circular switched-beam phased array antenna, *IEEE Microwave Wireless Compon. Lett.* **11**(1):186–191 (Jan. 2001).
78. Y. Konishi, Phased array antennas, *IEICE Trans. Commun.* **E86-B**(3):954–867 (March 2003).
79. S. Takatsu, H. Aruga, T. Sakura, H. Nakaguro, A. Akaishi, N. Kadowaki, and T. Araki, Development results of Ka-band multibeam active phased array antenna for Gigabit Satellite, *Proc. Int. Symp. Antennas and Propagation*, Fukuka, Aug. 2003, Vol. 1, pp. 177–180.
80. M. E. Bialkowski and N. C. Karmakar, A two-ring circular phased array antenna for mobile satellite communications, *IEEE Trans. Anten. Propag.* **41**(3):14–23 (June 1999).
81. R. A. Hansen, *Phased Array Antennas*, Wiley, 1998.
82. T. Ohira, Adaptive array antenna beamforming architectures as viewed by a microwave circuit designer, *Proc. IEEE Asia-Pacific Microwave Conf.* Sydney, Australia, Dec. 2000, pp. 828–833.
83. Y. Ogawa and T. Ohgane, Advances in adaptive antenna technologies in Japan, *IEICE Trans. Commun.* **E84-B**(7):1704–1712 (2001).
84. R. A. Soni, R. M. Buehrer, and R. D. Benning, Intelligent antenna system for cdma2000, *IEEE Signal Process. Mag.* **19**(4):54–67 (2002).
85. B. Widrow, P. E. Mantey, L. J. Griffiths, and B. B. Goode, Adaptive antenna systems, *IEEE Trans. Anten. Propag.* **55**(12):2143–2159 (Dec. 1967).
86. B. D. V. Veen and K. M. Buckley, Beamforming: A versatile approach to spatial filtering, *IEEE ASSP Mag.* **5**(2):4–24 (April 1988).
87. L. C. Godara, Application of antenna arrays to mobile communications, part II: Beam-forming and direction-of-arrival considerations, *IEEE Proc.* **85**(8):1195–1245 (Aug. 1997).
88. S. Anderson, B. Hagerman, H. Dam, U. Forssen, J. Karlsson, F. Kronstedt, S. Mazur, and K. J. Molnar, Adaptive antennas for GSM and TMP systems, *IEEE Pers. Commun. Mag.* **6**(3):74–86 (1999).
89. S. Bellofiore, J. Foutz, C. A. Balanis, and A. S. Spanias, Smart-antenna systems for mobile communication networks. Part 2. Beamforming and network throughput, *IEEE Anten. Propag. Mag.* **44**(4):106–114 (Aug. 2002).
90. C. Sun, A. Hirata, T. Ohira, and N. C. Karmakar, Fast beamforming of electronically steerable parasitic array radiator antennas: Theory and experiment, *IEEE Trans. Anten. Propag.* **52**(7):1819–1832 (2004).
91. L. Himmel, S. H. Dodington, and E. G. Parker, *Electronically Controlled Antenna System*, U.S. Patent 3,560,978 (Feb. 2, 1978).
92. S. H. Black and R. B. Formeister, *Direction Finding System*, U.S. Patent 3,725,938 (April 3, 1973).
93. M. Gueguen, *Electronically Step-by-Step Rotated Directive Radiation Beam Antenna*, U.S. Patent 3,856,799 (Nov. 5, 1974).
94. R. F. Harrington, Reactively controlled directive arrays, *IEEE Trans. Anten. Propag.* **AP-26**(3):390–395 (May 1978).
95. R. Dinger, Reactively steered adaptive array using microstrip patch elements at 4 GHz, *IEEE Trans. Anten. Propag.* **32**(8):848–856 (Aug. 1984).
96. R. Milne, A small adaptive array antenna for mobile communications, *Proc. Antennas and Propagation Society Int. Symp.*, June 1985, Vol. 23, pp. 797–800.
97. D. V. Thiel, S. O'Keefe, and J. W. Lu, Electronic beam steering in wire and patch antenna systems using switched

- parasitic elements, *Proc. IEEE Antennas and Propagation Society Int. Symp.*, 1996, Vol. 1, pp. 21–26.
98. A. Sibille, C. Roblin, and G. Poncelet, Circular switched monopole arrays for beam steering wireless communications, *IEEE Electron. Lett.* **33**(7):551–552 (March 1997).
 99. S. L. Preston, D. V. Thiel, J. W. Lu, S. G. O’Keefe, and T. S. Bird, Electronic beam steering using switched parasitic patch elements, *Electron. Lett.* **33**(1):7–8 (Jan. 1997).
 100. S. L. Preston, D. V. Thiel, T. A. Smith, S. G. O’Keefe, and J. W. Lu, Base-station tracking in mobile communications using a switched parasitic antenna array, *IEEE Trans. Anten. Propag.* **46**(6):841–844 (1998).
 101. S. L. Preston, D. V. Thiel, and J. W. Lu, A multibeam antenna using switched parasitic and switched active elements for space-division multiple access applications, *IEICE Trans. Electron.* **E82-C**(7):1202–1210 (1999).
 102. R. Vaughan, Switched parasitic elements for antenna diversity, *IEEE Trans. Anten. Propag.* **47**(2):399–405 (Feb. 1999).
 103. T. Svantesson and M. Wennstrom, High-resolution direction finding using a switched parasitic antenna, *Proc. IEEE 11th Signal Processing Workshop*, Aug. 2001, pp. 508–511.
 104. T. Ohira and K. Gyoda, Electronically steerable passive array radiator antennas for low-cost analog adaptive beamforming, *Proc. IEEE Conf. Phased Array Systems and Technology*, May 2000, pp. 101–104.
 105. D. Thiel and S. Smith, *Switched Parasitic Antennas for Cellular Communications*, Artech House, Norwood, MA, 2001.
 106. C. Sun and N. C. Karmakar, A DOA estimation technique based on a single-port smart antenna for position location services, *Proc. Asia-Pacific Microwave Conf.*, Kyoto, Japan, Nov. 2002, Vol. 1, pp. 196–199.
 107. P. K. Varlamos and C. N. Capsalis, Direction-of-arrival estimation (DoA) using switched parasitic planar arrays and the method of genetic algorithms, *Wireless Pers. Commun.* **28**(1):59–75 (Jan. 2004).
 108. C. A. Balanis, *Antenna Theory: Analysis and Design*, 2nd ed., Wiley, 1997.
 109. S. Leonov and A. Leonov, *Handbook of Computer Simulation in Radio Engineering, Communications, and Radar*, Artech House, Norwood, MA, 2001.
 110. T. Ohira and K. Gyoda, Hand-held microwave direction-of-arrival finder based on varactor-tuned analog aerial beamforming, *Proc. IEEE Asia-Pacific Microwave Conf.*, Taipei, Taiwan, ROC, Dec. 2001, pp. 585–588.
 111. C. Sun, A. Hirata, T. Ohira, and N. C. Karmakar, Experimental study of a fast beamforming algorithm for ESPAR antennas, *Proc. European Conf. Wireless Technologies*, Munich, Oct. 2003, pp. 241–244.
 112. C. Sun, A. Hirata, T. Ohira, H. Yamada, and N. C. Karmakar, A novel antenna array calibration with a linear space error correction, *Proc. European Conf. Wireless Technologies*, Munich, Oct. 2003, pp. 301–304.
 113. (Online), <http://www.qsl.net/wb6tpu/swindex.html>.
 114. R. Jana and S. Dey, 3G wireless capacity optimization for widely spaced antenna arrays, *IEEE Pers. Commun. Mag.* **7**(6):32–35 (Dec. 2000).
 115. J. S. Colburn, Y. Rahmat-Samii, M. A. Jensen, and G. J. Pottie, Evaluation of personal communications dual-antenna handset diversity performance, *IEEE Trans. Vehic. Technol.* **47**(3):737–746 (Aug. 1998).
 116. C. B. Dietrich, Jr., K. Dietze, J. R. Nealy, and W. L. Stutzman, Spatial, polarization, and pattern diversity for wireless handheld terminals, *IEEE Trans. Anten. Propag.* **49**(9):1271–1281 (2001).

ALTIMETERS

HALIT EREN
Curtin University of Technology
Bentley, Australia

1. INTRODUCTION

Altitude, for the purposes of this article, is the elevation of an object above a given level. (In astronomy, navigation, and surveying, altitude means the angular height of a celestial body above the plane of the horizon.) *Altimeters* are instruments that measure altitude. Altimeters represent an advanced technology, finding diverse commercial and military applications ranging from air transport to space exploration. Many companies (Table 1) offer a wide range of altimeters and altimeter-related products.

There are three main types of altimeter:

1. The pressure altimeter, which uses changes in the atmospheric pressure to infer altitudes.
2. The radio detection and ranging (or *radar*) altimeter, which measures the time required for a continuous wave (CW) or pulse of radio energy to travel from an object in the atmosphere to the ground and back.
3. The optical altimeter, based on laser optics, operating mainly on pulsed energy transmission, as in the case of laser radar (LIDAR).

Altimeters are usually associated with aircraft, but they are also used in applications such as geodesy and surveying, navigation weapon guidance systems, parachute jumping, and mountaineering. The accuracy and the sophistication of the sensors and the associated electronics and computing power of altimeters depend on the measurement requirements. For example, in remote sensing applications, the selection of the sensors depends on the platform of the operation, as illustrated in Fig. 1.

Altimeters can be divided into two categories:

1. Instruments that measure the altitude of an object above a fixed Earth reference level (e.g., sea level).
2. Instruments that measure the distance between an object and some earth reference.

Instruments in the first category are of the barometric types that use the static air pressure at some altitude to infer height above a reference level. The second category is much broader and is based on the use of electromagnetic waves to determine altitudes. Some devices in this category are radar altimeters, laser altimeters, and the Global Positioning System (GPS).

2. BAROMETRIC ALTIMETERS

Barometric altimeters are based on the measurement of pressure, which varies depending on the atmospheric layers. Atmosphere of the Earth may be divided into several layers: troposphere (0–16 km from sea level),

Table 1. List of Manufacturers and Suppliers

Aeronautical Instrument & Radio Co. 234 Garibaldi Avenue Lodi, NJ 07644 Tel: 973-473-0034 Fax: 973-473-8748	Garmin International, Inc. 1200-T E, 151st St. Olathe, KS 66062 Tel: 913-397-8200 Fax: 913-397-8282	Pathfinder Instruments 2075 Corte Del Nogal, Suite X Carlsbad, CA 92009 Tel: 800-284-9698 Fax: 760-438-3953
Aerospace Industries, Inc. 333 N, Broadway, Suite 3011-T Jericho, NY 11753 Tel: 888-200-2681 Fax: 516-932-3307	GEC-Marconi Hazeltine Corp. 164-T Totowa Road, P.O. Box 975 Wayne, NJ 07474-0975 Tel: 973-633-6000 Fax: 973-633-6431	PLX, Inc. 40-T W, Jefryn Blvd. Deer Park, NY 11729 Tel: 800-586-4190 Fax: 516-586-4196
A. I. R., Inc. 8401 Baseline Road Boulder, CO 80303 Tel: 303-499-1701 Fax: 303-499-1767	Honeywell Inc. P.O. Box 524 Minneapolis, MN 55440 Tel: 612-951-1000 Fax: 612-951-2294	Rockwell, Collins Commercial Avionic 400-T Collins Road N.E. Cedar Rapids, IA 52498 Tel: 319-295-4085 Fax: 319-295-4777
Allen Osborne Associates, Inc. 756-T Lakefield Rd., Bldg, J Westlake Village, CA 91361 Tel: 805-495-8420 Fax: 805-373-6067	Jewell Electrical Instruments 124 Joliette Street Manchester, NH 03102 Tel: 603-669-6400 Fax: 603-669-5962	Shelby Jones Co., Inc. 8800 West Chester Pike Upper Darby, PA 19082 2619 Tel: 800-377-6060 Fax: 610-449-7010
AlliedSignal Inc. 101 Columbia Rd., Customer Operations Morristown, NJ 07962 Tel: 800-707-4555 Fax: 602-365-3348	Landis & Staefa, Inc. 1000 Deerfield Pkwy Buffalo Grove, IL 60089 Tel: 847-215-1050 Fax: 847-215-9026	Scientific Sales, Inc. P.O. Box 6725-T Lawrenceville, NJ 08648 Tel: 800-788-5666 Fax: 609-844-0466
American Paulin System 1455-T Rocky Knolls Road Cottonwood, AZ 86326 Tel: 520-634-0980	Laser Technology, Inc. 7070 S. Tucson Way, Dept. T Englewood, CO 80112 Tel: 800-873-8916 Fax: 303-649-9710	Terra Tech, Inc. P.O. Box 5547 Eugene, OR 97405 0547 Tel: 541-345-0597
Atmospheric Instruments Research Inc. 8401 Baseline Rd., Dept. T Boulder, CO 80303 Tel: 303-499-1701, Ext. 300 Fax: 303-499-1767	Leica, Herbrugg CH; 9435 Herbrugg Switzerland Tel: 41 (71) 70 33 84 Fax: 41 (71) 70 39 99	UMA, Inc. 260 Main St. Dayton, VA 22821 Tel: 703-879-2040 Fax: 703-879-2738
Azimuth Corp. 13-T Park Drive Westford, MA 01886 3511 Tel: 978-692-8500 Fax: 978-629-8510	Magellan Corp. 960 Overland Court San Dimas, CA 91773 Tel: 909-394-5000 Fax: 909-394-7050	Watrous & Co., Inc. Griffing Street, P.O. Box 996 Cutchogue, NY 11935 0996 Tel: 516-734-5504 Fax: 516-734-7931
COSCO, Inc. 95 N, Lincoln St. Denver, CO 80203 Tel: 800-372-6726 Fax: 303-777-3331	Optech Inc. 100 Wildcat Road North York, ON M3J3H4 Canada Tel: 416-661-5904 Fax: 416-661-4168	

stratosphere (16–50 km), mesosphere (50–80 km), thermosphere (80–640 km), and exosphere (outer space). To determine the altitude of an object, the atmospheric pressure is compared with a reference pressure by a mechanism such as shown in Fig. 2. Over the years, many different mechanisms have been developed for barometric

altitude measurements. However, they all rely on the use of a relation between air pressure and altitude.

In most modern barometric altimeters, integrated circuit (IC) pressure transducers are used, as shown in Fig. 3. A wide variety of pressure transducers are available with different specifications that are suitable

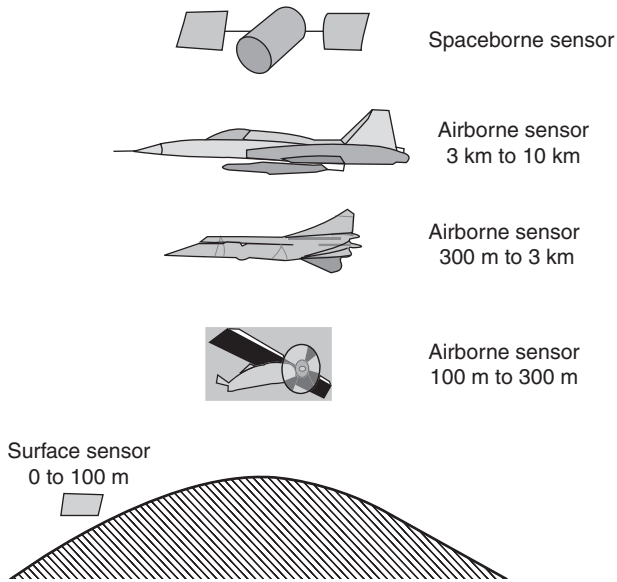


Figure 1. Use of altimeters at various altitudes. Altimeters are designed to operate accurately at certain ranges. Developed in recent (as of 2003) years, the altimeters carried by the geostationary satellites offer very high accuracy.

for a large range of barometric altimeter applications. The performance of pressure transducers depends on the characteristics of the atmospheric pressure.

2.1. Principles of Operation and the Effect of Atmospheric Pressure

Certain assumptions are made to allow the altitude–pressure relationship to be simplified so that the altitude above sea level at any point in Earth’s atmosphere can be related to air pressure by a single-valued function. The assumptions are often referred to as a *standard atmosphere* and are primarily concerned with the atmospheric conditions at sea level, chemical composition of the atmosphere, and atmospheric temperature distribution. These assumptions are based on a mixture of observations, measurements, and theories that are internationally accepted.

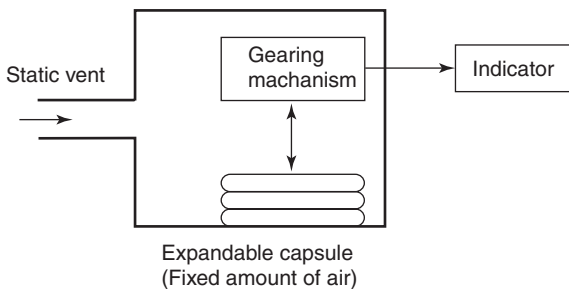


Figure 2. A typical barometric altimeter. In this type a constant volume of air is trapped in the bellows. Depending on the air pressure in the chamber, the bellows changes its volume. The change in volume is scaled by a gearing mechanism connected to an analog indicator.

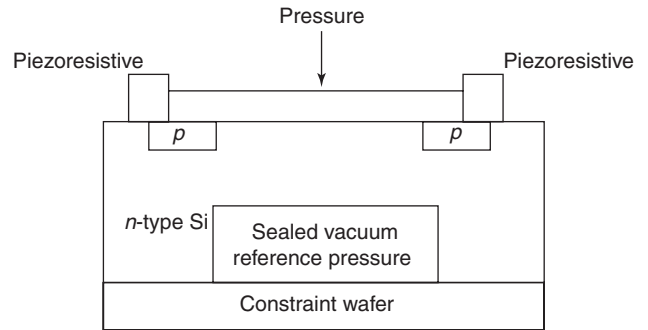


Figure 3. A barometric altimeter based on piezoresistive integrated circuit. The characteristics of silicon allow construction of a thin diaphragm that can be deflected by an applied pressure, thus resulting in changes in resistance of the piezoresistive elements located on the diaphragm. The signal-processing and voltage regulation circuits are also integrated in the IC chip.

The concept of the standard atmosphere has a threefold purpose: (1) it sets a reference for testing, design, and performance comparisons between instruments and the body carrying the altimeter, such as an aircraft, a balloon, or a parachute jumper; (2) it allows the derivation of the pressure–altitude relationship to be simplified both mathematically and physically within the altimeter; and (3) finally, if all objects with altitude-measuring devices are set to the same reference, the vertical separation between these objects when they are in common airspace can be reliably inferred and safety can be increased. The International Standard Atmosphere (ISA) assumptions are summarized as follows:

1. The temperature at sea level T_0 and the pressure at sea level P_{s0} are assumed to be constant at $T_0 = 288.15\text{ K}$ and $P_{s0} = 101,325\text{ Pa}$ (1013.25 mbar, 29.92 in.Hg).
2. The temperature decreases linearly with increasing height until a height known as the *tropopause* is reached, above which the temperature remains constant until the *stratopause* height is reached. The region below the tropopause is known as the *troposphere*. The law relating temperature T to altitude H to the tropopause height is given by

$$T = T_0 - LH \tag{1}$$

where L is the temperature decrease rate and is defined to be $-6.5 \times 10^{-3}\text{ K/m}$. At and above the tropopause (11,000 m), T remains constant at $T = T_T = 216.65\text{ K}$ (-56.5°C).

3. The stratopause is defined to occur at 20,000 m. The region between the tropopause and the stratopause is known as the *stratosphere*.
4. At heights above the stratopause the temperature starts to increase linearly with height; this region is known as the *chemosphere* (top of the stratosphere, all of the mesosphere, and lower part of the thermosphere). The temperature increase rate is defined to be $1.0 \times 10^{-3}\text{ K/m}$. The chemosphere is defined to have a height limit of 32,004 m. The temperature in

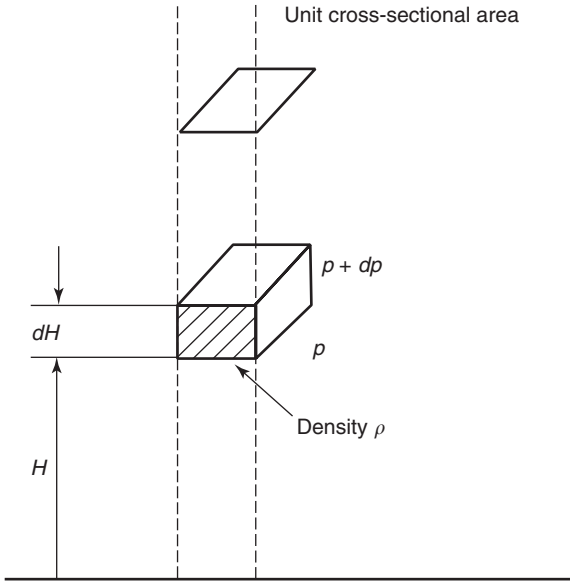


Figure 4. Change in the atmospheric pressure due to air density. These changes in the air pressure can be related to altitude by using the gas laws.

the chemosphere is given by

$$T = T_T + L(H - H_S) \tag{2}$$

where H_S is the height of the stratopause.

Using these assumptions, the altitude–static pressure relationship can now be derived by considering Fig. 4. A small change in pressure dp of air with density ρ , due to a small change in height dH , can be found by equating the forces acting in the vertical plane on an elemental volume of air, so that

$$-dp = \rho g dH \tag{3}$$

where g is the gravitational acceleration. From the ideal gas law

$$p = \rho R_a T \tag{4}$$

where T is the air temperature (in Kelvins) and R_a is the gas constant for a unit mass of dry air.

Combining Eqs. (1) and (2) through the variable ρ results in the following equation:

$$\frac{-dp}{p} = \frac{g}{R_a T} dH \tag{5}$$

The value of g , the gravitational acceleration, is known to decrease with increasing distance from the center of Earth. The equation governing this is

$$g = \frac{R^2}{(R + H)^2} g_0 \tag{6}$$

where R is the radius of Earth and g_0 is the gravitational acceleration at Earth’s surface, where its value is approximately equal to 9.807 m/s^2 . This degradation of g ,

however, can be assumed to be insignificant in the evaluation of the pressure altitude. This additional assumption further simplifies the derivation.

The assumptions stated imply that the relation between the pressure altitude and the static pressure must be derived separately in three regions, namely the troposphere, the stratosphere, and the chemosphere. First, considering the troposphere, by substitution of Eq. (1) into Eq. (5), and integrating both sides to eliminate the dp and dH , we obtain

$$-\int_{P_{s0}}^{P_s} \frac{1}{p} dp = \frac{g_0}{R_a} \int_0^H \frac{1}{T_0 - LH} dH \tag{7a}$$

where P_{s0} is the pressure at height $H = 0$ and P_s is the pressure at height H . Using the integration rule $(1/u)du = \ln|u| + c$ and the equality $\ln A - \ln B = \ln(A/B)$, we have

$$\ln \frac{P_s}{P_{s0}} = \frac{g_0}{R_a L} \ln \frac{T_0 - LH}{T_0} \tag{7b}$$

Solving for P_s gives

$$P_s = P_{s0} \left(1 - \frac{L}{T_0} H\right)^{g_0/LR_a} \tag{8}$$

Similarly, for the two other regions of concern, their appropriate temperature equations, $T = T_T$ and Eq. (2) can be substituted into Eq. (5) and integrated.

Considering the constants implied in the ISA and additionally noting that $R_a = 287.053 \text{ J/(K} \cdot \text{kg)}$, the following equations are found to relate the static pressure to the pressure altitude H_p

1. Troposphere (–914.4 to 11,000 m):

$$P_s = 1013.25(1 - 2.25577 \times 10^{-5} H_p)^{5.255879} \text{ mbar} \tag{9}$$

2. Stratosphere (11,000 m to 20,000 m):

$$P_s = 226.32e^{0.0001576885(H_p - 11,000)} \text{ mbar} \tag{10}$$

3. Chemosphere (20,000–32,004 m):

$$P_s = 54.7482[1 + 4.61574 \times 10^{-6}(H_p - 20,000)]^{-34.163215} \text{ mbar} \tag{11}$$

It can be seen that these relationships are nonlinear. The nonlinearity can be observed graphically by plotting altitude on the horizontal axis against pressure as shown in Fig. 5.

2.2. Construction, Errors, and Use of Barometric Altimeters

A barometric altimeter must be able to display altitude linearly; therefore, a linearization, such as the gain adjustment, is necessary. The linearization is usually done by a calibratable mechanism to allow for variations in aneroid chambers. This mechanism introduces a gain that counters the nonlinear effects of pressure versus height, by means of nonlinear compression/expansion of the aneroid chamber. Gearing is also introduced, so that one

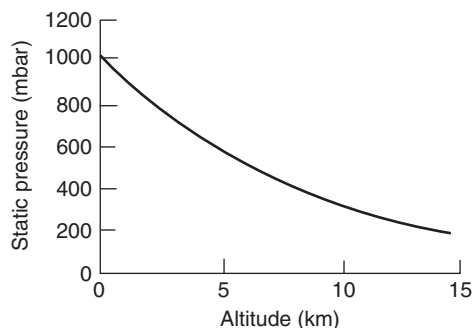


Figure 5. Static pressure versus pressure altitude. The pressure changes in a nonlinear manner. Linearization techniques must be employed to measure and display altitudes by barometric methods.

revolution of the altimeter pointer is equivalent to a 330 m height displacement.

The linearizing part of the mechanism of an aneroid barometric altimeter is usually located at the center of the altimeter body. The temperature compensation is realized via a bimetallic strip, which alters its curvature as temperature increases. These features are necessary to compensate for the changes in the modulus of elasticity of the material that the aneroid chamber is made from. For example, if the sea-level temperature of an aneroid chamber were to decrease, its elasticity would increase. Since the chamber has a vacuum, it is in natural shape when fully expanded (i.e., at very low atmospheric pressure). If the chamber material becomes more elastic, it tries to resume its original shape. This results in the display of a height greater than the actual height. Since the atmospheric pressure decreases as the chamber is moved away from sea level, the extra height effect of the elasticity of the chamber increases as the altitude increases.

The static pressure port is placed on the backplate of the altimeter for use in a small aircraft. In modern aircraft this port is connected to a line that is in turn connected to either a pitot tube or a static vent. The pitot tube is often seen as a small probe-like object pointed forward and located at the front of the aircraft to measure the airspeed. In altitude measurements, it fulfills the function of supplying a static pressure that is independent of the velocity of the aircraft.

It is important to note that pitot tubes can introduce errors into altitude measurements. The tubes are mechanically designed to introduce minimum errors and also are positioned on the aircraft so that the attitude does not affect the airflow onto the tube. A badly designed or positioned pitot tube can cause shockwaves to occur at high air velocities and also cause extra air to be forced into the static measurement holes, thus increasing the pressure.

In an effort to attempt to alleviate some of the problems caused by pitot tubes, the use of static vents has become common in modern aviation. They are designed to be mounted flush on the fuselage of an aircraft. In particular, these vents find extensive use in military applications where the removal of the probe-like pitot tube has improved stealth capabilities.

One problem common to all types of static-pressure-driven instruments is ice formation and water buildup inside the tubes or vents. To prevent ice formation, these tubes and vents contain heating elements. Where there is ice, there can be water. Variations in pressure and temperature can cause water to condense in tubes and ports. In the interests of instrument functionality and minimization of errors, there must be provisions to check static lines for water and remove it.

A typical modern barometric altimeter is approximately 35×30 mm and has a liquid crystal display (LCD). It can also function as a barometer and can be set for the minimum and maximum altitudes, the absolute altitude, the speed of ascent and descent, the reduced and absolute air pressures, the weather forecast, and time and altitude alarms. Typically, the range of measurement of the barometric altimeter is -700 to $10,000$ m, and it updates information once every second. It has a pressure range from 600 to 1100 mbar with $\pm 0.5\%$ accuracy and 0.1 mbar resolution. The altitude resolution is about 0.1 m. Altimeters with high precision find applications in geosciences, surveying, aviation, meteorology, recreation, and the laboratory.

2.3. Further Comments on Application of Barometric Altimeters in Aircraft

Barometric altimeters find extensive use in most modern aircraft as backup instruments. These altimeters are composed mechanically of sector gears, pinion, backlash springs, crankshafts, aneroid capsules, and pointers on a dial. A series of pointers on a graduated dial may be used to indicate altitude in hundreds, thousands, or tens of thousands of feet or meters. The barometric dial records the air pressure in millibars. Because atmospheric pressure is measured relative to sea level, the pressure altimeter must be manually adjusted in order to compensate for variations in pressure caused by weather changes.

In aircraft, the barometric altimeters can be set to show either altitude above sea level or altitude above an airfield once the height of the airfield above the sea level is known. If the pilot wishes to adjust the altimeter to display the height above sea level, the corrected sea-level pressure needs to be entered. When the corrected sea-level pressure is compared with the pressure at the airfield, the height of the airfield from sea level can be found. The sea-level pressure at that particular time must be known, however, because it may differ from the ISA assumption, indicating that the height of the airfield is higher or lower than what it actually is. Airfields continuously broadcast updated information on the pressure so that the pilot may correct the altimeter. The correct setting is called QNH, the adjusted sea-level pressure.

On the other hand, a pilot may wish to set the altimeter so that it displays the altitude above a particular airfield. To do this the pressure height of the airfield needs to be entered into the altimeter. Such pressures are denoted QFE and are given relative to the sea-level pressure. For example, an airfield 304.8 m above sea level, on a day when the sea-level pressure is as per ISA (1013.25 mbar), has a QFE of 977.4 mbar. This value is calculated from

Eq. (9). In summary, the barometric pressure knob is used to correct any variation in the sea-level pressure from the ISA assumed value of 1013.25 mbar.

Recalling the ISA assumptions, the temperature variations and airspeed effects are ignored. However, these effects can be taken into account by the application of computers and suitable analog-to-digital converters (ADCs) to the real-time signals generated by the instruments. The computers use complex models to take into account many variables affecting the altitude measurements. This means that the computer-driven altitude display can be corrected in real time, so that the pilot has a very accurate altitude reading at all times.

Altimeters are prone to the following errors: (1) instrument errors due to manufacture, installation, maintenance, and so on; (2) instrument lag; and (3) position error due to placement of vents and blockage of the static vents by ice. In response, the availability of computers has prompted the development of advanced pressure-measuring devices, such as the vibrating pressure sensor and the solid-state capsule pressure sensor.

As illustrated in Fig. 6, vibrating sensors work on the principles of detecting change in the natural resonant frequency of a vibrating system within a cylinder as the air pressure changes. This means that the electrical output of this sensor, when amplified, will be a frequency that changes proportionally with the pressure it is exposed to. Modern ADCs can detect very small differences in output frequency due to density variations as well as the large frequency variations due to pressure changes. This type of setup, which is enclosed, is very rugged and is in wide use today in commercial aircraft.

The second type of sensor, the capsule type, typically uses a vacuum chamber. The difference between these and the older aneroid chambers is in the materials from which the diaphragm is constructed. Typical materials are silicon, quartz, or ceramic compounds. These newer diaphragm materials are chemically engineered to have perfect mechanical properties in that they are very linear, do not suffer from hysteresis, and have a very stable modulus of elasticity.

The capsule-type transducers rely on two main methods. The first method involves the impregnation of the

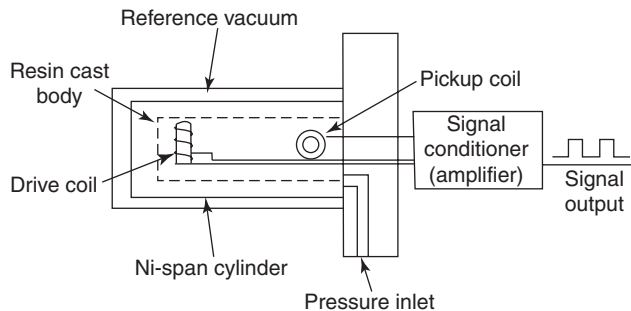


Figure 6. Vibrating sensor barometric altimeter. The natural frequency of the vibrating element depends on the air pressure inside a cylinder chamber. The signal of natural vibration is picked up and processed to obtain the pressure, and hence the altitude of the mechanism above sea level.

diaphragm with a Wheatstone bridge, thus allowing an excitation to be applied and a pressure-dependent voltage to appear at the output. This voltage varies with the change in resistance of the impregnated resistors as the diaphragm flexes due to pressure, similarly to a resistive strain gauge. The second method is to form an area of metallization on the bottom side of the diaphragm and the bottom of the vacuum chamber. This creates a capacitor, and these sensors are highly sensitive to small variations in its capacitance. However, temperature variations and accelerations can severely affect both these types of sensors. Thus the temperature is measured near the device and fed into the ADC for correction. For the acceleration effect, ensuring that the device is mounted so that its axis of movement is orthogonal to the acceleration is sufficient compensation. It should be noted that these devices are designed to be minimally sensitive to gravitational effects.

It can be concluded that barometric altimeters are likely to continue to be used extensively in the near future to measure altitudes of up to 15,000 m. Radar altimeters are expected to expand their role of providing accurate landing references, and low-altitude radar altimeters will continue to be used mainly for special-purpose military operations.

3. RADAR (RADIO) ALTIMETRY

Radar and laser altimeters, also termed *active ranging sensors*, are based on the transmission of electromagnetic or optical energy directed at an object and the detection of the reflected energy from the object. The reflected energy is suitably processed to reveal information about the altitude as well as other parameters such as the atmospheric conditions, including pollution. Radar altimeters can provide height information at high altitudes, where barometric systems are not effective. They can also provide high-quality images, as illustrated in Fig. 7.

Aviation radar altimeters, which have been in use for many years, measure height above the ground or sea. They transmit either continuous waves (CW) or pulsed waves and normally operate in the 4.2–4.4-GHz band to provide inputs to, for example, automatic landing systems or autostabilization systems for aircraft and helicopters. The basic operating principles of radio and radar altimeters are similar. The only difference is that the term *radio altimeter* often refers to continuously modulated waves, whereas the term *radar altimeter* refers to pulsed waves, mainly used in aircraft, spacecraft, and satellites.

3.1. Radar Altimeters Used in Satellites

The radar altimeter is a single-frequency radar system that broadcasts a pulsed tone directly downward, as illustrated in Fig. 8. It has highly sensitive devices for signal detection and processing. A satellite altimeter is a nadir-pointing active microwave sensor designed to measure characteristics of the surface of Earth. The time it takes for the reflected signal to be received directly is translated into the height above the terrain.

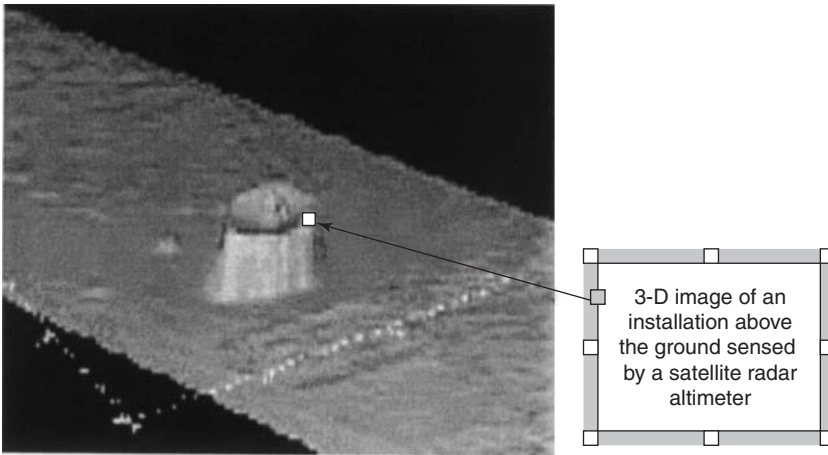


Figure 7. A typical example of remote sensing. Active remote sensors transmit electromagnetic energy and pick up the return signals. By appropriate data processing three-dimensional images can be constructed.

If a pulse is transmitted toward a target surface at an accurately measured time t_1 , it reflects back to the source after a time t_2 . The time difference $t_d = t_1 - t_2$ is equal to the round-trip distance to the reflecting surface divided by the propagation speed c :

$$t_d = \frac{2h}{c} \text{ or } h = \frac{ct_d}{2} \quad (12)$$

The accuracy of the measured distance h can be expressed by

$$\Delta h = \Delta c \frac{t_d}{2} + c \frac{\Delta t_d}{2} \quad (13)$$

Here, the time difference accuracy Δt_d depends mainly on the sharpness of the pulse, which is equal to

$$\Delta t = \frac{1}{B} \quad (14)$$

where B is the signal bandwidth.

If the speed of the pulse is taken to be constant, the range resolution can be found from

$$\Delta h = \frac{c}{2B} \quad (15)$$

Higher accuracy is achieved by detailed analysis of the received signal; this is achieved by averaging a large number

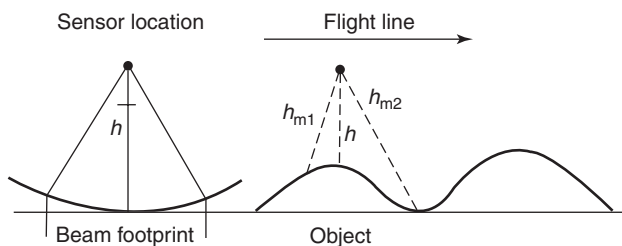


Figure 8. Geometry of a pulse-limited radar altimeter. The pulse intersects the nearest point on the ground, and the illuminated disk spreads rapidly. This gives a maximum size for the footprint. The geometry of the beam-limited altimeter is similar.

of echoes. Range errors can arise from pulse dispersion due to backscattering from the rough surface and to the propagation characteristics of the atmosphere. Consequently, the returned pulse is distorted and fading occurs, as illustrated in Fig. 9. The distortion in the waveform of the echo signal makes the altimeter signal less than perfect.

There are different types of radar altimeters, such as beam-limited altimeters, pulse-limited altimeters, synthetic aperture radar altimeters, imaging altimeters, and scanning altimeters. The operation principles of the altimeters are similar, but they vary in size of footprint, direction of the beam, and purpose of usage. The details in the differences of these altimeters are not given in this article, but interested readers can find further information in the references (e.g., Elachi [1]).

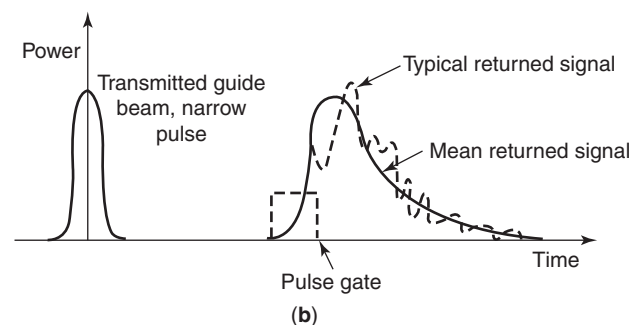
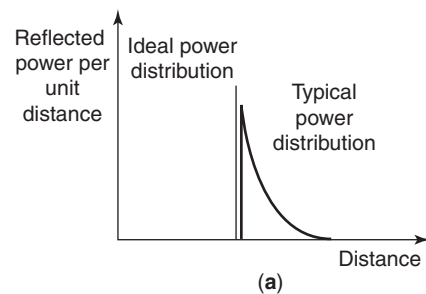


Figure 9. Waveforms of returned pulses: (a) ideal power distribution and typical power distribution of the returned signal—the distortion is due to imperfect mirroring of the signal back to the sensor; (b) pulse shape of wide-beam, narrow-pulse altimeter.

In most modern radar altimeters, high measurement accuracy is required. This necessitates good information on the effect of the ionosphere and atmosphere as well as sound understanding of the errors introduced by the sensor dynamics and signal-processing electronics. The signal-processing electronics comprises many components such as oscillators, modulators, mixers, power amplifiers, filters, demodulators, digitizers, compressors, and computers. All these devices have to be of good quality and highly accurate. Judicious selection of all the discrete components and circuits is necessary for good conformity and matching.

The first satellite altimeter was tested in 1973, as parts of several Skylab missions conducted by the United States. At that time, a typical resolution was 1–2 m; modern altimeters are capable of resolutions down to 2 cm (TOPEX/Poseidon). As an example, the discussion here focuses on one of the latest satellite altimeters, for the NASA TOPEX/Poseidon satellite used in oceanic applications.

The TOPEX/Poseidon mission, a joint mission between NASA and the Centre Nationale d'Etudes Spatiales (CNES), the French space agency, was designed to make high-precision measurements of the ocean surface possible. The application areas of this system are mainly for weather reports and predictions, in geodesy and geophysics. The TOPEX altimeter was the first dual-frequency satellite altimeter operating in space to perform these important measurements. The TOPEX used several methods for determining distance, such as the round-trip time discussed previously, and the shape of the reflected pulse. In particular, the shape of the reflected pulse provided a wealth of information on wave height in the ocean and the sea-surface windspeeds.

The TOPEX altimeter uses a 13.6-GHz signal as its primary pulse, and a secondary frequency of 5.3 GHz. The use of two frequencies is helpful in removing the adverse effects of variations in the propagation speed of the pulse due to variations in the atmospheric conditions of Earth.

NASA has built a self-calibration mechanism into the TOPEX altimeter. While over land, twice a day, the altimeter spends 5 min calibrating itself. The TOPEX is known to be extremely reliable and robust because of this self-calibration capability and its ability to compensate for ionospheric effects.

To obtain a high degree of precision, the satellite that carries TOPEX needs to know its exact position relative to points on Earth. The GPS helps the satellite determine its position with a precision of about 2 cm. A laser Doppler system and a ground station are also used to verify this reading. Another satellite system with importance for altitude measurements has been the Geosat follow-on meteorological-oceanographic (GFO METOC) satellite. It is owned by the U.S. Navy and is used for determining thermal fronts, eddies, ice edge locations, surface windspeeds, and wave heights.

The GFO and the GPS systems mentioned above are also used for position and altitude determinations, but their design is more elaborate than is needed for the accuracy of TOPEX. In these systems, an onboard water vapor detector is used to help correct ionospheric interference. Essentially,

the GFO was a test to determine whether a low-cost, light-weight, and compact satellite could be used to provide the U.S. Navy and its associated agencies with real-time ocean data. But the expectations for the GFO to replace TOPEX in a cost-effective manner have failed so far.

Spaceborne altimeters are primarily pulse-limited, and therefore they cannot deliver the required accuracy of surface height measurements over icy land. This is because the spreading and slope of the reflected pulse cause severe errors. In addition, during land height measurements, sudden changes in the slopes of the topography often result in a loss of tracking. Although techniques have been developed to improve the spatial resolution of radar altimeters for accurate elevation estimates over the terrain, most of them result in a significant increase in cost and complexity compared with a conventional altimeter.

In a typical noise-modulated radar altimeter, the principle of operation is based on the dependence of the cross-correlation function of the random modulation (Gaussian noise) on the finite correlator bandwidth, smoothing methods, extraneous noise disturbance, component characteristics, and changes in altitude during measurements.

3.2. Radio Altimeters

Like radar altimetry, radio altimetry is based on the use of electromagnetic (EM) waves to determine the distance between a reference point and an object that reflects the waves. Radio altimeters are used mostly in aircraft. Unlike radar altimetry, radio altimetry is based on continuous EM waves. Generally, it uses a frequency-modulated (FM) carrier, whose frequency is varied at a constant rate. The carrier reaches the surface below and reflects back to the transmitter with a delay. The reflection appears as a time-shifted version of the transmitted signal; thus the phase shift can be utilized. This time difference equates to a frequency difference, which can easily be detected using a superheterodyne receiver. Figure 10 illustrates the time difference in the transmitted and received signals. A typical radio altimeter operates at about 4.3 GHz. A low-frequency (100-Hz) triangular waveform modulates the carrier over a range of about ± 50 MHz.

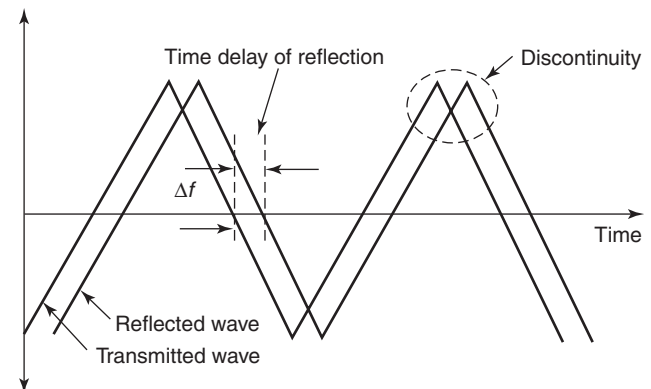


Figure 10. The transmitted and received waveforms of a radio altimeter. The time difference between the transmitted waveform and the reflected wave from the target is an indication of the distance between the two objects.

All radio and radar altimeters have three basic components: one or two antennas, a transmitter receiver, and an indicator. The type of antenna varies, depending on where it is fixed on the aircraft (on a flat or skewed area under the fuselage). Antennas are designed specifically for each system, so changing the unit also involves changing the antenna. The transmitter–receiver is the core of the device. The indicator consists of an electronic digital display or a common analog display.

As mentioned before, frequency differences can be measured using a superheterodyne receiver. In the signal-processing section, the received signal is multiplied with the transmitted signal on an instantaneous basis. In this way, according to the superheterodyne principle, a sum and a difference frequency are created. A lowpass filter is used to remove the component containing the sum of the frequencies, leaving only the difference, as required for further processing. The difference frequency can then be applied to a signal processor for digital display, or perhaps to a frequency-to-voltage converter allowing the altitude to be displayed in analog form. This technique allows the display of instantaneous altitudes as well as changes in altitude.

It is important to note that in the determination of altitudes by radar altimeters the speed of an EM wave in air is assumed to be constant: 3×10^8 m/s. Although this assumption may be valid in some situations, the presence of water vapor in the atmosphere can affect the speed and introduce serious errors in the measurements. Apart from this common shortcoming of radio altimeters, specific altimeters have their own. For example, a conventional FM counter radio altimeter has the following shortcomings: (1) the step error can be severe, (2) an upper measurable limit is introduced by the spurious beat, and (3) there is a tendency to overcount because of unwanted far-distance propagation. The step errors can be reduced by the *modulation synchronous phase-switching method*, using switching-type phase shifters placed at the transmitting (or receiving) antenna feeders. This results in an increase in the phase at every period of the frequency modulation. The upper limits and overcounting errors can be eliminated by the *frequency offset method*. In this method, the time-varying phase shifts are made at higher rates than the modulation repetitions.

Used in an aircraft, the radio altimeter measures its distance above the ground rather than above sea level. A cathode-ray tube indicates the time that a pulse of radio energy takes to travel from the aircraft to the ground and back to the aircraft. The altitude is equal to one-half the time multiplied by the speed of the pulse. Radio altimeters are used especially in automatic navigation and instrument landing systems (ILSs). They are also used in remote sensing applications for military intelligence gathering, mapping, and surveying.

4. LASER ALTIMETERS

Laser altimeters are essentially a form of laser range finding devices, and are used widely for accurate distance measurements. The operation principles are similar to

those of radar altimeters in depending on the time difference between the transmitted and received signals. Thus, the distance is measured by timing a light pulse traveling from a laser light emitter and back to a detector located in the vicinity of the transmitter.

Laser rangefinders are commonly used in land surveying. Airborne laser measurements can be used to directly measure topography, stream channel cross sections, gully cross sections, soil surface roughness, vegetation canopy heights, and vegetation cover and distributions. These laser measurements can be used for the estimation of forest biomass and volume, aerodynamic roughness, and leaf area indices. Airborne laser altimeters provide quick and accurate measurements for evaluating changes in land surface features and can be an additional and useful tool for remote sensing of watershed properties and water resource management.

In laser altimeter applications, three measurement techniques are used: (1) the interferometric method, which is extensively used in short-distance measurements, up to 100 m in free air; (2) amplitude-modulated laser beam telemetry, suitable for distances of 100 m–50 km; and (3) the pulsed laser radar method, for altitudes over 10 km. All these methods are based on the measurement of the propagation time of the laser pulse over the distance under investigation. Therefore, the evaluation of the true geometric distance depends on corrections for factors such as the air refractivity, the beam angles, and the signal processing techniques. On the basis of these principles, various types of laser altimeters are available commercially, depending on the application requirements and the range of the altitudes. In extra-long-range applications, optical radar altimeters, which are based on sending infrared pulses of about 5 ns duration, are found to be accurate.

4.1. Amplitude-Modulated Laser Beam Altimeters

Although interferometric methods for distance measurements are extensively used for short-distance applications, they are clearly not suitable for long-range distance measurements. For those a common method involves amplitude modulation of the laser beam. In this method the modulated beam is projected toward the target and the light returned from the target is collected by a telescope to be sent to a detector, as illustrated in Fig. 11. The phase of the amplitude modulation of the returning light is compared with that of the emitted light. The differences in the phases occur because of the time required for the light to travel to the target and back to the telescope. To describe the operations, an equation can be written in terms of intensities of transmitted beam $I(t)$ and the received beam $I(t - \tau)$

$$I(t) = \alpha I(t - \tau) \quad (16)$$

where τ is the transit time, or propagation time delay, of the lightbeam, and α is the attenuation coefficient, which takes into account propagation efficiency and losses during transmission. The transit time for the sinusoidal modulation, the geometric distances, and the refractive index

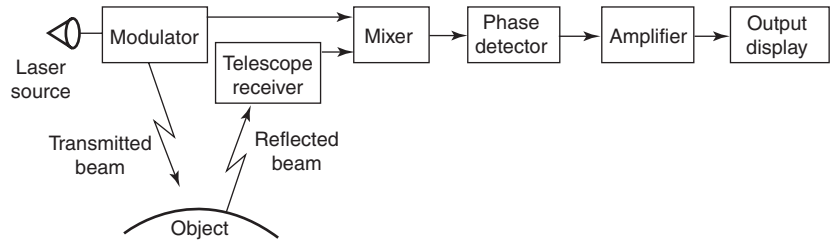


Figure 11. A laser-beam-modulated altimeter. The phase difference between the transmitted and returned signals is measured. The phase comparison technique allows the evaluation of altitudes at high precision from distances of several hundred kilometers.

of the spectral distribution of the lightbeam can be used to find the relationship between the phase shift Φ and the total pathlength L

$$\Phi = \frac{2\pi n_g L}{\lambda_v} \quad (17)$$

where n_g is the group index of refraction of air and the λ_v is the wavelength in vacuum.

4.2. Pulsed Laser Radar

Another approach to laser-based altitude measurement is to make use of the round-trip transit time for a very short pulse, as illustrated in Fig. 9b. Often the acronym LIDAR (light detection and ranging) is used, as an optical counterpart of “radar.” Using lasers to measure altitude results in good accuracy and spatial resolution, but in doing so the advantage of all-weather capability of a microwave altimeter is lost. Such measurements can only be carried out in favorable atmospheric conditions.

Pulsed laser radars commonly use Q -switched laser switches with high peak power. The accuracy of the time measurement depends on the characteristics of the propagation medium and on the resolving capabilities of the photodetector and the timing system. In topographical applications, the statistical characteristics of the received signals for the short-pulse laser altimeters can be directly related to the statistics of the surface profile. In the signal analysis the effects of laser speckle, shot noise, and the surface profile of the ground target need to be considered carefully.

In pulsed radar applications, the altitude to be measured can be found from the expression

$$E_R = \frac{E_0 A_R \eta A_T t^2}{\Omega_0 L^2 \Omega_T} \quad (18)$$

where E_0 is the transmitted pulse energy, A_T and A_R are the areas of the target and the received system, Ω_0 and Ω_T are the solid angles over which the emitted and reflected energy are spread, t is the atmospheric transmission time, η is the diffusion or reflection coefficient, and E_R is the received energy. This equation indicates that the energy follows an inverse-square law. If the intensity of the returned signal is high, Eq. (18) can be used for altitude measurements. If it is low, various probability methods (e.g., the Poisson distribution) are used to estimate the number of photoelectrons.

Solid-state lasers can deliver pulses with time duration of typically 20 ns and peak power up to 1000 MW. Semi-

conductor laser diodes provide high-efficiency pumping of solid-state lasers with the promise of long-lived, reliable operation. In the next generation of laser altimeters, 100-W quasi-CW laser diode bars are likely to find applications. Even with the use of power laser equipment to generate the transmitted signals, the pulse intensity of the returned signals is very weak. To overcome this problem, highly sensitive photodiodes and photomultipliers are used for detection.

In this article, two different systems are discussed in order to explain the scope and the potential of practical laser altimeters: the shuttle laser altimeter (SLA) and the raster scanning airborne laser (RASCAL). The first type, the SLA, is in its second generation of development. Constructed by NASA, this altimeter is used to determine the shape of land surfaces and vegetation canopies. At present, the accuracy of the SLA-2 is within ≈ 1.5 m (vertically) for each 100-m-diameter footprint. The signal-processing component of the system is able to recognize the differences between the reflection from the soil surface and the reflections from other objects; hence the information can be separated and relief plots can be computed.

The mission objective was to compile a database of laser echo returns for every possible surface condition on Earth. The SLA-2 is constructed as an engineering experiment, and NASA is planning the introduction of a third-generation altimeter, the SLA-3. This instrument is planned to have an ultrahigh repetition rate, a smaller footprint than SLA-2, and the ability to penetrate vegetation canopies so that it can provide a contour of the surface under the canopy.

Operation of the SLA-2 is very complex, but it can be broken down into the following three major components: the laser transmitter (a Q -switched, diode-pumped Nd:YAG device, by McDonnell-Douglas), the 38-cm-diameter telescope antenna, and the altimeter receiver connected to a waveform digitizer. A variable-gain amplifier is used to accommodate a greater range of return amplitudes of the returned signals, thus increasing the accuracy and the altitude range. The actual laser return-pulse detection is performed via a silicon avalanche photodiode detector, which in turn is connected directly to the waveform digitizer.

The second altimeter is the RASCAL, also from NASA. The operational principle of the RASCAL is similar to that of the SLA, but the device is configured specifically to operate in aircraft. The RASCAL sensor was developed in 1995 at the Goddard Space Flight Center for airborne mapping of surface topography. The RASCAL is a

second-generation laser altimeter with application to both Earth (airborne) and other planetary surface (space-based) topography determinations. It differs from earlier nadir-profiling laser altimeters by an increase in pulse repetition rate by two orders of magnitude and provision for a near-contiguous scan pattern. It was first operated in a NASA airborne remote sensing program station in California in September 1995, where its high spatial resolution (better than 2 m) in three-dimensional images of topography was demonstrated.

The complicated part of RASCAL is the need for accurate positioning of the laser relative to the aircraft and Earth. Through the use of the aircraft's GPS and inertial navigation system, the NASA team has, in its words, "brute-forced" the solution to this problem and gained a reliable model for exact positioning information. The accuracy of this system has been described as "not as good as [it] should be," and there are plans to build a laser capable of 1 ns pulse width at 10 kHz to help correct this. The return-pulse energy-sampling system is not at its optimum yet, either. By the use of the RASCAL, so far, postprocessed data have been used to re-create many footprints with diameters of 1 m, spaced approximately every 1.5 m in both directions in a pattern 100 m wide. An average accuracy of better than 20 cm with a precision of ± 5 cm is achievable.

A plot obtained from the RASCAL system data is shown Fig. 7. It showed up in postprocessing, when the analyzing team apparently did not realize that they had flown over a satellite tracking station. Although the desired accuracy is lacking, this typical plot shows the potential of the system.

Besides terrestrial applications, laser altimeters, LIDARs, and other ranging systems have been important parts of space missions to the Earth's moon, asteroids, and Mars; and more are planned and contemplated in the future exploration of the solar system. In 1997 the *Mars Global Surveyor* (MGS) entered into orbit around Mars. One of the four scientific instruments on the MGS is the Mars orbiter laser altimeter (MOLA), which has started to map the topography of the planet with unprecedented accuracy. In 1999 the *Near Earth Asteroid Rendezvous* (NEAR) spacecraft, which carries the NEAR laser rangefinder (NLR), arrived at the asteroid Eros. The NLR was to study the shape and the dynamics of the body of Eros for a period of a year. The MOLA and the NLR, along with the Clementine laser altimeter that went to the moon in 1992, represent a new class of active remote sensing instruments for investigations of science in the solar system.

5. GLOBAL POSITIONING SYSTEM (GPS)

The GPS was begun 1978 and completed in 1994 with 21 active and 3 spare satellites. The GPS allows users to determine their exact position, velocity, and time at any time of day, in any weather conditions, free of charge. In discussions of the GPS, it is convenient to break the system into three blocks or segments: the space segment, the user segment, and the control segment.

5.1. The Space Segment

The GPS satellites orbit Earth at an approximate altitude of 20,000 km, and have an orbit period of 12 sidereal hours. The orbits have been arranged so that a user can have a direct line of sight to at least four satellites at all times at any place on Earth.

Each satellite transmits a unique code, which is based on a pseudorandom sequence allocated before launching. Having received this code, the users can employ autocorrelation techniques to recover these sequences. Given an accurate time reference and the propagation time from the satellite to the receiver, the distance can be determined. If the distances from each satellite in sight and the locations of satellites are known, the relative position and thus the coordinates of the receiver can be calculated easily. For precise calculations, the clock references of the GPS satellites must be known exactly. The clocks on the satellites are known to be stable within 0.003 s per 1000 years.

The satellites transmit signals at 1575.42 and 1227.60 MHz; these two transmissions are known as the L1 and L2 signals. The L1 signal is described as being made up of a *precision* code (P) and a *coarse acquisition* code (C/A). The L2 contains only the P code, which when encrypted is called the "Y code."

5.2. The User Segment

Users of the GPS often have handheld GPS receivers. A receiver determines a pseudorange to work out the time that the signal takes to reach to the receiver. Performing this operation for more satellites in sight, the receiver can work out where the user is either on the face of or above Earth.

The P and C/A codes are sometimes referred as the *precise positioning service* (PPS) and the *standard positioning service* (SPS), respectively. As these names would suggest, the PPS is more accurate than the SPS; this is due to a smaller bit period in the P code. The PPS has been withheld from public use, but is earmarked to be released for civilian use in the near future. A third frequency, which will give better accuracy, is planned to be released for the public. However, the Russian Global Navigation Satellite System (GLONASS) uses a single frequency, thus giving better accuracy for civilian use.

5.3. The Control Segment

The control segment consists of operators of the GPS network at a number of stations on Earth. The requirement of this segment is to maintain the GPS time, monitor and control the satellite orbit positions, and predict variations for compensation of any detected inaccuracies. The network has a master control station situated in Colorado Springs in the United States, and five additional monitoring stations. The positions of these stations are known precisely, and they are used to check and calibrate the GPS. The stations are distributed roughly along the equator and are geographically suitable for general system maintenance. At the moment, the number of stations is said not to be sufficient; however, more stations are being

planned to allow the determination of precise orbital paths of the satellites.

5.4. Theory of Operation

The theory of operation of the GPS is too complicated for detailed treatment in this article. Here, a brief explanation will be given to provide a basic understanding of GPS-based altimeters, particularly concerning accuracy and errors.

The GPS makes use of the time of arrival; that is, the satellites send out signals that contain some information such as the exact time of signal transmission and satellite locations. Once received, the information in the signal can be processed to calculate the time taken for the signal to arrive from the satellite at the receiver. By repeating this operation with the information from at least four satellites, the latitude, longitude, and height of the user can be determined in reference to the satellites and thus, in turn, in reference to fixed points on Earth.

Each satellite transmits a binary phase shift-keyed sequence that is spread spectrally, by its pseudorandom code; this allows all of the satellites to transmit on the same L1 and L2 carriers. They all use the same bandwidths at 2.0463 MHz for the C/A codes and 20.98 MHz for the P codes. This is called *code-division multiple access* (CDMA), and it relies on the properties of pseudorandom codes to work.

Pseudorandom codes have the property of strong autocorrelation. This means that when a pseudorandom code is overlaid on itself and correlated, the result will be slightly negative for all positions except an identical overlaying, in which the result becomes positive. A delay time is added to the internally generated pseudorandom code, to provide a positive, strong correlation with the received signal.

If the internal clock of the GPS receiver were exactly synchronized with the satellite's clock, the measured time delay would be representative of the actual physical distance between the satellite and the receiver. It is very unlikely, however, that the satellite and receiver clocks will be synchronized exactly. As a result, some differences in time, called *clock bias*, arise. The GPS receivers must determine the magnitude of the clock bias by taking delay times of the other satellites into consideration. This means that the measured delay times are the combination (physical distance)/(speed of light) + (clock bias) as explained above.

It is convenient to define a *pseudorange*, which is the delay time multiplied by the speed of light. This is a pseudodistance from the receiver to the satellite, with clock bias factored in. The actual process that the receiver executes can be summarized as follows:

1. The receiver tracks four or more satellites and determines the delay time from each satellite.
2. The receiver calculates all the pseudoranges (i.e., multiplies the times by c).
3. The receiver then corrects the pseudorange results for errors such as the satellite clock difference, the clock bias, the ionospheric effects, and time.

The information sent by satellites, for the computation, is in the form of 50-bps (bits per second) frames superimposed on the C/A and P codes, called the *NAV messages*. It takes about 12.5 min to download 25 of the 1500-bit frames to the receiver. The precise position of the satellite, the clock time, and other relevant information is included in the NAV message. Because of the time required to download the message, the NAV message is defined to be valid for 4 h.

4. When all of the pseudoranges have been corrected, the receiver performs a simultaneous solution of four equations with four unknowns. The four unknown quantities are the Cartesian coordinates x, y, z and the time.

Now that the receiver has solved the equations, the latitude, longitude, and altitude of the user can be calculated and displayed. The accuracy of these results depends on statistical analysis, and thus on the percentage of time of availability of satellites.

The GPS has a number of errors that need to be considered in altitude determinations. Some of these are the receiver clock error, the multipath error, and the ionospheric and tropospheric propagation errors.

As mentioned, the U.S. Department of Defense (DoD) is planning to allow civilian users to use the PPS system instead of the SPS. This will give substantial improvement in accuracy of the position and altitude determinations, as shown in Table 2. In this table, the formal specified accuracies are shown in bold. The percentages 50%, 63%, and 95% are the probable fractions of time for the receiver to be located within the given distances of an exact position calculated statistically. For example, the measured vertical height of the receiver in the SPS system is within 140 m of the central value 95% of the time. This can be compared with 28 m for the PPS system. The distance error of 140 m is clearly too large to be useful in aircraft applications, at low altitudes, but may be acceptable at high altitudes.

A method of improving this accuracy is called *differential GPS* (DGPS), and it can help provide an SPS user with subcentimeter accuracy in many cases. The DGPS uses a ground station that is geodetically fixed (with exact latitude and longitude), and it continuously tracks all visible satellites. Given the precise location and altitude of the DGPS station, and that the satellites transmit their

Table 2. Accuracy in GPS Systems

	Accuracy					
	50% of Time		63% of Time		95% of Time	
	PPS	SPS	PPS	SPS	PPS	SPS
Position (m)						
Horizontal	8	40	10.5	50	21	100
Vertical	9	47	14	70	28	140
Spherical	16	76	18	86	36	172
Velocity (x, y, z) (m/s)	0.07	—	0.1	—	0.2	—
Time (ns)	68	115	100	170	100	340

positions in the NAV message, the DGPS can apply corrections based on the measured delay times. By transmitting corrected information about the visible satellite positions to a GPS receiver via a radio channel, the computation at the receiver can be improved.

The GPS is a powerful tool for accurate determination of altitudes if one has access to a PPS system, and an altitude accuracy better than 100 m can be achieved even with the SPS system. Handheld GPS receivers are now commonly available for a few hundred dollars in consumer retail outlets.

6. REMOTE SENSING

Remote sensing is the science of detecting, measuring, and analyzing an object on the ground from a distance. It comprises mainly measurements of electromagnetic radiation from the ground, in the form of energy reflected by active sensors or emitted by passive sensors in various spectral ranges picked up by aircraft or satellites. Also, remote sensing may encompass aerial photography and similar methods whose results are generally displayed in the form of photographlike images. In aircraft applications, images from different flight paths can be combined to allow an interpreter to perceive features in three dimensions, and identify specific types of rock, soil, vegetation, and other entities, where they have distinctive reflectance values in different spectral regions of the electromagnetic radiation.

Remote sensing systems are made from distinct components as shown in Fig. 12: (1) an active or a passive remote sensor that employs detecting mechanisms to sense or scan the object, (2) a device for recording and imaging of the information received, and (3) the analysis and display system that makes the information useful. In some cases, analysis and display systems are combined and operate concurrently with the sensing system to process and display the data instantaneously. In other cases, the data are recorded and analyzed later. The displays are usually in the form of aerial photographs or television pictures.

An important feature of remote sensing is the identification of signatures, which is used to sense the desired objects against a complex background or surroundings. For example, it may be necessary to identify a particular mineral, crop blight, or type of air or water pollution. Signature, as applied to imagery, usually refers to visual characteristics that identify the subject and separate it from other similar objects.

Image formation is another important aspect of remote sensing. In this regard, there are two categories of

systems: (1) imaging sensor systems, which can be subdivided into framing systems (e.g., aerial photographic cameras, vidicons) and scanning systems, (e.g., radar), and (2) nonimaging sensor systems, also known as spectral data systems (e.g., spectroradiometers, radar scatterometers).

Remote sensors may be surface-based and stationary or mobile, or airborne in aircraft, helicopters, or balloons; or carried aboard spacecraft, such as satellites, a space shuttle, or a space station. These bases are known as the *sensor platforms*. The resolution, or detail, with which a remote sensor can monitor a subject generally depends on the distance from the sensor platform to the object. Generally, remote sensors that employ the shortest wavelengths provide the best resolution. For example, microwave sensors, which operate at wavelengths longer than those of thermal infrared sensors, can be expected to have poorer resolution. However, the longer wavelengths have the best penetrating power. Microwaves, for example, can penetrate through clouds, whereas visible light and infrared light do not. Therefore, microwave radar systems are often used to sense subjects that are not visible to optical wavelength laser radar systems. Also, microwave systems can be used to penetrate vegetation for geologic mapping, to monitor snow depths, to indicate soil moisture, and so on.

Remote sensing finds many applications, such as in military equipment; air transport; deep-space research; geography; environmental monitoring such as oceanography, hydrology, meteorology, and pollution control; monitoring snow depth and ice cover, flood control, hydroelectric generation, and water transport management; agriculture and forestry; and lightning and fire sensing. The geographic and geologic applications include land-use and terrain mapping, geological mapping, and detection of mineral deposits. Oceanographic applications encompass monitoring of waves, currents, temperatures, salinity, turbidity, and other parameters and phenomena related to oceans and seas.

The technology of remote sensors varies from system to system. For example, in a typical infrared remote sensing system, the thermal infrared energy is detected by an optical-mechanical scanner. The detector is cooled by a liquid nitrogen or liquid helium jacket that encloses it, and a rotating mirror directs radiation coming from various directions onto the sensor. Infrared radiation permits mapping surface temperatures to a precision of less than a degree and thus shows the effects of phenomena that produce temperature variations, such as groundwater movements.

In another system, Landsat images are commonly used. They are produced with data obtained from a multispectral scanner carried aboard certain U.S. Landsat satellites orbiting Earth at an altitude of about 900 km. Images covering an area of over 185 km² are available for virtually every part of Earth's surface. Scanner measurements are made in four spectral bands: green and red in the visible portion of the spectrum, and two infrared bands. The data are usually displayed by arbitrarily assigning different colors to the bands and then superimposing these to make representative images.

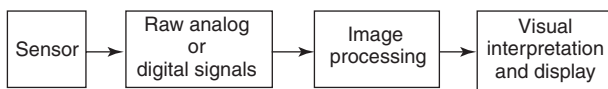


Figure 12. Components of remote sensing for image processing. The sensed signals are stored and processed either online or offline.

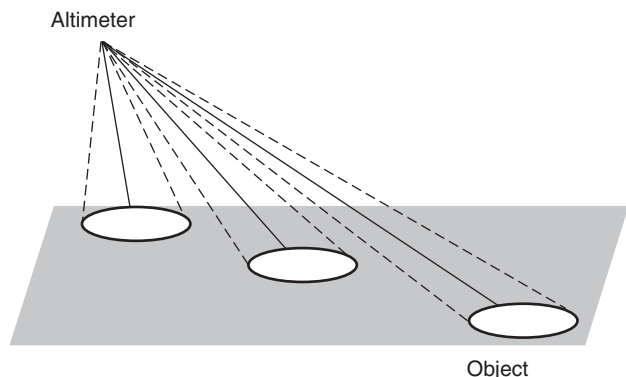


Figure 13. The geometry of a scanning beam altimeter. The scanning is realized either electronically or mechanically. Processing of the returned signals from each scan gives accurate three-dimensional images.

Topographic mapping of the earth, moon, and planets can be accomplished with high resolution and accuracy using satellite laser altimeters. These systems employ nanosecond laser pulses and microradian beam divergences to achieve submeter vertical range resolution from orbital altitudes of several hundred kilometers.

Conventional altimeters provide a topographic surface profile. In most cases the surface topography is required over an area. This can be achieved by multiple orbit traces displaced across the track by successive revolutions of an element making a large number of accurately positioned orbital passes. Often a multibeam or scanning beam altimeter is used to provide three-dimensional images. The corresponding geometry is illustrated in Fig. 13. The accurate performance of the altimeter depends on the effects of the target surface characteristics, spacecraft pointing jitter, and waveform digitizer characteristics. The ranging accuracy is critically dependent on the pointing accuracy and stability of the altimeter, especially over high-relief terrain where surface slopes are large. At typical orbital altitudes of several hundred kilometers, single-shot accuracy of a few centimeters can be achieved when the pointing jitter is on the order of 10μ rad or less.

7. SURFACE HEIGHT MEASUREMENT AND HEIGHT ACCURACY

Surface height measurement is an important concept associated with altimeter technology. In general, height measurement has many applications, ranging from the microscopic scale of measuring step heights in wafers in integrated circuits and height measurements of machined metal surfaces, to the very large scales of ice formation on Earth's surface and wave heights in the oceans. Consequently, the instrumentation suitable for these measurements ranges from microscopes and interferometers to GPS and satellite radar.

In large-scale applications, many methods are used to determine heights on land: (1) spirit leveling (most accurate but slow), (2) measuring vertical angles and distances

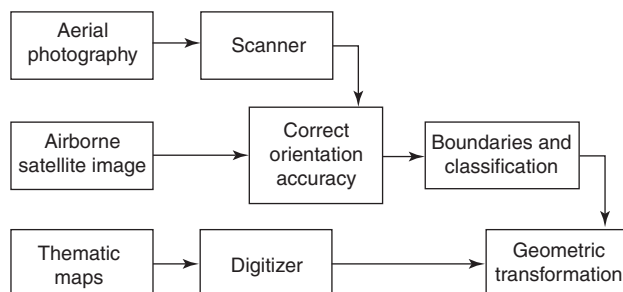


Figure 14. Use of different methods in remote sensing. Several methods are combined electronically to give extremely accurate mapping. In this particular case aerial photography, airborne satellite images, and digitized thematic maps are combined.

(accurate and faster), (3) measuring differences in atmospheric pressure, (4) using photographic techniques such as aerial surveying, and (5) using radar and satellite systems. The last two techniques are accurate but require expensive and sophisticated equipment, as discussed earlier. Often, more than one technique is employed to obtain accurate geographic information, as illustrated in Fig. 14.

In spirit leveling, a horizontal telescope fitted with crosshairs, rotating around a vertical axis on a tripod, is used to adjust a bubble, which is exactly centered. The reading on a graduated vertical staff is observed through the telescope. If such staffs are placed on successive ground points, and the telescope is truly leveled, the difference between the readings at the crosshairs will equal that between the heights of the points. By moving the level and the staffs alternately along a path or road and repeating this procedure, differences in height can be measured accurately over long horizontal distances. In some stringent surveys, the error may be kept to less than a centimeter over a distance of 100 km.

For faster work in hilly areas, where lower accuracy is usually acceptable, trigonometric height determination is employed, using a theodolite to measure vertical angles and measuring or calculating the distances by triangulation. To increase precision, the observations are made simultaneously in both directions so that aerial refraction is eliminated.

The third method of height determination depends on measurements of atmospheric pressure differences with a sensitive aneroid barometer, which can respond to pressure differences small enough to correspond to 0.3–0.6 m in height. To obtain reliable results, it is necessary to use a reference barometer, as the air pressure changes constantly. An alternative to the barometer for the pressure measurements is the use of an apparatus for measuring the boiling point of a liquid, since the boiling temperature depends on the atmospheric pressure.

A relatively new method of surface height measurement is the use of satellite and radar systems. The analysis of the signals received simultaneously from several satellites gives heights as accurately as positions. Heights determined in this way are useful in previously unmapped areas as a check on results obtained by faster relative

methods, but they are not accurate enough for mapping developed areas or for engineering projects. For example, absolute and relative height measurements with the differential GPS systems are accurate to about 30 m, whereas in photogrammetric surveys subcentimeter accuracy can be achieved over a wide area, typically 5 km^2 .

Another application of the satellite systems is in the oceans, to measure the sea level, since the surface of the sea acts as a reflector for radar waves. The accuracy of the measurements depends on how precisely the satellite orbit is known, and on the reduction of dynamic effects on the sea surface such as semidiurnal and diurnal tides.

A typical application of altimeters is in aircraft to determine their height above the surface. Radar systems are often used for geometric height estimation of civil and military aircraft. A typical system consists of a standard altimeter backed up with secondary surveillance radar (SSR) operating on mode S coupled to an omnidirectional antenna fixed under the airplane. The geometric height is derived by various methods, such as the trilateration method, and the systematic errors are compensated for by deriving the profile of the effect on height measurements of the bias in range measurements. Various curve-fitting techniques are used, which estimate both the geometric height and any nonzero systematic errors.

High single-point precision and high point density can be obtained by airborne laser altimetry, using GPS positioning and inertial navigation system (INS) attitude determination. However, these methods are subject to various error sources, which include (1) internal laser sensor errors; (2) GPS and INS errors; (3) atmospheric effects; (4) terrain roughness, reflectivity, and slope; (5) presence, height, and type of vegetation; and (6) integration and synchronization of laser, GPS, and INS. When well calibrated, laser altimeters can give subcentimeter accuracy. However, the accuracy may be very sensitive to terrain type, terrain coverage, and filters used to remove undesired objects, such as buildings and trees. In particular, pointing accuracy, which depends on the pointing jitter of the scanning mirror and INS attitude determination, is a main error source, especially over high-relief terrain.

BIBLIOGRAPHY

1. C. Elachi, *Spaceborne Radar Sensing Applications and Techniques*, Institute of Electrical and Electronics Engineers, New York, 1988.

FURTHER READING

- N. Ackroyd and R. Lorimer, *A GPS Users' Guide*, Lloyd's of London Press, New York, 1994.
- H. J. Buiten and J. P. G. W. Clevers, *Land Observation by Remote Sensing: Theory and Applications*, Gordon & Breach Science, Yverdon, Switzerland, 1993.
- B. Clarke, *GPS Aviation Applications*, McGraw-Hill, New York, 1996.
- R. P. G. Collinson, *Introduction to Avionics*, Chapman & Hall, London, 1996.
- N. E. Fancey, I. D. Gardiner, and R. A. Vaughan, *The Determination of Geophysical Parameters from Space*, Institute of Physics, Philadelphia, 1996.
- A. Helfrick, *Practical Aircraft Electronic Systems*, Prentice-Hall, Englewood Cliffs, NJ, 1995.
- E. H. J. Pallett and S. Coyle, *Automatic Flight Control Systems*, Blackwell Scientific, Oxford, 1993.
- RASCAL laser altimeter instrument home page (online), available at <http://denali.gsfc.nasa.gov/research/laser/rascal/index.html>.
- J. F. Ready, *Industrial Applications of Lasers*, 2nd ed., Academic Press, San Diego, 1997.
- P. A. Roocke, *Intelligent Barometric Altimeter*, thesis, School of Electrical and Computer Engineering, Curtin Univ. Technology, Perth, Western Australia, 1990.
- R. Rummel and F. Sanso, *Satellite Altimetry in Geodesy and Oceanography*, Springer-Verlag, Berlin, 1993.
- G. Seeber, *Satellite Geodesy*, de Gruyter, Berlin, 1993.
- G. Siouris, *Aerospace Avionics Systems*, Academic Press, San Diego, 1993.
- SLA (Shuttle Laser Altimeter) home page (online), available at <http://ssppgse.gsfc.nasa.gov/hh/tas/experiments/sla.html>.
- TOPEX altimeter home page (online), available at http://podaac.jpl.nasa.gov:2031/SENSOR_DOCS/topex_alt.html.

AMPLITUDE SHIFT KEYING

FUQIN XIONG
Cleveland State University
Cleveland, Ohio

1. INTRODUCTION

In some digital communication systems, such as satellite communication and cellular telephone systems, digital message data, such as binary 0 and 1, must be impressed on a high-frequency carrier signal before being transmitted. The carrier is usually a voltage signal such as a cosine function of time t

$$s(t) = A \cos(2\pi f_c t + \theta)$$

where A is the amplitude, f_c is the carrier frequency, and θ is the initial phase. Each of these three parameters or a combination of some of them can be used to carrier the message data. The process of impressing a message on to a carrier by associating one or more parameters of the carrier with the message is called modulation, and the process of extracting the message from the modulated signal is called *demodulation*.

The most important properties of a modulation scheme are the bandwidth efficiency, bit error probability, and system complexity.

The *bandwidth efficiency* is defined as number of bits per unit bandwidth (1 Hz) that a modulation scheme communicates, and it is determined by the power spectral

density (PSD) of a digitally modulated signal. Even though the carrier signal of a digitally modulated signal is a deterministic signal, the data bits that modulate the carrier are typically random. Therefore the digitally modulated signal is typically a random signal. For random signals, their spectral property is described by PSD [1, App. A], unlike that for deterministic signals where spectrum can be found using Fourier series or Fourier transform, depending on whether the signal is periodical or aperiodic, respectively.

Bit error probability is also commonly referred as *bit error rate* (BER), although the latter is only an approximation of the former. It is largely determined by the signal energy to noise energy ratio or simply signal-to-noise ratio (SNR), as well as signaling format. One modulation scheme may need less SNR than the other for the same BER, then we say the former is more power efficient than the latter.

System complexity refers to mainly complexities of the modulator, demodulator, and synchronization subsystems, which are also determined by signalling format.

The three basic digital modulations are the amplitude shift keying (ASK), frequency shift keying (FSK), and phase shift keying (PSK). As these terms suggest, while keeping all other parameters of the carrier unchanged, ASK uses the data to vary the amplitude, FSK uses the data to change the frequency, and PSK uses the data to control the phase of the carrier, respectively. Binary forms of all three of them are the simplest ones, where the modulating digital message are binary. If the messages are M -ary, where M is an integer, then the modulations are MASK, MFSK, or MPSK.

Both ASK and FSK are the simplest to implement, but ASK is more bandwidth-efficient; that is, for the same system bandwidth ASK can transmit more data. ASK and PSK have the same bandwidth efficiency, but PSK is more power-efficient, that is, for the same SNR (signal-to-noise ratio), the PSK has a lower bit error rate. However, PSK is more difficult to implement than ASK. Even though PSK has gained more popularity, ASK and FSK are still used in many communication systems because of their implementation simplicity.

This article is about ASK. We will first introduce the simplest ASK, the On-Off keying (OOK), in Section 2. After that we will describe a general form M -ary ASK (MASK) in Section 3, where a general form of the power spectral density expression is given and optimum detection and its error probability expression is derived. In Section 4, bipolar symmetric MASK and its PSD, BER, modulator, and demodulator are presented. Section 5 discusses unipolar MASK and its PSD, BER, modulator and demodulator. MASK and MPSK are compared in Section 6. Finally, in Section 7, two advanced forms of modulations related to ASK, the QAM, and ASK-OFDM are briefly discussed.

2. ON-OFF KEYING

The simplest ASK scheme is the binary unipolar ASK also known as *on-off keying* (OOK), where binary data 1 and 0

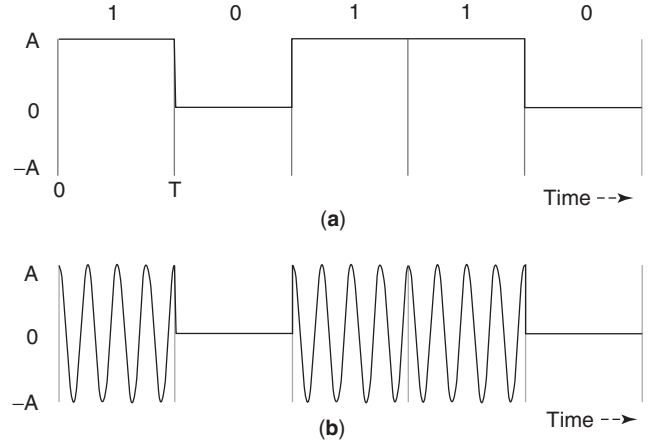


Figure 1. OOK waveforms: (a) data waveform; (b) modulated OOK signal waveform.

are represented by the presence and the absence of a carrier burst, respectively. The OOK signal set is

$$\begin{aligned} s_1(t) &= A \cos 2\pi f_c t \text{ for } a = 1, \quad 0 \leq t \leq T \\ s_2(t) &= 0 \text{ for } a = 0, \quad 0 \leq t \leq T \end{aligned} \quad (1)$$

where a is the binary data. Figure 1 illustrates an OOK signal, where (b) is the baseband data waveform corresponding to the data sequence (10110). The baseband waveform voltage is either A volts or 0, depending on whether the data bit is 1 or 0. When the data bit is 1, there is a burst of carrier signal of A volts in (b), otherwise there is not.

In the following we examine the properties of OOK in terms of its spectrum and bit error probability. We will give expressions without derivations. We defer the derivations to the section on noncoherent unipolar M -ary ASK, of which OOK is only one special case.

2.1. Power Spectral Density and Bandwidth

It is well known that for a bandpass random signal $s(t)$, the PSD is completely determined by the PSD of its complex envelope or equivalent baseband signal [1–3]

$$\Psi_s(f) = \frac{1}{2} [\Psi_{\tilde{s}}(f - f_c) + \Psi_{\tilde{s}}(-f - f_c)] \quad (2)$$

where $\Psi_{\tilde{s}}(f)$ is the PSD of the complex envelope. Thus it suffices to have $\Psi_{\tilde{s}}(f)$ instead of $\Psi_s(f)$.

Assuming that the random data bits are uncorrelated and equally likely, the baseband PSD expression of OOK is given by [1, p. 422]

$$\Psi_{\tilde{s}}(f) = \frac{A^2 T}{4} \left(\frac{\sin \pi f T}{\pi f T} \right)^2 + \frac{A^2}{4} \delta(f) \quad (3)$$

where $\delta(f)$ is the Dirac delta function, which is a discrete spectral line at zero frequency, reflecting the DC component

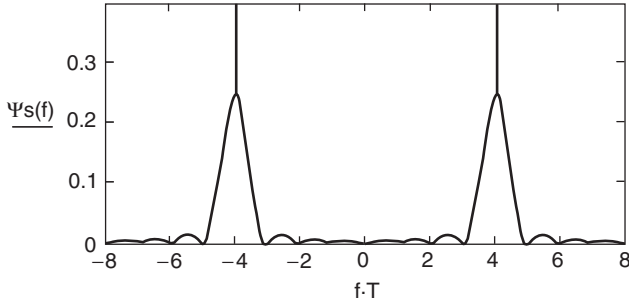


Figure 2. PSD of OOK and unipolar MASK with a rectangular pulse, from Eqs. (3) and (2), with $A = \sqrt{2}$ and $T = 1$.

of the baseband signal. The rest is a continuous part of the PSD, representing the variation in the data sequence.

Figure 2 shows the PSD of OOK. In the figure we set $A = \sqrt{2}$ and $T = 1$ for unity average symbol pulse energy and $f_c = 4/T$. In fact, the shape of the PSD in this figure is for any unipolar M -ary ASK with rectangular pulse. From the figure we can see that the main spectral components are within the null-to-null bandwidth, which is $2/T$. That is, the null-to-null bandwidth is twice the symbol rate.

2.2. Modulator and Demodulator

The modulator of OOK is very simple (Fig. 3a). The binary data sequence is used as a control signal that connects the output with the oscillator through the switch when the bit is 1 and disconnects the switch when the bit is 0. The demodulator can be in two different forms: the coherent (Fig. 3b) and the noncoherent (Fig. 3c). The coherent demodulator requires a carrier recovery circuit that synchronizes in frequency and phase the local oscillator in the receiver with the received signal

$$r(t) = s(t) + n(t)$$

where $n(t)$ is the additive white Gaussian noise (AWGN) whose two-sided power spectral density is $N_0/2$. The

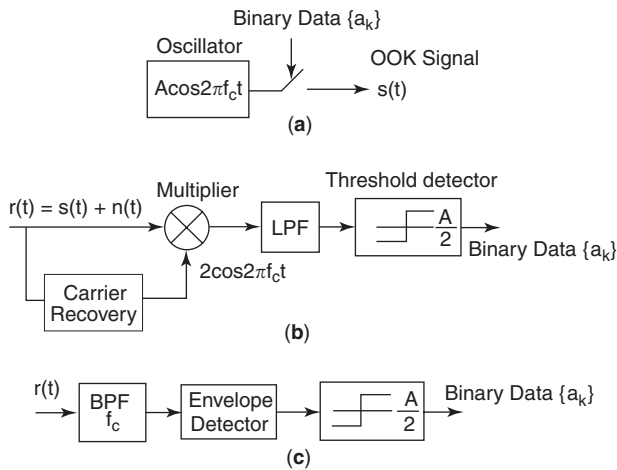


Figure 3. OOK modem: (a) modulator; (b) coherent demodulator; (c) noncoherent demodulator.

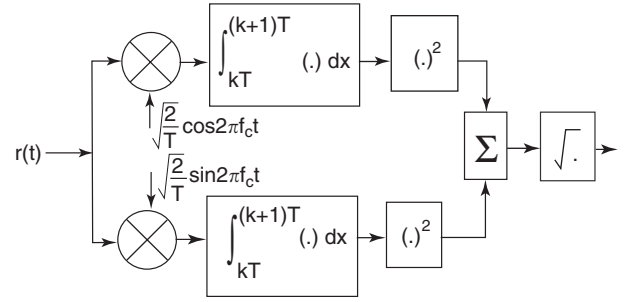


Figure 4. Quadrature envelope detector.

received signal is first multiplied with the recovered carrier $2 \cos 2\pi f_c t$, and the product then passes a lowpass filter (LPF). The LPF rejects the double-frequency part of the product and high-frequency noise. The result is $A + n$, where n is the residual noise. This signal is sent to the threshold detector, whose threshold is set at $A/2$. If the signal is above $A/2$ threshold, the output is set to 1; otherwise the output is set to 0. In the noncoherent demodulator, the first stage is a bandpass filter (BPF) with a center frequency of f_c and adequate bandwidth. This BPF has the function of selecting the desired signal and rejecting the noise. The filtered signal then passes an envelope detector, which extracts the envelope of the modulated carrier, namely, the noise-corrupted baseband pulses. Finally, the noise-corrupted baseband pulses pass the threshold detector to produce the binary data sequence.

The envelope detector can be implemented in the form of a quadrature detector as shown in Fig. 4. It can also be approximately implemented in other forms. For example, the well-known AM demodulator consisting of a diode followed by a resistor and a capacitor in parallel is an envelope detector.

2.3. Bit Error Probability

Bit error probability expressions for OOK are given below without proof. Later we can see that these expressions can be derived as special cases from M -ary cases.

The bit error probability for coherent demodulation of OOK is

$$P_b = Q\left(\sqrt{\frac{E_b}{N_0}}\right) \quad (4)$$

where E_b is the average bit energy and

$$Q(x) = \int_x^\infty \frac{1}{\sqrt{2\pi}} e^{-\frac{u^2}{2}} du \quad (5)$$

is the Q function. The bit error probability for noncoherent demodulation of OOK is [5].

$$P_b = \frac{1}{2} \exp\left(-\frac{E_b}{2N_0}\right) + \frac{1}{2} Q\left(\sqrt{\frac{E_b}{N_0}}\right) \quad (6)$$

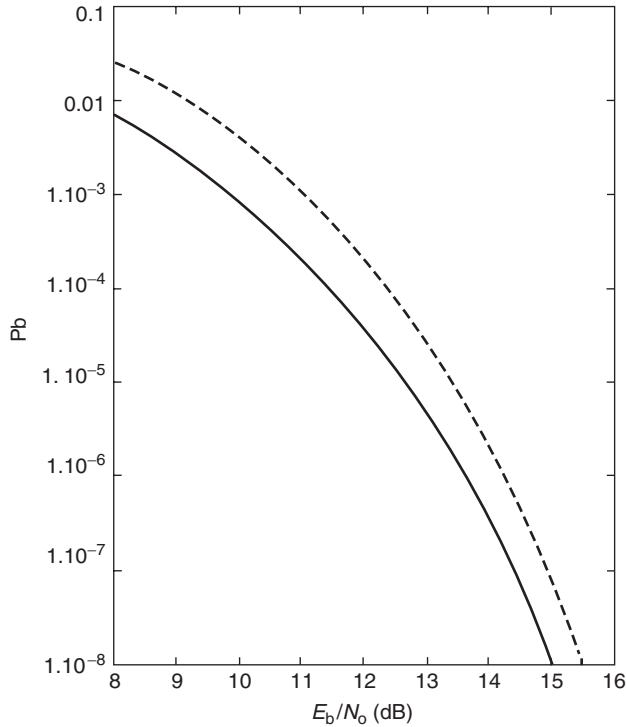


Figure 5. OOK bit error probabilities: solid line—coherent demodulation; dotted line—noncoherent demodulation.

Figure 5 shows the BERs of coherent and noncoherent OOK; the former demodulator has a better BER. The noncoherent is relatively easier to implement since it does not require the carrier synchronization. The noncoherent demodulator is more robust against channel impairments such as fading and also is suitable for systems where synchronization is difficult such as a frequency-hopping multiple-access system.

3. *M*-ARY ASK (MASK)

OOK is simple but not bandwidth-efficient. To improve bandwidth efficiency, we need to go from binary to *M*-ary, where *M* is usually a power of 2.

In *M*-ary ASK (MASK), data bits are grouped into *n*-tuples, where $n = \log_2 M$. Each *n*-tuple is mapped into an amplitude A_i . Thus a symbol in MASK is a burst of carrier signal with an amplitude determined by the *n*-tuple and it represents *n* bits instead of only one bit as in OOK. As we will see later (Sections 4.1 and 5.1), the bandwidth of the MASK signal's PSD is determined by the symbol duration. By keeping the symbol duration the same, an MASK system and an OOK system will need the same bandwidth, but the bit rate of the MASK system will be *n* times that of the OOK system.

In the basic symbol period $[0, T]$, an MASK signal with a pulseshape $p(t)$ can be expressed as

$$s_i(t) = A_i p(t) \cos 2\pi f_c t, \quad 0 \leq t \leq T \quad (7)$$

for $i = 1, 2, \dots, M$. The distribution of amplitudes varies. The most common choices are the symmetric uniform spacing bipolar distribution and uniform spacing unipolar distribution. The amplitudes of the symmetric uniform spacing bipolar distribution is given by

$$A_i = (2i - 1 - M)A, \quad i = 1, 2, \dots, M \quad (8)$$

where $A > 0$. The amplitude spacing is $2A$. For example, if $M = 4$, then $A_i \in (-3A, -A, A, 3A)$. The amplitude distribution of the uniform spacing unipolar distribution is given by

$$A_i = (i - 1)A, \quad i = 1, 2, \dots, M \quad (9)$$

The amplitude spacing is A . If $M = 4$, then $A_i \in (0, A, 2A, 3A)$. OOK is just a special case of the unipolar MASK when $M = 2$.

A bipolar MASK can be demodulated only coherently since noncoherent demodulation cannot distinguish the sign of the signal. A unipolar MASK can be demodulated noncoherently as well as coherently. However, it is generally used in a system where coherent demodulation is difficult; thus noncoherent demodulation is preferred. If coherent demodulation is feasible, the symmetric uniform spacing bipolar MASK is preferred over the uniform spacing unipolar MASK since the former has better BER performance. In the following two sections, we will discuss coherent symmetric uniform spacing bipolar MASK and noncoherent uniform spacing unipolar MASK. But first, we examine the power spectral densities of both.

3.1. Power Spectral Density

Consider a sequence of MASK symbols in the form of

$$s(t) = \sum_{k=-\infty}^{\infty} A_k p(t - kT \cos 2\pi f_c t), \quad -\infty < t < \infty \quad (10)$$

where A_k are the amplitudes controlled by the data *n*-tuples. Assuming that the data are uncorrelated, the PSD of the complex envelope of the bandpass MASK signal is [1, (A.18)]

$$\Psi_s(f) = \frac{\sigma_A^2 |P(f)|^2}{T} + \left(\frac{m_A}{T}\right)^2 \sum_{k=-\infty}^{\infty} \left|P\left(\frac{k}{T}\right)\right|^2 \delta\left(f - \frac{k}{T}\right) \quad (11)$$

where $P(f)$ is the Fourier transform of $p(t)$, σ_A^2 is the variance of A_k , and m_A is the mean value of A_k .

Now let us assume that $p(t)$ is rectangular with unit amplitude; then

$$|P(f)| = \left| T \frac{\sin \pi f T}{\pi f T} \right| \quad (12)$$

and

$$P \frac{k}{T} = T \frac{\sin \pi k}{\pi k} = \begin{cases} T, & k = 0 \\ 0, & k \neq 0 \end{cases}$$

then the PSD of the complex envelope of the bandpass MASK signal is

$$\Psi_s(f) = \sigma_A^2 T \left(\frac{\sin \pi f T}{\pi f T} \right)^2 + (m_A)^2 \delta(f) \quad (13)$$

3.2. Optimum Detection and Error Probability

It is well known from detection theory that for a noise-corrupted signal, the optimum detection starts by correlating the signal with a set of orthonormal basis functions from which the signal is constructed [4, Chap. 2] [1, App. B]. The outputs of the correlators are called sufficient statistics. Then, based on the probability distributions of the sufficient statistics and the detection criterion (usually minimum error probability), the detection rule is established.

To derive the optimum demodulator of the MASK, we first assume that the pulse shaping function is the unit amplitude rectangular pulse; then we can rewrite (7) in terms of an orthonormal basis function $\phi(t)$

$$s_i(t) = A_i \cos 2\pi f_c t = s_i \phi(t), \quad 0 \leq t \leq T \quad (14)$$

Note that there is only one basis function

$$\phi(t) = \sqrt{\frac{2}{T}} \cos 2\pi f_c t \quad (15)$$

and its energy is normalized, that is, $\int_0^T \phi^2(t) dt = 1$ and s_i is the projection of $s(t)$ onto the orthonormal basis function, given by

$$s_i = \int_0^T s_i(t) \phi(t) dt = A_i \sqrt{\frac{T}{2}} \quad (16)$$

Assuming that the received signal is

$$r(t) = s_i(t) + n(t)$$

then the sufficient statistic is the correlator output

$$r = \int_0^T r(t) \phi(t) dt \quad (17)$$

and the detector compares r to s_i and chooses the closest (minimum distance decision rule) [1].

The error probability of the coherent detection for an MASK with equal amplitude spacings can be derived as follows. Assuming an AWGN channel with two-sided noise PSD of $N_0/2$, we obtain

$$r = \int_0^T r(t) \phi(t) dt = \int_0^T [s_i(t) + n(t)] \phi(t) dt = s_i + n$$

where n is Gaussian with zero mean and a variance of $N_0/2$ [1, App. B]. Thus r is Gaussian with mean s_i and variance $N_0/2$.

$$f(r/s_i) = \frac{1}{\sqrt{\pi N_0}} \exp \left[-\frac{(r - s_i)^2}{N_0} \right] \quad (18)$$

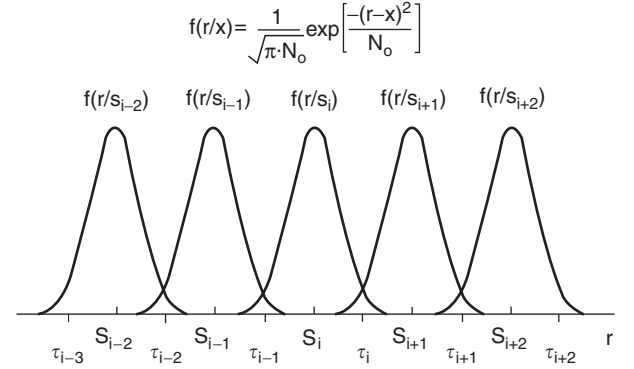


Figure 6. Thresholds and decision regions for MASK. (From Xiong [1], copyright © 2000 Artech House.)

Now we assume that signals s_i are equally spaced. Figure 6 shows the probability distribution densities of r conditioned on equally spaced s_i , where τ_i are thresholds. This figure can help us derive the error probability.

Assuming that, s_i is transmitted, a symbol error occurs when the noise n exceeds in magnitude one-half the distance between two adjacent levels. This probability is the same for each s_i except for the two outside levels, where an error can occur in one direction only. Assuming all amplitude levels are equally likely, the average symbol error probability is

$$P_s = \frac{M-1}{M} \Pr \left(|r - s_i| > \frac{\Delta}{2} \right)$$

where Δ is the distance between adjacent signal levels, and also is the distance between adjacent thresholds. Thus

$$\begin{aligned} P_s &= \frac{M-1}{M} \Pr \left(|r - s_i| > \frac{\Delta}{2} \right) \\ &= \frac{M-1}{M} \frac{2}{\sqrt{\pi N_0}} \int_{\Delta/2}^{\infty} e^{-x^2/N_0} dx \\ &= \frac{M-1}{M} \frac{2}{\sqrt{2\pi}} \int_{\Delta/\sqrt{2N_0}}^{\infty} e^{-x^2/2} dx \end{aligned}$$

That is

$$P_s = \frac{2(M-1)}{M} Q \left(\sqrt{\frac{\Delta^2}{2N_0}} \right) \quad (19)$$

Note that this expression is applicable to any uniformly spaced MASK, whether it is bipolar or unipolar, symmetric or asymmetric.

Now if the MASK signal's pulse shaping function is an arbitrary energy function rather than rectangular, we can write (7) as

$$s_i(t) = A_i p(t) \cos 2\pi f_c t = s_i \phi(t), \quad 0 \leq t \leq T \quad (20)$$

where

$$\begin{aligned} \phi(t) &= \sqrt{2/E_p} p(t) \cos 2\pi f_c t \\ s_i &= A_i \sqrt{E_p}/2 \end{aligned} \tag{21}$$

where E_p is the energy of pulseshaping signal $p(t)$ in $[0, T]$. Note that $\int_0^T \phi^2(t) dt \cong 1$ for $f_c \gg 1/T$. Thus for most practical cases where $f_c \gg 1/T$, the optimum demodulator for the rectangular pulse case is still applicable for other pulseshapes and the symbol error probability expression (19) is still valid.

4. BIPOLAR SYMMETRIC M-ARY ASK

As mentioned in the previous section, a bipolar MASK can be demodulated only coherently and is preferred over the unipolar MASK since the former has better BER performance. In this section, we will examine coherent symmetric uniform-spacing bipolar MASK in terms of its PSD, system structure, and BER.

4.1. Power Spectral Density and Bandwidth

The PSD of the complex envelope of the symmetric bipolar MASK (not necessarily uniformly spaced) is obtained by setting $m_A = 0$ in (11):

$$\Psi_s(f) = \frac{\sigma_A^2 |P(f)|^2}{T} \tag{22}$$

The above shows that the PSD of symmetric bipolar MASK is determined by the PSD of the pulseshaping function $p(t)$. If the pulse is rectangular, then, from (13), we have

$$\Psi_s(f) = \sigma_A^2 T \left(\frac{\sin \pi f T}{\pi f T} \right)^2 \tag{23}$$

The passband PSD can be obtained by substituting the baseband PSD expressions into (2). Figure 7 shows the passband PSD of the bipolar MASK with rectangular pulse (where we set $\sigma_A^2 T = \frac{1}{2}$). The null-to-null bandwidth is $2/T$. Note that unlike the PSD for OOK there is no discrete spectral line at the carrier frequency.

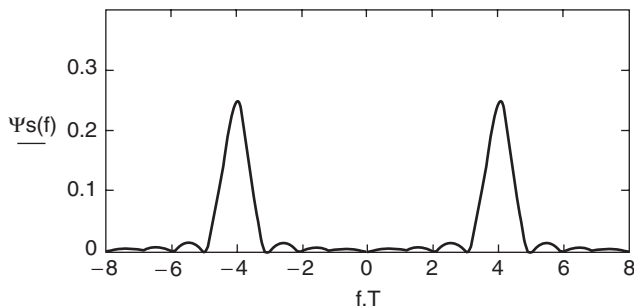


Figure 7. PSD of bipolar MASK with rectangular pulse, and $\sigma_A^2 T = \frac{1}{2}$.

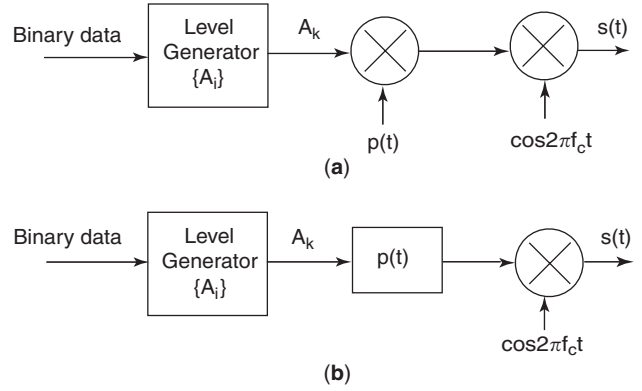


Figure 8. MASK modulator. (From Xiong [1], copyright © 2000 Artech House.)

4.2. Modulator and Demodulator

The modulator is shown in Fig. 8. Figure 8a is a direct implementation of (7). The level generator takes $n = \log_2 M$ bits from the binary datastream and maps them into an amplitude level $A_k \in \{A_i\}$, where the subscript k indicates the k th symbol interval. The mapping is preferably gray-coding so that the n -tuples representing the adjacent amplitudes differ by only one bit. The functions of the remaining blocks are self-explanatory. The equivalent implementation is shown in Fig. 8b. It is more practical for hardware implementation. The $p(t)$ multiplier is replaced with a filter with an impulse response $p(t)$. In order to generate a pulse $A_i p(t)$, the input to the filter must be an impulse $A_i \delta(t)$. In practice, this can be realized by a very narrow pulse with amplitude A_i .

The optimum receiver implementing the minimum distance rule is shown in Fig. 9, where the last block is a threshold detector. Figure 9a is a direct implementation of (17) and the minimum distance rule. In Fig. 9b, the correlation with $p(t)$ is replaced by a matched filter and a sampler [1, p. 419]. Figure 9b is more practical for hardware implementation.

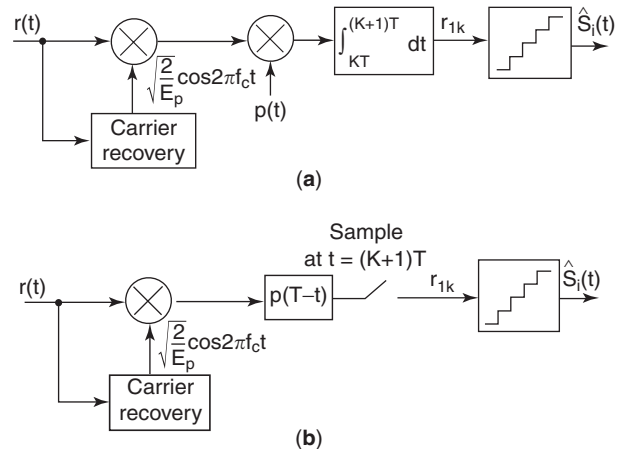


Figure 9. Optimum coherent demodulators for MASK. (From Xiong [1], copyright © 2000 Artech House.)

The threshold detector has $M-1$ thresholds, each placed in the middle of two signal points (refer to Fig. 7). The correlator computes the r , and the threshold detector is actually computing the distance of r to the amplitudes s_i , $i = 1, 2, \dots, M$ and chooses the smallest. Note that the reference signal can be any scaled version of $\phi(t)$ as long as the thresholds are scaled accordingly.

The recovery of coherent carrier and the symbol timing clock are assumed in the coherent demodulator. A description of techniques of carrier and timing recovery is beyond the scope of this article, but it can be found in common communication books.

4.3. Error Probability

The error probability of bipolar symmetric uniformly spaced MASK is obtained from (19), but we need to figure out what Δ is. For bipolar symmetric uniformly spaced MASK, the amplitudes A_i are given in (8). In terms of signal projection s_i , from (21) we can write

$$\begin{aligned} s_i &= A_i \sqrt{E_p/2} = (2i-1-M)A \sqrt{E_p/2} \\ &= (2i-1-M)A_0, \quad i = 1, 2, \dots, M \end{aligned} \quad (24)$$

where $A_0 = A \sqrt{E_p/2}$. Then

$$\Delta = |s_i - s_{i-1}| = 2A_0$$

Thus from (19) we have

$$P_s = \frac{2(M-1)}{M} Q \left(\sqrt{\frac{2A_0^2}{N_0}} \right) \quad (25)$$

The symbol error probability can be expressed in terms of the average energy of the signals. The average symbol energy of the signals is

$$\begin{aligned} E_s &= \frac{1}{M} \sum_{i=1}^M E_i = \frac{1}{M} \sum_{i=1}^M s_i^2 \\ &= \frac{1}{M} \sum_{i=1}^M (2i-1-M)^2 A_0^2 = \frac{1}{M} \frac{M(M^2-1)A_0^2}{3} \\ &= \frac{1}{3} (M^2-1)A_0^2 \end{aligned} \quad (26)$$

As a result, (25) becomes

$$P_s = \frac{2(M-1)}{M} Q \left(\sqrt{\frac{6E_s}{(M^2-1)N_0}} \right) \quad (27)$$

Since the average energy per bit is $E_b = E_s / \log_2 M$, (27) can be written as

$$P_s = \frac{2(M-1)}{M} Q \left(\sqrt{\frac{6(\log_2 M)E_b}{(M^2-1)N_0}} \right) \quad (28)$$

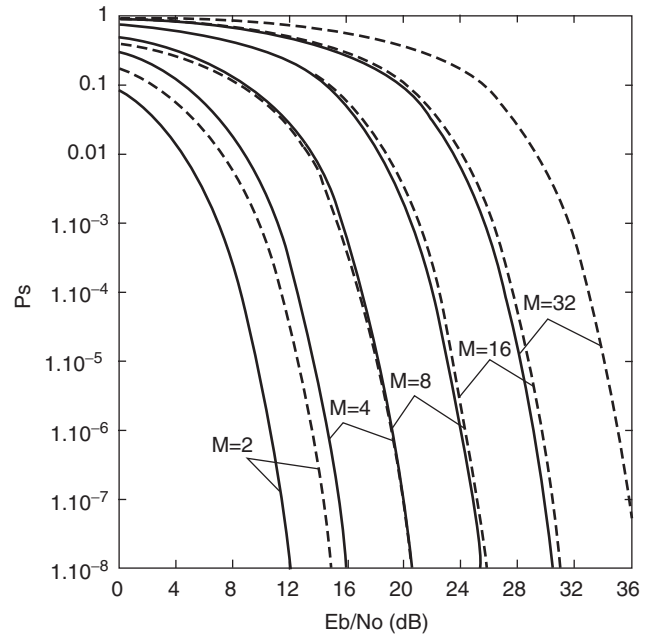


Figure 10. Symbol error probability of coherent bipolar symmetric uniformly spaced MASK (solid line) and coherent unipolar uniformly spaced MASK (dotted line).

Figure 10 shows the curves of the symbol error probability of the bipolar symmetric uniformly spaced MASK versus E_b/N_0 . We emphasize that (27) to (28) depend on only average energy of the signal symbols, not the function form of $p(t)$. In general, bit error probability is not simply related to symbol error probability. However, for Gray coded¹ n -tuple-to-amplitude mapping, the adjacent symbols differ by only one bit. At high signal-to-noise ratios, the most likely errors are the adjacent symbols, so in this case

$$P_b \approx \frac{P_s}{\log_2 M} \quad (29)$$

5. UNIPOLAR M -ARY ASK

As pointed out in Section 2, a unipolar MASK can be demodulated noncoherently as well as coherently. Even though coherent unipolar MASK is not a usual choice since the symmetric bipolar MASK is better in terms of BER, for the sake of completeness and also because of the ease in doing this, we will present the error probability expression. Then we will focus on the noncoherent unipolar MASK. But first we examine its power spectral density.

¹The bits-to-amplitude mapping could be arbitrary as long as the mapping is one-to-one. However, a method called Gray coding is usually used. Gray coding assigns n -tuples with only one-bit difference to two adjacent amplitudes. When an M -ary symbol error occurs, it is most likely that the signal is detected as one of the signals with the adjacent amplitudes; thus only one of the n bits is in error. Gray coding keeps the bit error rate at the minimum for a given symbol error rate.

5.1. Power Spectral Density and Bandwidth

In general, the PSD of unipolar MASK is given by (11). For uniformly spaced amplitudes and rectangular symbol pulse, the PSD of the complex envelope is given in (13). The passband PSD shape is shown in Fig. 2.

For the amplitudes given in (9), the mean value of the amplitudes is

$$m_A = \frac{1}{M} (0 + A + \dots + (M-1)A) = \frac{(M-1)A}{2}$$

and then

$$\Psi_s(f) = \sigma_A^2 T \left(\frac{\sin \pi f T}{\pi f T} \right)^2 + \frac{(M-1)^2 A^2}{4} \delta(f) \quad (30)$$

5.2. Modulator and Demodulator

The structure of modulator for unipolar MASK is almost the same as that for bipolar MASK as shown in Fig. 8. The difference is only in the settings of the level generator due to the signal's unipolarity. The signal levels are now only positive and equally spaced.

The structure of coherent demodulator for unipolar MASK is almost the same as that for bipolar MASK as shown in Fig. 9. The difference is only in the settings of the threshold detector due to the signal's unipolarity. The thresholds now are only positive and equally spaced.

The structure of noncoherent demodulator for unipolar MASK is almost the same as that for OOK as shown in Fig. 3. The difference is in the threshold detector, which must now have multiple equally-spaced thresholds.

5.3. Coherent Demodulation and Error Probability

The symbol error probability is again given by (19), but we need to figure out what Δ is. For unipolar uniformly spaced MASK, the amplitudes are given in (9). In terms of signal projection s_i , from (21) we can write

$$s_i = A_i \sqrt{E_p/2} = (i-1)A \sqrt{E_p/2} \quad (31)$$

$$= (i-1)A_0, \quad i = 1, 2, \dots, M$$

where $A_0 = A \sqrt{E_p/2}$. Then

$$\Delta = |s_i - s_{i-1}| = A_0$$

Thus from (19) we have

$$P_s = \frac{2(M-1)}{M} Q \left(\sqrt{\frac{A_0^2}{2N_0}} \right) \quad (32)$$

The average symbol energy of the signals is

$$\begin{aligned} E_s &= \frac{1}{M} \sum_{i=1}^M E_i = \frac{1}{M} \sum_{i=1}^M s_i^2 \\ &= \frac{1}{M} \sum_{i=1}^M (i-1)^2 A_0^2 = \frac{1}{M} \sum_{j=0}^{M-1} j^2 A_0^2 \\ &= \frac{1}{6} (2M^2 - 3M + 1) A_0^2 \end{aligned}$$

Table 1. Comparison between Bipolar and Unipolar Uniformly Spaced MASK

M	2	4	8	16	32	64	∞
$R(M)$	2	2.8	3.333	3.647	3.818	3.908	4
$10 \log R(M)$ (dB)	3.01	4.472	5.229	5.619	5.819	5.919	6.02

As a result, (32) becomes

$$P_s = \frac{2(M-1)}{M} Q \left(\sqrt{\frac{3E_s}{(2M^2 - 3M + 1)N_0}} \right) \quad (33)$$

In terms of average energy per bit, (33) can be written as

$$P_s = \frac{2(M-1)}{M} Q \left(\sqrt{\frac{3(\log_2 M)E_b}{(2M^2 - 3M + 1)N_0}} \right) \quad (34)$$

This expression is plotted in Fig. 10 (dotted line). The P_b at high SNRs can be estimated by (29). When $M=2$, the unipolar MASK is OOK, $P_s = P_b$. Substituting $M=2$ into (34), we obtain the exact expression in (4).

Comparing (28) and (34) reveals that the ratio of the expression in the square root sign of (28) over that of (34) is

$$R(M) = \frac{2(2M^2 - 3M + 1)}{M^2 - 1}$$

Table 1 shows some values of $R(M)$. It shows that the bipolar uniformly spaced MASK is superior to the unipolar uniformly spaced MASK. The asymptotic ratio is 4 or 6 dB. This confirms the statement we said earlier that coherent unipolar MASK is not a usual choice since the symmetric bipolar MASK is better in terms of BER.

5.4. Noncoherent Demodulation and Error Probability

When carrier synchronization is difficult or beyond simple system complexity, noncoherent unipolar MASK can be used. The noncoherent demodulator is the same as that for OOK in Fig. 3c except that the threshold detector must have multiple thresholds. The thresholds and symbol error probability for noncoherent demodulation of the unipolar uniformly spaced MASK in AWGN channel has been derived [6]. We summarize the derivation here and present the results.

Recall that the unipolar uniformly spaced MASK signal set is $(0, A, 2A, \dots, (M-1)A)$. When the amplitude $A_0 = 0$ is transmitted, the output of the envelope detector (Fig. 4), denoted as η , has Rayleigh distribution (the first probability density function (pdf) in Fig. 11). An error will occur if the envelope η has a value greater than the threshold γ . The probability of error for this case will be

$$p(e|A_0) = \int_{\gamma}^{\infty} \frac{\eta}{\sigma^2} \exp\left(-\frac{\eta^2}{2\sigma^2}\right) d\eta$$

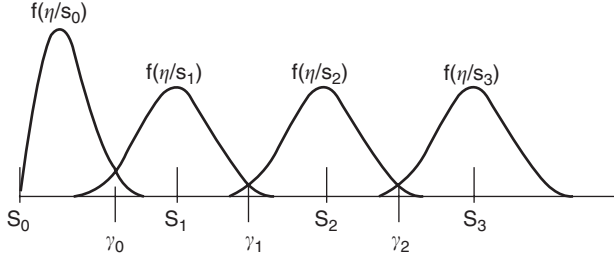


Figure 11. Threshold and decision regions for unipolar noncoherent MASK ($M=4$).

where $\sigma^2 = N_0/2$ is the variance² of the AWGN [1,7]. At high signal-to-noise ratio, the optimum threshold (γ_0) can be closely approximated by $\sqrt{E_{\min}}/2$ [8], where $E_{\min} = A^2 T/2$ is the energy of the symbol with the minimum non-zero amplitude. Therefore

$$p(e|A_0) = \exp\left(-\frac{E_{\min}}{4N_0}\right)$$

The other case that should be considered separately is the case when the symbol A_{M-1} is transmitted (see the last pdf in Fig. 11). In this case, the probability density function of the envelope η is Rician and is centered at $(M-1)\sqrt{E_{\min}}$. An error will occur if the value of the envelope η has a value less than the threshold. At high signal-to-noise ratio, the Rician distribution is closely approximated by a Gaussian distribution [8]. Using the Gaussian approximation, the probability of error for this case will be

$$p(e|A_{M-1}) \approx \int_{-\infty}^{\gamma_{M-2}} \frac{1}{\sigma\sqrt{2\pi}} \exp\left[-\frac{(\eta - (M-1)\sqrt{E_{\min}})^2}{2\sigma^2}\right] d\eta$$

Since we have used the Gaussian approximation, the threshold will be taken as the intersection of the adjacent probability density functions $p(\eta|A_{M-1})$ and $p(\eta|A_{M-2})$, that is, $\gamma_{M-2} = (M-1.5)\sqrt{E_{\min}}$, then

$$p(e|A_{M-1}) \approx Q\left(\sqrt{\frac{E_{\min}}{2N_0}}\right)$$

All other transmitted symbols have the same Rician distribution with different means. Because of the equal spacing of these signals and their thresholds, they have equal probability of error. Regardless of what symbol was transmitted, we can assume that the Rician pdf is centered at the zero point and an error will occur if η exceeds the upper or lower threshold, that is, if $\eta > \sqrt{E_{\min}}/2$ or $\eta < -\sqrt{E_{\min}}/2$. Since the Gaussian approximation has symmetric pdf around its mean, the average probability

²The envelope detector must be a quadrature receiver with orthonormal reference carriers.

of error can be expressed as

$$\begin{aligned} p(e|A_i) &\approx 2 \int_{\gamma_i}^{\infty} \frac{1}{\sigma\sqrt{2\pi}} \exp\left(-\frac{\eta^2}{2\sigma^2}\right) d\eta \\ &= 2Q\left(\sqrt{\frac{E_{\min}}{2N_0}}\right), \quad i=1, \dots, M-2 \end{aligned}$$

Multiplying the three conditional probabilities by $(1/M)$, $(1/M)$ and $[(M-2)/M]$, respectively, and adding them will give

$$P_s = \frac{1}{M} \left[\exp\left(-\frac{E_{\min}}{4N_0}\right) + (2M-3)Q\left(\sqrt{\frac{E_{\min}}{2N_0}}\right) \right]$$

The average symbol energy E_s is related to the minimum symbol energy by

$$\begin{aligned} E_s &= \frac{1}{M} \sum_{i=1}^M E_i = \frac{1}{M} \sum_{i=1}^M (i-1)^2 \left(A^2 \frac{T}{2}\right) = \frac{1}{M} \sum_{j=0}^{M-1} j^2 \left(A^2 \frac{T}{2}\right) \\ &= \frac{1}{6} (2M^2 - 3M + 1) \left(A^2 \frac{T}{2}\right) = \frac{1}{6} (2M^2 - 3M + 1) E_{\min} \end{aligned}$$

or

$$E_{\min} = \frac{6E_s}{2M^2 - 3M + 1} = 2B_M E_s$$

where

$$B_M = \frac{3}{2M^2 - 3M + 1} \quad (35)$$

This equation can be written in terms of E_s/N_0 using the following equation

$$P_s = \frac{1}{M} \left[\exp\left(-\frac{E_s}{2N_0} B_M\right) + (2M-3)Q\left(\sqrt{\frac{E_s}{N_0} B_M}\right) \right] \quad (36)$$

or in terms of E_b/N_0

$$\begin{aligned} P_s &= \frac{1}{M} \left[\exp\left(-\frac{1}{2} (\log_2 M) B_M \frac{E_b}{N_0}\right) \right. \\ &\quad \left. + (2M-3)Q\left(\sqrt{(\log_2 M) B_M \frac{E_b}{N_0}}\right) \right] \end{aligned} \quad (37)$$

where E_b is the average energy per bit. When $M=2$, the above reduces to the P_b expression for OOK (6). Figure 12 shows the symbol error probability given above for noncoherent demodulation (dotted lines), together with those for coherent demodulation. From the figure we can see that the noncoherent demodulation incurs a small performance degradation. When M is high, the degradation is negligible.

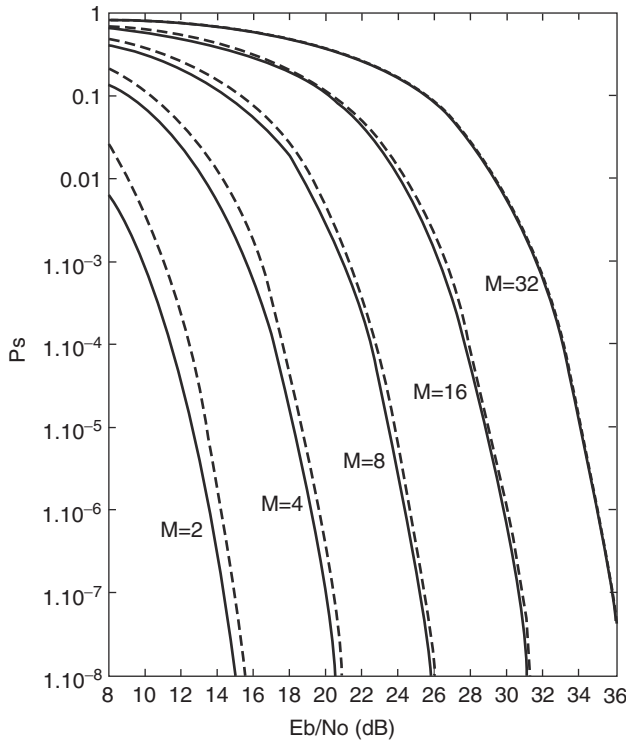


Figure 12. Symbol error probability of unipolar uniformly spaced MASK: solid line—coherently demodulated; dotted line—noncoherently demodulated.

6. COMPARISON WITH MPSK

For the same symbol rate and the pulshape, MPSK and MASK have the same PSD and hence the same bandwidth. Thus it makes sense to compare their BER performances.

In comparison to MPSK, starting from $M = 4$, the error probability of bipolar MASK is inferior to that of the MPSK. The P_s of the MPSK is given by [1, (4.24)]

$$P_s \approx 2Q\left(\sqrt{\frac{2E_s}{N_0}} \sin \frac{\pi}{M}\right) \tag{38}$$

Comparing (38) and (27), the ratio (MASK over MPSK) of the arguments inside the square root sign of the Q function is

$$R_M = \frac{3}{(M^2 - 1) \sin^2 \frac{\pi}{M}} \tag{39}$$

and is tabulated in Table 2. If $M \geq 32$ the degradation is constantly 5.17 dB. This is easily seen from (39). For

Table 2. Power Penalty of MASK over MPSK

M	2	4	8	16	32	64	128
$R(M)$	1	0.4	0.325	0.309	0.305	0.304	0.304
$10 \log R(M)$ (dB)	0	-3.98	-4.88	-5.10	-5.16	-5.17	-5.17

large M , $\sin \pi/M \cong \pi/M$, and $R_M \cong 3/\pi^2 \cong 0.304$. Another fact is that in both bipolar MASK and MPSK, for the same error probability, the power increase is 6 dB for doubling M for large M . This means in terms of increasing bandwidth efficiency with increased M , both schemes pay the same penalty in BER performance. However, MASK still has a fixed 5.17 dB disadvantage against MPSK. This shows MASK is inferior to MPSK in terms of error probability. However, we will see that going to two-dimensional MASK, namely, QAM, improves error rate performance significantly. As a result, QAM is superior to MPSK when $M > 4$. We will briefly discuss QAM in the next section.

7. ADVANCED MODULATIONS RELATED TO ASK

Two important modulations arise from ASK. One is the quadrature amplitude modulation or QAM. Another is the ASK-OFDM (orthogonal frequency division multiplexing).

QAM is constructed by adding two MASK signals together as below [$p(t)$ is pulshape]

$$s_i(t) = A_{i1}p(t) \cos 2\pi f_c t - A_{i2}p(t) \sin 2\pi f_c t$$

As can be seen, the second carrier is a sine function that is orthogonal to the first carrier. The first component is the in-phase or I component, and the second component is the quadrature or Q component. The system complexity of QAM doubles that of MASK since it requires I and Q branches in its modulator and demodulator. However, the BER performance of QAM is much better than MASK. In fact, the BER performance of an M -ary QAM is exactly the same as that of a \sqrt{M} -ary MASK whose bandwidth efficiency is only half that of QAM [13]. Also the BER performance of an M -ary QAM is even better than that of MPSK when $M > 4$. For example, for the same BER, the MPSK needs 1.65, 4.20, and 7.02 dB more SNR for $M = 8, 16,$ and 32 , respectively [1].

Orthogonal frequency-division multiplexing is a bandwidth-efficient multiple-carrier modulation scheme, especially good for frequency-selective fading channels, where data are separated into N datastreams. Each of them modulates a subcarrier. Then these N modulated signals are summed to form the final signal, which in turn modulates a higher-frequency carrier for transmission. The common modulations used in OFDM are QAM or MPSK [9]. Noncoherent OOK or MASK were also proposed to be used in frequency-hopping multiple-access system since carrier synchronization is difficult in such system [11,12]. An OFDM scheme that uses QAM or MPSK or noncoherent MASK (including OOK) requires that the N subcarriers be separated in frequency by $1/T$ for them to be orthogonal to each other so that they can be separated in the demodulator. These types of OFDM can be conveniently implemented by the pair of inverse fast Fourier transform (IFFT) for modulation and FFT for demodulation [10]. MASK-OFDM has been proposed [13], where coherent MASK is used for modulation that requires a frequency separation of only $1/2 T$ and can be conveniently implemented by the pair of fast cosine transform (FCT)

and inverse FCT (IFCT) for modulation and demodulation, respectively. Since the BER performance of MASK is inferior to that of QAM, the order of the MASK has to be reduced to \sqrt{M} to match the BER performance of QAM. By doing so, the bandwidth advantage of MASK-OFDM is lost. However, the system complexity of MASK-OFDM is reduced in comparison to that of QAM-OFDM.

BIBLIOGRAPHY

1. F. Xiong, *Digital Modulation Techniques*, Artech House, Boston/London, 2000.
2. J. G. Proakis, *Digital Communications*, 2nd Ed., New York: McGraw-Hill, 1989.
3. S. Haykin, *Digital Communications*, Wiley, New York, 1988.
4. H. L. Van Trees, *Detection, Estimation, and Modulation Theory, Part I*, Wiley, New York, 1968.
5. F. G. Stremmler, *Introduction to Communication Systems*, 3rd Ed., Addison-Wesley, 1990.
6. A. J. Al-Dweik and F. Xiong, Frequency-hopped multiple-access communication with noncoherent OFDM-MASK in AWGN channels, *Int. Conf. Military Communications (MIL-COM) 2001*, McLean, VA, Oct. 28–31 2001.
7. A. D. Whalen, *Detection of Signals in Noise*, Academic Press, 1971.
8. R. E. Ziemer and W. H. Tranter, *Principles of Communications*, Houghton-Mifflin, 1985.
9. A. R. S. Bahai and B. R. Saltzberg, *Multi-Carrier Digital Communications, Theory and Applications of OFDM*, Kluwer/Plenum, 1999.
10. S. B. Weinstein and P. M. Ebert, Data transmission by frequency division multiplexing using the discrete Fourier transform, *IEEE Trans. Commun.* **19**(5): 628–634 (Oct. 1971).
11. S. H. Kim and S. W. Kim, Frequency-hopped multiple-access communication with multicarrier on-off keying in Rayleigh fading channels, *IEEE Trans. Commun.* **48**(10): 1692–1701 (Oct. 2000).
12. A. Al-Dweik and F. Xiong, FHMA communication with noncoherent OFDM-ASK in AWGN channels, *IEEE Trans. Commun.* **51**(1): 33–36 (Jan. 2003).
13. F. Xiong, M-ary amplitude shift keying OFDM system, *IEEE Trans. Commun.* **51**(10): 1638–1642 (Oct. 2003).

ANALYTICAL AND ADAPTIVE MODELING OF NONLINEAR HIGH-POWER AMPLIFIERS

MOHAMED IBNKAHLA
Queen's University
Kingston, Ontario, Canada

1. INTRODUCTION

Communication channels are equipped with high-power amplifiers (HPA), which are used to amplify the transmit-

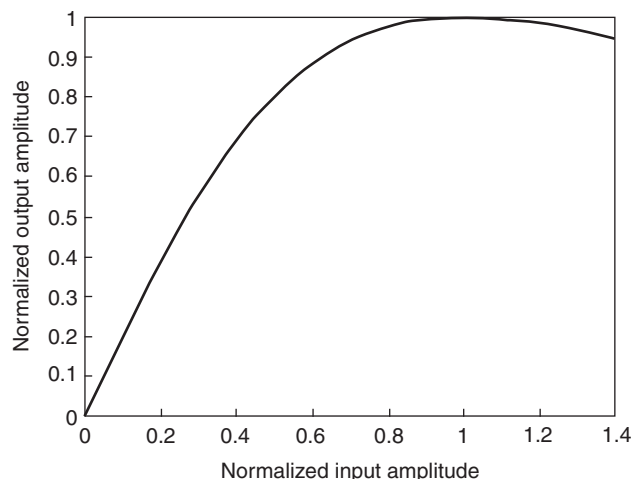


Figure 1. Example of amplitude conversion of a TWT amplifier.

ted signal in order to reach an acceptable signal-to-noise ratio (SNR). In general, these amplifiers have nonlinear characteristics. For example, traveling-wave-tube (TWT) amplifiers (see examples of amplitude and phase conversions in TWT amplifiers in Figs. 1 and 2, respectively) and solid-state power (SSP) amplifiers are widely used in satellite communications for their excellent power efficiency [15]. However, these amplifiers cause nonlinear distortions to the transmitted signals, due to their nonlinear behavior.

For low input levels, the output power of a nonlinear HPA is essentially a linear function of the input power. As the input drive increases, the output power increases nonlinearly until the point of maximum power output is reached. Beyond this point (referred to as “saturation”), any additional increase in the input power level does not result in an additional increase in output power (see, e.g., Fig. 1). The operating point of the TWT is usually given in terms of input or output backoff from saturation. Generally, an amplifier will be most efficient when it operates at or near saturation.

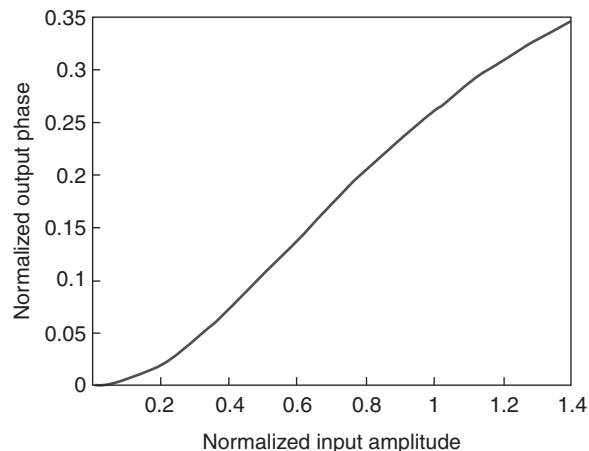


Figure 2. Example of phase conversion of a TWT amplifier.

The closer an amplifier is driven to saturation, the greater the amount of distortion it produces. Distortion may also be produced in the phase, which may change nonlinearly with the input power level.

HPA modeling serves a variety of purposes. For example, if the required measured physical data are unavailable, an analytical model is desirable. This model can be used in order to run computer simulations that measure a variety of signal and channel configurations without imposing instrumentation limitations. The analytical expressions derived by the model can be used in order to conduct performance analysis of the communication channel, to study the efficiency of the design through computer simulations, or to optimize the channel resources over various amplifier and channel conditions. Moreover, analytical models can be used in order to design and optimize the different parts of the transmitter and the receiver, such as modulation scheme and predistortion technique at the transmitter; and demodulation scheme, detection device, and equalization algorithm at the receiver. This article presents a survey of nonlinear amplifier models, including memoryless amplifiers and amplifiers with memory. There is a special focus on adaptive neural network (NN) approaches.

2. NONLINEAR MEMORYLESS HIGH-POWER AMPLIFIERS

2.1. Signal Representation

TWT amplifiers exhibit two nonlinear conversions: amplitude-to-amplitude (AM/AM) and amplitude-to-phase (AM/PM) conversions. Two equivalent frequency-independent representations have been proposed for these nonlinearities: amplitude–phase (A-P) representation and in-phase – quadrature (I-Q) representation [24].

Let the TWT input wave be expressed as

$$x(t) = r(t) \cos(\omega_0 t + \phi_0) \quad (1)$$

where ω_0 is the carrier frequency and $r(t)$ and ϕ_0 are the input signal amplitude and phase, respectively.

For the A-P representation, the output signal is expressed as

$$y(t) = A(r(t)) \cos(\omega_0 t + \phi(r(t)) + \phi_0) \quad (2)$$

where $A(r)$ and $\phi(r)$ are the AM/AM and AM/PM conversions, respectively.

For the I-Q representation, the output signal is represented by its in-phase and quadrature components

$$p(t) = P(r(t)) \cos(\omega_0 t + \phi_0) \quad (3)$$

$$q(t) = -Q(r(t)) \sin(\omega_0 t + \phi_0) \quad (4)$$

where $P(r)$ and $Q(r)$ are the in-phase and quadrature conversions, respectively. These can be shown from the

AM/AM and AM/PM conversions to be:

$$P(r) = A(r) \cos(\phi(r)) \quad (5)$$

$$Q(r) = A(r) \sin(\phi(r)) \quad (6)$$

2.2. Nonlinear Distortion Effect on Digitally Modulated Signals

When the input signal is digitally modulated, the HPA nonlinearity rotates the signal constellation. This causes an alteration in the decision region. Figure 3 displays the effect of nonlinearity on the constellation of a 16-quadrature amplitude modulation (16-QAM) signal. The decision regions are used by the receiver to decode the received symbols. If a received symbol falls in the decision region of a certain constellation point, then the receiver decides that the transmitted symbol is that particular constellation point.

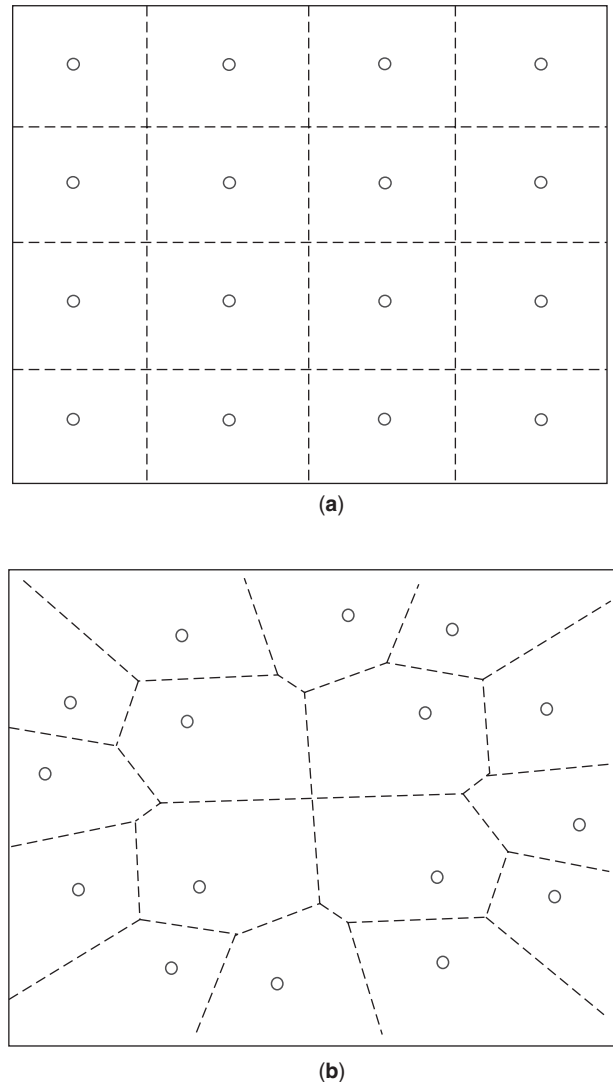


Figure 3. TWT input (a) and output (b) constellations with amplifier working close to saturation.

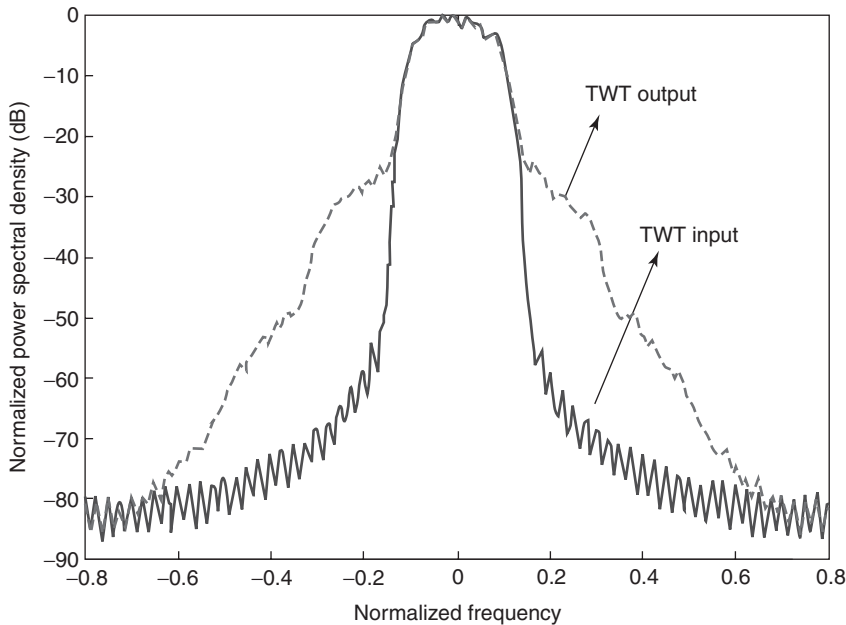


Figure 4. Example of spectral regrowth generated by a TWT amplifier.

When the decision regions are distorted, the receiver can no longer use the ideal decision regions of the transmitted constellation in order to decode the received signal. The receiver must know the constellation at the output of the amplifier, which is difficult since the characteristics and the operating point of the amplifier may change. Moreover, as can be seen in Fig. 3b, some symbols become closer to each other in the distorted constellation, leading to an increase in the symbol error rate (SER).

2.3. Intermodulation Distortions and Spectral Regrowth

Another major consequence of amplifier nonlinearities is the generation of intermodulation distortion (IMD) products [17]. IMD products are located at frequencies above and below those of the input carriers, and at frequency intervals equal to separations between input carriers. IMD products cannot be easily eliminated through filtering, as they are located close to the desired input signal bandwidth. IMD products not only corrupt the amplified signal itself but also cause adjacent-channel interference due to spectral regrowth (Fig. 4), which is more serious because it acts as interference to the adjacent channels. This interference is tightly controlled by the communications standards being used, and must be reduced to the allowable limit. Thus, this phenomenon has a direct impact on the system capacity and performance.

Distortion is most often evaluated in terms of the ratio of the carrier to the third-order IMD products (i.e., IMD terms closest to the carrier). IMD terms can also be non-symmetric. This imbalance is due to the presence of both amplitude- and phase-induced IMD products [17].

Interference produced in the adjacent channel is characterized by the adjacent-channel power ratio (ACPR), which is the power in the main channel divided by the power in the lower plus upper adjacent channels [25].

HPA amplifier design depends on tradeoffs between three main performance indicators: output power, efficiency, and sideband regrowth. However, a certain amount of power amplifier nonlinearity has to be accepted in order to guarantee satisfactory amplifier efficiency.

Moreover, these amplifiers not only are nonlinear, but also can possess memory. If the reciprocal of the bandwidth of the input signal is much larger than the memory of the amplifier (as is the case for most amplifiers driven with narrowband signals), then the amplifier can be modeled as memoryless for that particular input signal. This means that the output is a function of the input at the present time only.

An accurate and verified simulation model for an HPA is required to reliably study the effects of the nonlinearity on the system level, and to give an insight into the problem of finding an appropriate tradeoff between power amplifier efficiency and system capacity. Therefore, an optimal operating point is imperative in order to maximize the output power and minimize the degradation due to distortions.

2.4. Amplifier Backoff

Backoff (BO) defines how far the HPA is operating from the saturation point. The *input saturation power* is defined as the maximum power that can be provided by the amplifier with the highest efficiency. Beyond saturation, the amplifier has no more gain in power. There are two ways of defining backoff: (1) relative to the input [input backoff (IBO)] and (2) relative to the output [output backoff (OBO)]. IBO is the ratio of the saturation power to the desired drive (input) power. OBO is the ratio of the saturation power to the actual output power. Increasing the IBO or OBO reduces nonlinear distortions, but also leads to less output power.

3. ANALYTICAL MODELS

Considerable work has been done in the literature for developing analytical expressions of TWT characteristics. The analytical models have been categorized based on the form of the mathematical representation to elucidate the general characteristics of the models falling in each category.

3.1. Power Series

The power series representation is one of the most commonly used methods to represent nonlinear devices because it identifies the contribution of different power terms. Since the AM/AM conversion, $A(r)$, is an odd function of r , and the AM/PM conversion, $\phi(r)$, is an even function, the following expansion is generally assumed

$$A(r) = \sum_{m=0}^{\infty} a_m r^{2m+1} \quad (7)$$

$$\phi(r) = \sum_{m=0}^{\infty} p_m r^{2m} \quad (8)$$

where parameters $\{a_m\}$ and $\{p_m\}$ have to be determined (e.g., through an optimization procedure).

The power series or Taylor expression must be used with some caution because the series may not converge for all values and sometimes converges slowly. The series requires a large number of terms and heavy computation. The power series model can closely approximate the amplifier curve for a limited range. A common drawback with this model is the explosion of the predicted variable magnitude. This occurs when large values are assigned to some predictions. This type of behavior necessitates the censoring of the predicted variable value. Hence, it is difficult to test strong nonlinearities in simulation when there is a very large envelope variation in the input signal.

The classic work using this model was performed by Chapman and Millard [4]. They accounted for the effect of the AM/PM conversion, which was represented by a single constant coefficient k determined through a measured technique:

$$\phi(r) = kr^2 \quad (9)$$

This relation does not hold over the complete operating region of the TWT amplifier.

Medhurst and Roberts [21] proposed a representation of the AM/AM characteristic by using the sum of the linear and cubic terms and used a two-tone test for verification:

$$y(t) = a_1 x(t) + a_3 x^3(t) \quad (10)$$

3.2. Softlimiter Approach

The input/output relationship can simply be modeled as an ideal softlimiter that has two distinct regions: the perfect linear region and the saturation region. However, the linear region of a practical TWT amplifier is not as perfectly linear as that of the soft limiter. Moreover, this representation does not give a completely realistic model

of the TWT. The limitation of this model is that it requires the envelope amplitude function $A(r)$ not to fall off beyond saturation.

3.3. Exponential Expression

Berman and Mahle [2] gave a three-parameter analytical expression of the AM/PM conversion, which gives reasonably good agreement over the whole range, especially for small input power and above saturation

$$\phi(r) = k_1(1 - \exp(-k_2 r^2)) + k_3 r^2 \quad (11)$$

where k_1 , k_2 , k_3 are the TWT constants obtained from a measured transfer characteristic by a cut-and-dry method or by an optimization routine. The slope for zero input power is given by $2k_1 k_2$. Moreover, for a large input signal power, $\phi(r)$ approaches $k_3 r^2$.

Thomas et al. [27] proposed a four-parameter formula for $A(r)$. The amplitude nonlinearity was analytically modeled by fitting the single-carrier input/output power data with a portion of cosine centered around saturation. This leads to the following function representation

$$A(r) = \begin{cases} 10^{\alpha[\cos(\log_{10}(r/r_s)/\beta)-1]}, & r > r_s \\ r, & r < r_s \end{cases} \quad (12)$$

where r_s is the input saturation power and α and β are constants chosen to fit the data that can be calculated through optimization routines.

3.4. Error Function

The error function closely follows the AM-AM characteristics of a typical TWT amplifier. However, this approach can result in higher error for different amplifiers which may not follow the typical characteristic closely. Pawula [22] presented the input-output relationship of nonlinearity by an error function characteristic using

$$A(r) = \alpha \sqrt{\frac{\pi}{2}} \operatorname{erf}\left(\frac{r}{\beta}\right) \quad (13)$$

where α is the gain parameter and β is the limiter parameter.

3.5. Bessel Functions

The Bessel function was also considered for analytical modeling because of its analytical and numerical convenience as it simplifies the calculation of the output spectrum. However, it requires a large number of terms to fit the measured data.

Kaye et al. [18] came up with the quadrature model and used a sum of Bessel functions of the first kind of order 1. In order to compute the power spectra of the outputs of the nonlinearities in the I-Q representation, they suggested to represent them by a convergent series of functions that are, on one hand, simple to determine from the measured data and, on the other hand, convenient for the power spectrum calculations. This model is

expressed as

$$P(r)[\text{or } Q(r)] = \sqrt{2} \sum_{m=1}^L b_m J_1 \left(\frac{\sqrt{2}r(2m-1)\pi}{R} \right), \quad (14)$$

$$r \leq \frac{R}{2\sqrt{2}}$$

where $J_1(\cdot)$ is the Bessel function of the first kind of order 1.

Simbo and Potano [26] used a complex Bessel function expansion to simultaneously account for the AM/AM and AM/PM conversion of the TWT. Group delay and amplitude variation preceding the input of the nonlinear device was modeled using a Fourier series expression. However, the function has a high computational complexity for the calculation of the coefficients:

$$A(r)e^{j\phi(r)} = \sum_{m=1}^L b_k J_1(\alpha m r) \quad (15)$$

where $\{b_m\}$ are complex coefficients, and α is a constant that scales the input level.

For the I-Q representation, Hetrakul and Taylor [9] proposed two-parameter formulas using a modified Bessel function of the first kind

$$P(r) = C_1 r e^{-C_2 r^2} J_0(C_2 r^2) \quad (16)$$

$$Q(r) = S_1 r e^{-S_2 r^2} J_1(S_2 r^2) \quad (17)$$

where, $J_k(\cdot)$ is the modified Bessel function of the first kind of order k . The coefficients C_1, C_2, S_1, S_2 are computed from a conventional optimization subroutine, so as to yield the least-squares fit to the actual measured data. The Bessel function approximation needs four coefficients to give a good fit to the TWT nonlinearity, up to and beyond saturation. Note that for large input power values, the formulas approach certain constants.

3.6. Rational Functions: Saleh's Model

A very comprehensive work was published by Saleh [24] for both A-P and I-Q representations. The model presented by Saleh is widely used in the literature. It is a frequency-independent model and can be made frequency-dependent by adding filters that reflect the frequency selectivity:

A-P Representation. The AM/AM and AM/PM curves are modeled as

$$A(r) = \frac{\alpha_a r}{1 + \beta_a r^2} \quad (18)$$

$$\phi(r) = \frac{\alpha_p r^2}{1 + \beta_p r^2} \quad (19)$$

Note that for a large value of r , $A(r)$ is proportional to $1/r$ and $\phi(r)$ approaches a constant.

I-Q Representation. The in-phase and quadrature curves are modeled as follows:

$$P(r) = \frac{\alpha_P r}{1 + \beta_P r^2} \quad (20)$$

$$Q(r) = \frac{\alpha_Q r^3}{(1 + \beta_Q r^2)^2} \quad (21)$$

Note that for a large value of r , both $P(r)$ and $Q(r)$ are proportional to $\frac{1}{r}$.

Saleh used a minimum mean-square-error (MMSE) procedure for fitting the formulas to the experimental data. With only two parameters, this is the most widely used model for TWT amplifiers in the literature. Note that, for high input power signals, $A(r)$ and $\phi(r)$ approach $\alpha_a/\beta_a r$ and α_p/β_p , respectively. Therefore, this model is suited for amplifiers that have these specific asymptotic behaviors.

4. NEURAL NETWORKS FOR MODELING MEMORYLESS TWT AMPLIFIERS

This section employs multilayer neural networks [8] to model TWT amplifiers. The main advantage of NN models over classical models is that they offer better MSE approximation performance than do classical TWT models [12]. NNs are adaptive, which makes them appropriate for online modeling. Classical models are based on offline optimization procedures that do not allow online modeling. Moreover, NNs can model a variety of nonlinear amplifiers using the same parametrized structure (e.g., a structure with five neurons). Only the NN weight values change from one TWT model to another. On the contrary, most classical models have been designed for specific families of TWT amplifiers (e.g., TWTs having a given asymptotic behavior). Therefore, they may not always be appropriate for emerging generations of TWT and SSP amplifiers.

4.1. NN Structure and Learning Algorithms:

Figure 5 shows the modeling scheme of a TWT characteristic using a two-layer neural network (NN) [10]. The NN has a scalar input, M neurons in the first layer, and a scalar output. A set of input-output data (collected from the physical TWT measurements, or from the transmission channel input-output signals) is presented to the NN. The network output at time n is expressed as

$$s(n) = \sum_{k=1}^M c_k f(w_k x(n) + b_k) \quad (22)$$

where $x(n)$ is the input sample at time n and f is the activation function (which is taken in this article as the hyperbolic tangent function); $\{w_k\}$, $\{b_k\}$, and $\{c_k\}$, $k = 1, \dots, M$, are the NN weights. We denote the vector containing the network weights by θ : $\theta = [w_1, \dots, w_M, b_1, \dots, b_M, c_1, \dots, c_M]^T$ where $(\cdot)^T$ denotes the transpose.

To perform the modeling task, the NN weights are updated using a learning algorithm that minimizes the squared error between the TWT output and the NN outputs

$$J(n) = \frac{1}{2} \|e(n)\|^2 \quad (23)$$

where

$$e(n) = y(n) + N_0(n) - s(n) \quad (24)$$

where $y(n)$ is the TWT output and $N_0(n)$ is a zero-mean white Gaussian noise with variance σ^2 .

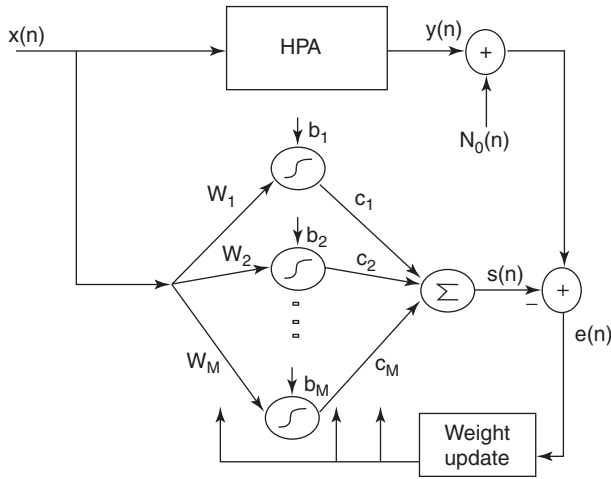


Figure 5. NN adaptive modeling of a nonlinear TWT amplifier.

In the following, we present two approaches to update the NN weights: the classical backpropagation (BP) algorithm and natural gradient (NG) algorithm.

The BP algorithm follows the ordinary gradient descent to update the weight vector θ :

$$\theta(n+1) = \theta(n) - \mu \nabla_{\theta}(J(n)) \quad (25)$$

where μ is a small positive constant, and ∇_{θ} is the ordinary gradient with respect to θ :

$$\nabla_{\theta}(J(n)) = -e(n) \cdot \nabla_{\theta} s(n) \quad (26)$$

$$= -e(n) \cdot \begin{pmatrix} x(n)c_1 f'(w_1 x(n) + b_1) \\ \vdots \\ x(n)c_M f'(w_M x(n) + b_M) \\ f(w_1 x(n) + b_1) \\ \vdots \\ f(w_M x(n) + b_M) \\ c_1 f'(w_1 x(n) + b_1) \\ \vdots \\ c_M f'(w_M x(n) + b_M) \end{pmatrix}$$

The NG algorithm follows the steepest-descent direction of the loss function, which is given by [1]

$$-\tilde{\nabla}_{\theta} J(n) = -G^{-1} \nabla_{\theta} J(n) \quad (27)$$

where G^{-1} is the inverse of the Fisher information matrix (FIM):

$$G = [g_{ij}(\theta)] = \left[E \left(\frac{\partial J(n)}{\partial \theta_i} \frac{\partial J(n)}{\partial \theta_j} \right) \right] \quad (28)$$

Therefore, the NG algorithm adjusts the NN weights as follows:

$$\theta(n+1) = \theta(n) - \mu G^{-1} \nabla_{\theta}(J(n)) \quad (29)$$

The calculation of the expectations in the FIM requires knowledge of the probability distribution functions (pdf values) of x and s , which are not always available. Moreover, the calculation of the inverse of the FIM is computationally very costly. A modified Kalman filter technique has been proposed [1] for an online estimation of the FIM inverse

$$\hat{G}^{-1}(n+1) = (1 + \varepsilon_n) \hat{G}^{-1}(n) - \varepsilon_n \hat{G}^{-1}(n) \nabla_{\theta} s(n) (\nabla_{\theta} s(n))^t \hat{G}^{-1}(n) \quad (30)$$

where $\nabla_{\theta} s(n)$ is the ordinary gradient of s [see Eq. (26)], and ε_n is a positive updating rate. The choice of ε_n depends on how fast/stable the algorithm is desired to be. For example, if $\varepsilon_n = c_e/n$ (where c_e is a small positive constant), then Kalman filtering is equivalent to an online calculation of the arithmetic mean. However, when ε_n is a constant, the convergence is faster but the algorithm may be less stable.

In order to reach a good tradeoff between convergence speed and stability, we will use a search-and-converge method in which ε_n is defined by

$$\varepsilon_n = \frac{\varepsilon_0 + \frac{c_e n}{\tau}}{1 + \frac{c_e n}{\tau \varepsilon_0} + \frac{n^2}{\tau}} \quad (31)$$

where τ is a positive time constant, and ε_0 is a small positive constant. Here, small n corresponds to a “search” phase (where ε_n is close to ε_0), and large n corresponds to a “converge” phase (ε_n is equivalent to c_e/n).

Simulation Example 1. Here, a neural network composed of $M = 5$ neurons is used to model the AM/AM characteristic of a TWT amplifier. The NG and the BP algorithms are compared. The simulations show that the value of $\mu = 0.005$ represents a good tradeoff (for each algorithm) between convergence speed and stability. Figure 6a shows the learning curve for each algorithm. It can be seen that the NG descent has a much faster convergence. The resulting MSE approximation performances are 9×10^{-6} and 3.0×10^{-5} for the NG and BP algorithms, respectively. Figure 6b illustrates the resulting AM/AM models and the original TWT input–output data that have been used for learning. Note that, for this amplifier, classical models such as Saleh [24] and Thomas [27] expressions give 1.4×10^{-4} and 2.0×10^{-4} as MSE errors, respectively. Therefore, the NG approach outperforms both the classical models and the BP algorithm. For asymptotic behavior, NN models approach a constant (due to the shape of the neuron activation function), which is desirable in TWT modeling as it ensures stability for high input power fluctuations. The desired asymptotic constant can be included as an additional constraint value during the learning process. Finally, the odd and even BP algorithms can be employed (if needed by the user to ensure strict even

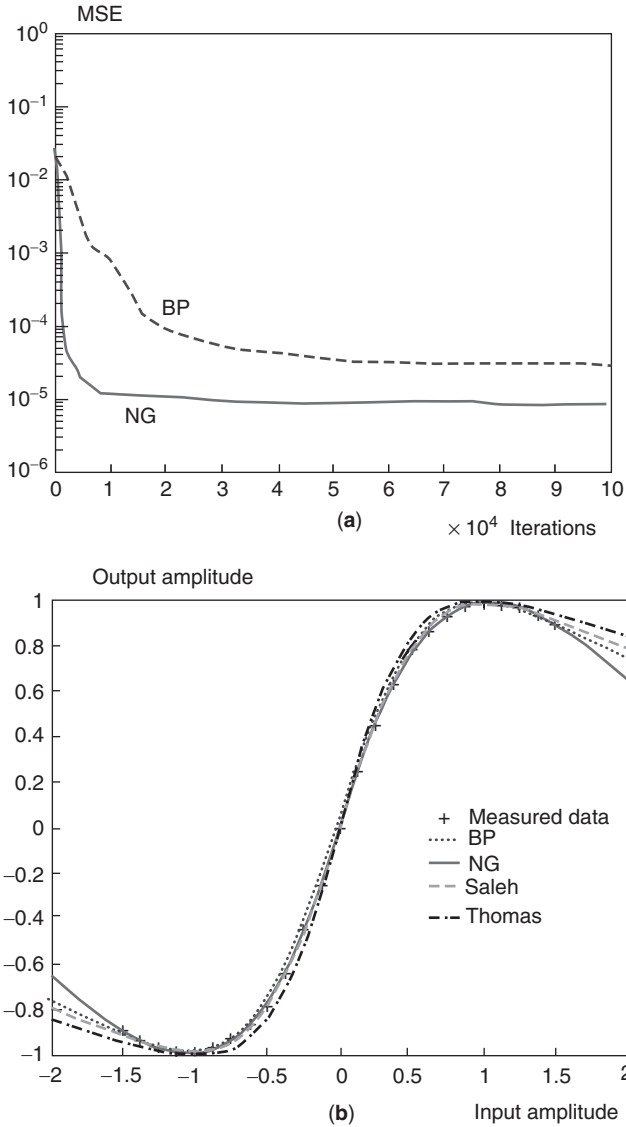


Figure 6. Modeling the AM/AM conversion of Intelsat IV TWT amplifier: (a) learning curves of the BP and NG algorithms; (b) comparison between the different models. (This figure is available in full color at <http://www.mrw.interscience.wiley.com/erfme>.)

or odd characteristics) [10]. See Table 1 for additional computer simulation results.

5. MODELING AND IDENTIFICATION OF NONLINEAR AMPLIFIERS WITH MEMORY

As discussed above, some nonlinear amplifiers may contain a memory that cannot be neglected. Moreover, the

transmission channel may also be considered as a nonlinear system with memory. This is because the uplink and downlink channels may introduce some memory because of thermal and electrical effects, multi-path propagation, or other filtering processes in the channel [15]. Several approaches, including those discussed below, have been proposed in the literature to model nonlinear amplifiers with memory.

5.1. Volterra Model

In the Volterra model, the input-output relationship is expressed as follows

$$\begin{aligned}
 y(t) = & h_0 + \int_{-\infty}^{+\infty} h_1(\tau_1)x(t - \tau_1)d\tau_1 \\
 & + \int_{-\infty}^{+\infty} \int_{-\infty}^{+\infty} h_2(\tau_1, \tau_2)x(t - \tau_1) \\
 & \times x(t - \tau_2)d\tau_1d\tau_2 \\
 & + \int_{-\infty}^{+\infty} \int_{-\infty}^{+\infty} \int_{-\infty}^{+\infty} h_3(\tau_1, \tau_2, \tau_3)x(t - \tau_1) \\
 & \times x(t - \tau_2)x(t - \tau_3)d\tau_1d\tau_2d\tau_3 + \dots
 \end{aligned} \quad (32)$$

where the Volterra kernels $\{h_1(\tau_1), h_2(\tau_1, \tau_2), h_3(\tau_1, \tau_2, \tau_3), \dots\}$ have to be obtained through an optimization or adaptive procedure.

Volterra series can approximate nonlinear amplifier characteristics [3,16,28,30] and predistortion devices [3,6,16] relatively well. The major drawback of this model is its complexity, which increases immensely with the length of the memory and the order of the nonlinearity.

5.2. Wiener Model (Filter-Memoryless Nonlinearity or Two-Box Model)

In this model, the amplifier is modeled by a linear filter followed by a memoryless nonlinearity (Fig. 7). This model is very simple and can provide a good approximation of the memory and the nonlinearity. The characterization of the filter and nonlinearity can be made through adaptive or optimization procedures [11,24].

5.3. Wiener-Hammerstein Model (Three-Box Model)

The amplifier is modeled by a linear filter followed by a memoryless nonlinearity followed by a linear filter (Fig. 8). This model has been shown to accurately predict intermodulation products and yield excellent characterization of several TWT and SSP amplifier behaviors. The different boxes can be determined through measurement and data processing [5], or they can be determined

Table 1. MSE Performance of Different Models for Approximation of I-Q and A-P TWT Characteristics

Characteristic	BP NN	NG NN	Saleh [24]	Hetrakul-Taylor [9]	Thomas et al. [27]	Berman and Mahle [2]
In-phase	6.1×10^{-3}	2.6×10^{-4}	3.20×10^{-3}	3.30×10^{-3}	—	—
Quadrature	6.2×10^{-3}	2.7×10^{-4}	5.20×10^{-4}	1.60×10^{-3}	—	—
AM/AM	3.0×10^{-5}	9.0×10^{-6}	1.40×10^{-4}	—	2.00×10^{-4}	—
AM/PM	8.1×10^{-5}	3.2×10^{-6}	1.38×10^{-4}	—	—	8.00×10^{-4}

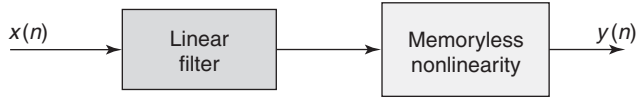


Figure 7. Wiener model.

adaptively (e.g., using neural networks and adaptive filtering) [11]. In this model, a physical interpretation of the different parts of the model can be easily made. This leads to an easy design and optimization of communication system (predistortion, equalization, IMD calculation, etc.).

5.4. Parallel Wiener Model

This model is composed of several parallel Wiener blocks that are summed together to yield the output. These models are more complicated than the two-box and the three-box models, but may yield better accuracy if the nonlinearity is complicated [19].

5.5. Memory Polynomial

The memory polynomial model (see Fig. 9) is composed of a cascade of polynomials separated by unit delays. The output can be expressed in discrete time as

$$y(n) = \sum_{k=0}^L F_k(x(n-k)) \tag{33}$$

where $F_k(x)$ is the k^{th} polynomial.

An extension of this model has been proposed in Ref. 20, allowing the unit delays to be sparse delay taps. This allows longer-time-constant memory effects to be modeled in parallel with short-time-constant effects using fewer parameters. The different parameters in this model can be characterized using an adaptive sliding-window approach.

The following section details the Wiener modeling approach using neural networks and adaptive filtering.

6. WIENER MODELING USING ADAPTIVE FILTERING AND NEURAL NETWORKS

The nonlinear channel to be modeled in this section is a nonlinear Wiener system composed of a linear filter $H(z) = \sum_{k=0}^{N_h-1} h_k z^{-k}$ followed by a zero-memory amplitude nonlinearity $g(\cdot)$ (Fig. 10). The phase nonlinearity is not considered in this section, but it can easily be included in the scheme with small changes to the algorithm [11,13,14].

The nonlinear system output signal is corrupted by a zero-mean additive white Gaussian noise (AWGN) $N_0(n)$. It can be expressed at time n as

$$d(n) = y(n) + N_0(n)$$

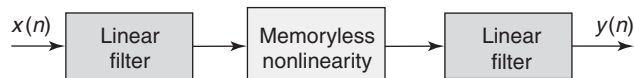


Figure 8. Wiener-Hammerstein model (three-box model).

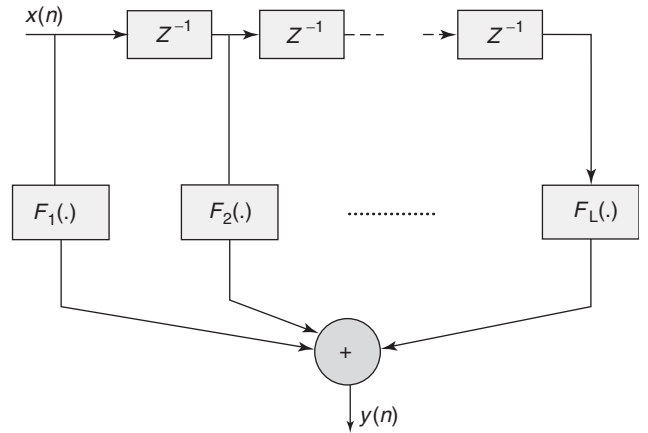


Figure 9. Memory polynomial model.

where

$$y(n) = g\left(\sum_{k=0}^{N_h-1} h_k x(n-k)\right) \tag{34}$$

The NN model (Fig. 10) is composed of an adaptive filter, $Q(z) = \sum_{k=0}^{N_q-1} q_k z^{-k}$, followed by a two-layer (zero-memory) adaptive neural network. The two-layer NN is composed of a scalar (real-valued) input, M neurons in the input layer, and a scalar output.

The adaptive structure has two goals:

1. Identify the linear filter H by the adaptive filter Q .
2. Model the nonlinearity $g(\cdot)$ by the zero-memory nonlinear NN.

The learning is performed by using the input-output signals only (i.e., we consider the unknown nonlinear system as a blackbox).

The NN output at time n is expressed as

$$\begin{aligned} s(n) &= \sum_{k=1}^M c_k f\left(w_k \sum_{i=0}^{N_q-1} q_i x(n-i) + b_k\right) \\ &= \sum_{k=1}^M c_k f(w_k Q^t X(n) + b_k) \end{aligned} \tag{35}$$

where $\{w_k\}$, $\{b_k\}$, and $\{c_k\}$ (where $k=1, \dots, M$) are the NN weights, $Q = [q_0 \ q_1 \ \dots \ q_{N_q-1}]^T$, and $X(n) = [x(n) \ x(n-1) \ \dots \ x(n-N_Q+1)]^T$.

The network and filter parameters are updated in order to minimize the loss function J_n (or squared error) between the system output and the NN output

$$J(n) = \frac{1}{2} \|e(n)\|^2 \tag{36}$$

where

$$e(n) = d(n) - s(n) \tag{37}$$

We denote the system parameter vector to be updated by $\theta = [w_1 w_2 \dots w_M b_1 b_2 \dots b_M c_1 c_2 \dots c_M q_0 q_1 \dots q_{N_q-1}]^T$. The BP and NG approaches that can be used to update the system are

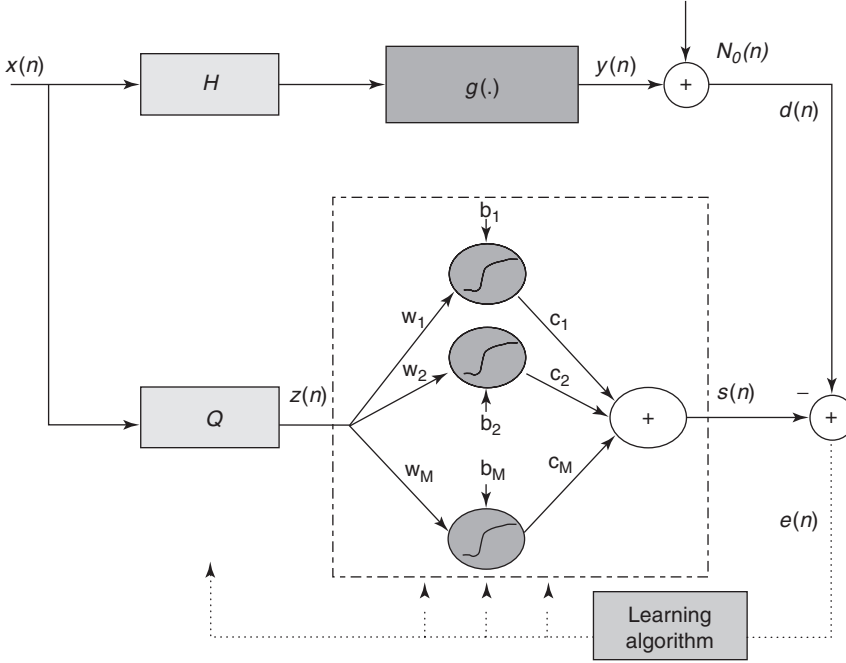


Figure 10. Neural network modeling and identification structure.

BP Algorithm. The BP algorithm updates the weights according to the ordinary gradient descent

$$\theta(n+1) = \theta(n) - \mu \nabla_{\theta} J(n) \quad (38)$$

where μ is a small positive constant, and ∇_{θ} represents the ordinary gradient with respect to vector θ , which is expressed as

$$\nabla_{\theta} J(n) = -e(n) \nabla_{\theta} s(n) \quad (39)$$

where

$$\nabla_{\theta} s(n) = \begin{pmatrix} c_1 \mathbf{Q}^t \mathbf{X}(n) f'(w_1 \mathbf{Q}^t \mathbf{X}(n) + b_1) \\ \vdots \\ c_M \mathbf{Q}^t \mathbf{X}(n) f'(w_M \mathbf{Q}^t \mathbf{X}(n) + b_M) \\ c_1 f'(w_1 \mathbf{Q}^t \mathbf{X}(n) + b_1) \\ \vdots \\ c_M f'(w_M \mathbf{Q}^t \mathbf{X}(n) + b_M) \\ f(w_1 \mathbf{Q}^t \mathbf{X}(n) + b_1) \\ \vdots \\ f(w_M \mathbf{Q}^t \mathbf{X}(n) + b_M) \\ x(n) \sum_{k=1}^M c_k w_k f'(w_k \mathbf{Q}^t \mathbf{X}(n) + b_k) \\ \vdots \\ x(n - N_Q + 1) \sum_{k=1}^M c_k w_k f'(w_k \mathbf{Q}^t \mathbf{X}(n) + b_k) \end{pmatrix} \quad (40)$$

where f' denotes the first derivative of f .

The NG Algorithm. The NN weights are updated according to the NG descent

$$\theta(n+1) = \theta(n) - \mu \tilde{\nabla}_{\theta} J(n) \quad (41)$$

where $\tilde{\nabla}_{\theta}$ represents the NG

$$-\tilde{\nabla}_{\theta} J(n) = -\Gamma^{-1} \nabla_{\theta} J(n)$$

where Γ^{-1} is the FIM inverse:

$$\Gamma = [\gamma_{i,j}] = \left[E \left(\frac{\partial J(n)}{\partial \theta_i} \frac{\partial J(n)}{\partial \theta_j} \right) \right] \quad (42)$$

Here again, the FIM can be approximated online using a modified Kalman technique

$$\hat{\Gamma}^{-1}(n+1) = (1 + \varepsilon_n) \hat{\Gamma}^{-1}(n) - \varepsilon_n \hat{\Gamma}^{-1}(n) \times \nabla_{\theta} s(n) (\nabla_{\theta} s(n))^t \hat{\Gamma}^{-1}(n) \quad (43)$$

where $\nabla_{\theta} s(n)$ is the (ordinary) gradient of $s(n)$ [see Eq. (40)].

Simulation Example 2. For the unknown structure to be identified, the following amplitude nonlinearity is taken:

$$g(x) = \frac{\alpha x}{1 + \beta x^2}, \quad \alpha = 2, \quad \beta = 1$$

The input signal has been taken as a white Gaussian sequence with variance 1 and filter H is taken as $H = [1.49 \ 1.36 \ 1.07 \ 0.67 \ 0.27 \ -0.057 \ -0.263 \ -0.325 \ -0.263 \ -0.125]^T$. The noise variance is $\sigma = 0.002$ and the learning rate is fixed to $\mu = 0.007$.

Filter Q is composed of 10 weights that have been initialized with 0 values. The NN is composed of $M = 5$ neurons. Figure 11 displays the learning curves of the BP and NG algorithms. The NG algorithm is faster and yields a lower MSE than does the BP algorithm (the MSE after

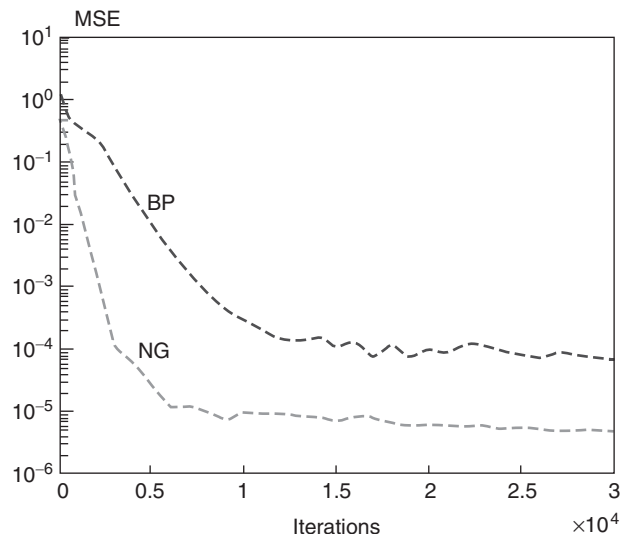


Figure 11. MSE learning curve for identification of the filter nonlinearity model. (This figure is available in full color at <http://www.mrw.interscience.wiley.com/erfme>.)

convergence equals 5×10^{-5} for the NG and 5.5×10^{-4} for the BP).

Figure 12 shows the frequency responses of the exact filter and the models obtained through the BP and NG algorithms, respectively. The frequency responses of the models are scaled versions of the exact filter frequency response. The amplitude conversion model obtained by the memoryless NN compensates for the scaling factor introduced by the adaptive filter. Figure 13 shows the AM/AM curves obtained through the NG and BP algorithms, respectively, which fit very well with the exact nonlinearity.

One major advantage of this NN adaptive approach is that it allows one to identify (or extract) the memoryless nonlinearity and estimate the memory of the amplifier, even in the case where the amplifier is not physically composed of separated blocks (i.e., a linear filter followed by a memoryless nonlinearity).

In Ref. 11, an adaptive structure composed of an adaptive filter, followed by a memoryless NN followed by an adaptive filter, has been used to characterize an SSP amplifier using physical measured data. The adaptive structure was able to extract the amplifier memoryless nonlinearity and characterize its frequency response. See also Refs. 7, 23, and 29 for other NN and adaptive

Figure 12. Filter frequency response: true filter and model. (This figure is available in full color at <http://www.mrw.interscience.wiley.com/erfme>.)

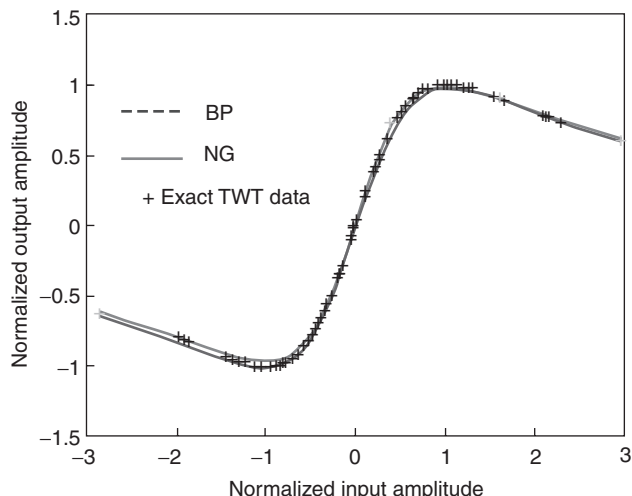
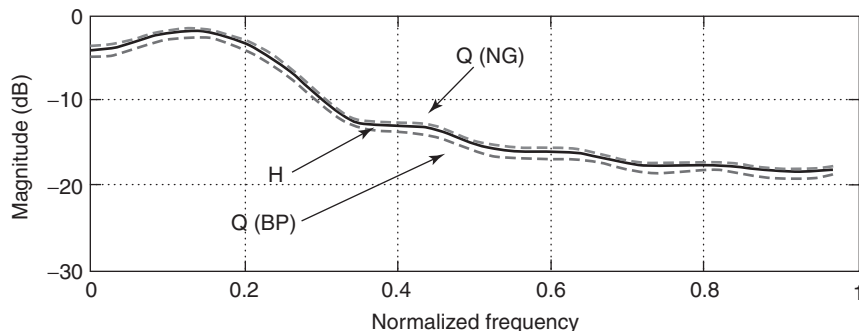


Figure 13. Identification of the memoryless nonlinearity. (This figure is available in full color at <http://www.mrw.interscience.wiley.com/erfme>.)

approaches used to efficiently model, identify, simulate, and characterize nonlinear microwave circuits with memory.

Acknowledgments

This work has been supported in part by the Natural Sciences and Engineering Research Council of Canada (NSERC), the Ontario Premier’s Research Excellence Award (PREA), and Communications Information Technology Ontario (CITO).

BIBLIOGRAPHY

1. S. I. Amari, H. Park, and K. Fukumizu, Adaptive method for realizing natural gradient learning for multi-layer perceptrons, *Neural Comput.* **12**:1399–1409 (2000).
2. A. L. Berman and C. E. Mahle, Nonlinear phase shift in traveling-wave tubes as applied to multiple access communications satellites, *IEEE Trans. Commun. Technol.* **COM-18**(1): 37–48 (Feb. 1970).
3. E. Biglieri, S. Barberis, and M. Catena, Analysis and compensation of nonlinearities in digital transmission systems, *IEEE J. Select. Areas Commun.* **6**:42–50 (Jan. 1988).
4. R. C. Chapman and J. B. Millard, Intelligible crosstalk between frequency modulated carriers through AM-PM conversion, *IEEE Trans. Commun. Syst.* **CS-12**:160–166 (June 1964).

5. C. J. Clark, C. P. Silva, A. A. Moulthrop, and M. S. Muha, Power-amplifier characterization using a two-tone measurement technique, *IEEE Trans. Microwave Theory Techn.* **50**(6):1590–1602 (June 2002).
6. A. D'Andrea, V. Lottici, and R. Reggiannini, RF power amplifier linearization through amplitude and phase predistortion, *IEEE Trans. Commun.* **44**(11), (Nov. 1996).
7. X. Ding, V. K. Devabhaktuni, B. Chattaraj, M. C. E. Yagoub, M. Deo, J. Xu, and Q. J. Zhang, Neural-network approaches to electromagnetic-based modeling of passive components and their applications to high-frequency and high-speed nonlinear circuit optimization, *IEEE Trans. Microwave Theory Techn.* **52**(1):436–449 (Jan. 2004).
8. S. Haykin, *Neural Networks: A Comprehensive Foundation*, IEEE Press, 1997.
9. P. Hetrakul and D. P. Taylor, The effects of nonlinearity on binary CPSK signal transmission, *IEEE Trans. Commun.* **COM-24**:546–553 (May 1976).
10. M. Ibnkahla, J. Sombrin, F. Castanié, and N. J. Bershad, Neural networks for modeling non linear memoryless channels, *IEEE Trans. Commun.* **45**(7):768–771 (July 1997).
11. M. Ibnkahla, N. J. Bershad, J. Sombrin, and F. Castanié, Neural network modeling and identification of non linear channels with memory: Algorithms, applications and analytic models, *IEEE Trans. Signal Process.* **46**(5), (May 1998).
12. M. Ibnkahla, Applications of neural networks to digital communications—a survey, *EURASIP J. Appl. Signal Process.* **80**:1185–11215 (2000).
13. M. Ibnkahla, Nonlinear system identification using neural networks trained with natural gradient descent, *EURASIP J. Appl. Signal Process.* 1229–1237 (Dec. 2003).
14. M. Ibnkahla, J. Yuan, and R. Boutros, Neural networks for transmission over nonlinear channels, in M. Ibnkahla, ed., *Signal Processing for Mobile Communications Handbook*, CRC Press, 2004, Chap. 19.
15. M. Ibnkahla, Q. Rahman, A. Sulyman, H. Al-Asady, J. Yuan, and A. Safwat, High speed satellite mobile communications: Technologies and challenges, *Proc. IEEE* (special issue on gigabit wireless communications: technologies and challenges) 312–339 (Feb. 2004).
16. G. Karam and H. Sari, A data predistortion technique with memory for QAM radio systems, *IEEE Trans. Commun.* **39**(2):336–344 (Feb. 1991).
17. A. Katz, TWT linearization, *Microwave J.* 78–89 (April 1996).
18. A. R. Kaye, D. A. George, and M. J. Eric, Analysis and compensation of bandpass nonlinearities for communications, *IEEE Trans. Commun.* 965–972 (Oct. 1972).
19. H. Ku, M. D. McKinley, and J. S. Kenney, Quantifying memory effects in RF power amplifiers, *IEEE Trans. Microwave Theory Techn.* **50**(12):2843–2849 (Dec. 2002).
20. H. Ku and J. S. Kenney, Behavioral modeling of power amplifiers considering IMD and spectral regrowth asymmetries, *Proc. IMS 2003*, Philadelphia, PA, 2003.
21. R. G. Medhurst and J. H. Roberts, Distortion of SSB transmission due to AM-PM conversion, *IEEE Trans. Commun. Syst.* **CS-12**:166–176 (June 1964).
22. R. Pawula, The effects of quadratic AM-PM conversion in frequency-division multiplexed multiple-access communication satellite systems, *IEEE Trans. Commun.* **28**(10):1785–1793 (Oct. 1980).
23. D. Root, J. Wood, and N. Tuffillaro, New techniques for nonlinear behavioral modeling of microwave/RF ICs from simulation to nonlinear microwave measurements, *Proc. DAC 2003*, June 2003, pp. 85–90.
24. A. Saleh, Frequency-independent and frequency-dependent nonlinear models of TWT amplifiers, *IEEE Trans. Commun.* **29**(11) (1981).
25. J. F. Sevic and J. Staudinger, Simulation of power amplifier adjacent-channel power ratio for digital wireless communication systems, *Proc. IEEE 47th Vehicular Technology Conf. VTC'97*, Phoenix, AZ, May 4–7, 1997, pp. 681–685.
26. O. Simbo and B. A. Potano, A general theory for intelligible crosstalk between frequency-division multiplexed angle-modulated carriers, *IEEE Trans. Commun.* **COM-24**(9) (Sept. 1976).
27. M. Thomas, M. Weidner, and S. Durrani, Digital amplitude-phase keying with M-ary alphabets, *IEEE Trans. Commun.* **22**:168–180 (1974).
28. J. Vuolevi, *Analysis Measurement and Cancellation of the Bandwidth and Amplitude Dependence of Internodulation Distortion in RF Power Amplifiers*, Ph.D. dissertation, Univ. Oulou, Finland, 2001.
29. J. Xu, M. Yagoub, R. Ding, and Q. Zhang, Neural based dynamic modeling of nonlinear microwave circuits, *Proc. IEEE MTTTS 2002*, June 2003, pp. 1101–1104.
30. G. T. Zhou, Analysis of spectral regrowth of weakly nonlinear power amplifiers, *IEEE Commun. Lett.* **4**(11):357–359 (Nov. 2000).

ANISOTROPY AND BIANISOTROPY

TOM G. MACKAY
 University of Edinburgh
 Edinburgh, United Kingdom
 AKHLESH LAKHTAKIA
 Pennsylvania State University
 University Park, Pennsylvania

1. LINEAR ANISOTROPY AND BIANISOTROPY

Free space or vacuum is isotropic. Its electromagnetic response characteristics are contained in the frequency-domain constitutive relations

$$\left. \begin{aligned} \underline{D}(\underline{r}, \omega) &= \varepsilon_0 \underline{E}(\underline{r}, \omega) \\ \underline{H}(\underline{r}, \omega) &= \mu_0^{-1} \underline{B}(\underline{r}, \omega) \end{aligned} \right\} \quad (1)$$

wherein \underline{r} is the position vector and ω is the angular frequency. The induction field phasors $\underline{D}(\underline{r}, \omega)$ and $\underline{H}(\underline{r}, \omega)$ are scalar multiples of the primitive field phasors $\underline{E}(\underline{r}, \omega)$ and $\underline{B}(\underline{r}, \omega)$, respectively. The constants of proportionality—the permittivity $\varepsilon_0 = 8.854 \times 10^{-12}$ F/m and the permeability $\mu_0 = 4\pi \times 10^{-7}$ H/m of free space—are fundamental to the structure of modern electromagnetic theory [1].

The dielectric media that students are introduced to in their first electromagnetism course are also isotropic, with

$$\left. \begin{aligned} \underline{D}(\underline{r}, \omega) &= \varepsilon(\omega) \underline{E}(\underline{r}, \omega) \\ \underline{H}(\underline{r}, \omega) &= \mu_0^{-1} \underline{B}(\underline{r}, \omega) \end{aligned} \right\} \quad (2)$$

as the constitutive relations. The permittivity scalar ε must be complex-valued and frequency-dependent due to causality. Isotropic magnetic media are described by the constitutive relations

$$\left. \begin{aligned} \underline{D}(\underline{r}, \omega) &= \varepsilon_0 \underline{E}(\underline{r}, \omega) \\ \underline{H}(\underline{r}, \omega) &= \mu^{-1}(\omega) \underline{B}(\underline{r}, \omega) \end{aligned} \right\} \quad (3)$$

wherein the permeability scalar μ is frequency-dependent and complex-valued. Electromagnetically, the most complex of all isotropic media are the isotropic chiral media [2] whose constitutive relations

$$\left. \begin{aligned} \underline{D}(\underline{r}, \omega) &= \varepsilon(\omega) \underline{E}(\underline{r}, \omega) + \chi(\omega) \underline{B}(\underline{r}, \omega) \\ \underline{H}(\underline{r}, \omega) &= \mu^{-1}(\omega) \underline{B}(\underline{r}, \omega) + \chi(\omega) \underline{E}(\underline{r}, \omega) \end{aligned} \right\} \quad (4)$$

employ three complex-valued scalars: ε , μ , and χ .

The induction and the primitive field phasors are aligned in all linear isotropic media, because the constants of proportionality in Eqs. (1)–(4) are scalars. In contrast, the macroscopic properties of anisotropy and bianisotropy denote the directionality of the primitive field phasors relative to the induction field phasors. Specifically, a medium is termed *dielectrically anisotropic* if $\underline{D}(\underline{r}, \omega)$ is not aligned with $\underline{E}(\underline{r}, \omega)$, and *magnetically anisotropic* if $\underline{H}(\underline{r}, \omega)$ is not aligned with $\underline{B}(\underline{r}, \omega)$. In a linear dielectric-magnetic medium, the field phasors are related in the frequency-domain constitutive relations¹

$$\left. \begin{aligned} \underline{D}(\underline{r}, \omega) &= \underline{\varepsilon}(\omega) \cdot \underline{E}(\underline{r}, \omega) \\ \underline{B}(\underline{r}, \omega) &= \underline{\mu}(\omega) \cdot \underline{H}(\underline{r}, \omega) \end{aligned} \right\} \quad (5)$$

by the 3×3 dyadics (i.e., second-rank Cartesian tensors) of permittivity $\underline{\varepsilon}$ and permeability $\underline{\mu}$. Any $n \times n$ dyadic can be interpreted as a $n \times n$ matrix throughout this article [3, Chapter 1].

Many examples of anisotropic dielectric media arise in the context of crystal optics [4,5]. The uniaxial and orthorhombic biaxial crystals, which may be characterized by the permittivity dyadics

$$\underline{\varepsilon}_{\text{uni}}(\omega) = \varepsilon_{11}(\omega) \underline{\hat{x}\hat{x}} + \underline{\hat{y}\hat{y}} + \varepsilon_{33}(\omega) \underline{\hat{z}\hat{z}} \quad (6)$$

and

$$\underline{\varepsilon}_{\text{ortho}}(\omega) = \varepsilon_{11}(\omega) \underline{\hat{x}\hat{x}} + \varepsilon_{22}(\omega) \underline{\hat{y}\hat{y}} + \varepsilon_{33}(\omega) \underline{\hat{z}\hat{z}} \quad (7)$$

respectively, are widely studied; here and hereafter, the Cartesian unit vectors are denoted by $\underline{\hat{x}}$, $\underline{\hat{y}}$, and $\underline{\hat{z}}$. Nematic and smectic liquid crystals are also described by Eqs. (6) and (7), respectively [6,7]. Permeability dyadics with forms analogous to (6) and (7) may be employed to describe diamagnetic and paramagnetic crystals [5]. An important noncrystalline example of anisotropic dielectric behavior is provided by an electron plasma in thermal motion, biased by a static magnetic field [3, Chapter 7]. The corresponding permittivity dyadic has the gyrotropic form

$$\underline{\varepsilon}_{\text{gyro}}(\omega) = \varepsilon_{11}(\omega) (\underline{\hat{x}\hat{x}} + \underline{\hat{y}\hat{y}}) + \varepsilon_{33}(\omega) \underline{\hat{z}\hat{z}} + \varepsilon_{12}(\omega) (\underline{\hat{x}\hat{y}} - \underline{\hat{y}\hat{x}}) \quad (8)$$

¹It is convenient for the solution of boundary-value problems in engineering practice to interchange the roles of $\underline{B}(\underline{r}, \omega)$ and $\underline{H}(\underline{r}, \omega)$ in frequency-domain constitutive relations.

when the biasing magnetostatic field is oriented parallel to $\underline{\hat{z}}$. Magnetically biased ferrites may be characterized in terms of a permeability dyadic analogous to the $\underline{\varepsilon}_{\text{gyro}}$ of (8) [3, Chapter 7].

The generalization from anisotropy to bianisotropy is achieved through the introduction of the magnetoelectric dyadics $\underline{\zeta}(\omega)$ and $\underline{\xi}(\omega)$; thereby, the bianisotropic constitutive relations emerge as [8,9]

$$\left. \begin{aligned} \underline{D}(\underline{r}, \omega) &= \underline{\varepsilon}(\omega) \cdot \underline{E}(\underline{r}, \omega) + \underline{\xi}(\omega) \cdot \underline{H}(\underline{r}, \omega) \\ \underline{B}(\underline{r}, \omega) &= \underline{\zeta}(\omega) \cdot \underline{E}(\underline{r}, \omega) + \underline{\mu}(\omega) \cdot \underline{H}(\underline{r}, \omega) \end{aligned} \right\} \quad (9)$$

If a particular medium is nonhomogeneous, its constitutive dyadics are functions of the position vector \underline{r} ; thus, the nonhomogeneous counterparts of (9) are as follows:

$$\left. \begin{aligned} \underline{D}(\underline{r}, \omega) &= \underline{\varepsilon}(\underline{r}, \omega) \cdot \underline{E}(\underline{r}, \omega) + \underline{\xi}(\underline{r}, \omega) \cdot \underline{H}(\underline{r}, \omega) \\ \underline{B}(\underline{r}, \omega) &= \underline{\zeta}(\underline{r}, \omega) \cdot \underline{E}(\underline{r}, \omega) + \underline{\mu}(\underline{r}, \omega) \cdot \underline{H}(\underline{r}, \omega) \end{aligned} \right\} \quad (10)$$

In the remainder of this article, unless stated otherwise, homogeneity is assumed.

The most commonplace example of bianisotropy arises when a linear isotropic dielectric and/or magnetic medium rigidly attached to a constantly moving reference frame is considered from a stationary reference frame. From the perspective of a stationary observer, the moving medium is bianisotropic [3,10]. Thus, if an isotropic dielectric-magnetic medium with permittivity ε and permeability μ is traveling with uniform velocity \underline{v} , then the constitutive dyadics of the moving medium from the perspective of a stationary observer are

$$\left. \begin{aligned} \underline{\varepsilon}_{\text{mov}} &= \varepsilon [\alpha \underline{I} + (1 - \alpha) \underline{\hat{v}\hat{v}}] \\ \underline{\xi}_{\text{mov}} &= \beta \underline{\hat{v}} \times \underline{I} \\ \underline{\zeta}_{\text{mov}} &= -\beta \underline{\hat{v}} \times \underline{I} \\ \underline{\mu}_{\text{mov}} &= \mu [\alpha \underline{I} + (1 - \alpha) \underline{\hat{v}\hat{v}}] \end{aligned} \right\} \quad (11)$$

where $\underline{I} = \underline{\hat{x}\hat{x}} + \underline{\hat{y}\hat{y}} + \underline{\hat{z}\hat{z}}$ denotes the 3×3 identity dyadic and

$$\alpha = \frac{1 - \varepsilon_0 \mu_0 |\underline{v}|^2}{1 - \varepsilon \mu |\underline{v}|^2}, \quad \beta = \frac{|\underline{v}| (\varepsilon \mu - \varepsilon_0 \mu_0)}{1 - \varepsilon \mu |\underline{v}|^2}, \quad \underline{\hat{v}} = \frac{1}{|\underline{v}|} \underline{v} \quad (12)$$

More exotic examples of bianisotropy arise from direct generalizations of the anisotropic forms (6)–(8). For example, (7) leads to the conceptualization of the orthorhombic biaxial bianisotropic form [11,12]

$$\underline{\gamma}_{\text{ortho}} = \gamma_{11} \underline{\hat{x}\hat{x}} + \gamma_{22} \underline{\hat{y}\hat{y}} + \gamma_{33} \underline{\hat{z}\hat{z}}, \quad (\gamma = \varepsilon, \xi, \zeta, \mu) \quad (13)$$

Media described by the gyrotropic form (8), when mixed with isotropic chiral media [2] and homogenized, give rise to the class of bianisotropic media known as *Faraday chiral media* (FCM) [13,14]. These are described by the constitutive dyadics

$$\underline{\gamma}_{\text{FCM}} = \gamma_{11} (\underline{\hat{x}\hat{x}} + \underline{\hat{y}\hat{y}}) + \gamma_{33} \underline{\hat{z}\hat{z}} + \gamma_{12} (\underline{\hat{x}\hat{y}} - \underline{\hat{y}\hat{x}}), \quad (14)$$

$$(\gamma = \varepsilon, \xi, \zeta, \mu)$$

with $\underline{\xi}_{\text{FCM}} = -\underline{\zeta}_{\text{FCM}}$.

Artificial bianisotropic media have been fabricated since at least the 1890s, when Bose [15] reported experimental results on the passage of microwaves through an ensemble of jute spirals. But the fabrication of artificial bianisotropic media intensified only about a century later, following renewal of interest in chirality [2]. Electrically small wire structures with twists have to be represented by both electric and magnetic dipoles, insofar as scattering is concerned [16]. Hence, ensembles of twisted wires—which can be fabricated in many ways [17,18]—are effectively bianisotropic continua at sufficiently low frequencies.

In the most general linear scenario, each of the four constitutive dyadics $\underline{\underline{\epsilon}}$, $\underline{\underline{\zeta}}$, $\underline{\underline{\xi}}$, and $\underline{\underline{\mu}}$ contains nine complex-valued scalars; in matrix notation, we obtain

$$\underline{\underline{\gamma}} = \begin{pmatrix} \gamma_{11} & \gamma_{12} & \gamma_{13} \\ \gamma_{21} & \gamma_{22} & \gamma_{23} \\ \gamma_{31} & \gamma_{32} & \gamma_{33} \end{pmatrix}, \quad (\gamma = \epsilon, \zeta, \xi, \mu) \quad (15)$$

However, for consistency with the special theory of relativity, all linear media must satisfy the Post constraint [19,20]

$$\text{Trace} \left[(\underline{\underline{\mu}})^{-1} \cdot (\underline{\underline{\zeta}} + \underline{\underline{\xi}}) \right] = 0 \quad (16)$$

Hence, a maximum of 35 independent, complex-valued, frequency-dependent parameters are needed to characterize a bianisotropic medium. The number of parameters may be further reduced by imposing conditions such as Lorentz reciprocity [21]

$$\underline{\underline{\epsilon}} = \underline{\underline{\epsilon}}^T, \quad \underline{\underline{\zeta}} = -\underline{\underline{\zeta}}^T, \quad \underline{\underline{\mu}} = \underline{\underline{\mu}}^T \quad (17)$$

where the superscript ^T denotes the *transpose*. Also, if the effects of dissipation are neglected, then the approximation [3, Section 2.5]

$$\underline{\underline{\epsilon}} = \underline{\underline{\epsilon}}^+, \quad \underline{\underline{\zeta}} = \underline{\underline{\zeta}}^+, \quad \underline{\underline{\mu}} = \underline{\underline{\mu}}^+ \quad (18)$$

may be implemented, with the superscript ⁺ indicating the *conjugate transpose*.

2. POINT GROUPS FOR LINEAR CONSTITUTIVE DYADICS

The specific form of the constitutive dyadics of a medium reflects the spacetime symmetry of the underlying medium physics. In particular, it is the *point group symmetry* of the anisotropic or bianisotropic medium that determines the form of Eq. (15) [22]. Each point group consists of all those space, time and spacetime transformations that bring the medium into self-coincidence. The number of different point groups is 122. These are conventionally divided into the three classes [23,24]: G_1 and G_2 containing 32 point groups each, and G_3 containing 58 point groups. Class G_1 describes those media which are invariant under the time-reversal operation. Lorentz-reciprocal media (17), including anisotropic diamagnetic and paramagnetic media, belong to G_1 . The 32 point groups of G_1 give rise to the seven classical crystallographic systems—

triclinic, monoclinic, orthorhombic, tetragonal, trigonal, hexagonal and cubic [5]—whose point groups and associated constitutive dyadic forms are listed in Table 1. (The 230 *space groups* corresponding to the 32 point groups of G_1 —which specify the symmetry elements of the underlying Bravais lattice—may be found in standard sources such as Ref. 25. The class G_2 does not contain the time reversal operation, whereas point groups of G_3 contain the time-reversal operation in combination with rotation–reflection operations. The classes G_2 and G_3 describe magnetic media (ferromagnetics, antiferromagnetics and ferrimagnetics [23]) and the most general bianisotropic media [26]. The 90 point groups belonging to G_2 and G_3 , together with their corresponding constitutive dyadic forms, are cataloged elsewhere [22,24].

3. PLANE-WAVE PROPAGATION

In the frequency domain, the source-free Maxwell curl postulates are given as [3]

$$\left. \begin{aligned} \nabla \times \underline{\underline{H}}(\underline{\underline{r}}, \omega) + i\omega \underline{\underline{D}}(\underline{\underline{r}}, \omega) &= \underline{\underline{0}} \\ \nabla \times \underline{\underline{E}}(\underline{\underline{r}}, \omega) - i\omega \underline{\underline{B}}(\underline{\underline{r}}, \omega) &= \underline{\underline{0}} \end{aligned} \right\} \quad (19)$$

wherein an $\exp(-i\omega t)$ time dependency has been assumed for the field phasors. The combination of (19) with the bianisotropic constitutive relations (9) yields a self-consistent system of differential equations that may be conveniently expressed in six-vector/dyadic notation as

$$\underline{\underline{L}}(\nabla) + i\omega \underline{\underline{K}}(\omega) \cdot \underline{\underline{F}}(\underline{\underline{r}}, \omega) = \underline{\underline{0}} \quad (20)$$

The linear differential operator $\underline{\underline{L}}(\nabla)$ and 6×6 constitutive dyadic $\underline{\underline{K}}(\omega)$ have the representations

$$\underline{\underline{L}}(\nabla) = \begin{bmatrix} \underline{\underline{0}} & \nabla \times \underline{\underline{I}} \\ -\nabla \times \underline{\underline{I}} & \underline{\underline{0}} \end{bmatrix}, \quad \underline{\underline{K}}(\omega) = \begin{bmatrix} \underline{\underline{\epsilon}}(\omega) & \underline{\underline{\zeta}}(\omega) \\ \underline{\underline{\xi}}(\omega) & \underline{\underline{\mu}}(\omega) \end{bmatrix} \quad (21)$$

and the 6-vector electromagnetic field phasor $\underline{\underline{F}}(\underline{\underline{r}}, \omega)$ is defined as

$$\underline{\underline{F}}(\underline{\underline{r}}, \omega) = \begin{bmatrix} \underline{\underline{E}}(\underline{\underline{r}}, \omega) \\ \underline{\underline{H}}(\underline{\underline{r}}, \omega) \end{bmatrix} \quad (22)$$

Eigenanalysis of the system

$$\underline{\underline{L}}(\underline{\underline{ik}}) + i\omega \underline{\underline{K}}(\omega) \cdot \underline{\underline{F}}_0 = \underline{\underline{0}} \quad (23)$$

is very fruitful for the development of plane-wave solutions

$$\underline{\underline{F}}(\underline{\underline{r}}, \omega) = \underline{\underline{F}}_0 \exp(\underline{\underline{ik}} \cdot \underline{\underline{r}}) \quad (24)$$

of (20), where $\underline{\underline{k}}$ is the wavevector. In general, the associated dispersion relation

$$\det[\underline{\underline{L}}(\underline{\underline{ik}}) + i\omega \underline{\underline{K}}(\omega)] = 0 \quad (25)$$

provides a polynomial of degree four in the components of $\underline{\underline{k}}$. While the derivation of the roots $\underline{\underline{k}}$ of (25) and the

Table 1. The 32 Point Groups of G_1 in the International Notation^a

Medium Type	Crystal System	Point Group	Constitutive Dyadic Form	Number of real-valued scalars
Isotropic	Cubic	23 $m\bar{3}$ 432	$\begin{pmatrix} c_1 & 0 & 0 \\ 0 & c_1 & 0 \\ 0 & 0 & c_1 \end{pmatrix}$	2
		$\bar{4}3m$ $m\bar{3}m$		
Uniaxial	Tetragonal	4 $\bar{4}$ 4/m 422	$\begin{pmatrix} c_1 & 0 & 0 \\ 0 & c_1 & 0 \\ 0 & 0 & c_3 \end{pmatrix}$	4
		4/m m $\bar{4}2m$ 4/m mm		
	Hexagonal	6 $\bar{6}$ 6/m 622	$\begin{pmatrix} c_1 & 0 & 0 \\ 0 & c_1 & 0 \\ 0 & 0 & c_3 \end{pmatrix}$	4
	Trigonal	3 $\bar{3}$ 32	$\begin{pmatrix} c_1 & 0 & 0 \\ 0 & c_1 & 0 \\ 0 & 0 & c_3 \end{pmatrix}$	4
		3 m $\bar{3}m$		
Biaxial	Orthorhombic	222 $mm2$ mmm	$\begin{pmatrix} c_1 & 0 & 0 \\ 0 & c_2 & 0 \\ 0 & 0 & c_3 \end{pmatrix}$	6
	Monoclinic	2 m 2/m	$\begin{pmatrix} c_1 & 0 & r_1 \\ 0 & c_2 & 0 \\ r_1 & 0 & c_3 \end{pmatrix}$	7
	Triclinic	1 $\bar{1}$	$\begin{pmatrix} c_1 & r_1 & r_2 \\ r_1 & c_2 & r_3 \\ r_2 & r_3 & c_3 \end{pmatrix}$	9

^aThe conventional constitutive dyadic forms are also listed [5]; therein, c_n denotes a complex-valued constitutive parameter whereas r_n denotes a real-valued constitutive parameter. Source: Ref. 23.

associated eigenvectors \mathbf{F}_0 is mathematically straightforward, it is a task best undertaken with the aid of a symbolic manipulation package because the process involves unwieldy expressions.

Propagation in a direction parallel to the unit vector $\hat{\mathbf{a}}$ requires determination of the wavenumber k , which is the magnitude of the wavevector $\underline{k} = k\hat{\mathbf{a}}$. In general, two distinct complex-valued solutions—say, k_1 and k_2 —emerge for every $\hat{\mathbf{a}}$. This phenomenon is known as *birefringence*, and every anisotropic/bianisotropic medium is generally birefringent. The difference between the real parts of k_1 and k_2 gives rise to optical rotation, which is the change in the tilt angle of the vibration ellipse of a plane wave on either reflection from or transmission through a birefringent layer. This phenomenon is commonly exploited in the construction of optical waveplates, polarizers, and prisms [4, Chapter 14], as well as microwave gyrators, isolators, and circulators [27, Section 6.8]. The operations of many liquid crystal devices are also based on birefringence [28]. The difference between the imaginary parts of k_1 and k_2 , called *dichroism*, is a measure of differential absorption of two orthogonally polarized plane waves incident on a birefringent layer.

If a wavenumber is independent of $\hat{\mathbf{a}}$, the corresponding solution $\mathbf{F}_0 \exp(ik\hat{\mathbf{a}} \cdot \mathbf{r})$ represents an *ordinary* plane wave;

otherwise, the solution represents an *extraordinary* plane wave. The amplitude vectors \underline{E}_0 and \underline{H}_0 of an ordinary plane wave are always normal to the direction of propagation, but those of an extraordinary plane wave may not be. The amplitude vectors \underline{D}_0 and \underline{B}_0 of both ordinary and extraordinary plane waves are normal to $\hat{\mathbf{a}}$. The time-averaged Poynting vector of an ordinary plane wave is aligned with the direction of propagation, but that of an extraordinary plane wave is generally not. Incidental unirefringence (i.e., $k_2 = k_1$) may arise for a specific $\hat{\mathbf{a}}$ —for instance, when $\hat{\mathbf{a}} = \hat{\mathbf{z}}$ in a uniaxial dielectric medium with permittivity specified by (6). Pathological unirefringence (i.e., $k_2 = k_1$ for all $\hat{\mathbf{a}}$) can also arise, for example, in a uniaxial dielectric–magnetic medium whose permittivity dyadic is a scalar multiple of its permeability dyadic [29]. Anomalous unirefringence is also possible for a specific $\hat{\mathbf{a}}$, when, in addition to $k_2 = k_1$, the amplitude vector $\mathbf{F}_{0_2} = ik_1 \mathbf{r} \cdot \hat{\mathbf{a}} \mathbf{F}_{0_1}$ turns out to be a function of \mathbf{r} whereas \mathbf{F}_{0_1} is spatially uniform [30]; the coalescence of the two plane waves—which exhibits a linear dependence on propagation distance—is known as a *Voigt wave* [31].

Many accounts of plane-wave propagation in complex media are available in the scientific literature. For comprehensive descriptions of plane-wave solutions in

anisotropic media, Ref. 3 is recommended. Propagation in bianisotropic media is an active area of research, using standard eigenanalysis [32], and results are also available for nonhomogeneous examples such as cholesteric liquid crystals [6,7] and helicoidal bianisotropic media [2,33]. The exquisitely beautiful palette of electromagnetic consequences of anisotropy and bianisotropy becomes evident in crystal optics [34,35].

4. DYADIC GREEN FUNCTIONS IN SPECTRAL FORM

In the presence of a six-vector electromagnetic source term $\underline{\mathbf{S}}(\underline{\mathbf{r}}, \omega)$, the Maxwell curl postulates (20) become

$$[\underline{\mathbf{L}}(\nabla) + i\omega\underline{\mathbf{K}}(\omega)] \cdot \underline{\mathbf{F}}(\underline{\mathbf{r}}, \omega) = \underline{\mathbf{S}}(\underline{\mathbf{r}}, \omega) \quad (26)$$

The linearity of (26) implies that its solution may be expressed in terms of a dyadic Green function $\underline{\mathbf{G}}(\underline{\mathbf{r}} - \underline{\mathbf{r}}', \omega)$ as

$$\underline{\mathbf{F}}(\underline{\mathbf{r}}, \omega) = \underline{\mathbf{F}}_h(\underline{\mathbf{r}}, \omega) + \int_V \underline{\mathbf{G}}(\underline{\mathbf{r}} - \underline{\mathbf{r}}', \omega) \cdot \underline{\mathbf{S}}(\underline{\mathbf{r}}', \omega) d^3\underline{\mathbf{r}}' \quad (27)$$

where field and source points are represented by $\underline{\mathbf{r}}$ and $\underline{\mathbf{r}}'$, respectively, with all source points confined to the region V . The field $\underline{\mathbf{F}}_h(\underline{\mathbf{r}}, \omega)$ represents the solution to the source-free version of (26); thus, $\underline{\mathbf{F}}_h(\underline{\mathbf{r}}, \omega)$ is the complementary function. The dyadic Green function itself arises as the solution to the differential equation

$$[\underline{\mathbf{L}}(\nabla) + i\omega\underline{\mathbf{K}}(\omega)] \cdot \underline{\mathbf{G}}(\underline{\mathbf{r}} - \underline{\mathbf{r}}', \omega) = \delta(\underline{\mathbf{r}} - \underline{\mathbf{r}}') \underline{\mathbf{I}} \quad (28)$$

in which the role of the source term is taken by the product of the Dirac delta function $\delta(\underline{\mathbf{r}} - \underline{\mathbf{r}}')$ and the 6×6 identity dyadic $\underline{\mathbf{I}}$. As the present context is that of unbounded space completely filled by a homogeneous medium, $\underline{\mathbf{G}}(\underline{\mathbf{r}} - \underline{\mathbf{r}}', \omega)$ is also required to satisfy the Sommerfeld radiation condition [36].

The method of Green functions is a powerful tool in the analysis of electromagnetic fields. However, the explicit delineation of the dyadic Green function for anisotropic and bianisotropic media continues to provide a

the Fourier transform of (28) yields

$$\underline{\tilde{\mathbf{G}}}(\underline{\mathbf{q}}, \omega) = \frac{1}{i\omega} \frac{\text{adj}[\underline{\tilde{\mathbf{A}}}(\underline{\mathbf{q}}, \omega)]}{\det[\underline{\tilde{\mathbf{A}}}(\underline{\mathbf{q}}, \omega)]} \quad (30)$$

where

$$\underline{\tilde{\mathbf{A}}}(\underline{\mathbf{q}}, \omega) = \begin{bmatrix} \underline{\mathbf{0}} & \frac{1}{\omega}(\underline{\mathbf{q}} \times \underline{\mathbf{I}}) \\ -\frac{1}{\omega}(\underline{\mathbf{q}} \times \underline{\mathbf{I}}) & \underline{\mathbf{0}} \end{bmatrix} + \underline{\mathbf{K}}(\omega) \quad (31)$$

While the analytic properties of the inverse Fourier transform

$$\underline{\mathbf{G}}(\underline{\mathbf{R}}, \omega) = \left(\frac{1}{2\pi}\right)^3 \frac{1}{i\omega} \int_q \frac{\text{adj}[\underline{\tilde{\mathbf{A}}}(\underline{\mathbf{q}}, \omega)]}{\det[\underline{\tilde{\mathbf{A}}}(\underline{\mathbf{q}}, \omega)]} \exp(i\underline{\mathbf{q}} \cdot \underline{\mathbf{R}}) d^3\underline{\mathbf{q}} \quad (32)$$

for anisotropic media are known [40], numerical techniques are needed to explicitly evaluate (32).

5. DYADIC GREEN FUNCTIONS IN CLOSED FORM

Closed-form representations of dyadic Green functions are available for all isotropic media [2]. In contrast, those representations have been found for only a limited set of anisotropic and bianisotropic media [37,39].

For a uniaxial dielectric-magnetic medium characterized by the constitutive dyadics

$$\left. \begin{aligned} \underline{\varepsilon}_{\text{uni}} &= \varepsilon_{11} \left(\hat{\mathbf{x}}\hat{\mathbf{x}} + \hat{\mathbf{y}}\hat{\mathbf{y}} \right) + \varepsilon_{33} \hat{\mathbf{z}}\hat{\mathbf{z}} \\ \underline{\mu}_{\text{uni}} &= \mu_{11} \left(\hat{\mathbf{x}}\hat{\mathbf{x}} + \hat{\mathbf{y}}\hat{\mathbf{y}} \right) + \mu_{33} \hat{\mathbf{z}}\hat{\mathbf{z}} \end{aligned} \right\} \quad (33)$$

the 3×3 dyadic components of the 6×6 dyadic Green function

$$\underline{\mathbf{G}}_{\text{uni}}(\underline{\mathbf{r}} - \underline{\mathbf{r}}', \omega) = \begin{bmatrix} \underline{\mathbf{G}}_{\text{uni}}^{ee}(\underline{\mathbf{r}} - \underline{\mathbf{r}}', \omega) & \underline{\mathbf{G}}_{\text{uni}}^{em}(\underline{\mathbf{r}} - \underline{\mathbf{r}}', \omega) \\ \underline{\mathbf{G}}_{\text{uni}}^{me}(\underline{\mathbf{r}} - \underline{\mathbf{r}}', \omega) & \underline{\mathbf{G}}_{\text{uni}}^{mm}(\underline{\mathbf{r}} - \underline{\mathbf{r}}', \omega) \end{bmatrix} \quad (34)$$

are given as [41]

$$\left. \begin{aligned} \underline{\mathbf{G}}_{\text{uni}}^{ee}(\underline{\mathbf{r}} - \underline{\mathbf{r}}', \omega) &= -i\omega\mu_{11} \left[\left(\varepsilon_{33}\varepsilon_{\text{uni}}^{-1} + \frac{\nabla\nabla}{\omega^2\varepsilon_{11}\mu_{11}} \right) g_\varepsilon(\underline{\mathbf{r}} - \underline{\mathbf{r}}', \omega) - \underline{\mathbf{T}}(\underline{\mathbf{r}} - \underline{\mathbf{r}}', \omega) \right] \\ \underline{\mathbf{G}}_{\text{uni}}^{em}(\underline{\mathbf{r}} - \underline{\mathbf{r}}', \omega) &= -\varepsilon_{11}\varepsilon_{\text{uni}}^{-1} \cdot (\nabla \times \underline{\mathbf{I}}) \cdot \left[\mu_{33}g_\mu(\underline{\mathbf{r}} - \underline{\mathbf{r}}', \omega)\underline{\mu}_{\text{uni}}^{-1} + \underline{\mathbf{T}}(\underline{\mathbf{r}} - \underline{\mathbf{r}}', \omega) \right] \\ \underline{\mathbf{G}}_{\text{uni}}^{me}(\underline{\mathbf{r}} - \underline{\mathbf{r}}', \omega) &= -\mu_{11}\underline{\mu}_{\text{uni}}^{-1} \cdot (\nabla \times \underline{\mathbf{I}}) \cdot \left[-\varepsilon_{33}g_\varepsilon(\underline{\mathbf{r}} - \underline{\mathbf{r}}', \omega)\varepsilon_{\text{uni}}^{-1} + \underline{\mathbf{T}}(\underline{\mathbf{r}} - \underline{\mathbf{r}}', \omega) \right] \\ \underline{\mathbf{G}}_{\text{uni}}^{mm}(\underline{\mathbf{r}} - \underline{\mathbf{r}}', \omega) &= -i\omega\varepsilon_{11} \left[\left(\mu_{33}\underline{\mu}_{\text{uni}}^{-1} + \frac{\nabla\nabla}{\omega^2\varepsilon_{11}\mu_{11}} \right) g_\mu(\underline{\mathbf{r}} - \underline{\mathbf{r}}', \omega) + \underline{\mathbf{T}}(\underline{\mathbf{r}} - \underline{\mathbf{r}}', \omega) \right] \end{aligned} \right\} \quad (35)$$

formidable challenge to theoreticians [37–39]. A spectral representation may be provided as the spatial Fourier transform [8]

$$\underline{\tilde{\mathbf{G}}}(\underline{\mathbf{q}}, \omega) = \int_{\underline{\mathbf{R}}} \underline{\mathbf{G}}(\underline{\mathbf{R}}, \omega) \exp(-i\underline{\mathbf{q}} \cdot \underline{\mathbf{R}}) d^3\underline{\mathbf{R}} \quad (29)$$

with $\underline{\mathbf{R}} = \underline{\mathbf{r}} - \underline{\mathbf{r}}'$. For the homogeneous bianisotropic medium characterized by the 6×6 constitutive dyadic $\underline{\mathbf{K}}(\omega)$,

The scalar Green functions $g_\varepsilon(\underline{\mathbf{r}} - \underline{\mathbf{r}}', \omega)$ and $g_\mu(\underline{\mathbf{r}} - \underline{\mathbf{r}}', \omega)$ in (35) are defined by

$$g_\gamma(\underline{\mathbf{R}}, \omega) = \frac{\exp\left(-i\omega^2\varepsilon_{11}\mu_{11}\sqrt{\gamma_{33}\underline{\mathbf{R}} \cdot \underline{\gamma}_{\text{uni}}^{-1} \cdot \underline{\mathbf{R}}}\right)}{4\pi\sqrt{\gamma_{33}\underline{\mathbf{R}} \cdot \underline{\gamma}_{\text{uni}}^{-1} \cdot \underline{\mathbf{R}}}}, \quad (36)$$

($\gamma = \varepsilon, \mu$)

while the dyadic $\underline{T}(\underline{r} - \underline{r}', \omega)$ is specified as

$$\begin{aligned} \underline{T}(\underline{R}, \omega) &= \left(\frac{\varepsilon_{33}}{\varepsilon_{11}} \underline{g}_\varepsilon - \frac{\mu_{33}}{\mu_{11}} \underline{g}_\mu \right) \frac{(\underline{R} \times \hat{\underline{z}})(\underline{R} \times \hat{\underline{z}})}{(\underline{R} \times \hat{\underline{z}})^2} \\ &+ \left[\underline{I} - \hat{\underline{z}}\hat{\underline{z}} - \frac{2(\underline{R} \times \hat{\underline{z}})(\underline{R} \times \hat{\underline{z}})}{(\underline{R} \times \hat{\underline{z}})^2} \right] \\ &\times \frac{g_\varepsilon \sqrt{\varepsilon_{33} \underline{R} \cdot \underline{\varepsilon}_{\text{uni}}^{-1} \cdot \underline{R}} - g_\mu \sqrt{\mu_{33} \underline{R} \cdot \underline{\mu}_{\text{uni}}^{-1} \cdot \underline{R}}}{i\omega \sqrt{\varepsilon_{11} \mu_{11}} (\underline{R} \times \hat{\underline{z}})^2} \end{aligned} \quad (37)$$

Although analytical progress has been reported towards closed-form dyadic Green functions for general uniaxial bianisotropic media described by the constitutive dyadics

$$\underline{\gamma}_{\text{uni}} = \gamma_{11} \underline{I} + (\gamma_{33} - \gamma_{11}) \hat{\underline{z}}\hat{\underline{z}}, \quad (\gamma = \varepsilon, \zeta, \zeta, \mu) \quad (38)$$

the case remains unsolved [39,42].

Closed-form representations of dyadic Green functions are available for the bianisotropic example provided by a uniformly moving isotropic dielectric–magnetic medium. In the case where $|\underline{v}|$ in (11) is smaller than the phase velocity of a wave in the stationary medium, the 3×3 dyadic Green functions (34) of the moving medium are [3,37]

$$\left. \begin{aligned} \underline{G}_{\text{mov}}^{ee}(\underline{r} - \underline{r}', \omega) &= -i\omega\mu\sqrt{\alpha^3} \left(\underline{I} + \frac{\underline{\varepsilon}_{\text{mov}} \cdot \nabla \nabla}{\mu(\omega\varepsilon\alpha)^2} \right) \frac{\exp(-i\omega\varepsilon\alpha\sqrt{\underline{\mu}\underline{R} \cdot \underline{\varepsilon}_{\text{mov}}^{-1} \cdot \underline{R}})}{4\pi\sqrt{\varepsilon\underline{R} \cdot \underline{\varepsilon}_{\text{mov}}^{-1} \cdot \underline{R}}} \\ \underline{G}_{\text{mov}}^{em}(\underline{r} - \underline{r}', \omega) &= \frac{1}{i\omega} \underline{\varepsilon}_{\text{mov}}^{-1} \cdot [\nabla \times \underline{I} - i\omega(\hat{\underline{v}} \times \underline{I})] \cdot \underline{G}_{\text{mov}}^{mm}(\underline{r} - \underline{r}', \omega) \\ \underline{G}_{\text{mov}}^{me}(\underline{r} - \underline{r}', \omega) &= -\frac{1}{i\omega} \underline{\mu}_{\text{mov}}^{-1} \cdot [\nabla \times \underline{I} - i\omega(\hat{\underline{v}} \times \underline{I})] \cdot \underline{G}_{\text{mov}}^{ee}(\underline{r} - \underline{r}', \omega) \\ \underline{G}_{\text{mov}}^{mm}(\underline{r} - \underline{r}', \omega) &= -i\omega\varepsilon\sqrt{\alpha^3} \left(\underline{I} + \frac{\underline{\mu}_{\text{mov}} \cdot \nabla \nabla}{\varepsilon(\omega\mu\alpha)^2} \right) \frac{\exp(-i\omega\mu\alpha\sqrt{\underline{\varepsilon}\underline{R} \cdot \underline{\mu}_{\text{mov}}^{-1} \cdot \underline{R}})}{4\pi\sqrt{\underline{\mu}\underline{R} \cdot \underline{\mu}_{\text{mov}}^{-1} \cdot \underline{R}}} \end{aligned} \right\} \quad (39)$$

Dyadic scalarization and factorization techniques are commonly implemented in establishing solutions to (28). In outline, the procedure is as follows. Formally

$$\underline{\mathbf{G}}(\underline{r} - \underline{r}', \omega) = [\underline{\mathbf{L}}(\nabla) + i\omega\underline{\mathbf{K}}(\omega)]^\dagger \underline{W}(\underline{r} - \underline{r}', \omega) \quad (40)$$

where the adjoint operation indicated by superscript \dagger is defined implicitly via

$$[\underline{\mathbf{L}}(\nabla) + i\omega\underline{\mathbf{K}}(\omega)]^\dagger \cdot [\underline{\mathbf{L}}(\nabla) + i\omega\underline{\mathbf{K}}(\omega)] = \mathcal{H}(\nabla, \underline{r}, \omega) \underline{\mathbf{I}} \quad (41)$$

The scalar Green function $W(\underline{r} - \underline{r}', \omega)$ in (40) is specified by the action of the scalar fourth-order operator $\mathcal{H}(\nabla, \underline{r}, \omega)$ in (41) as

$$\mathcal{H}(\nabla, \underline{r}, \omega) W(\underline{r} - \underline{r}', \omega) = \delta(\underline{r} - \underline{r}') \quad (42)$$

The construction of the adjoint operator $[\underline{\mathbf{L}}(\nabla) + i\omega\underline{\mathbf{K}}(\omega)]^\dagger$ for anisotropic and bianisotropic media involves straightforward, albeit lengthy, matrix–algebraic operations.

However, solutions to the fourth-order partial differential equation represented by (42) are generally elusive.

The general unavailability of the dyadic Green functions in closed form has meant that a cornerstone of electromagnetic scattering theory—the Huygens principle—has been formulated exactly only for the simplest of anisotropic media [43,44]. Field representations in non-Cartesian coordinate systems are generally unavailable; and the very few counterexamples [45,46] are exceedingly awkward to handle and restricted in scope.

6. DEPOLARIZATION DYADICS

Although closed-form representations of dyadic Green functions are relatively scarce, often in electromagnetic analyses it is sufficient to construct approximative solutions of restricted validity. An important example occurs in the homogenization of particulate composite materials [47,48], wherein the scattering response of an electrically small particle embedded within a homogeneous ambient medium is required. Relative to Eqs. (26) and (27), the particle represents an equivalent source $\underline{\mathbf{S}}(\underline{r}, \omega)$; and the field $\underline{\mathbf{F}}(\underline{r}, \omega)$ is sought for $\underline{r} \in V$ (i.e., in the source region). Provided the particle is sufficiently small compared with the electromagnetic wavelengths, the Rayleigh

approximation

$$\underline{\mathbf{F}}(\underline{r}, \omega) \approx \underline{\mathbf{F}}_h(\underline{r}, \omega) + \underline{\mathbf{D}}(\underline{r}, \omega) \cdot \underline{\mathbf{S}}(\underline{r}, \omega) \quad (43)$$

may be implemented, where

$$\underline{\mathbf{D}}(\underline{r}, \omega) = \int_V \underline{\mathbf{G}}(\underline{r} - \underline{r}', \omega) d^3 \underline{r}' \quad (44)$$

is the 6×6 *depolarization dyadic* of a region of the same shape, orientation, and size as the particle [48]. In the limiting case of a vanishingly small particle, the depolarization dyadic is nonzero because of the singularity of the Green function at the origin.

Consider an ellipsoidal particle with surface parameterized as

$$\underline{r}_e(\theta, \phi) = \eta \underline{U} \cdot \hat{\underline{r}}(\theta, \phi) \quad (45)$$

where $\hat{\underline{r}}(\theta, \phi)$ is the radial unit vector specified by the spherical polar coordinates θ and ϕ . The shape dyadic \underline{U} is a real-valued 3×3 dyadic with positive eigenvalues [49]; the normalized lengths of the ellipsoid semi-axes are specified by the eigenvalues of \underline{U} . In the limit $\eta \rightarrow 0$, the 6×6

depolarization dyadic for the ellipsoidal particle embedded within a homogeneous bianisotropic medium (with 3×3 constitutive dyadics $\underline{\underline{\epsilon}}_{\text{amb}}, \underline{\underline{\xi}}_{\text{amb}}, \underline{\underline{\zeta}}_{\text{amb}}$, and $\underline{\underline{\mu}}_{\text{amb}}$) is given as [50]

$$\underline{\underline{\mathbf{D}}}^{U/\text{amb}} = \begin{bmatrix} \underline{\underline{D}}_{ee}^{U/\text{amb}} & \underline{\underline{D}}_{em}^{U/\text{amb}} \\ \underline{\underline{D}}_{me}^{U/\text{amb}} & \underline{\underline{D}}_{mm}^{U/\text{amb}} \end{bmatrix} \quad (46)$$

where

$$\underline{\underline{D}}_{\lambda\lambda'}^{U/\text{amb}} = \underline{\underline{U}}^{-1} \cdot \underline{\underline{D}}_{\lambda\lambda'}^{U/\text{amb}} \cdot \underline{\underline{U}}^{-1}, \quad (\lambda, \lambda' = e, m) \quad (47)$$

$$\begin{aligned} & \underline{\underline{D}}_{\lambda\lambda'}^{U/\text{amb}} \\ &= \frac{1}{4\pi i \omega} \int_{\phi=0}^{2\pi} \int_{\theta=0}^{\pi} \frac{(\hat{\mathbf{q}} \cdot \underline{\underline{\tau}}_{\lambda\lambda'} \cdot \hat{\mathbf{q}}) \hat{\mathbf{q}} \hat{\mathbf{q}} \sin \theta d\theta d\phi}{(\hat{\mathbf{q}} \cdot \underline{\underline{\epsilon}}_{\text{amb}} \cdot \hat{\mathbf{q}})(\hat{\mathbf{q}} \cdot \underline{\underline{\mu}}_{\text{amb}} \cdot \hat{\mathbf{q}}) - (\hat{\mathbf{q}} \cdot \underline{\underline{\xi}}_{\text{amb}} \cdot \hat{\mathbf{q}})(\hat{\mathbf{q}} \cdot \underline{\underline{\zeta}}_{\text{amb}} \cdot \hat{\mathbf{q}})} \end{aligned} \quad (48)$$

$$\underline{\underline{\tau}}_{ee} = \underline{\underline{\mu}}_{\text{amb}}, \quad \underline{\underline{\tau}}_{em} = -\underline{\underline{\xi}}_{\text{amb}}, \quad \underline{\underline{\tau}}_{me} = -\underline{\underline{\zeta}}_{\text{amb}}, \quad \underline{\underline{\tau}}_{mm} = \underline{\underline{\epsilon}}_{\text{amb}} \quad (49)$$

$$\underline{\underline{\gamma}}_{\text{amb}} = \underline{\underline{U}}^{-1} \cdot \underline{\underline{\gamma}}_{\text{amb}} \cdot \underline{\underline{U}}^{-1}, \quad (\gamma = \epsilon, \xi, \zeta, \mu) \quad (50)$$

and

$$\hat{\mathbf{q}} = \hat{\mathbf{x}} \sin \theta \cos \phi + \hat{\mathbf{y}} \sin \theta \sin \phi + \hat{\mathbf{z}} \cos \theta \quad (51)$$

Thus, (48) provides the components of the integrated singularity of the dyadic Green function.

Explicit evaluations of the surface integrals in (48) are available for several classes of anisotropic media. For a spherical particle (i.e., $\underline{\underline{U}} = \underline{\underline{I}}$) immersed in the orthorhombic biaxial dielectric medium described by (7), the 3×3 depolarization dyadics are [51]

$$\left. \begin{aligned} \underline{\underline{D}}_{ee}^{I/\text{ortho}} &= \frac{1}{i\omega\epsilon_0} (D_x \hat{\mathbf{x}}\hat{\mathbf{x}} + D_y \hat{\mathbf{y}}\hat{\mathbf{y}} + D_z \hat{\mathbf{z}}\hat{\mathbf{z}}) \\ \underline{\underline{D}}_{em}^{I/\text{ortho}} &= \underline{\underline{D}}_{me}^{I/\text{ortho}} = \underline{\underline{0}} \\ \underline{\underline{D}}_{mm}^{I/\text{ortho}} &= \frac{1}{3i\omega\mu_0} \underline{\underline{I}} \end{aligned} \right\} \quad (52)$$

with

$$\left. \begin{aligned} D_x &= \frac{\sqrt{\epsilon_{22}}}{(\epsilon_{22} - \epsilon_{11})\sqrt{\epsilon_{33} - \epsilon_{11}}} [F(v_1, v_2) - E(v_1, v_2)] \\ D_y &= \frac{1}{\epsilon_{22} - \epsilon_{11}} \left\{ \frac{\epsilon_{11} - \epsilon_{22}}{\epsilon_{33} - \epsilon_{22}} - \sqrt{\frac{\epsilon_{33} - \epsilon_{11}}{\epsilon_{22}}} \right. \\ & \left. \left[\frac{\epsilon_{11}}{\epsilon_{33} - \epsilon_{11}} F(v_1, v_2) - \frac{\epsilon_{22}}{\epsilon_{33} - \epsilon_{22}} E(v_1, v_2) \right] \right\} \\ D_z &= \frac{1}{\epsilon_{33} - \epsilon_{22}} \left[1 - \sqrt{\frac{\epsilon_{22}}{\epsilon_{22} - \epsilon_{11}}} E(v_1, v_2) \right] \end{aligned} \right\} \quad (53)$$

where $F(v_1, v_2)$ and $E(v_1, v_2)$ are elliptic integrals of the first and second kinds [52], respectively, and their arguments are

$$v_1 = \tan^{-1} \sqrt{\frac{\epsilon_{33} - \epsilon_{11}}{\epsilon_{11}}}, \quad v_2 = \sqrt{\frac{\epsilon_{33}(\epsilon_{22} - \epsilon_{11})}{\epsilon_{22}(\epsilon_{33} - \epsilon_{11})}} \quad (54)$$

The form of the depolarization dyadics (52) also arises for an ellipsoidal particle embedded in an isotropic dielectric

medium [51,53]. The depolarization dyadics for uniaxial dielectric media follow from (52) as special cases (e.g., $\epsilon_{11} = \epsilon_{22}$) [54]. Furthermore, the depolarization dyadics for gyrotropic dielectric media (8) are precisely the same as those for uniaxial dielectric media, since the surface integrals in (48) are insensitive to skew-symmetric dyadic components [50]. In addition to the representation (52) for spherical/ellipsoidal particles, depolarization dyadics associated with certain infinitely long cylindrical particles in biaxial anisotropic media have also been derived [55,56]. Closed-form representations of depolarization dyadics are not available for the general bianisotropic medium (15), but are established for certain ellipsoidal particles embedded in uniaxial bianisotropic media [50].

7. HOMOGENIZATION

Consider the electromagnetic response of an assembly of particulate media. Provided that the component particles are small compared with the electromagnetic wavelengths, the assembly may be viewed as an effectively homogeneous composite medium (HCM) [47,48]. By the process of homogenization, complex anisotropic and bianisotropic media may be conceptualized—and fabricated—even when the component media themselves are relatively simple. A variety of formalisms have been developed for the purpose of estimating the constitutive properties of HCMs. Three widely used homogenization formalisms—namely, those of Maxwell Garnett, Bruggeman and the strong property fluctuation theory (SPFT)—are outlined in this section. The HCM considered is that arising from two particulate component media, labeled as a and b , which are characterized by the 6×6 constitutive dyadics $\underline{\underline{\mathbf{K}}}_a$ and $\underline{\underline{\mathbf{K}}}_b$, respectively, at the angular frequency ω of interest. The volume fractions of the media a and b are denoted by f_a and $f_b = 1 - f_a$, respectively.

The Maxwell Garnett homogenization formalism is perhaps the simplest and most often utilized formalism. If medium a is present as identically oriented, ellipsoidal particles described by the shape dyadic $\underline{\underline{U}}^a$, then the Maxwell Garnett estimate of the HCM constitutive dyadic is [57]

$$\underline{\underline{\mathbf{K}}}_{\text{MG}} = \underline{\underline{\mathbf{K}}}_b + f_a \underline{\underline{\alpha}}^{a/b} \cdot \left(\underline{\underline{I}} - i\omega f_a \underline{\underline{D}}^{I/b} \cdot \underline{\underline{\alpha}}^{a/b} \right)^{-1} \quad (55)$$

The 6×6 depolarization dyadic $\underline{\underline{D}}^{I/b}$ is that associated with a sphere embedded in medium b , while the dyadic $\underline{\underline{\alpha}}^{a/b}$ is the generalized polarizability density dyadic

$$\underline{\underline{\alpha}}^{a/b} = (\underline{\underline{\mathbf{K}}}_a - \underline{\underline{\mathbf{K}}}_b) \cdot \left[\underline{\underline{I}} + i\omega \underline{\underline{D}}^{U^a/b} \cdot (\underline{\underline{\mathbf{K}}}_a - \underline{\underline{\mathbf{K}}}_b) \right]^{-1} \quad (56)$$

of a particle of medium a embedded in medium b . The estimate (55) is valid for $f_a < 0.3$ only. However, this limitation has been overcome in recent (as of 2004) incremental and differential refinements to the Maxwell Garnett formalism [58]. If $\underline{\underline{D}}^{I/b}$ is replaced by $\underline{\underline{D}}^{U^a/b}$ in (55), then the HCM constitutive dyadic estimate of the Bragg-Pippard formalism [59] results.

The Bruggeman formalism rests on the assertion that the net polarizability density is zero throughout the HCM.

A characteristic feature is that the component media a and b are treated symmetrically. Thus, the Bruggeman homogenization formalism has the advantage over the Maxwell Garnett formalism of being applicable for all volume fractions $f_a \in (0,1)$ [47]. For component media a and b distributed as ellipsoids with shape dyadics $\underline{\underline{U}}^a$ and $\underline{\underline{U}}^b$, respectively, the Bruggeman estimate of the HCM constitutive dyadic $\underline{\underline{K}}_{\text{Br}}$ is obtained by solving the equation [57]

$$f_a \underline{\underline{\alpha}}^{a/\text{Br}} + f_b \underline{\underline{\alpha}}^{b/\text{Br}} = \underline{\underline{0}} \quad (57)$$

with $\underline{\underline{\alpha}}^{a/\text{Br}}$ and $\underline{\underline{\alpha}}^{b/\text{Br}}$ defined and interpreted similarly to $\underline{\underline{\alpha}}^{a/b}$. Half a century after its intuitive initial enunciation [60], Eq. (57) was found to arise naturally within the SPFT [61,62]. For isotropic dielectric–magnetic media, the HCM permittivity and permeability may be extracted simply from (57) as roots of quadratic polynomials. But for anisotropic and bianisotropic media, (57) represents a nonlinear relation in terms of the HCM constitutive parameters embodied in $\underline{\underline{K}}_{\text{Br}}$. Iterative solutions to the nonlinear forms of (57) are straightforwardly computed by applying the Jacobi method [63], for example.

The SPFT provides an approach to homogenization based on the iterative refinement of the Bruggeman estimate $\underline{\underline{K}}_{\text{Br}}$. Unlike the Maxwell Garnett and Bruggeman formalisms, the SPFT accommodates a comprehensive description of the distributional statistics of the component media [61]. Thereby, coherent scattering losses may be accounted for. Successive SPFT iterates recruit successively higher-order spatial correlation functions. Suppose that the particulate geometries of both component media a and b are characterized by the ellipsoidal shape dyadic $\underline{\underline{U}}$. Then the n th-order SPFT estimate of the HCM constitutive dyadic is obtained as [62]

$$\underline{\underline{K}}_{\text{Dy}}^{[n]} = \underline{\underline{K}}_{\text{Br}} - \frac{1}{i\omega} \left(\underline{\underline{I}} + \underline{\underline{\Sigma}}^{[n]} \cdot \underline{\underline{D}}^{U/\text{Br}} \right)^{-1} \cdot \underline{\underline{\Sigma}}^{[n]} \quad (58)$$

wherein the subscript Dy on $\underline{\underline{K}}_{\text{Dy}}^{[n]}$ derives from the central equation in the SPFT, namely, the Dyson equation [61]. The mass operator term $\underline{\underline{\Sigma}}^{[n]}$ —which is an infinite series—is defined in terms of the dyadic Green function $\underline{\underline{G}}_{\text{Br}}(\underline{\underline{R}}, \omega)$ associated with $\underline{\underline{K}}_{\text{Br}}$, together with the normalized polarizability density dyadic $\underline{\underline{\chi}}_l = -i\omega \underline{\underline{\alpha}}^{l/\text{Br}}$ ($l = a, b$). In the derivation of (58), the long-wavelength approximation is invoked. For $n = 0$ and $n = 1$, the SPFT estimates of the HCM constitutive dyadic are degenerate with those of the Bruggeman formalism:

$$\underline{\underline{K}}_{\text{Dy}}^{[0]} = \underline{\underline{K}}_{\text{Dy}}^{[1]} = \underline{\underline{K}}_{\text{Br}} \quad (59)$$

At the level of the so-called bilocal approximation (i.e., $n = 2$), the mass operator is given by

$$\underline{\underline{\Sigma}}^{[2]} = \left(\underline{\underline{\chi}}_a - \underline{\underline{\chi}}_b \right) \cdot \left[\mathcal{P} \int \Gamma(\underline{\underline{R}}) \underline{\underline{G}}_{\text{Br}}(\underline{\underline{R}}) d^3 \underline{\underline{R}} \right] \cdot \left(\underline{\underline{\chi}}_a - \underline{\underline{\chi}}_b \right) \quad (60)$$

and $\underline{\underline{K}}_{\text{Dy}}^{[2]}$ is thus delivered by (58). In (60), \mathcal{P} denotes principal value integration and $\Gamma(\underline{\underline{R}})$ is a two-point covariance function. Evaluations of the mass operator (60) for physically motivated choices of $\Gamma(\underline{\underline{R}})$ have revealed that $\underline{\underline{K}}_{\text{Dy}}^{[2]}$ is largely insensitive to the precise form of the

covariance function [64]. Finite integral representations of $\underline{\underline{K}}_{\text{Dy}}^{[2]}$ are available for both anisotropic [64,65] and bianisotropic [62] composites. In addition, the SPFT iterative procedure converges at the level $n = 2$, at least for weakly anisotropic composites [66].

The constitutive dyadic forms that result from homogenization processes have been extensively investigated [63]. HCMs with biaxial symmetry have come under particular scrutiny [67]. A biaxial HCM arises when the component media present two distinct distinguished axes. These distinguished axes can have either a geometric origin (e.g., component media present as spheroids) or an electromagnetic origin (e.g., component media characterized by uniaxial constitutive dyadics). Furthermore, orthorhombic biaxial HCM structures generally develop, provided that the distinguished axes of the component media are mutually perpendicular; for nonperpendicular distinguished axes, the more general monoclinic or triclinic biaxial HCM form arises.

8. NONLINEAR ANISOTROPY

A general description of bianisotropic nonlinearity (and, therefore, also anisotropic nonlinearity) proceeds as follows: The nonlinear constitutive relations are expressed in six-vector/dyadic notation as [68]

$$\underline{\underline{C}}(\underline{\underline{r}}, \omega) = \underline{\underline{K}}_0 \cdot \underline{\underline{F}}(\underline{\underline{r}}, \omega) + \underline{\underline{Q}}(\underline{\underline{r}}, \omega) \quad (61)$$

where $\underline{\underline{K}}_0$ is the 6×6 constitutive dyadic of free space, and the six-vector

$$\underline{\underline{C}}(\underline{\underline{r}}, \omega) = \begin{bmatrix} D(\underline{\underline{r}}, \omega) \\ B(\underline{\underline{r}}, \omega) \end{bmatrix}. \quad (62)$$

The six-vector $\underline{\underline{Q}}(\underline{\underline{r}}, \omega)$ is the sum of linear and nonlinear parts

$$\underline{\underline{Q}}(\underline{\underline{r}}, \omega) = \underline{\underline{Q}}^{\text{lin}}(\underline{\underline{r}}, \omega) + \underline{\underline{Q}}^{\text{nl}}(\underline{\underline{r}}, \omega) \quad (63)$$

The linear part

$$\underline{\underline{Q}}^{\text{lin}}(\underline{\underline{r}}, \omega) = \left(\underline{\underline{K}}^{\text{lin}}(\omega) - \underline{\underline{K}}_0 \right) \cdot \underline{\underline{F}}(\underline{\underline{r}}, \omega) \quad (64)$$

involves $\underline{\underline{K}}^{\text{lin}}$ as the 6×6 constitutive dyadic to characterize the linear response of the nonlinear medium. The exclusively nonlinear response of the medium, under the simultaneous stimulation by an ensemble of $M > 1$ fields $\underline{\underline{F}}(\underline{\underline{r}}, \omega_m)$, ($m = 1, 2, \dots, M$), is characterized by the six-vector $\underline{\underline{Q}}^{\text{nl}}(\underline{\underline{r}}, \omega)$. At the frequency $\omega = \omega_{\text{nl}}$, the j th element of $\underline{\underline{Q}}^{\text{nl}}(\underline{\underline{r}}, \omega_{\text{NL}})$ is given by

$$\begin{aligned} & \mathcal{Q}_j^{\text{nl}}(\underline{\underline{r}}, \omega_{\text{nl}}) \\ &= \sum_{j_1=1}^6 \sum_{j_2=1}^6 \cdots \sum_{j_m=1}^6 \cdots \sum_{j_M=1}^6 \\ & \times \left\{ \chi_{jj_1 j_2 \dots j_m \dots j_M}^{\text{nl}}(\omega_{\text{nl}}; \mathcal{W}) \prod_{n=1}^M [F_{j_n}(\underline{\underline{r}}, \omega_n)] \right\} \end{aligned} \quad (65)$$

for $j \in [1, 6]$, where $\mathcal{W} = \{\omega_1, \omega_2, \dots, \omega_M\}$ and not all members of \mathcal{W} have to be distinct. The angular frequency ω_{nl} is the

sum

$$\omega_{\text{nl}} = \sum_{m=1}^M a_m \omega_m, \quad a_m = \pm 1 \quad (66)$$

If $a_n = -1$, then $F_{j_n}(r, \omega)$ in (65) should be replaced by its complex conjugate. The nonlinear susceptibility tensor

$$\chi_{j_1 j_2 \dots j_m \dots j_M}^{\text{nl}}(\omega_{\text{nl}}; \mathcal{W}) \quad (67)$$

delineates the nonlinear constitutive properties. A vast range of nonlinear electromagnetic phenomena may be described in terms of (65) [69,70].

The homogenization of nonlinear anisotropic composites has been carried out with various homogenization formalisms [71,72], including the Maxwell Garnett [68,73] and Bruggeman [73,74] formalisms, and the SPFT [75]. For example, the anisotropic dielectric HCM with permittivity dyadic given by the sum of linear and nonlinear contributions

$$\underline{\underline{\epsilon}}(\omega) = \underline{\underline{\epsilon}}^{\text{lin}}(\omega) + \underline{\underline{\chi}}^{\text{nl}}(\omega) |\underline{\underline{E}}(\omega)|^2 \quad (68)$$

is found to arise from isotropic nonlinear component media distributed as ellipsoidal particles [74,75]. Furthermore, the degree of nonlinearity exhibited by the HCM described by (68) can exceed the degree of nonlinearity present in the component phases. This nonlinearity enhancement—which is itself an anisotropic phenomenon—has significant potential for technological applications [76].

BIBLIOGRAPHY

1. E. J. Post, Separating field and constitutive equations in electromagnetic theory, in W. S. Weiglhofer and A. Lakhtakia, eds., *Introduction to Complex Mediums for Optics and Electromagnetics*, SPIE Press, Bellingham, WA, pp. 2003, pp. 3–26.
2. A. Lakhtakia, Chirality, in K. Chang, ed., *Encyclopedia of RF and Microwave Engineering*, Wiley, Hoboken, NJ, 2005.
3. H. C. Chen, *Theory of Electromagnetic Waves*, TechBooks, Fairfax, VA, 1993.
4. M. Born and E. Wolf, *Principles of Optics*, 6th ed., Pergamon Press, Oxford, UK, 1980.
5. J. F. Nye, *Physical Properties of Crystals*, Clarendon Press, Oxford, UK, 1985.
6. S. Chandrasekhar, *Liquid Crystals*, 2nd ed., Cambridge Univ. Press, Cambridge, UK, 1992.
7. P. G. de Gennes and J. A. Prost, *The Physics of Liquid Crystals*, 2nd ed., Clarendon Press, Oxford, UK, 1993.
8. J. A. Kong, Theorems of bianisotropic media, *Proc. IEEE* **60**:1036–1046 (1972).
9. W. S. Weiglhofer, Constitutive characterization of simple and complex mediums, in W.S. Weiglhofer and A. Lakhtakia, eds., *Introduction to Complex Mediums for Optics and Electromagnetics*, SPIE Press, Bellingham, WA, 2003, pp. 27–61.
10. C. T. Tai, *Dyadic Green Functions in Electromagnetic Theory*, 2nd ed., IEEE Press, Piscataway, NJ, 1994.
11. W. S. Weiglhofer and A. Lakhtakia, On electromagnetic waves in biaxial bianisotropic media, *Electromagnetics* **19**:351–362 (1999).
12. T. G. Mackay and W. S. Weiglhofer, Homogenization of biaxial composite materials: bianisotropic properties, *J. Opt. A: Pure Appl. Opt.* **3**:45–52 (2001).
13. N. Engheta, D. L. Jaggard, and M. W. Kowarz, Electromagnetic waves in Faraday chiral media, *IEEE Trans. Anten. Propag.* **40**:367–374 (1992).
14. W. S. Weiglhofer and A. Lakhtakia, The correct constitutive relations of chiroplasmas and chiroferrites, *Microwave Opt. Technol. Lett.* **17**:405–408 (1998).
15. J. C. Bose, On the rotation of polarisation of electric waves by a twisted structure, *Proc. Roy. Soc. Lond. A* **63**:146–152 (1898).
16. A. Lakhtakia, ed., *Selected Papers on Natural Optical Activity*, SPIE Optical Engineering Press, Bellingham, WA, 1990.
17. I. P. Theron and J. H. Cloete, The optical activity of an artificial non-magnetic uniaxial chiral crystal at microwave frequencies, *J. Electromagn. Waves Appl.* **10**:539–561 (1996).
18. K. W. Whites and C. Y. Chung, Composite uniaxial bianisotropic chiral materials characterization: Comparison of predicted and measured scattering, *J. Electromagn. Waves Appl.* **11**:371–394 (1997).
19. E. J. Post, *Formal Structure of Electromagnetics*, Dover, New York, 1997.
20. A. Lakhtakia and W. S. Weiglhofer, Constraint on linear, spatiotemporally nonlocal, spatiotemporally nonhomogeneous constitutive relations, *Int. J. Infrared Millim. Waves* **17**:1867–1878 (1996).
21. C. M. Krowne, Electromagnetic theorems for complex anisotropic media, *IEEE Trans. Anten. Propag.* **32**:1224–1230 (1984).
22. V. Dmitriev, Some general electromagnetic properties of linear homogeneous bianisotropic media following from space and time-reversal symmetry of the second-rank and antisymmetric third-rank constitutive tensors, *Eur. Phys. J. Appl. Phys.* **12**:3–16 (2000).
23. A. S. Nowick, *Crystal Properties via Group Theory*, Cambridge Univ. Press, Cambridge, UK, 1995.
24. V. Dmitriev, Tables of the second rank constitutive tensors for linear homogeneous media described by the point magnetic groups of symmetry, *Prog. Electromagn. Res.* **28**:43–95 (2000).
25. T. Hahn, ed., *International Tables for Crystallography*. Vol. A: *Space-Group Symmetry*, 5th ed., Kluwer Academic Publishers, Dordrecht, The Netherlands, 2002.
26. D. B. Litvin, Point group symmetries, in W. S. Weiglhofer and A. Lakhtakia, ed., *Introduction to Complex Mediums for Optics and Electromagnetics*, SPIE Press, Bellingham, WA, 2003, pp. 79–102.
27. R. E. Collin, *Foundations for Microwave Engineering*, McGraw-Hill, New York, 1966.
28. S. D. Jacobs, ed., *Selected Papers on Liquid Crystals for Optics*, SPIE Optical Engineering Press, Bellingham, WA, 1992.
29. A. Lakhtakia, V. K. Varadan, and V. V. Varadan, Plane waves and canonical sources in a gyroelectromagnetic uniaxial medium, *Int. J. Electron.* **71**:853–861 (1991).
30. A. Lakhtakia, Anomalous axial propagation in helicoidal bianisotropic media, *Opt. Commun.* **157**:193–201 (1998).
31. W. Voigt, On the behaviour of pleochroitic crystals along directions in the neighbourhood of an optic axis, *Phil. Mag.* **4**:90–97 (1902).
32. A. Lakhtakia, Frequency-dependent continuum electromagnetic properties of a gas of scattering centers, *Adv. Chem. Phys.* **85**(2):311–359 (1993).
33. A. Lakhtakia and W. S. Weiglhofer, Further results on light propagation in helicoidal bianisotropic mediums: oblique propagation, *Proc. Roy. Soc. Lond. A* **453**:93–105 (1997); erratum 454:3275 (1998).
34. P. J. Collings, *Liquid Crystals*, Princeton Univ. Press, Princeton, NJ, 1990.

35. C. D. Gribble and A. J. Hall, *Optical Mineralogy: Principles and Practice*, University College London Press, London, UK, 1992.
36. L. B. Felsen and N. Marcuvitz, *Radiation and Scattering of Waves*, IEEE Press, Piscataway, NJ, 1994.
37. W. S. Weiglhofer, Analytic methods and free-space dyadic Green's functions, *Radio Sci.* **28**:847–857 (1993).
38. W. S. Weiglhofer, Frequency-dependent dyadic Green functions for bianisotropic media, in T. W. Barrett and D. M. Grimes, eds., *Advanced Electromagnetism: Foundations, Theory and Applications*, World Scientific, Singapore, pp. 376–389, 1995.
39. F. Olyslager and I. V. Lindell, Electromagnetics and exotic media: A quest for the holy grail, *IEEE Anten. Propag. Mag.* **44**(2):48–58 (2002).
40. P. G. Cottis and G. D. Kondylis, Properties of the dyadic Green's function for an unbounded anisotropic medium, *IEEE Trans. Anten. Propag.* **43**:154–161 (1995).
41. W. S. Weiglhofer, Dyadic Green's functions for general uniaxial media, *IEE Proc. Part H* **137**:5–10 (1990).
42. W. S. Weiglhofer and I. V. Lindell, Analytic solution for the dyadic Green function of a nonreciprocal uniaxial bianisotropic medium, *Arch. Elektron. Übertrag.* **48**:116–119 (1994).
43. N. R. Ogg, A Huygen's principle for anisotropic media, *J. Phys. A: Math. Gen.* **4**:382–388 (1971).
44. A. Lakhtakia, V. K. Varadan and V. V. Varadan, A note on Huygens's principle for uniaxial dielectric media, *J. Wave-Mat. Interact.* **4**:339–343 (1989).
45. X. B. Wu and K. Yasumoto, Cylindrical vector-wave-function representations of fields biaxial Ω -medium, *J. Electromagn. Waves Appl.* **11**:1407–1423 (1997).
46. J. C. Monzon, Three-dimensional field expansion in the most general rotationally symmetric anisotropic material: Application to scattering by a sphere, *IEEE Trans. Anten. Propag.* **37**:728–735 (1989).
47. A. Lakhtakia, ed., *Selected Papers on Linear Optical Composite Material*, SPIE Optical Engineering Press, Bellingham, WA, 1996.
48. A. Lakhtakia, On direct and indirect scattering approaches for homogenization of particulate composites, *Microwave Opt. Technol. Lett.* **25**:53–56 (2000).
49. A. Lakhtakia, Orthogonal symmetries of polarizability dyadics of bianisotropic ellipsoids, *Microwave Opt. Technol. Lett.* **27**:175–177 (2000).
50. B. Michel and W. S. Weiglhofer, Pointwise singularity of dyadic Green function in a general bianisotropic medium, *Arch. Elektron. Übertrag.* **51**:219–223 (1997); erratum **52**:310 (1998).
51. W. S. Weiglhofer, Electromagnetic depolarization dyadics and elliptic integrals, *J. Phys. A: Math. Gen.* **31**:7191–7196 (1998).
52. I. S. Gradshteyn and I. M. Ryzhik, *Table of Integrals, Series, and Products*, Academic Press, London, 1980.
53. H. Fricke, The Maxwell–Wagner dispersion in a suspension of ellipsoids, *J. Phys. Chem.* **57**:934–937 (1953).
54. B. Michel, A Fourier space approach to the pointwise singularity of an anisotropic dielectric medium, *Int. J. Appl. Electromagn. Mech.* **8**:219–227 (1997).
55. P. G. Cottis, C. N. Vazoura, and C. Spyrou, Green's function for an unbounded biaxial medium in cylindrical coordinates, *IEEE Trans. Anten. Propag.* **47**:195–199 (1999).
56. W. S. Weiglhofer and T. G. Mackay, Needles and pillboxes in anisotropic mediums, *IEEE Trans. Anten. Propag.* **50**:85–86 (2002).
57. W. S. Weiglhofer, A. Lakhtakia, and B. Michel, Maxwell Garnett and Bruggeman formalisms for a particulate composite with bianisotropic host medium, *Microwave Opt. Technol. Lett.* **15**:263–266 (1997); erratum **22**:221 (1999).
58. B. Michel, A. Lakhtakia, W. S. Weiglhofer, and T. G. Mackay, Incremental and differential Maxwell Garnett formalisms for bianisotropic composites, *Compos. Sci. Technol.* **61**:13–18 (2001).
59. J. A. Sherwin and A. Lakhtakia, Bragg–Pippard formalism for bianisotropic particulate composites, *Microwave Opt. Technol. Lett.* **33**:40–44 (2002).
60. D. A. G. Bruggeman, Berechnung verschiedener physikalischer Konstanten von heterogenen Substanzen, I. Dielektrizitätskonstanten und Leitfähigkeiten der Mischkörper aus isotropen Substanzen, *Ann. Phys. Lpz.* **24**:636–679 (1935).
61. L. Tsang and J. A. Kong, Scattering of electromagnetic waves from random media with strong permittivity fluctuations, *Radio Sci.* **16**:303–320 (1981).
62. T. G. Mackay, A. Lakhtakia, and W. S. Weiglhofer, Strong-property-fluctuation theory for homogenization of bianisotropic composites: Formulation, *Phys. Rev. E* **62**:6052–6064 (2000); erratum **63**:049901 (2001).
63. B. Michel, Recent developments in the homogenization of linear bianisotropic composite materials, in O. N. Singh and A. Lakhtakia, eds., *Electromagnetic Fields in Unconventional Materials and Structures*, Wiley, New York, 2000, pp. 39–82.
64. T. G. Mackay, A. Lakhtakia, and W. S. Weiglhofer, Homogenisation of similarly oriented, metallic, ellipsoidal inclusions using the bilocal-approximated strong-property-fluctuation theory, *Opt. Commun.* **197**:89–95 (2001).
65. N. P. Zhuck, Strong-fluctuation theory for a mean electromagnetic field in a statistically homogeneous random medium with arbitrary anisotropy of electrical and statistical properties, *Phys. Rev. B* **50**:15636–15645 (1994).
66. T. G. Mackay, A. Lakhtakia, and W. S. Weiglhofer, Third-order implementation and convergence of the strong-property-fluctuation theory in electromagnetic homogenization, *Phys. Rev. E* **64**:066616 (2001).
67. T. G. Mackay and W. S. Weiglhofer, A review of homogenization studies for biaxial bianisotropic materials, in S. Zouhdi, A. Sihvola, and M. Arsalane, eds., *Advances in Electromagnetics of Complex Media and Metamaterials*, Kluwer, Dordrecht, The Netherlands, 2003, pp. 211–228.
68. A. Lakhtakia and W. S. Weiglhofer, Maxwell Garnett formalism for weakly nonlinear, bianisotropic, dilute, particulate composite media, *Int. J. Electron.* **87**:1401–1408 (2000).
69. R. W. Boyd, *Nonlinear Optics*, Academic Press, London, 1992.
70. T. Kobayashi, Introduction to nonlinear optical materials, *Nonlin. Opt.* **1**:91–117 (1991).
71. J. P. Huang, J. T. K. Wan, C. K. Lo, and K. W. Yu, Nonlinear ac response of anisotropic composites, *Phys. Rev. E* **64**:061505 (2001).
72. A. V. Goncharenko, V. V. Popelnukh, and E. F. Venger, Effect of weak nonsphericity on linear and nonlinear optical properties of small particle composites, *J. Phys. D: Appl. Phys.* **35**:1833–1838 (2002).
73. O. Levy and D. Stroud, Maxwell Garnett theory for mixtures of anisotropic inclusions: application to conducting polymers, *Phys. Rev. B* **56**:8035–8046 (1997).
74. M. N. Lakhtakia and A. Lakhtakia, Anisotropic composite materials with intensity-dependent permittivity tensor: The Bruggeman approach, *Electromagnetics* **21**:129–138 (2001).
75. T. G. Mackay, Geometrically derived anisotropy in cubically nonlinear dielectric composites, *J. Phys. D: Appl. Phys.* **36**:583–591 (2003).
76. R. W. Boyd, R. J. Gehr, G. L. Fischer, and J. E. Sipe, Nonlinear optical properties of nanocomposite materials, *Pure Appl. Opt.* **5**:505–512 (1996).